LUND UNIVERSITY

Operando Gas Imaging in Heterogeneous Catalysis

Zhou, Jianfeng

2018

Document Version:
Publisher's PDF, also known as Version of record

Link to publication

Citation for published version (APA):
Zhou, J. (2018). *Operando Gas Imaging in Heterogeneous Catalysis*. [Doctoral Thesis (compilation), Faculty of Engineering, LTH]. Department of Physics, Lund University.

Total number of authors:
1

General rights
Unless other specific re-use rights are stated the following general rights apply:
Copyright and moral rights for the publications made accessible in the public portal are retained by the authors and/or other copyright owners and it is a condition of accessing publications that users recognise and abide by the legal requirements associated with these rights.
• Users may download and print one copy of any publication from the public portal for the purpose of private study or research.
• You may not further distribute the material or use it for any profit-making activity or commercial gain
• You may freely distribute the URL identifying the publication in the public portal

Read more about Creative commons licenses: https://creativecommons.org/licenses/

Take down policy
If you believe that this document breaches copyright please contact us providing details, and we will remove access to the work immediately and investigate your claim.

LUND UNIVERSITY

PO Box 117
221 00 Lund
+46 46-222 00 00

Operando Gas Imaging in Heterogeneous Catalysis

JIANFENG ZHOU
DEPARTMENT OF PHYSICS | FACULTY OF ENGINEERING | LUND UNIVERSITY

Operando Gas Imaging in Heterogeneous Catalysis

Operando Gas Imaging in Heterogeneous Catalysis

Jianfeng Zhou

LUND
UNIVERSITY

Thesis for the degree of Doctor of Philosophy
Thesis advisors: Dr. Johan Zetterberg, Prof. Edvin Lundgren
Faculty opponent: Prof. Dr. Christof Schulz

To be presented, with the permission of the Faculty of Engineering of Lund University, for public criticism in the Rydberg lecture hall (Rydbergsalen) at the Department of Physics on Friday, 16th of November 2018 at 09:15.

Organization	Document name
LUND UNIVERSITY Division of Combustion Physics Department of Physics Box 118 SE-221 00, Lund Sweden	DOCTORAL DISSERTATION Date of issue September 27 2018
Author(s) Jianfeng Zhou	Sponsoring organization

Title and subtitle

Operando gas imaging in heterogeneous catalysis

Abstract

This thesis deals with the development and application of laser-based techniques, for gas phase characterization/gas imaging in heterogeneous catalysis. Two techniques are presented: planar laser-induced fluorescence (PLIF) and degenerate four wave mixing (DFWM).

This thesis is mainly focused on PLIF for the visualization of CO_2 and CO in the vicinity of a catalyst during CO oxidation reaction at semi-realistic conditions, i.e. up to 300 mbar and 400 ^oC. The catalytic CO oxidation on a Pd(100) single crystal model catalyst is used as a showcase throughout this thesis. With its high temporal and spatial resolution, PLIF can deliver 2D spatially resolved gas phase measurements on a sub-second time scale, which allows to follow the dynamic changes in the gas phase above a sample during catalytic processes. The 2D spatially resolved gas phase data facilitates revealing the gas-surface correlation information which is otherwise hidden or difficult to obtain when conventional techniques, e.g. mass spectroscopy (MS), are used. As the gas flow and the reactor geometries have a strong effect on the gas phase above a highly active catalyst, the visualization of CO_2 distribution by PLIF has been used for flow characterization and design of catalytic reactors for studying model catalysts. Furthermore, by combining PLIF and surface sensitive techniques, surface optical reflectance (SOR) and high-energy surface X-ray diffraction (HESXRD), the gas phase and surface can be studied simultaneously. In this way, we can obtain new insights into the spatial and temporal correlations between the gas phase and surface change in *operando* studies by taking advantages of the high spatial and temporal resolution of PLIF, respectively.

For the other gas detection technique, DFWM, only a brief introduction with an example of the detection of CH_3OH is given, aiming at showing its potential application in catalysis.

Key words: planar laser-induced fluoresence, degenerate four wave mixing, gas phase, CO oxidation, model catalyst, hetergeneous catalysis

Classification system and/or index terms (if any)

Supplementary bibliographical information		Language English
ISSN and key title 1102-8718		ISBN 978-91-7753-864-6 (print) 978-91-7753-865-3 (pdf)
Recipient's notes	Number of pages 278	Price
	Security classification	

I, the undersigned, being the copyright owner of the abstract of the above-mentioned dissertation, hereby grant to all reference sources permission to publish and disseminate the abstract of the above-mentioned dissertation.

Signature Jianfeng Zhou Date 2018-09-27

Operando Gas Imaging in Heterogeneous Catalysis

Jianfeng Zhou

LUND
UNIVERSITY

Photocover © Jianfeng Zhou
Cover Illustration: A laser sheet above a Pd single crystal sample.

pp 1-78 © Jianfeng Zhou
Paper I © 2017 by the authors (CC-BY)
Paper II © 2017 by the authors (CC-BY)
Paper III © 2017 American Chemical Society
Paper IV © 2016 by the authors (CC-BY)
Paper V © 2016 by the authors (CC-BY)
Paper VI © 2016 American Chemical Society
Paper VII © 2017 American Chemical Society
Paper VIII © 2015 by the authors (CC-BY)
Paper IX © 2018 by the authors (CC-BY)
Paper X © by the Authors
Paper XI © by the Authors
Paper XII © 2015 Springer

Department of Physics, Faculty of Engineering, Lund University
Lund Reports on Combustion Physics, LRCP-216

ISBN 978-91-7753-864-6 (print)
ISBN 978-91-7753-865-3 (pdf)
ISSN 1102-8718
ISRN LUTFD2/TFCP-216-SE

Printed in Sweden by Media-Tryck, Lund University
Lund 2018

To my wife and my son

Contents

Abstract

This thesis deals with the development and application of laser-based techniques, for gas phase characterization/gas imaging in heterogeneous catalysis. Two techniques are presented: planar laser-induced fluorescence (PLIF) and degenerate four wave mixing (DFWM).

This thesis is mainly focused on PLIF for the visualization of CO_2 and CO in the vicinity of a catalyst during CO oxidation reaction at semi-realistic conditions, i.e. up to 300 mbar and 400 °C. The catalytic CO oxidation on a Pd(100) single crystal model catalyst is used as a showcase throughout this thesis. With its high temporal and spatial resolution, PLIF can deliver 2D spatially resolved gas phase measurements on a sub-second time scale, which allows to follow the dynamic changes in the gas phase above a sample during catalytic processes. The 2D spatially resolved gas phase data facilitates revealing the gas-surface correlation information which is otherwise hidden or difficult to obtain when conventional techniques, e.g. mass spectroscopy (MS), are used. As the gas flow and the reactor geometries have a strong effect on the gas phase above a highly active catalyst, the visualization of CO_2 distribution by PLIF has been used for flow characterization and design of catalytic reactors for studying model catalysts. Furthermore, by combining PLIF and surface sensitive techniques, surface optical reflectance (SOR) and high-energy surface X-ray diffraction (HESXRD), the gas phase and surface can be studied simultaneously. In this way, we can obtain new insights into the spatial and temporal correlations between the gas phase and surface change in *operando* studies by taking advantages of the high spatial and temporal resolution of PLIF, respectively.

For the other gas detection technique, DFWM, only a brief introduction with an example of the detection of CH_3OH is given, aiming at showing its potential application in catalysis.

Popular summary

Catalysis is a vital technology for our modern society. Around 90% of the chemicals used in our daily life are produced with the use of catalysts which make the chemical production more efficient. In addition, catalysis is essential in the field of emission control, e.g. catalysts in the exhaust pipe of fossil fuel-powered cars for converting toxic gases into less harmful ones. An important category of catalysis is heterogeneous catalysis, in which the reactants are in a different phase than the catalyst. The exhaust treatment in cars is an example of this.

Due to the economic and environmental importance of catalysis, there is a great need and interest in research and development of novel catalysts. Research on industrial catalysis is often based on trial and error approaches, which could make the development processes both costly and time consuming. But if we have a fundamental understanding of the catalytic processes on the smallest scale, i.e. the atomic scale, then we can design a catalyst with optimized performance.

Aiming at a fundamental understanding of the catalytic processes on the atomic scale, surface science approaches have been used for catalysis studies. Most conventional surface science studies have been performed at very low pressures (10^{-9} to 10^{-6} mbar), mainly due to the limitations of surface probe techniques. In contrast, industrial catalysts are often operated at ambient (i.e. 1 bar) or even higher pressures. The huge difference in pressures indicates that the knowledge obtained from fundamental studies might not always apply in real world applications.

The advance of surface techniques in the past two decades has make it possible to perform significantly more fundamental studies at elevated pressures. It has been found that as pressure increases, the gas phase starts to play a complex role in the gas-surface interaction. For example, in the case of CO oxidation on transition metals, as soon as the catalyst becomes highly active, i.e. the reaction rate becomes very high, the gas composition close to the surface changes significantly, which in turn could affect the surface properties of the catalyst. In this way, the structure-activity correlation changes. As the changes take place very fast, e.g. at sub-second scale, it is important to follow the change of the gas phase close to the catalyst for a better understanding of a catalyst's

performance.

Conventional gas detection techniques, such as mass spectroscopy (MS) and Fourier transform infrared spectroscopy (FTIR), are often used to analyze the gases at the outlet of a reactor. These techniques have the benefits of measuring several species simultaneously and being easy to operate, but they cannot easily detect the gas composition close to a sample. In this context, laser-based techniques can be used for gas detection, as they can provide *in-situ* measurements with high spatial and temporal resolution in a non-invasive manner.

This thesis is focused on the development and application of laser-based techniques, particularly planar laser-induced fluorescence (PLIF) for gas phase characterization/gas imaging during catalytic processes. In addition, we have combined PLIF with surface sensitive techniques to study the gas phase and surface at the same time, aiming at a deeper understanding of the gas-surface correlations in the processes.

List of publications

This thesis is based on the following papers:

I **A convenient setup for laser-induced fluorescence imaging of both CO and CO_2 during catalytic CO oxidation**

J. Zhou, S. Pfaff, E. Lundgren and J. Zetterberg
Applied Physics B, 2017, 123, 87

II **Visualization of gas distribution in a model AP-XPS reactor by PLIF: CO oxidation over a Pd (100) catalyst**

J. Zhou, S. Blomberg, J. Gustafson, E. Lundgren and J. Zetterberg
Catalysts 2017, 7, 29

III **Simultaneous imaging of gas phase over and surface reflectance of a Pd(100) single crystal during CO oxidation**

J. Zhou, S. Blomberg, J. Gustafson, E. Lundgren and J. Zetterberg
The Journal of Physical Chemistry C 2017, 121, 23511-23519

IV **2D and 3D imaging of the gas phase close to an operating model catalyst by planar laser induced fluorescence**

S. Blomberg, **J. Zhou**, J. Gustafson, J. Zetterberg and E. Lundgren
Journal of Physics: Condensed Matter 2016, 28, 453002

V **Comparison of AP-XPS and PLIF measurements during CO oxidation over Pd single crystals**

S. Blomberg, J. Zetterberg, J. Gustafson, **J. Zhou**, C. Brackmann and E. Lundgren
Topics in Catalysis 2016, 59, 478-486

VI **Strain dependent light-off temperature in catalysis revealed by planar laser-induced fluorescence**

S. Blomberg, J. Zetterberg, **J. Zhou**, L. R. Merte, J. Gustafson, M. Shipilin, A. Trinchero, L. A. Miccio, A. Magaña, M. Ilyn, F. Schiller, J. E. Ortega, F. Bertram, H. Grönbeck and E. Lundgren
ACS Catalysis 2017, 7, 110-114

VII **Novel *in situ* techniques for studies of model catalysts**

E. Lundgren, C. Zhang, L. R. Merte, M. Shipilin, S. Blomberg, U. Hejral, **J. Zhou**, J. Zetterberg and J. Gustafson
Accounts of Chemical Research 2017, 50, 2326-2333

VIII **Spatially and temporally resolved gas distributions around heterogeneous catalysts using infrared planar laser-induced fluorescence**

J. Zetterberg, S. Blomberg, J. Gustafson, J. Evertsson, **J. Zhou**, E.C. Adams, P.A. Carlsson, M. Aldén and E. Lundgren
Nature Communications 2015, 6, 7076

IX **Combining synchrotron light with laser technology in catalysis research**

S. Blomberg, J. Zetterberg, J. Gustafson, **J. Zhou**, M. Shipilin, S. Pfaff, U. Hejral, P. A. Carlsson, O. Gutowski, F. Bertram and E. Lundgren
Journal of Synchrotron Radiation 2018, 25, 1389-1394

X **Experimental and modeling studies of the gas phase of model catalysts in a stagnation flow**

J. Zhou, S. Matera, S. Pfaff, S. Blomberg, E. Lundgren and J. Zetterberg
Submitted to the Journal of Physical Chemistry C

XI **Combining HESXRD with LED reflectance and PLIF for *operando* catalyst surface characterization**

S. Pfaff, **J. Zhou**, U. Hejral, J. Gustafson, M. Shipilin, S. Albertin, S. Blomberg, O. Gutowski, A. C. Dippel, E. Lundgren and J. Zetterberg
In manuscript

XII **Non-intrusive detection of methanol in gas phase using infrared degenerate four-wave mixing**

J. Zhou, A. L. Sahlberg, H. Nilsson, E. Lundgren and J. Zetterberg
Applied Physics B 2015, 121, 123-130

The following papers are not included due to overlapping content or beyond the scope of this thesis:

A **Planar laser induced fluorescence applied to catalysis**

J. Zetterberg, S. Blomberg, **J. Zhou**, J. Gustafson and E. Lundgren
In *Operando* Research in Heterogeneous Catalysis, Springer International Publishing: 2017; 131-149

B **Non-intrusive *in situ* detection of methyl chloride in hot gas flows using infrared degenerate four-wave mixing**

A. L. Sahlberg, **J. Zhou**, M. Aldén and Z. S. Li
Journal of Raman Spectroscopy 2015, 46, 695-701

C **Investigation of ro-vibrational spectra of small hydrocarbons at elevated temperatures using infrared degenerate four-wave mixing**

A. L. Sahlberg, **J. Zhou**, M. Aldén and Z. S. Li
Journal of Raman Spectroscopy 2016, 47, 1130-1139

D **Combining HESXRD and LED reflectance during a catalytic reaction**

S. Albertin, **J. Zhou**, U. Hejral, S. Pfaff, M. Shipilin, S. Blomberg, O. Gutowski, A. C. Dippel, J. Gustafson, J. Zetterberg and E. Lundgren
In manuscript

E **Self-sustained reaction oscillations in a new light**

U. Hejral, S. Albertin, **J. Zhou**, S. Pfaff, M. Shipilin, S. Blomberg, O. Gutowski, A. C. Dippel, J. Gustafson, J. Zetterberg and E. Lundgren
In manuscript

F **Mid-infrared polarization spectroscopy measurements of species concentrations and temperature in a low pressure flame**

A. L. Sahlberg, D. Hot, R. L. Pedersen, **J. Zhou**, M. Aldén and Z. S. Li
Submitted to Applied Spectroscopy

Acknowledgements

In the long journey towards a PhD, one has to face all the highs and lows. I feel incredibly grateful to all the great people I have worked with during my PhD journey. Without their help, the work presented in this thesis would not have been achieved.

First of all, I would like to express my sincere gratitude to my main supervisor Johan Zetterberg for his continuous support and guidance for my PhD study. You were always there when I got stuck on problems in the lab or writing papers. Besides of being an amazing supervisor, you have always been very open to share your opinions on a lot of non-work related things, making me feel like a friend to you. And you never forgot to remind me to enjoy the sunny weather when I was busy with manuscript writing or experiments during the summer. I am grateful for all the trust you put on me.

My sincere thanks also go to my co-supervisor Professor Edvin Lundgren at the division of Synchrotron Radiation Research. You are always very kind to your students, very keen on research and have a great sense of humor. Your endless inspiring ideas have helped me enormously with my research. I have always been impressed by your quick and insightful feedback on my manuscripts and thesis. Very often I got your prompt response to my emails in the evenings, over the weekends or even during the summer holidays.

I am so grateful to Zhongshan Li who gave me the opportunity to work as a project assistant at the division from 2013 to 2014. The one-year working experience has made me decide to pursue a PhD degree at the division. I am also very grateful to Professor Marcus Aldén. Without his tremendous efforts in keeping the division running, such a great workplace would not have existed.

I would like to give a special thank you to Anna-Lena Sahlberg and Sebastian Pfaff. Anna-Lena, you are such a nice person to work with in the lab. Thank you so much for sharing the knowledge on non-linear laser spectroscopy when we worked together in the IR lab. Sebastian, you are one of the most open-minded and smartest people I have ever met. I feel so lucky to have worked with you in the same group. This thesis would not have been completed so smoothly without your help. Thank you for being

a great source of conversation during all the lunchtime we had together, as well as of the knowledge about the Swedish system.

Special thanks also go to the co-workers at the division of Synchrotron Radiation Research, especially Sara Blomberg and Johan Gustafson for their significant contribution to the work presented in this thesis. Sara, you have impressed me a lot with your great enthusiasms in science and work commitment. Thank you for sharing with me the skills in experiments, conference presentations, paper writing, etc. Johan, thank you for the endless interesting discussions about CO oxidation over a Pd(100) and for the teaching about HESRXD. Great thanks also go to Uta Hejral, Mikhail Shipilin and Stefano Albertin, who have made the two beamtimes at Desy so joyful, fruitful and memorable. All of you were also great company during the conferences we have together been to.

I would like to acknowledge Sebastian Matera, my collaborator from Free University of Berlin for his modeling work in the stagnation flow project. I really appreciate his great patience in explaining theoretical physical chemistry to me in many long emails. Thanks to Professor Henrik Grönbeck from Chalmers University of Technology for organizing the great KAW meetings, from which I have learned a lot of knowledge on catalysis and have met so many interesting people from Chalmers. Thanks to Professor Jason Weaver from University of Florida for arranging the STINT workshop in Fort Myers, which is one of my most memorable conference trip.

Thanks to Minna Ramkull and Cecilia Bille for their tireless efforts in assisting me with all kinds of paper work. Thanks to Robert Collin for the carefulness of his work in keeping our experiments safe. Thanks to Igor Buzuk for his phenomenal skill in fixing electronics for us. Thanks to Rutger Lorensson for his smart solutions in solving mechanic problems. Our division would not have been functioning that well without all of you.

In the beginning of my PhD, I shared office with Dina Hot, Sandra Török, Panagiota Stamatoglou and Samuel Jansson in the E324. I really appreciate all their smiles, which have created a very friendly working environment. For the most of my PhD, Karolina Dorozynska has been my office mate. It has been a great pleasure sharing office with you, Karolina. Thanks a lot for your willingness to chat with me whenever I got bored with the monitors and turned around my chair.

I would also like to acknowledge those who have either helped me with solving technical problems or shared their equipment with me for my research work. They are Zhenkan Wang, Dina Hot (again), Christian Brackmann, Andreas Ehn, Edouard Berrocal, Elias Kristensson, Jinlong Gao, Zheming Li, Jiajian Zhu, Fahed Abou Nada and Chengdong Kong. Special thanks to Christoffer Pichler who developed a Labview program during his bachelor project in our group. The program has facilitated a lot of experiments in my research.

My deepest thanks go to my parents and my wife for all their love, support, understanding and tolerance over the past years. Without them, I would not have gone this far. Fangfang, we met in Lund eight years ago when we both started as a master student. Then we became friends, partner, and got married and had our baby. Thank you so much for being in my life, sharing all the happiness and sadness of mine. Thanks to Kevin, you have been a great source of happiness and you make me forget all the troubles every time when I picked you up from the daycare. I love you all so much!

Chapter 1

Introduction

Catalysis is a process in which the rate of a chemical reaction is increased due to the presence of a substance called catalyst, which is not consumed by the catalytic reaction. Catalysis is a vital technology for our modern society. Approximately 90% of the chemicals used in our daily life are produced via catalytic processes in which catalysts are present at one stage or another [1]. Another important application of catalysis can be seen in the field of emission control [2]. One daily life example of that is the three-way catalyst used by almost every gasoline-fueled vehicle for cleaning the exhaust gases, such as CO, NOx and hydrocarbons.

Industrial catalysis can be divided into two types, heterogeneous and homogeneous catalysis. In heterogeneous catalysis, the reactants are in a different phase compared to the catalyst, and the reaction takes place on the catalyst surface. For example, in CO oxidation on transition metals, the CO and O_2 molecules in the gas phase are interacting with the metal in the solid phase. In fact, most large-scale industrial catalytic processes as well as the emission control in cars mentioned above, are in the form of heterogeneous catalysis.

Due to the economic and environmental importance of heterogeneous catalysis, it is of great interest in research and the development of novel, more efficient catalysts with e.g. higher conversion and selectivity. Research on industrial catalysis is often based on trial and error approaches, as it is extremely complex and difficult to study industrial catalytic processes at the atomic scale. Bottom-up approaches utilizing the atomic design of catalysts are therefore considered to be the ultimate solutions for future catalysis technology. This has been the driving force for using surface science approaches to study catalysis for a fundamental understanding of catalytic processes [3].

On the one hand, fundamental catalysis studies are often performed in a well-controlled environment, i.e. at low pressure, e.g. 10^{-9} to 10^{-6} mbar. In contrast,

industrial catalysts are often operated at ambient or even higher pressures. This is referred to as the so-called pressure gap. On the other hand, model catalysts with simple and well-defined structures, e.g. single crystals are often employed in fundamental studies. Industrial catalysts, however, are often materials consisting of nanoparticles which are supported by oxide supports with complex and undefined structures. This is referred to another gap called the materials gap. As can be imagined, it is difficult for fundamental studies to bridge the two gaps at the same time. Instead, the pressure and material gaps can be bridged one at a time. For example, we can perform fundamental studies with simplified model catalysts at more realistic pressures to bridge the pressure gap. Aiming at this goal, recent years have seen great efforts in the development and application of surface techniques for *operando* studies of catalytic reactions [4], including ambient-pressure X-ray photoemission spectroscopy (AP-XPS) [5], high-pressure scanning tunneling microscopy/atomic force microscopy (HP-STM/AFM) [6, 7], surface X-ray diffraction (SXRD) [8], polarization modulated infrared absorption spectroscopy (PM-IRAS) [9, 10], environmental transmission electron microscopy (E-TEM) [11], and surface optical reflectance (SOR) [12, 13].

CO oxidation on transition metals has been studied intensively and is widely used as a model system [14, 15] in the field of catalytic surface science, due to the simplicity of the reaction involving only three different molecules, as well as its importance in applied catalysis for emission control as mentioned above. The reaction process is well known under ultra-high vacuum (UHV) conditions. However, the reaction mechanisms and the active phases responsible for the high activity of the catalyst, particularly at elevated pressures, are still under debate [16, 17, 18, 19]. The main debate about the active phase is whether the metallic surface or the surface oxide is the most active phase.

One of the main difficulties in identifying the active phase in the case of CO oxidation on transition metals lies in the fact that as soon as the catalyst becomes highly active the gas phase close to the surface changes significantly, which in turn affects the surface structure of the catalyst and thereby changes the structure-activity correlation. In addition, gas flow and reactor geometries can strongly affect heat and mass transport during the exothermic reaction of CO oxidation [20, 21, 22, 23], thus increasing the complexity of the gas phase, and the difficulty in comparing experiments with different reactor geometries. In this context, *in situ* knowledge of the gas phase close to the catalyst will be of great value and facilitate making meaningful structure-function interpretation, as the catalyst surface is interacting with and is sensitive to the gas molecules close to it.

Traditionally, techniques such as mass spectrometry (MS) and Fourier transform infrared spectrometry (FTIR) are often used to analyze gases at the outlet of a reactor. These techniques have the advantages of measuring several species simultaneously, but

they are usually not capable to detect the gas composition close to a sample in an easy manner. Although capillary sampling MS techniques are capable to provide spatially resolved gas measurements [24], they cannot deliver 2D spatially resolved gas phase measurements on a sub-second time scale, required to follow dynamic changes in the gas phase. They are also intrusive with the capillaries, which may introduce uncertainty in the data interpretation. For FTIR, although it can be modified for spatially resolved measurements [25], it is a line-of-sight technique which lacks spatial resolution along the light propagation direction.

In order to overcome the limitations of poor spatial and temporal resolution, as well as the intrusiveness from conventional methods, laser-based techniques can be used for gas detection during catalytic reactions. In fact, laser-based diagnostics have been widely used in the combustion community as an indispensable technique for flame studies, which can provide spatially and temporally resolved gas phase information (e.g. concentration and temperature), in a non-invasive manner [26, 27, 28]. In contrast, it has been much less applied in the catalysis community for gas detection. Table 1.1 lists most of the representing works on laser diagnostics in catalysis for gas detection.

In this thesis, two laser-based techniques will be presented for studying the gas phase during catalytic reactions, planar laser-induced fluorescence (PLIF) and degenerate four wave mixing (DFWM). This thesis will be mainly focused on the development and application of PLIF for the detection of CO_2 and CO in the vicinity of a catalyst during CO oxidation reaction at semi-realistic conditions. The catalytic CO oxidation on a Pd(100) single crystal will be used as a showcase throughout the thesis. One of the key results in this work shows that a prominent boundary layer of CO_2 is formed over a highly active catalyst and the gas composition close to the catalyst, as measured by PLIF, is significantly different from the gas composition at the gas outlet, as measured by an MS. As the CO_2 distribution above a highly active catalyst is strongly dependent on the gas flow and the reactor geometry, the visualization of the CO_2 distribution by PLIF can be used for flow characterization of catalytic reactors. Furthermore, by combining PLIF and surface sensitive techniques, we can obtain new insights into the spatial and temporal correlations between the gas phase and surface change in *operando* studies, thanks to the high spatial and temporal resolution of PLIF. For the other gas detection technique, DFWM, a brief introduction and an example will be given, aiming at showing its potential application in catalysis.

The remainder of the thesis is organized as follows. Chapter 2 provides the background of surface science approaches in heterogeneous catalysis using simplified model systems. Chapter 3 describes the essential experimental equipment used in this work. Chapter 4 gives some fundamentals of PLIF and DFWM, as well as a detailed description of the evaluation process of CO_2 and CO PLIF data. Chapter 5 presents two surface techniques, SOR and high-energy surface X-ray diffraction (HESXRD), which

Table 1.1: Related catalysis works on laser diagnostics for gas detection

Catalyst	Reaction	Gas	Press. (mbar)	Temp. (°C)	Ref.
Pt-foil/ Pt(111)	Catalytic water formation reaction	OH	1.3×10^{-3} -13.3	427-1127	[29, 30, 31, 32, 33, 34, 35]
La_2O_3/ Nd_2O_3	O_2 + CH_4/H_2O	OH	1000	370	[36]
V_2O_5	Oxidation of naphthalene to naphthoquinone	Naphthoquinone	1000	370	[37]
Pt	Catalytic combustion of methanol/air	CH_2O	x	x	[38]
Pt	Catalytic combustion of methane/air	OH	1-16 bar	600-1100	[39]
Rh	Partial oxidation of methane	CH_2O	5 bar	200-350	[40]
Rh(553)	Catalytic CO oxidation	CO_2	100	< 500	[41]
$PdCeO_2$/ $PtPdCeO_2$	Catalytic CO oxidation	CO_2	100	< 400	[42]
Pd(110)	Catalytic CO oxidation	CO/CO_2	150	< 400	[43]
Pd(100)	Catalytic CO oxidation	CO/CO_2	150	< 400	[44, 45, 46]
Ag/Al_2O_3	Hydrogen assisted NH_3 oxidation	NH_3	310	160	[47]
Rh pallet	CO_2 hydrogenation	CO_2	300	300	[47]
Pt/Al_2O_3	Catalytic reduction of NO	NO	1000	300	[48]

have been combined with the PLIF technique for simultaneous measurements of the gas phase and the surface in *operando* studies. Chapter 6 presents the key results based on the original work. Chapter 7 gives a summary and an outlook for future work.

Chapter 2

Catalysis and Surface Science

As the properties of a catalyst surface are crucial in the catalytic process, surface science approaches have been used for fundamental understanding of catalysis [49]. This chapter will give the background of the surface science approach in catalysis, with the focus on a very simplified model system, CO oxidation on a Pd single crystal.

2.1 Heterogeneous Catalysis

In heterogeneous catalysis, the catalytic reaction takes place on the catalyst surface. Figure 2.1 shows an example with CO oxidation. The reaction starts with adsorption of CO and O_2 molecules in the gas phase on the catalyst surface. Then the surface reaction takes place on the surface, producing CO_2 that subsequently leaves the surface (into the gas phase). It can also be seen from the figure that the energy barrier in a non-catalytic reaction path is much higher than the barrier of each step in a catalytic reaction path. This means that the reaction is more energetically favorable following a catalyzed path than a non-catalyzed path.

2.2 Model Catalysts

One of the most common types of industrial catalysts is the monolith catalyst. As shown in Fig. 2.2, a monolith catalyst has a honeycomb-shaped block structure as substrate on which active materials, e.g. metal particles, are deposited. The metals are usually in the form of nanoparticle in order to maximize the surface area. It is difficult to perform fundamental studies on these nanoparticles because their structures are very ill-defined. One common way of studying them is to simplify the system by using model catalysts. For example, well-defined extended surfaces of single crystals can be used to mimic the properties of the extended facets in a nanoparticle [1]. To

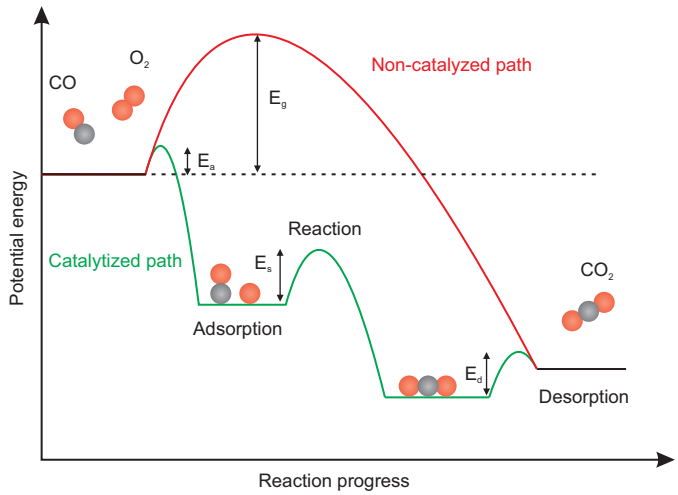

Figure 2.1: Schematic of the energetics associated with a catalytic and a non-catalytic CO oxidation reaction. Activation energies: E_g for gas phase reaction; E_a for adsorption; E_s for surface reaction; E_d for desorption.

add more complexity, vicinal surfaces of single crystals can be used to mimic the edges of a nanoparticle. In this way, the material gap between surface science and industrial catalysis can to some extent be bridged.

A single crystal is a material in which atoms are located in a specific building block, i.e. the unit cell, that repeats periodically and many of them build the entire crystal. There are different classes of building block or unit cell for single crystal materials. Here only the face-centered cubic (fcc) class is discussed, as Pd single crystals that are used as model catalysts throughout this thesis belong to this class.

As shown in Fig. 2.3, by slicing the crystal through different planes we can get planes with different atom orientations. They are named (100), (110) and (111) planes according to the Miller indices. These planes are atomically flat, and are referred to as low index surfaces. As can be clearly seen, the atoms on these surfaces have different numbers of neighboring atoms. For example, an atom has 4 nearest neighbors in the (100) surface while it has 6 in the (111) surface. The coordination of atoms has a significant effect on the reactivity of the atoms, because different coordination numbers means different ability of absorbing or desorbing molecules. Generally, the (100) atoms are more reactive than the (111) atoms.

Instead of being cut in the low index planes, the crystal can be cut at a small angle relative to one of the low index planes. In this way a so-called vicinal plane can be obtained. Depending on the cutting angle, the width of terraces and the height of steps

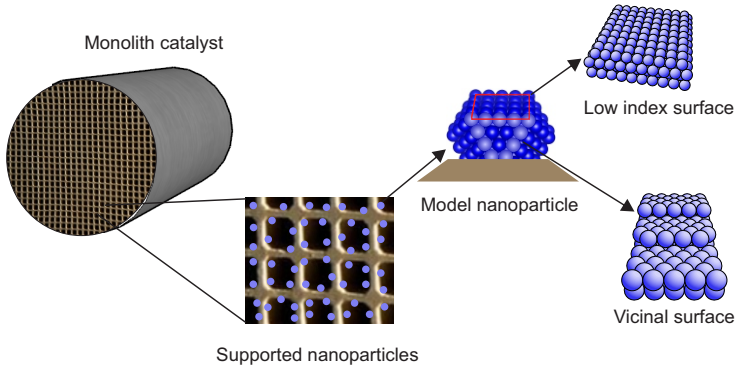

Figure 2.2: The relation between an industrial catalyst and model catalysts used for surface science studies.

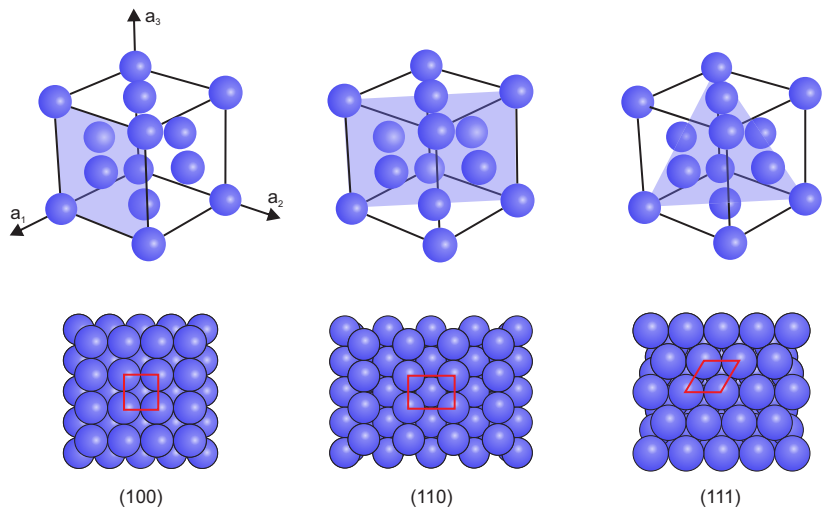

Figure 2.3: Low index surfaces of an fcc crystal. The shaded planes indicate the cutting orientations to obtain the corresponding low index surface. The surface unit cells are marked in red.

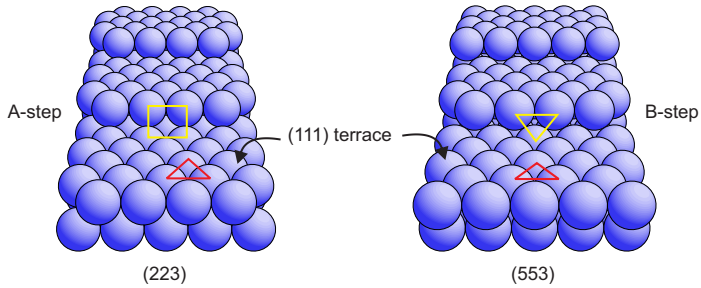

Figure 2.4: Vicinal surfaces of (223) and (553), which have the same terrace orientation but different types of step. The yellow square indicates the A-type step in the (223) surface while the yellow triangle indicates the B-type step in the (553) surface.

can be varied. Figure 2.4 shows two vicinal surfaces, named (223) and (553), respectively. Both surfaces contain (111) terraces but they have different step orientations—the (223) has steps with a (100) orientation, also called the A-type step, while the (553) has steps with a (111) orientation, also called the B-type step. Due to the role of steps, a Pd(553) surface exhibits a lower activation temperature than a Pd(111) surface during CO oxidation, as shown by a side-by-side comparison measurement with PLIF, which will be presented in Chapter 6 (see Fig. 6.9).

There is one more type of single crystal that has been used as model catalyst in this work. That is a Pd crystal with a curved shape, as shown in Fig. 2.5a, also named cylindrically shaped crystal. The crystal is polished around the the (111) plane, and the terrace width and the step height are determined by the miscut angle, as illustrated in Fig. 2.5b. The cylindrical shaped crystal is polished at varying angles, resulting in terraces on both sides with decreasing terrace width, as illustrated in Fig. 2.5c. Both sides contains terraces with a (111) orientation, but one side has A-type steps while the other side has B-type steps. Due to the role of the steps in releasing strain on the mircoterraces, the side with B-type steps shows a lower activation temperature than the side with A-type steps for a Pd(111) curved crystal, as studied in Paper VI and will be presented in Chapter 6 (see Fig. 6.7).

2.3 Surface Structures

As mentioned above, a catalytic reaction in heterogeneous catalysis proceeds with the adsorption of molecules on the catalyst surface. The surface structures of catalysts are therefore of importance to study. As this thesis focuses on a Pd(100) surface, a brief introduction of the oxygen induced structures of the Pd(100) surface is given here.

By exposing a Pd(100) surface to a small amount of O_2 at UHV and room tem-

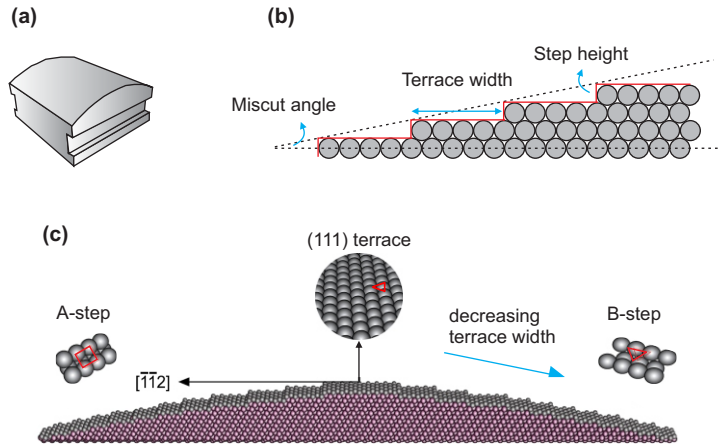

Figure 2.5: Cylindrical shaped Pd crystal. (a) A macroscopic view of the crystal. (b) The relation among the miscut angle, the terrace width and the step height. (c) A schematic of the crystal from a microscopic view.

perature, two well-known chemisorbed structures can be formed, p(2×2) with 0.25 monolayer (ML) of O_2 , and c(2×2) with 0.5 ML of O_2 [50], as shown in Fig. 2.6a and b, respectively. At higher partial pressures of O_2 and higher temperatures, a Pd oxide (PdO) with $\sqrt{5} \times \sqrt{5} - R27^\circ$ structure can be formed on the surface, as shown in Fig. 2.6c. The surface oxide has an O_2 coverage of 0.8 ML and consists of a single PdO(101) plane [51, 52, 53, 54].

It has been shown that under reaction conditions with a low excess of O_2, an epitaxial PdO forms on the Pd surface, and with further increase of O_2, a polycrystalline PdO starts to grow locally and eventually covers the entire surface [55]. Studies have suggested that the $\sqrt{5} \times \sqrt{5} - R27^\circ$ surface oxide and the epitaxial PdO(101) have distinct properties due to the Coordinately Unsaturated Sites (CUS) [56], at which CO may adsorb and O_2 dissociates, compared to the polycrystalline PdO which could transform into PdO(100)-the most stable PdO surfaces [57]. Due to the oxide formation, the surface can get roughened during the oxidation processes [58]. Both oxide formation and surface roughening can lead to a decrease of the optical reflectivity of the surface [13]. This is discussed in more detail in Paper III and XI.

2.4 CO Oxidation

CO oxidation on Pt-group metals is one of the simplest model reactions to study [14]. Nevertheless, the exact reaction mechanisms responsible for the catalytic reaction are not yet fully understood. There are three reaction mechanisms that have been pro-

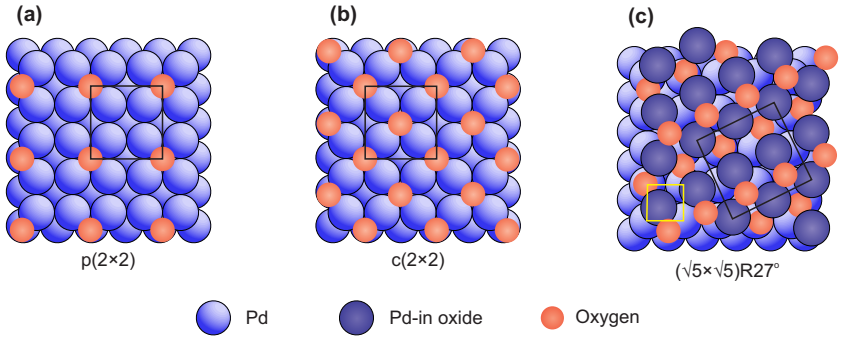

Figure 2.6: Oxygen induced structures of Pd(100). (a) p(2×2) chemisorbed O_2 with 0.25 ML. (b) c(2×2) chemisorbed O_2 with 0.5 ML. (c) $\sqrt{5} \times \sqrt{5} - R27°$ surface oxide with 0.8 ML. Surface unit cells are marked in black while the unit cell of the Pd in the bulk in (c) is marked in yellow.

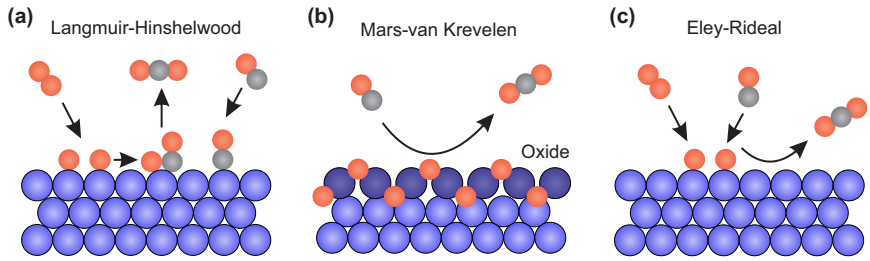

Figure 2.7: Three different reaction mechanisms proposed for describing CO oxidation over Pt-group metals.

posed to describe the reaction, as depicted in Fig. 2.7. In the Langmuir-Hinshelwood mechanism, the reaction starts with adsorption of both CO and O_2 on the surface. If the O_2 molecules receive enough energy, it will dissociate into two oxygen atoms. The adsorbed oxygen atoms and CO molecules then diffuse on the surface until they react with each other forming CO_2, which subsequently desorbs from the surface. This mechanism was suggested for CO oxidation on Pd(100) by Gao *et al.* [10]. In the Mars-van Krevelen mechanism, absorbed CO molecules react with oxygen atoms embedded in the surface of a catalyst, e.g. surface oxides, and form CO_2. Due to the presence of oxides on the surface, this mechanism generally requires oxidizing conditions. This mechanism was suggested for CO oxidation on Pd(100) in Refs. [58, 59]. In the Eley-Rideal mechanism, the CO molecules in the gas phase directly react with the adsorbed oxygen atoms on the surface without being absorbed. This mechanism was suggested for CO oxidation on a PdO surface by Hirvi *et al.* [60].

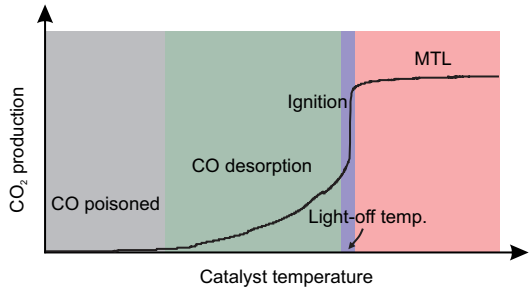

Figure 2.8: The CO_2 production as a function of temperature, showing the different reaction phases during CO oxidation over a Pd catalyst.

This work focuses on CO oxidation over Pd surfaces. A typical experiment is performed in a gas mixture of CO and O_2 when the temperature of catalyst is slowly increased. A typical MS trend of the CO_2 signal as a function of temperature is shown in Fig. 2.8. When the temperature is low at the beginning of the ramp, almost no CO_2 is produced, indicating an inactive surface. In this phase, the CO molecules are occupying the adsorption sites on the surface, i.e. inhibiting the O_2 molecules from dissociating on the surface. This phase is thus called the CO poisoned phase. As the temperature increases further, production of CO_2 is detected, however, the surface is not yet highly active. In this low active phase, the CO molecules are desorbing from the surface, leaving sites for the O_2 molecules to dissociate and react with the CO. In the CO desorption phase, information of the kinetics of the reaction, e.g. activation energies, can be extracted, as presented in Paper VII. As the temperature of the catalyst further increases, a jump can be seen in the CO_2 production, indicating the ignition of the catalyst. The corresponding temperature can be called light-off, ignition or activation temperature. After the ignition, the CO_2 production stabilizes at a constant value even with the further increase of the temperature. This is due to the fact that the reaction rate is so high that the reaction is not limited by the kinetic rate anymore, but by the ability of reactants diffusing and reaching onto the surface. This phenomenon is called mass transfer limitation (MTL), and the corresponding reaction phase is the MTL regime. The MTL regime is of great interest to study as it is the highly active phase of the catalyst. This is also the main reason why this thesis work is focused on the gas phase measurements in the MTL regime.

Self-sustained reaction oscillations in heterogeneous catalysis is an interesting phenomenon in which the catalytic reaction undergoes periodic cycles of high and low activity at a constant condition, e.g. heating and flow [61, 62]. For CO oxidation over Pt-group metals, the oscillation phenomenon has been studied for many years with an attempt to get a fundamental understanding of the underlying reaction mechanisms

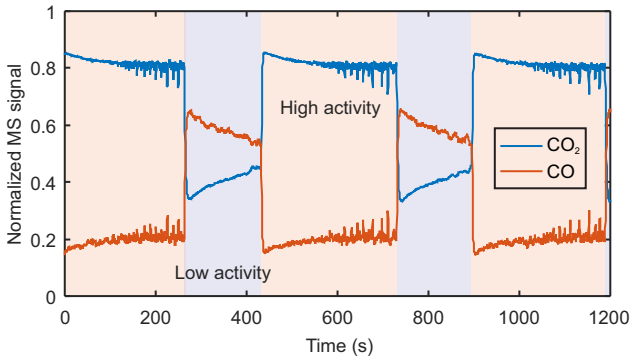

Figure 2.9: Self-sustained reaction oscillations over a Pd(100) surface during CO oxidation, measured by an MS.

[58, 63, 59]. Figure 2.9 shows the CO and CO_2 signal measured by an MS during CO oxidation over a Pd(100), illustrating the oscillating activity of the catalyst. In this work, we have studied the oscillations in CO oxidation over a Pd(100) catalyst with a focus on the dynamic changes of the gas compositions above the catalyst surface. In Paper III and IV, we have shown that the gas composition close to the surface changes dramatically during the high activity regime leaving a more oxidizing environment, compared to the low activity regime. We show that the alternative changes of the gas environment play an important role in the oxidation and reduction processes of the surface during the oscillations.

Chapter 3

Experimental Equipment

In this chapter, the essential experimental equipment used in the present work are described in detail, including light sources, detectors and catalytic reactors. Figure 3.1 shows the overview of the experimental setup, including gas and heating systems, for CO_2 and CO PLIF measurements during catalytic CO oxidation.

3.1 Light Source

3.1.1 IR Sources

Two different IR laser systems have been used for the detection of CO_2. One is broadband, and the other is narrowband. Comparisons of the key parameters between the two systems are presented in table 3.1.

Broadband

The broadband IR laser source was generated as follows. The fundamental 1064 nm laser beam with around 350 mJ/pulse from an injection seeded single-mode Nd:YAG

Table 3.1: Comparisons of the key parameters between the two IR laser systems for CO_2 PLIF measurements

CO_2 PLIF	Excitation wavelength (μm)	Linewidth (cm^{-1})	Linewidth (nm)	Pulse energy (mJ)	Pulse length (ns)	Rep. rate (Hz)
Broadband	2.7	10	7.3	7	5	10
Narrowband	2.7	0.025	0.018	4	5	10

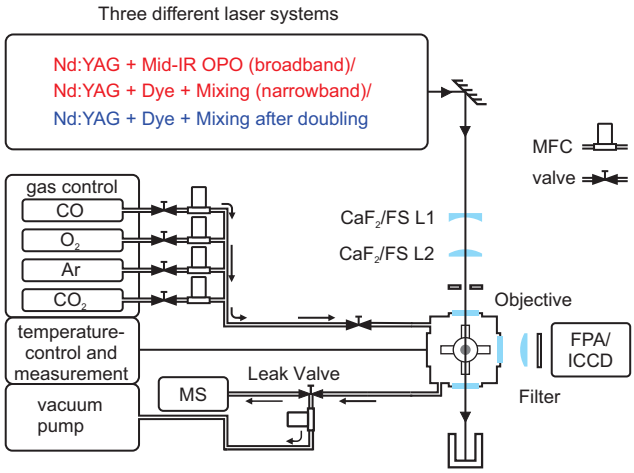

Figure 3.1: A schematic of the experimental setup for CO_2 and CO PLIF measurements.

laser (Continuum, Powerlite DLS 8010) was used to pump an infrared optical parametric oscillator (IR OPO; GWU, versaScan-L 1064) with an $LiNBO_3$ crystal, which produced a signal beam at around 1.7 µm and an idler beam at around 2.7 µm, with 8 and 7 mJ/pulse, respectively. The idler beam was then used to probe CO_2. The full width of half maximum (FWHM) of the idler beam was estimated in this work to be around 10 cm^{-1}. The beam divergence of the broadband IR beam was found to be substantially larger than that of the narrowband IR beam.

Narrowband

The second harmonic of an injection seeded Nd:YAG laser (Spectra Physics PRO 290-10) was used to pump a double-grating dye laser (Sirah, PRC-D-18) running on LDS 765 dye (Exiton), with ethanol as solvent. This produced tunable laser light around 763 nm, which was then difference frequency mixed in a $LiNbO_3$ crystal with part of the residual 1064 nm output from the Nd:YAG laser, generating mid-infrared laser pulses at round 2.7 µm. This mid-IR laser light was further amplified in another $LiNbO_3$ crystal pumped by the rest of the residual 1064 nm light. This process generated tunable mid-IR laser light with a repetition rate of 10 Hz, pulse length of 4 ns, and pulse energy of 4 mJ. The FWHM of the mid-IR output was measured to be 0.025 cm^{-1} [64]. For the detection of CO_2, the wavelength was tuned to 2.7 µm. For the detection of methanol, the same narrowband IR laser system was used but with two different dyes, LDS 798 and LDS 765, to generate IR beams in two wavelength ranges, 2960-3030 cm^{-1} and 3650-3700 cm^{-1}, respectively.

Table 3.2: Characteristics of the UV source for CO PLIF measurements

CO PLIF	Excitation wavelength (nm)	Linewidth (cm^{-1})	Linewidth (nm)	Pulse energy (mJ)	Pulse length (ns)	Rep. rate (Hz)
UV source	230.1	0.5	0.0026	10	5	10

3.1.2 UV Source

CO was detected via two-photon excitation at 230.1 nm. The UV beam was generated from the following process: the second harmonic with 800 mJ/pulse from the injection seeded Nd:YAG laser (Continuum, Powerlite DLS 8010) was used to pump a dye laser (Continuum, Vista) running on R610 dye (Exiton), which produced a fundamental output at 587.2 nm with pulse energy of 150 mJ, and a linewidth of 0.05 cm^{-1}. The fundamental beam was then frequency doubled by a BBO crystal, giving a UV beam at 293.6 nm with pulse energy of around 30 mJ. This UV beam was mixed in another BBO crystal with the residual 1064 nm beam from the Nd:YAG laser, generating a laser light at 230.1 nm. The key parameters of the UV beam are summarized in table 3.2.

3.1.3 LED

A light-emitting diode (LED, Thorlabs M625L3) was used for the surface optical reflectance (SOR) measurements. The power of the LED can be tuned up to 700 mW by an LED driver. The nominal wavelength of the LED is 625 nm.

3.1.4 X-Ray

The X-ray source at beamline P07 at PETRA III at Deutsches Elektronen-Synchrotron (DESY) was used for the HESXRD measurements. During the experiments, the beam had a photon energy of 85 keV and photon intensity on the order of 5×10^{10} photons per s. The unfocused and focused beam sizes at the sample position were about 1.2×1 mm^2 and 2×30 μm^2, respectively. For optimized surface sensitivity, the beam was incident on the sample surface at a grazing angle of 0.04°.

3.2 Detectors

3.2.1 IR Camera

For CO_2 imaging, a liquid-nitrogen-cooled InSb IR camera (Santa Barbara Focal Plane, SBF LP134) was used. The pixel resolution of the camera is 256×256. An objective (f=50 mm, f/2.3) was mounted on the camera. The objective is coated for transmission

of 2-6 μm. The maximum frame rate of the camera is 200 fps. Up to 4 interference filters can be put on the rotatable mount inside the camera for detection of specific gases.

3.2.2 IR Point Detector

An InSb point detector (Judson technologies, J10D-M204-R04M-60) was used for the IR-DFWM measurements of methanol. The detector is sensitive in the wavelength range of 1-5.3 μm, and requires use of liquid nitrogen cooling down to 77 K to reduce thermal noise. The round InSb chip is 4 mm in diameter. The signal from the detector was amplified by a PA-9 trans-impedance preamplifier.

3.2.3 ICCD Camera

For CO imaging, an intensified charge-coupled device (ICCD) camera (Princeton Instruments, PIMAX 3) with an objective (Nikkor f=50 mm, f/1.2) and a 31-mm extension ring was used. The pixel resolution of the camera is 1024×1024. The camera is capable of ultra-fast gating in nanosecond range, which favors the detection of fluorescence signal and discriminates background.

3.2.4 CMOS Camera

A CMOS camera (Andor Zyla) was used for the surface optical reflectance measurements. The camera can be operated at a repetition rate up to 200 Hz. The pixel resolution of the camera is 2048×2048 and the sensor size is 13.3×13.3 mm.

3.2.5 2D X-Ray Detector

A 2D Perkin-Elmer detector with a 4-megapixel resolution was used for the detection of the X-ray diffraction signal in the HESXRD measurements. The active area is 410× 410 mm^2 and the pixel size is 0.2 × 0.2 mm^2. The detector is specially designed for high-energy radiation. However, tungsten metal pieces were used to protect the detector from strong Bragg reflections from the single crystal sample and the sapphire chamber.

3.3 Catalytic Reactors

Two different reactors have been used in this work. One is a mini reactor as shown in Fig. 3.2, and the other one is an UFO reactor, as shown in Fig. 3.3. Both reactors are built by Leiden Probe Microscopy BV (LPM), and are compatible with a cubical chamber, as shown in Fig. 3.2a, and a cylindrical sapphire/fused silica chamber, as

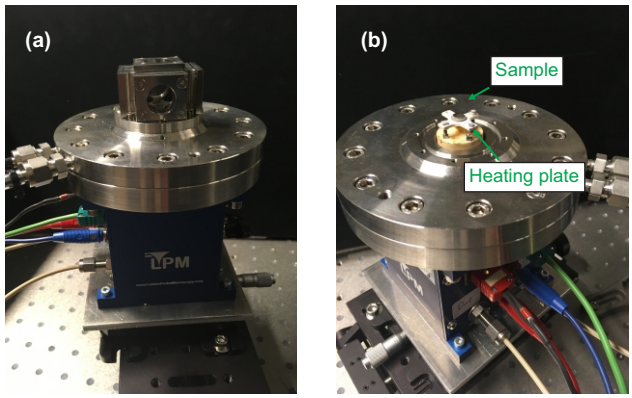

Figure 3.2: The mini catalytic reactor (a) with a cubical chamber, and (b) without the chamber.

shown in Fig. 3.3b. The cubical chamber has a volume of 23 cm^3 and five windows for optical accesses, while the cylindrical sapphire/fused silica chamber has a volume of around 18 cm^3. The sapphire chamber is transparent in both the mid-IR and the UV, and was used for the CO_2 PLIF measurements, while the fused silica one is transparent in the UV and was used for the CO PLIF measurements.

Both the mini and UFO reactors use similar gas and heating systems, as shown in Fig. 3.1. Gases were supplied to the reactors by individual mass flow controllers (MFC, Bronkhorst EL-FLOW). The maximum flow of the MFCs is 50/200 ml_n min^{-1}. A digital pressure controller (Bronkhorst EL-PRESS) at the gas outlet was used to regulate the gas pressure in the reactor from 1 mbar to 1 bar.

A boralectric heater was used to hold and heat the sample, as shown in Fig. 3.2b. The temperature of the heating plate was measured by a type-D thermocouple attached to the plate. The temperature of the heating plate was calibrated by phosphor thermometry under different gas conditions (flow and pressure), as referred to Ref. [65]. It was found that the temperature of a phantom sample (2 mm thick) positioned on the heating plate is similar to that of the center of the heating plate, and it is not very sensitive to the gas conditions. The following equation is used to calibrate the temperature of a heated sample in this work:

$$T_{sample} = T_{TC} \times 1.35 + 22.5 \tag{3.1}$$

where T_{TC} is the temperature measured by the thermocouple. Note that the equation holds its high accuracy for 50 °C $< T_{TC} <$ 400 °C.

The UFO reactor has two separate chambers, reactor chamber and preparation chamber. The reactor can be operated in two different configurations. In the first

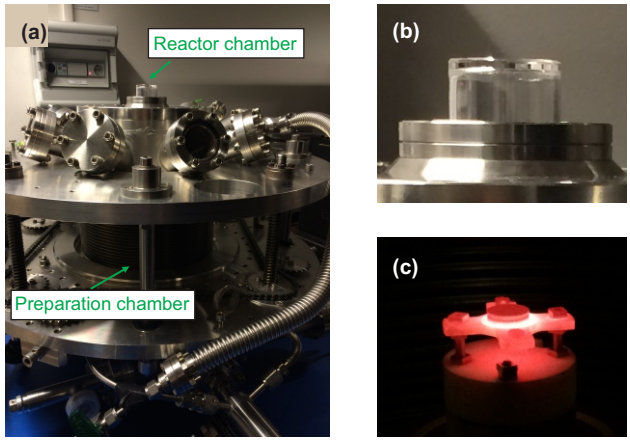

Figure 3.3: (a) The UFO reactor. (b) The cylindrical sapphire chamber. (c) A Pd(100) single crystal sample under annealing process at around 800 °C in the preparation chamber .

configuration, the top flange with the reactor chamber is moved up, as shown in Fig. 3.3a, and the sample is exposed to UHV and can be prepared in a routine way, e.g. sputtering and annealing, as shown in Fig. 3.3c. In the second configuration, the top flange with the reactor chamber is moved down. In this way, the reactor chamber is sealed from the UHV part by a gasket and can be operated at up to ambient pressure. A more detailed description of the UFO reactor can be found in Ref. [66]

3.4 Mass Spectrometer

A quadruple mass spectrometer (MS, Pfeiffer, QME 220) connected to the outlet of the reactor was used to analyze the gas composition. An automatic leak valve (LPM) was used to control the amount of gas from the outlet leaking into the MS for analysis, and to keep the pressure in the MS stable at 5×10^{-6} mbar during measurements.

Chapter 4

Laser-based Gas Detection Techniques

Laser-based techniques are widely used in the combustion community for flame diagnostics, as they can provide *in situ* and non-invasive detection of gases with high spatial and temporal resolution [26, 27]. In general, laser-based diagnostic techniques can be categorized into a two-by-two matrix, coherent and incoherent, linear and non-linear. For the two techniques to be present in this chapter, planar laser-induced fluorescence (PLIF) is an incoherent and linear technique, and degenerate four-wave mixing (DFWM) is a coherent and non-linear technique.

4.1 Planar Laser-Induced Fluorescence

Laser-induced fluorescence (LIF) is a highly sensitive, species specific and resonant technique that can be used for gas detection with high spatial resolution. If it is performed in a 2D fashion, it is called planar laser-induced fluorescence (PLIF), and a 2D information of the gas distribution can be obtained. LIF/PLIF is one of the most widely used techniques for the detection of molecules and radicals in flames [67, 28], e.g. CO [68], NO [69], OH, CH [70] and formaldehyde [71].

4.1.1 Principle

As shown in Fig. 4.1a, the gas molecules of interest are excited from the ground state to a higher state by a laser that is tuned to a specific transition between the two states, which can be electronic or rotational-vibrational. After the excitation, the molecules will de-excite from higher states (not necessarily the originally pumped state) to lower states via a variety of processes, such as collisional quenching (non-radiative) and spon-

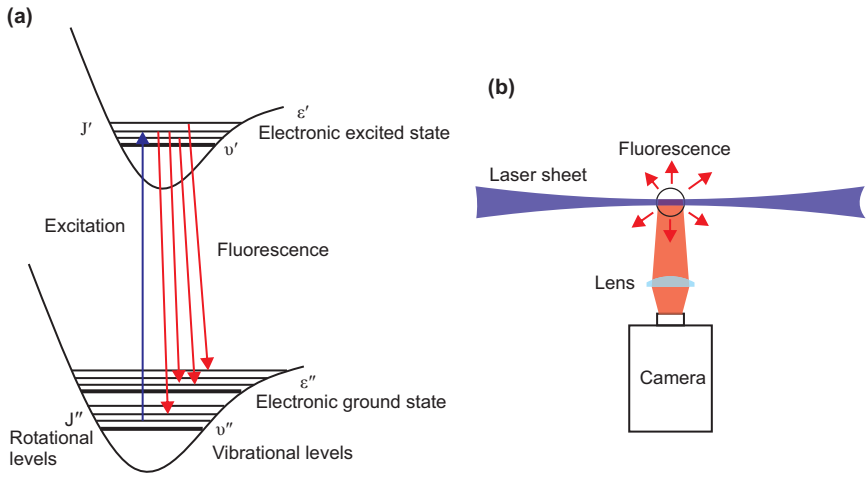

Figure 4.1: Working principle of PLIF. (a) Schematic potential energy curves for ground and excited electronic states with vibrational and rotational energy levels, showing the excitation and fluorescence transitions. (b) Schematic experimental arrangement for PLIF (top view).

taneous emission (radiative). The spontaneous emission in the de-excitation process is then called the fluorescence. Since the fluorescence signal originates from spontaneous emission processes, it is incoherent, i.e. light is emitted isotropically. As illustrated in Fig. 4.1b, by forming the excitation laser beam into a thin laser sheet, a 2D region of the gas molecules in the plane of the sheet will fluoresce. The fluorescence signal can then be imaged by a 2D detector, e.g. a camera, placed perpendicular to the laser sheet. The fluorescence is often at a longer wavelength compared to the excitation laser (not always the case), the signal can therefore be filtered spectrally.

4.1.2 Infrared PLIF of CO_2

Excitation Schemes

Although lacking accessible transitions in the UV/visible spectral range, the CO_2 molecule can be reached through several ro-vibrational transitions in the mid-infrared, e.g. the fundamental band at around 4.3 µm [72], the combination bands at around 2.7 µm $(10^01) \leftarrow (00^00)$ [41], and at around 2 µm $(12^01) \leftarrow (00^00)$ [73, 74]. For the fundamental band at 4.3 µm, the absorption cross section is very high, thus the laser beam is strongly attenuated in the ambient air, posing a challenge to large setups. For the absorption band at around 2 µm, the cross section is much lower compared to the other two bands, limiting the detection sensitivity. Due to these considerations, the com-

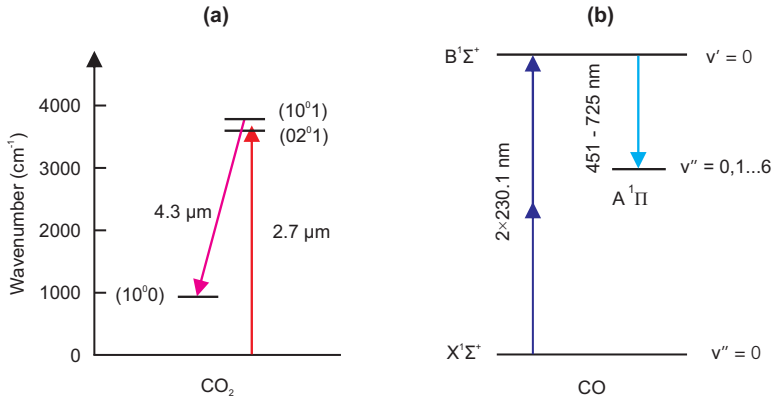

Figure 4.2: Schematic energy level diagrams of CO_2 and CO showing the excitation and fluorescence wavelengths.

bination band at around 2.7 μm was chosen in this work, as it can provide relatively strong absorption cross section while the attenuation of the laser beam by the ambient air is not so severe. Figure 4.2a shows the simplified energy-level diagram for IR-LIF of CO_2 with excitation at 2.7 μm.

Experimental Setups

Two different IR laser systems have been used in this work for the detection of CO_2. One is a broadband, and the other is a narrowband. Both laser systems can produce an IR laser beam at 2.7 μm. An InSb IR camera was used for imaging the fluorescence of CO_2. Due to the strong thermal background, a cold interference filter, centered at 4.26 μm and with FWHM of 200 nm, was placed inside the camera. Because of the rather long fluorescence lifetime (around 100 μs) [75], the exposure time was set to 15-30 μs to optimize the signal to background ratio, and a gate delay of 5-10 μs relative to the Q-switch of the YAG laser was used to avoid scattering from the laser and time jitter. During most of the experiments, the thermal background was continuously varying. The camera was therefore operated at 20 Hz with every second exposure measuring the background, which was to be subtracted on a single shot basis. Purging of N_2 was applied in the excitation beam and detection path in order to reduce the laser beam attenuation and the fluorescence signal loss in the ambient air. For the narrowband laser system, a shot-to-shot compensation scheme can be used to compensate the fluctuation of the signal due to the excitation laser energy variation and wavelength drifting and jittering. As shown in Fig. 4.3. Part of the laser was slit into a reference cell which was filled with a similar gas mixture at the same total pressure, as compared to the reactor cell. A point detector was used to record the fluorescence signal from the reference cell.

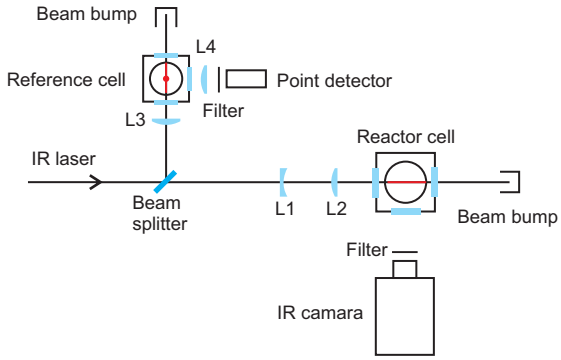

Figure 4.3: A schematic of the setup (top view) for shot-to-shot compensation with a reference cell.

Excitation Scans

Figure 4.4 shows two excitation scans of CO_2 using the narrowband IR laser system, at room temperature and 300 °C, respectively. Due to the narrow linewidth of the laser, which was measured to be 0.025 cm^{-1} [64], individual lines can be resolved in the spectra. The intensity of some lines, e.g. P(16) and P(22), are attenuated due to water absorption in the ambient air. Comparing the excitation scans of Fig. 4.4a and b, we can see that there is a slight difference in the shape of the spectra, which is due to the Boltzmann distribution at different temperatures. The line P(18) was picked to probe CO_2 in this work because its intensity is relatively less sensitive to the change of Boltzmann distribution.

To investigate the dependence of the fluorescence signal on temperature and pressure, the line P(18) was scanned with a higher resolution. The results are shown in Fig. 4.5. Figure 4.5a shows that the linewidth can be broadened substantially by increasing the CO_2 partial pressure from 2 to 14 mbar, while keeping the temperature and total pressure constant. Figure 4.5b shows that small side peaks are present at higher temperature. However, temperature has little effect on the linewidth. In Fig. 4.5c, we can see an obvious line broadening effect from increased total pressure. These dependences on temperature and pressure need to be taken into account when one evaluates the PLIF signal in an environment when the gas composition changes dynamically.

An excitation scan spectrum of CO_2 using the broadband IR laser system is shown in Fig. 4.6. Compared to the spectra in Fig. 4.4, the spectrum exhibits a very broad feature due to the broad linewidth of the laser. The FWHM was estimated to be around 10 cm^{-1} (7.3 nm), which is broad enough to cover a number of ro-vibrational lines in the $(00^00) \rightarrow (10^01)$ transition of CO_2 .

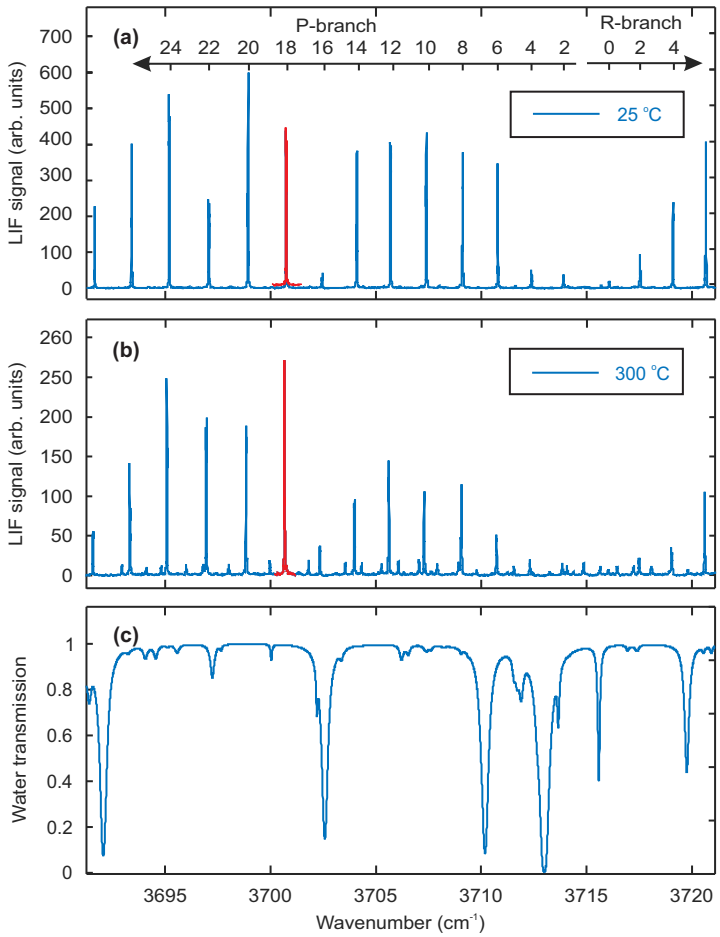

Figure 4.4: Excitation scans of CO_2 at room temperature (a) and 300 °C (b), using the narrowband IR laser system. (c) A simulated transmission spectrum of 0.5% water vapor in the ambient air for a path length of 1 m. Line P(18), marked as red in (a) and (b), is used for the excitation of CO_2 in this work.

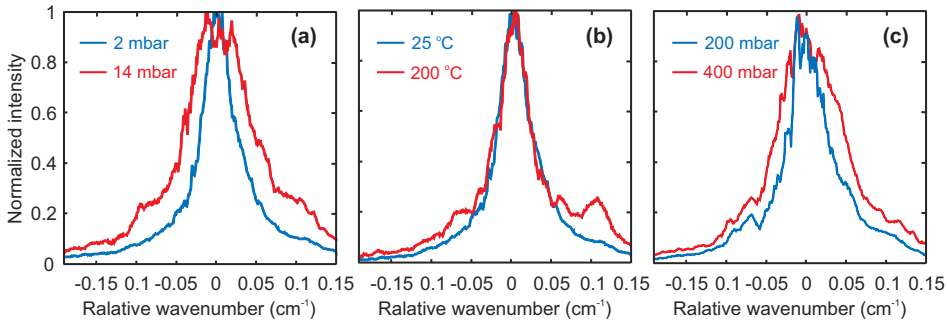

Figure 4.5: High resolution excitation scans of line P(18) of CO_2, showing the dependence of linewidth on CO_2 partial pressure, temperature and total pressure. (a) Two scans with different CO_2 partial pressures while at the same temperature of 25 °C and total pressure of 200 mbar. (b) Two scans at different temperatures while with the same CO_2 partial pressure of 2 mbar and at total pressure of 200 mbar. (c) Two scans at different total pressures while with the same CO_2 partial pressure of 4 mbar and at the same temperature of 25 °C. Ar is used as buffer gas.

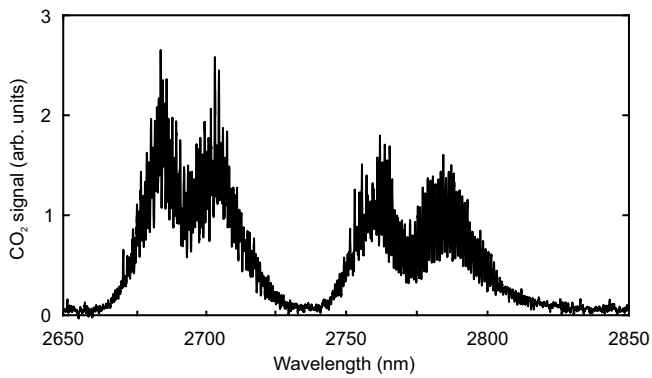

Figure 4.6: An excitation scan spectrum of CO_2 using a broadband Mid-IR OPO. 4% CO_2 is mixed with Ar at room temperature and 150 mbar total pressure.

Data Evaluation

The goal of the data evaluation is to transform the raw PLIF signal into a 2D distribution of the gas concentration. The main difficulty lies on the quantification of the PLIF signal. To perform quantitative LIF measurements, one has to take into account many factors, such as collisional quenching, stimulated emission and self-absorption. The first two are competing processes with the fluorescence, resulting in a signal loss. It is usually challenging to account for the collisional quenching, as it requires information about the local gas composition and temperature which are often unknown. In the current study, the situation is less complicated since the concentration of the reacting gases (CO and O_2) are known before reaction, and during reaction their relative concentration to the interrogated gas, i.e. CO_2, is predictable to some extent due to the simple reaction relationship. The quenching effect can therefore be studied beforehand and taken into account in the subsequent data evaluation. Stimulated emission was found to be present at the gas conditions used for the experiments when using the narrowband IR laser but the effect was insignificant. The effect of self-absorption of the CO_2 fluorescence signal can be minimized by limiting the total amount of CO_2, which can be done by limiting the initial CO and O_2 concentrations.

In this work the quantification of the PLIF signal was realized by calibration measurements with gas mixtures of known concentrations at similar gas conditions, e.g. temperature and pressure, as compared to the experiments. For the calibration, we can use the following expression for the LIF signal:

$$S_{LIF} = \eta_c E g f(T) \sigma_0 N \phi \tag{4.1}$$

where S_{LIF} is the fluorescence intensity, η_c is the collection efficiency, E is the laser energy, g is a function that describes the spectral overlap between the laser and the absorption spectral lineshape, $f(T)$ is the Boltzmann distribution of the energy levels of the molecule as a function of the temperature T, σ_0 is the absorption cross section, N is the number density of the absorber, and ϕ is the fluorescence quantum yield. The number density N can be described using the ideal gas law as

$$N = x \frac{P}{kT} \tag{4.2}$$

where x is the mole fraction of the absorber, P is the total pressure and k is the Boltzmann constant. And the fluorescence quantum yield ϕ, which indicates the fraction of excited molecules that fluoresces, can be described as

$$\phi = \frac{A}{A + \Sigma_i Q_i} \propto \frac{1}{\Sigma_i Q_i} \tag{4.3}$$

where A is the spontaneous emission rate, and Q_i is the quenching rate of gas i. The spontaneous emission rate is usually much smaller than the quenching rate.

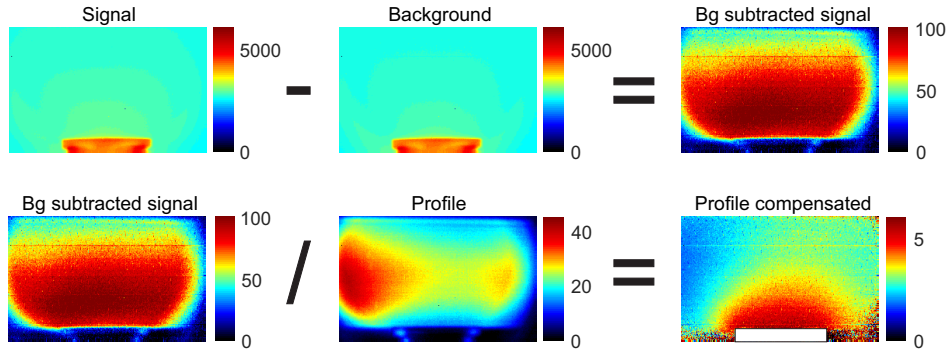

Figure 4.7: Processing of CO_2 PLIF images, showing background subtraction and profile compensation. Note that the signal image is taken under reaction conditions. In this case, the sample is active at 300 °C and 150 mbar, and in a 100 ml_n min^{-1} total flow.

As seen from Eq. 4.1, the LIF signal strength is proportional to the number density of the absorber N, the Boltzmann distribution $f(T)$, and the fluorescence quantum yield ϕ. In a typical measurement both the temperature and gas composition vary at the same time. All these parameters therefore have to be taken into account for a rigorous calibration.

For the present work, we treated the factors separately. Firstly, the number density and the Boltzmann distribution were compensated by a profile image taken with a homogeneous gas mixture of known CO_2 concentration at the same temperature and total pressure as when the signal image is taken. As shown in Fig. 4.7, dividing the signal image (background subtracted) by the profile image (background subtracted), we can account for the temperature gradient of the gas, which leads to gradients in both the number density and the Boltzmann distribution, as well as the inhomogeneity of the laser sheet profile.

In a typical experiment the temperature of the catalyst was ramped up, leading to a gradient of the temperature distribution above the sample, and a change of the gradient over time. Figure 4.8a shows two integrated LIF signals from two different regions above the sample, one close to the sample, and the other one away from the sample, as a function of sample temperature. The difference between the two signals clearly illustrates the temperature gradient in the gas phase. To account for the temperature gradient, we typically recorded two profile images over the temperature range used in the experiment, and then performed an interpolation between them. By doing that, we will have the right profile corresponding to each signal image at different temperatures and can then account for the temperature gradients for all signal images. Figure 4.8 shows an example of the correction of the LIF signal close to the catalyst for the tem-

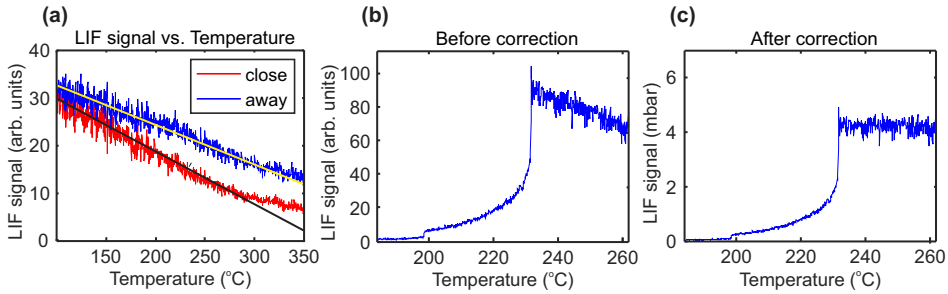

Figure 4.8: An example showing the correction of the CO_2 LIF signal trend above a catalyst for temperature variation in a typical experiment. (a) LIF signals as a function of temperature, one close to the sample (red), and the other away from the sample (blue). The solid lines shows that a linear fit can be applied up to about 300 °C. (b) LIF signal with background subtraction but before correction for the temperature. (c) LIF signal after correction for the temperature.

perature variation. After the correction, we can see that the LIF trend reaches a plateau as the reaction is in the MTL regime where the production of CO_2 does not change with the temperature increase. The LIF signal can then be calibrated using the concentration dependence curve shown in Fig. 4.9a. Note that the bending of the curve is due to the self-absorption of the signal, the self-broadening and self-quenching of CO_2.

Secondly, the effect of self-absorption of the CO_2 fluorescence signal was evaluated using the Beer-Lambert Law

$$\frac{S}{S_0} = \exp(-\frac{xPl}{kT}\sigma_0) = \exp(-Nl\sigma_0) \tag{4.4}$$

where S_0 is the initial signal intensity, S is the signal intensity after the re-absorption path, l is the path length, and mass path Nl is defined as the product of the number density and the path length. In a typical measurement under reaction conditions, the CO_2 distribution is mainly localized in a hemispherical cloud above the sample, as shown in Fig. 4.7, and the size of the cloud is much smaller than the dimension of the chamber. Furthermore, the partial pressure of the CO_2 was kept to be low. As a result, the mass path Nl is small such that the self-absorption effect is not significant.

Finally, the effect of collisional quenching should be evaluated. In this work, the collision quenching has not been studied systematically, i.e. for different gas mixture ratios or different pressures. Instead, only the maximum effect was studied for the mostly used gas mixture. A more detailed study is presented in Paper I, showing that the maximum uncertainty of the CO_2 signal due to the collisional quenching of CO and O_2 was estimated to be 25%.

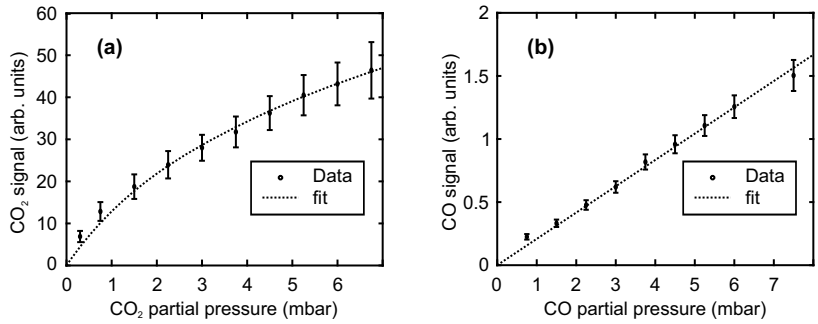

Figure 4.9: Concentration dependence of CO_2 (a) and CO (b) PLIF signal measured at 300 °C and 150 mbar.

An example of the shot-to-shot compensation of the signal for the laser energy fluctuation and wavelength drifting is shown in Fig. 4.10. A comparison of the uncompensated (blue) and the compensated signal (black) shows that the signal fluctuation is substantially reduced after the compensation. However, the good results are mainly due to the fact that the gas conditions used for the reference cell were similar to that for the reactor cell in which there was no reaction on going. In measurements where both the temperature and gas mixture ratio are varying over time for the reactor cell while they are constants for the reference cell, the compensation results are less satisfying, due to the different absorption across sections and fluorescence quantum yields of the CO_2 for the two cells.

Using CO_2 PLIF we can also measure the temperature gradient over a sample. Through dividing a profile at 300 °C by another profile at room temperature, and calibrating the divided image using a calibration curve–a fitting of the normalized LIF signal close to the sample as a function of temperature, as shown in Fig. 4.11a, a temperature distribution above the sample can be obtained, as shown in Fig. 4.11b. Note that both the number of density N the Boltzmann distribution $f(T)$ are taken into account in the calibration process. Interestingly, the temperature gradient above the sample is very similar to the CO_2 distribution when the sample is active, by comparing Fig. 4.11b with Fig. 4.7.

4.1.3 Two-Photon PLIF of CO

Excitation Schemes

The CO molecule does not have transitions in the UV/visible spectral range that can be accessible using linear one-photon excitation. However, nonlinear two-photon excitation can be used to reach the electronic transitions in the vacuum ultra violet (VUV),

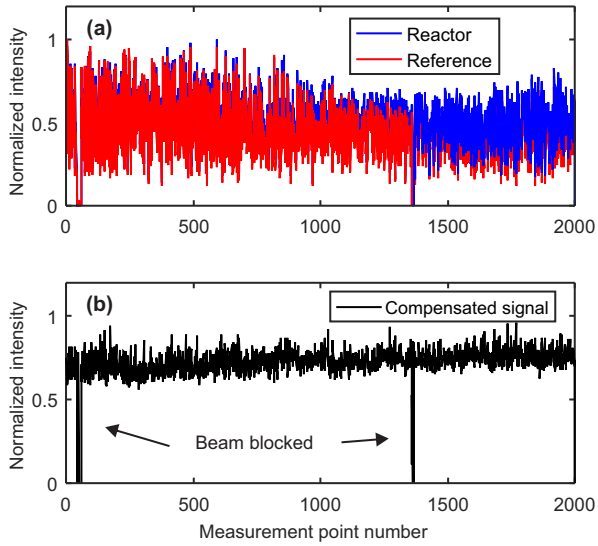

Figure 4.10: An example showing shot-to-shot compensation of the signal with a reference cell. (a) shows the LIF signal in the reactor cell (blue) and the signal in the reference cell (red). (b) shows the compensated signal, i.e. the blue signal divided by the red signal. All the signals are normalized for comparison. Gas mixture in the reactor cell contains 5% CO_2 and 95% Ar at 150 mbar, while in reference cell contains 10% CO_2 and 90% Ar at 150 mbar.

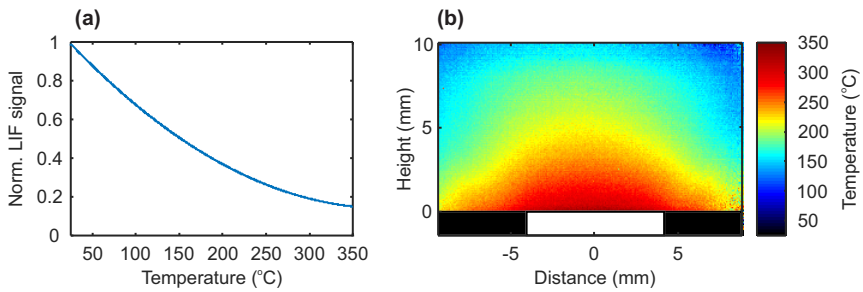

Figure 4.11: (a) A fitting of the normalized LIF signal close to a sample as a function of temperature in Fig. 4.8a. (b) The temperature gradient over an inactive sample at 300 °C and 150 mbar, and with 100 ml_n min^{-1} total flow. The cell is filled with 2% CO_2 in Ar.

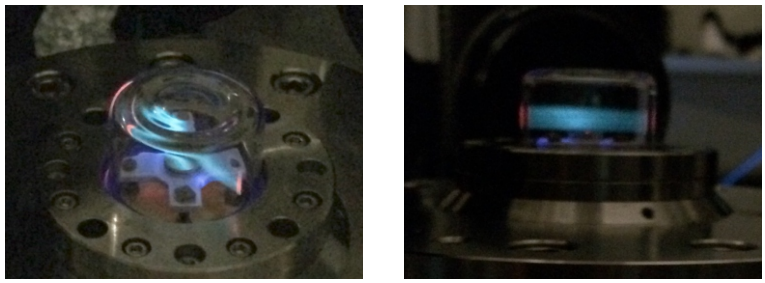

Figure 4.12: Single-shot CO PLIF image captured by an iPhone with an exposure time of 58 ms, showing the blue fluorescence from CO along the laser sheet, and the fluorescence background from the fused silica chamber (pink) and the sample holder (dark blue). 10% CO is mixed in Ar at a total pressure of 500 mbar.

e.g. the $B^1\Sigma^+ \leftarrow X^1\Sigma^+$ transition [76, 77, 78], and the $C^1\Sigma^+ \leftarrow X^1\Sigma^+$ transition [79]. In this work, the former excitation scheme was used and the subsequent fluorescence in $B^1\Sigma^+ \rightarrow A^1\Pi$ transition (Ångström band) was detected. Figure 4.2b shows a simplified schematic of the energy levels of CO.

Experimental Setup

The UV beam at 230.1 nm was used for the two-photon excitation of CO. An ICCD cemera was used to image the fluorescence signal. The camera chip was hardware-binned 2×2 or 4×4 for faster online data transfer. The intensifier gate was set to 150-250 ns, which is much longer than the collision-free lifetime (68 ns) of the fluorescence [80]. As the scattering and fluorescence from the chamber, windows, sample and sample holder are severe due to the strong UV beam, as shown in Fig. 4.12, a long-pass filter (GG455, Schott) was used to suppress light below 455 nm. In contrast to the CO_2 case, the background in the case of CO is much less temperature dependent. Therefore, the 20 Hz data acquisition scheme for the CO_2 detection was not needed for the CO detection.

Excitation Scan

An excitation scan spectrum of CO is shown in Fig. 4.13. In the spectrum some Q-branch lines from the $B^1\Sigma^+(\nu' = 0) \leftarrow X^1\Sigma^+(\nu'' = 0)$ transition can be resolved owing to the narrowband laser. By comparing the measured CO excitation spectrum with simulated CO absorption spectra in which the laser profiles are varied in width, the FWHM of the UV laser was estimated to 0.5 cm^{-1}. As the laser linewidth is much narrower than the linewidth of the CO transition at 230.1, the CO signal intensity is

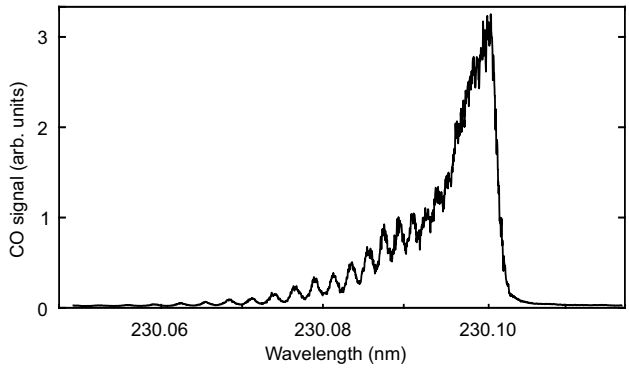

Figure 4.13: A two-photon excitation scan spectrum of 4% CO mixed with Ar at room temperature and 150 mbar total pressure.

not sensitive to a slight wavelength drift of the laser. In contrast, it is very sensitive to the energy of the laser due to the two-photon process.

Data Evaluation

As mentioned above, the background fluorescence is severe, thus needs to be subtracted from the signal images. The profile compensation process is similar to the CO_2 case. Compared to CO_2, the effect of self-absorption of the CO fluorescence signal was not taken into account, as the absorption cross section of the two-photon transition is small. The CO PLIF signal shows a quite linear dependence on the CO concentration, as shown in 4.9b. Similar to the case of CO_2, the collisional quenching for CO has not been investigated throughly in this work. Only the maximum uncertainty of the CO signal due to the quenching of CO_2 and O_2 has been studied for the mostly used gas mixture (refer to Paper I).

4.2 Degenerate Four Wave Mixing

Although this thesis is mainly focused on PLIF imaging, a brief introduction of the technique of mid-infrared degenerate four-wave mixing (IR-DFWM) is presented here with the intention of showing the potential of the technique in catalysis studies. A detailed study of IR-DFWM for the detection of methanol can be found in Paper XII.

DFWM is a non-linear, coherent technique that can provide high temporal and spatial resolution for gas detection. The theory of DFWM was first presented by Abrams and Lind in 1978 [81, 82]. UV/visible DFWM has been widely applied in combustion diagnostics for detection of molecules and radicals since the late 1980s

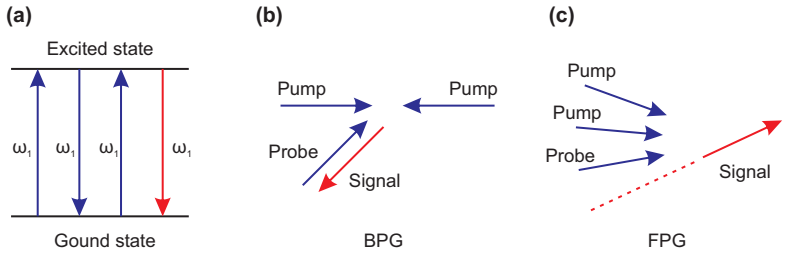

Figure 4.14: The principle of DFWM. (a) Transitions between allowed molecular states involved in resonant four-wave mixing processes. (b) DFWM with backward pump geometry, BPG. (c) DFWM with forward pump geometry, FPG.

[83]. Due to the lack of suitable lasers and detectors in the infrared region, IR-DFWM has been less widely used, compared to UV/visible DFWM. With the developments of lasers and infrared detectors, IR-DFWM has become an attractive technique for detection of molecules that lack accessible transitions in the UV/visible range, such as HF [84], HCl [85], CH_4 [86, 87] and C_2H_2 [86, 88]. One of the practical challenges in IR-DFWM experiments, compared to UV/visible DFWM, is the beam alignment due to the invisible IR laser beams. To overcome it, an infrared BOXCAR plate can be used for easy and stable alignment of IR-DFWM in the forward phase-matching geometry, and it has been used for the detection of C_2H_2 [89], HCl [89], CH_3Cl [90] and NH_3 [91]. All the studies mentioned above prove the potential of IR-DFWM as a powerful technique for *in situ* measurements of infrared active species with high spatial and temporal resolution.

4.2.1 Principle

DFWM is a non-linear, coherent process in which three beams are interacting with the gas molecules of interest. A laser-beam like signal is generated when the laser beams are tuned to a specific transition between two energy states of the interrogated molecule and fulfill the energy conservation and phase matching conditions. The energy conservation condition is automatically fulfilled in DFWM, as the beams are identical, as shown in Fig. 4.14a. For the phase matching, there are generally two types of geometry that can be used, backward pump geometry (BPG) and forward pump geometry (FPG), as shown in Fig. 4.14b and c, respectively. One way to conceptually visualize the DFWM process is that two beams as the pump beam generate an absorption grating in the interrogated media, and the third beam as the probe beam is diffracted from the induced grating, which results in a signal beam.

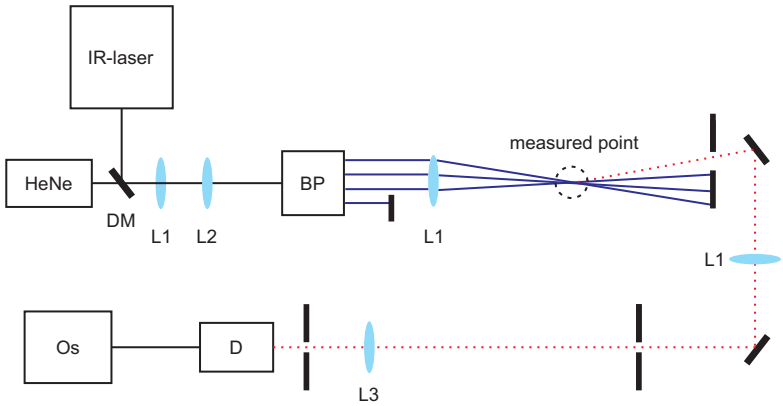

Figure 4.15: Schematic of the experimental IR-DFWM setup. *BP* BOXCAR plates, *DM* dichroic mirror, *BS* beam splitter, *L1*, *L2* and *L3* CaF_2 lens, *D* InSb detector, *Os* oscilloscope

4.2.2 Infrared DFWM of Methanol

Experimental Setup

The setup of IR-DFWM is shown in Fig. 4.15. The IR laser beam was split into four parallel beams with approximately even energy using a set of IR-BOXCAR plates. Three of the parallel laser beams were crossed using a focusing lens and the fourth laser beam was blocked. The signal was generated in the crossing volume of the three beams. As the signal follows the path of the fourth laser beam, thus this beam (when unblocked) can be used to trace the signal to the detector with a He-Ne laser. The signal beam was collimated using another lens and focused onto an IR point detector. As the IR-DFWM signal has the same wavelength as the interrogating beams, it is important to suppress the background. A number of apertures were therefore used to block background scattering. A digital oscilloscope was used to log the signal from the IR detector.

Excitation scan

Figure 4.16 shows a measured DFWM spectrum and a simulated absorption spectrum of methanol. The simulated absorption spectrum exhibits a broad feature. In contrast, the IR-DFWM spectrum shows sharp features labeled a-d. Each of these features contains several closely spaced transitions, resulting in a coherent enhancement of the IR-DFWM signal [90, 92], making the spectral feature more distinct. By scanning the feature at 2982 cm^{-1}, the detection limit is estimated to be 350 ppm at room temperature and atmospheric pressure.

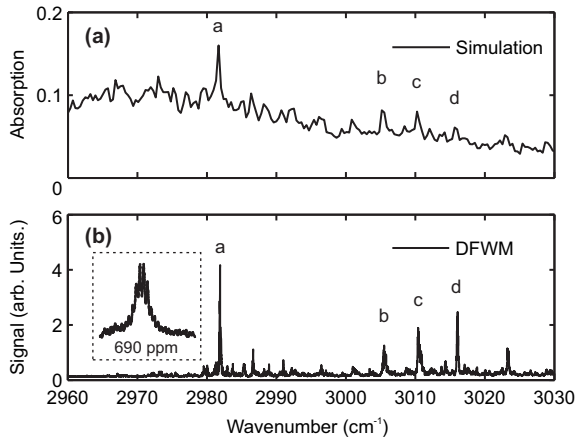

Figure 4.16: Comparison between a simulated absorption spectrum (a) and a measured DFWM specturm (b) of 3200 ppm methanol vapor at room temperature and atmospheric pressure. The absorption spectrum is simulated with a path length of 10 cm, using the HITRAN data base. The subfigure in (b) shows a high resolution scan of the feature labeled a, at 690 ppm.

Chapter 5

Surface Techniques Combined with PLIF

Every technique has it own limitations, it is therefore preferable to combine as many techniques as possible for *operando* studies of catalysis. In this work we have combined PLIF and surface techniques for simultaneous gas phase and surface measurements in order to correlate the gas phase and surface changes under *operando* conditions. There are two surface techniques to be presented here, surface optical reflectance (SOR) and high energy surface X-ray diffraction (HESXRD). The former can provide a macroscopic overview of the change of the catalyst surface, while the latter can reveal the microscopic structural changes of the surface.

5.1 Surface Optical Reflectance

5.1.1 Principle

The working principle of SOR is simple: a single crystal sample is first illuminated by an incoherent, collimated beam. The optical reflectance of the sample surface is then measured, and the decrease in the surface reflectivity under oxidation conditions can then be correlated to oxides formation and surface roughening [12, 13]. However, its main drawback is that it is difficult to distinguish between the two.

The setup of surface optical reflectance used in this work is shown in Fig. 5.1. Light from an LED was first collimated and spatially filtered by two spherical lenses and a small pinhole. The collimated beam was then sent to a beam splitter above a sample. The beam splitter reflects half of the beam onto the sample, and transmits half of the beam reflected by the sample towards a camera. A 4f bright-field configuration was used to image the sample surface. A more detailed description of the setup can be

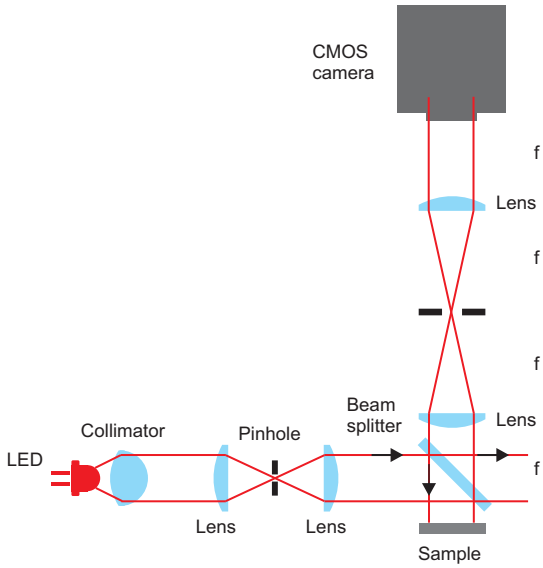

Figure 5.1: Experimental setup for SOR measurements.

found in Paper III.

An example of a SOR measurement during oxidation of a Pd(100) surface is shown in Fig. 5.2. Prior to the experiment, the sample was exposed to CO and Ar mixture at 320 °C and 125 mbar to ensure that the surface was oxide free. When the experiment started, the gas flow was switched to 4 ml_n min^{-1} of O_2 and 36 ml_n min^{-1} Ar (corresponding to 12.5 mbar of O_2 and 112.5 mbar of Ar). Figure 5.2 shows that the optical reflectance of the sample decreases over time during the oxidation process, which can be attributed to a combination of surface oxides formation and surface roughening.

5.1.2 PLIF and SOR

For simultaneous measurements of the gas phase and macroscopic surface change of a Pd(100) during CO oxidation, we have combined PLIF and SOR. The experimental setup is shown in Fig. 5.3. The broadband IR laser system that has been described in Chapter 4 was used for the detection of CO_2 above the sample. The CO_2 PLIF measurements were performed at 10 Hz, and the SOR measurements were operated at between 2-10 Hz, depending on the experiments.

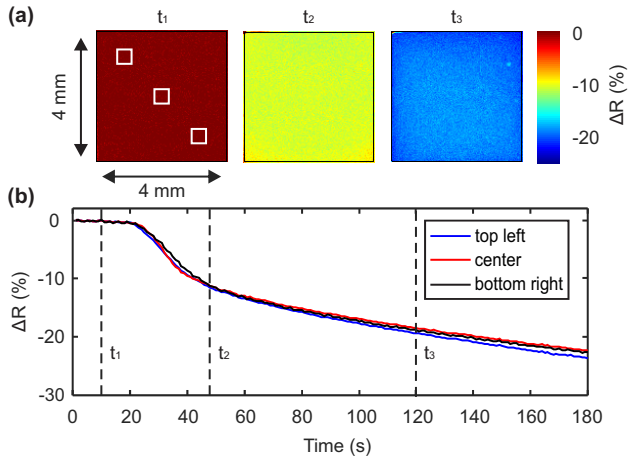

Figure 5.2: Surface reflectance changes of a Pd(100) surface during an oxidation process, in a gas flow of O_2 and Ar, at 320 °C. (a) Reflectance images showing the change of surface reflectance at different times during the process. (b) Change of the surface reflectance at different regions of the surface marked by the white squares in (a). Note that $t = 0$ is defined as when the gases were switched from pure Ar to O_2 and Ar mixtures. The optical reflectance change ΔR is defined as $(I - I_0)/I_0$, where I_0 is the reflected intensity at the start of the experiment and I the subsequently measured intensity.

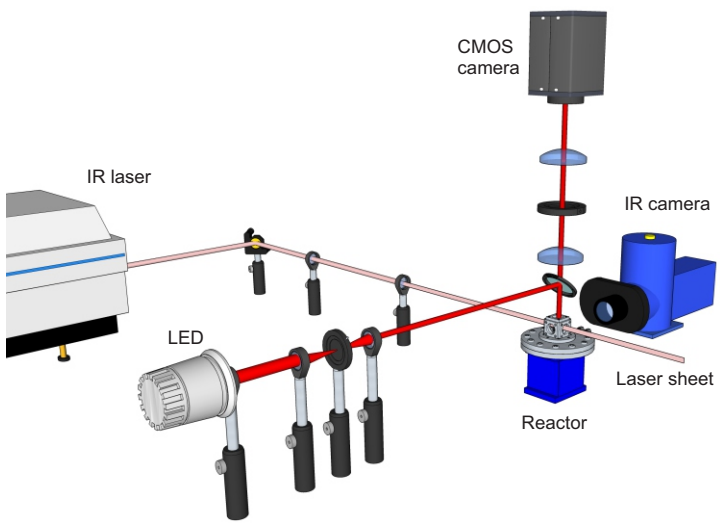

Figure 5.3: Experimental setup for simultaneous PLIF and SOR measurements.

5.2 High Energy Surface X-Ray Diffraction

SXRD is a surface-sensitive technique that has been widely used for surface structure determination of catalysts [93, 94, 95]. As compared to the electron-based surface characterization techniques, e.g. XPS where the mean-free-path of electrons limits the operation to low pressures, the main advantage of SXRD is that it can be applied at realistic pressures.

5.2.1 Principle

SXRD is a scattering-based technique based on the interference pattern of scattered light from the interaction between the incident X-ray beam and the periodic atoms of the sample surface. It is surface sensitive because the diffraction from a surface terminated crystal is sensitive to the atomic structure of the surface. Figure 5.4 illustrates the working principle of SXRD. With an X-ray beam incident on the sample at a certain incident angle, as shown in Fig. 5.4a. the diffracted beams can be detected using an X-ray detector at certain positions, depending on the orientation of the sample with respect to the incident beam.

To facilitate the searching for the diffracted beam and correlating it to the surface structure of the sample, two abstract tools are useful. The first tool is the reciprocal lattice which is a Fourier transformation of the real lattice (the atom positions of the crystal). For an infinite crystal, the reciprocal lattice consists of infinite points, known as Bragg peaks, at well-defined positions, as shown in Fig. 5.4b and c. For a truncated crystal with a surface, the crystal truncation rods (CTRs) arise, passing through the Bragg peaks and perpendicular to the crystal surface. When an adsorbate layer forms on the surface, additional rods appear in the reciprocal lattice. These rods are called superstructure rods (SRs), and they are only sensitive to the adsorbate layer. The second tool is the Ewald sphere. The significance of the Ewald sphere is that the intersection of the sphere with the reciprocal-lattice peaks/CTRs/SRs gives the direction of the diffracted beam at a certain photon energy of the incident X-ray. As illustrated in Fig. 5.4a, the Ewald sphere intersects with a part of a CTR but not the Bragg peaks in the reciprocal lattice. Thus, only that specific part of the CTR can be detected while the Bragg peaks cannot. By varying the sample orientation with respect to the incident beam, it is possible to detect all the reciprocal-lattice peaks/CTRs/SRs, from which the surface structure can be determined.

By combining a high energy X-ray beam and a large 2D detector, a large area of the reciprocal space can be detected at a fixed sample orientation. In this way, it is possible to determine the full surface structure on a sub-second time scale with a single-shot diffraction image. This gives rise to the technique called HESXRD which has been shown to be especially suited for surface structure determination in *operando* studies of

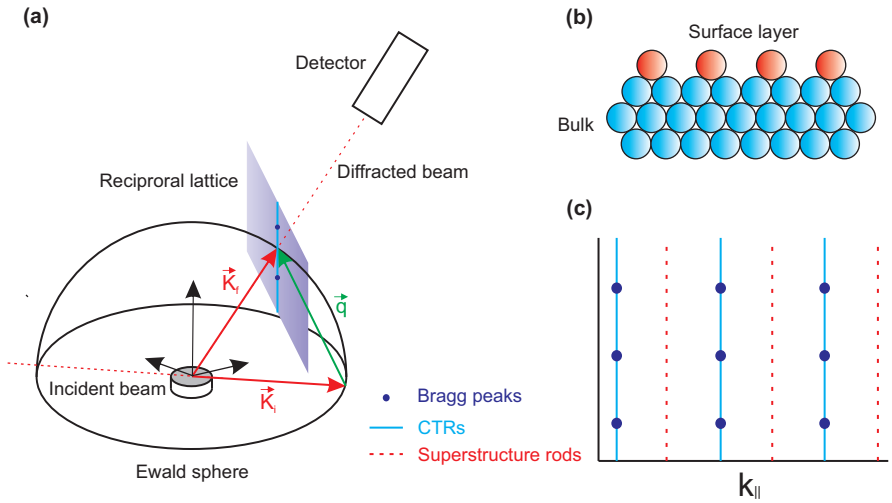

Figure 5.4: (a) Working principle of SXRD. (b) Truncated crystal with adsorbate layer. (c) Reciprocal lattice of the real space in (b). For simplicity, only a 2D slice of the reciprocal lattice is shown in (a).

model catalysts [96, 55, 97]. Figure 5.5 shows the setup of HESXRD where a large 2D detector is used for recording diffraction images. An example of a HESXRD image of a Pd(100) with a surface oxide is shown in Fig. 5.6, where both the CTR signal from the substrate and the SR signal from a surface oxide are detected at a fixed sample orientation with a single-shot image.

5.2.2 PLIF and HESXRD

As mentioned above, HESXRD is suited for *in situ* surface structure determination of a catalyst on a sub-second time scale under realistic catalytic reaction conditions. Traditionally, an MS is used with HESXRD for gas phase detection. The downsides of MS are the poor spatial resolution, and the often ill-defined time delay of the gas sampling with respect to the actual catalytic event. Trying to better correlate the changes of the gas phase and the surface structure, we have combined HESXRD with PLIF.

The experimental setup for combined measurements of PLIF and HESXRD is illustrated in Fig. 5.7. The experiments were performed at beamline P07 at PETRA III. Figure 5.8 shows a photo of the crowded experimental hutch at P07. The incident angle of the X-rays was set to 0.04°, close to the critical angle on Pd(100). The diffraction pattern was detected with a temporal resolution of 2 Hz by a 2D X-ray detector positioned at 1.75 m from the sample. The PLIF measurements of the gas phase were performed at 10 Hz. The detailed study can be found in Paper IX.

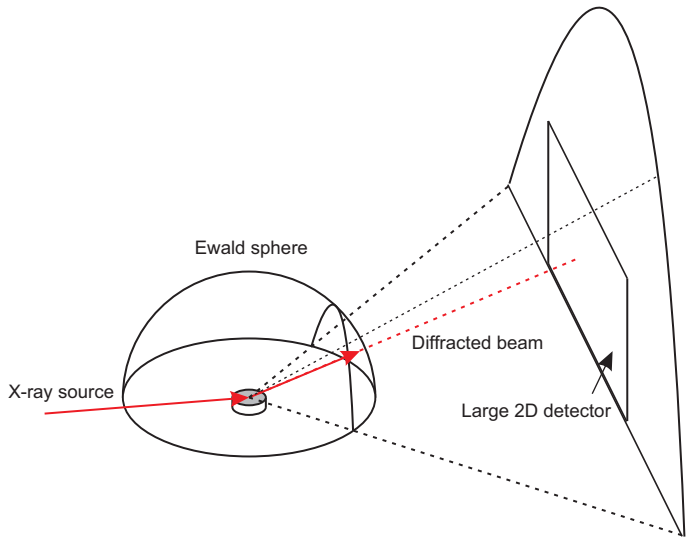

Figure 5.5: Schematic of experimental setup of HESXRD where a large 2D detector is used to capture a large part of reciprocal space.

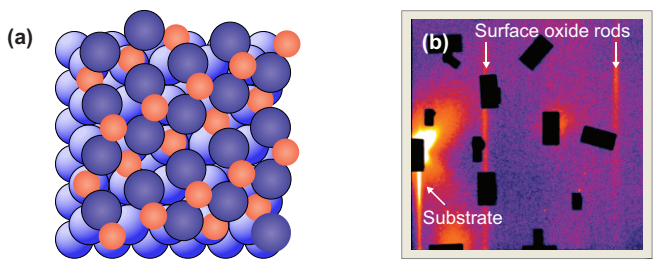

Figure 5.6: (a) Model of a Pd(100) crystal with $\sqrt{5} \times \sqrt{5} - R27°$ surface oxide. (b) HESXRD image of the crystal in (a), showing the CTR from the substrate and the SRs from the surface oxide. The dark rectangles in the diffraction image shows the positions of tungsten pieces which are used to protect the detector from strong Bragg peaks from the Pd(100) substrate and the sapphire reactor chamber used in the experiment.

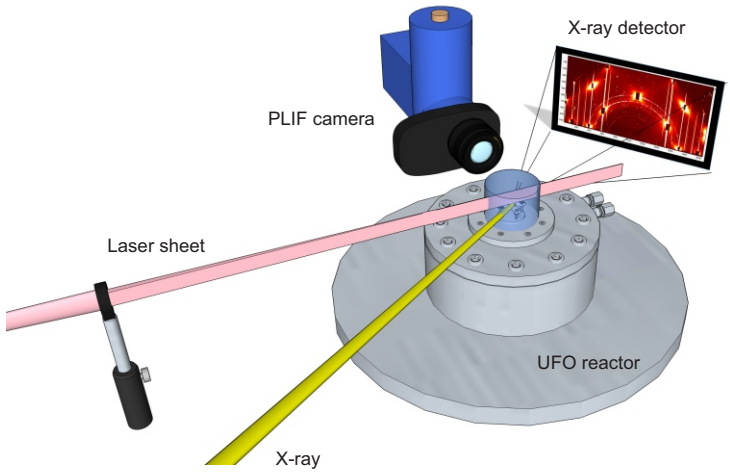

Figure 5.7: Experimental setup for simultaneous PLIF and HESXRD measurements.

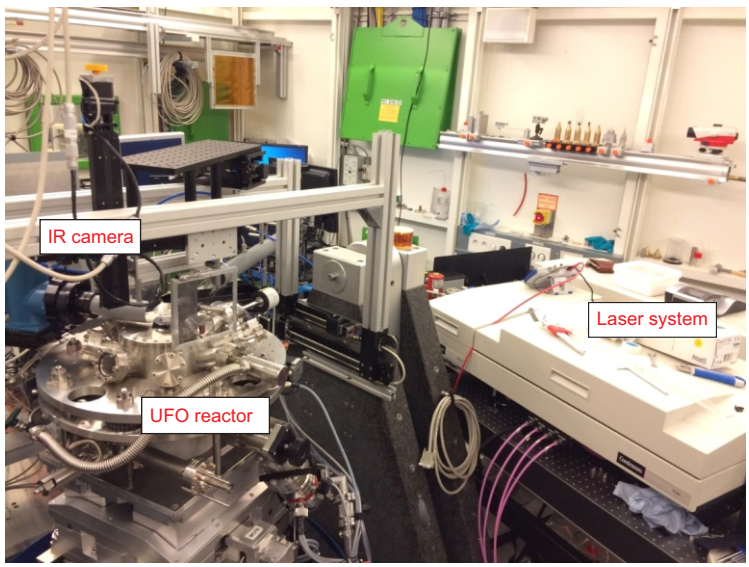

Figure 5.8: A photo of the experimental setup for simultaneous PLIF and HESXRD measurements at beamline P07 at PETRA III.

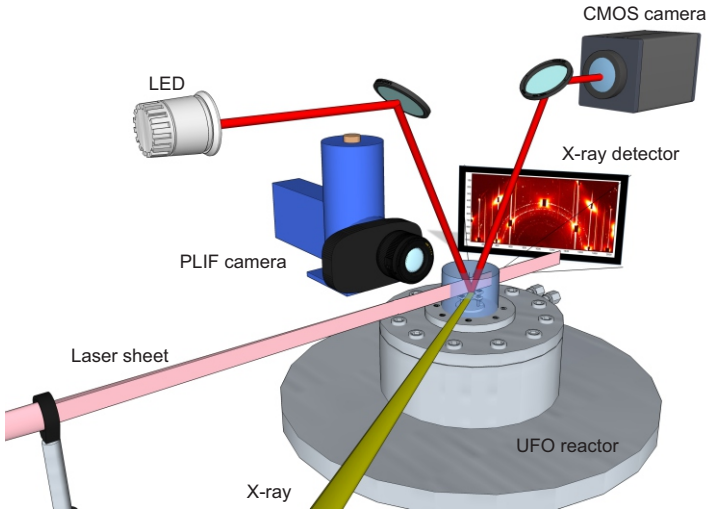

Figure 5.9: Experimental setup for simultaneous PLIF, HESXRD and SOR measurements.

5.3 Combination of PLIF, SOR and HESXRD

PLIF, SOR and HESXRD have been combined to study the CO oxidation over a Pd(100) surface at the same beamline at PETRA III. The experimental setup is shown in Fig. 5.9. Note that the SOR setup was mounted on the big flange of the UFO reactor so that the camera can image the sample at the same relative position when the reactor rotates. Both cameras and the X-ray detector were synced in time for the data acquisition. The combined setup allows us to directly correlate the macroscopic gas phase and surface morphology, and the microscopic structure of the surface during dynamic changes of the reaction. The detailed study can be found in Paper XI. The combined techniques have also been used for the study of self-sustained reaction oscillations of the Pd(100) during CO oxidation. The data is under analysis at the time of writing, and the results are therefore not included in this thesis.

Chapter 6

Applications to Catalysts at Work

In this chapter, the results from the original work will be presented and are divided into three categories based on the applications of PLIF. They are characterization of catalytic flow reactors (Paper I, II, V and IX), visualization of activity above samples (Paper IV, VI and VII), and gas-surface correlations in *operando* studies (Paper III, VIII, X and XI). All these results demonstrate PLIF as a powerful technique for studying the gas phase in catalysis with its distinct advantages of high spatial and temporal resolution and non-intrusiveness.

6.1 Characterization of Catalytic Flow Reactors

At semi-realistic gas conditions, the gas composition over a sample can change significantly when the reaction reaches the MTL regime, and the gas distribution depends on gas diffusion and the flow geometry of a reactor. Three types of flow reactor geometries are presented in this thesis. They are prototypical flow, cone flow and stagnation flow geometries, as shown in Fig. 6.1a-c, respectively. To characterize the gas flow, PLIF was used to image the CO_2 gas distribution over a Pd(100) single crystal sample under CO oxidation.

The prototypical flow geometry shown in Fig. 6.1a. is commonly used for *in situ* experiments for heterogeneous catalysis, e.g. SXRD [66]. Reactors with this type of geometry are usually designed in a way such that the gas over the sample is exchanged efficiently, as opposed to a batch reactor, in order to mimic the mass and heat transport in industrially relevant catalysis processes. In a prototypical flow reactor, a semi-spherical CO_2 cloud is formed above the sample in the MTL regime, as shown in Fig. 6.1a.

AP-XPS has been widely used for *in situ* studies of model catalysts under semi-realistic conditions [5]. To do this, a cone-shaped analyzer nozzle positioned just above the sample, is used to collect the photoelectrons [98]. In most situations, the analyzer

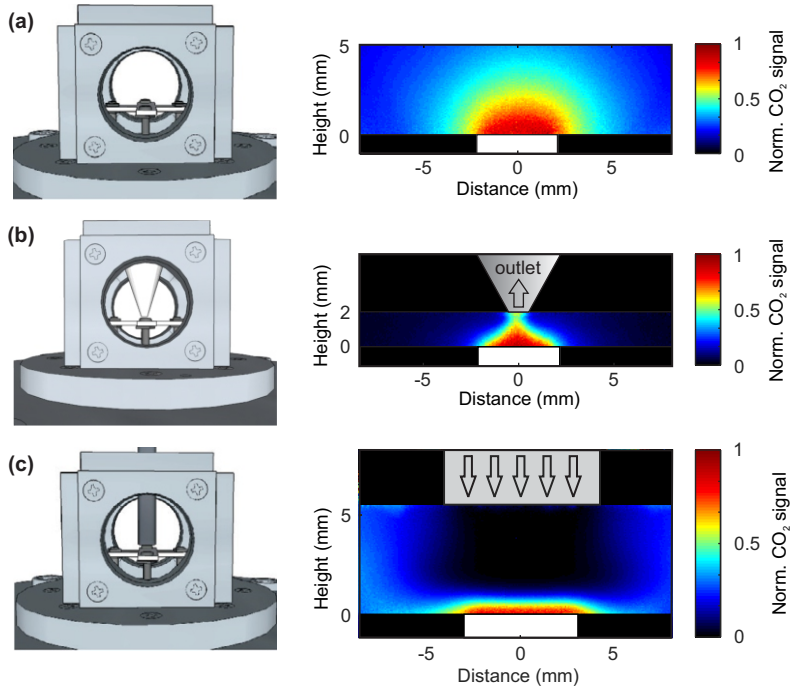

Figure 6.1: CO_2 gas distribution over a Pd(100) single crystal in the MTL regime for three different flow geometries. The sample temperature and gas compositions are the same for all the cases, with 4% CO, 4% O_2 and 92% Ar. For (a) and (b), the total flow is 120 ml_n min^{-1} and the total chamber pressure is 150 mbar. For (c), the total flow is 200 ml_n min^{-1} and the total chamber pressure is 300 mbar. All PLIF images are 500-shot averaged.

nozzle is connected to the gas differential pumping system and serves as a gas outlet. The presence with the nozzle can potentially affect the gas distribution close to the sample. In this work, a cone flow reactor was designed to mimic the gas flow in a real AP-XPS reactor where a cone-shaped nozzle positioned above the sample was used as the gas outlet. In this reactor, the CO_2 cloud over the sample in the MTL regime is formed into a cone-shape, as shown in Fig. 6.1b.

Stagnation flow reactors are important flow reactors in heterogeneous catalysis, as they offer great simplicity for fluid dynamics modeling due to the axial symmetry, and are closely relevant to industrial catalysis [99]. With a stagnation flow geometry, a very thin and flat CO_2 distribution is formed above a highly active sample, as shown in Fig. 6.1c.

6.1.1 Prototypical flow Reactor

We characterized the prototypical flow reactor by visualizing the CO_2 and CO gas distribution over a Pd(100) single crystal during CO oxidation. The results are presented in Fig. 6.2. In both the CO_2 and CO PLIF measurements, the sample was slowly heated at flows of 4 ml_n min^{-1} CO, 4 ml_n min^{-1} O_2 and 92 ml_n min^{-1} Ar at 150 mbar total pressure (corresponding to initial partial pressures of 6 mbar of CO, 6 mbar of O_2 and 138 mbar of Ar). At 253 °C, a homogeneous CO_2 distribution can be seen in Fig. 6.2a, which corresponds to a homogeneous CO distribution in Fig. 6.2d. Both the CO_2 and CO PLIF images indicate that the sample is inactive at low temperature. As the temperature increases further, the CO_2 partial pressure increases steadily while the CO partial pressure steadily drops, as shown in the MS trends in Fig. 6.2g and the LIF trends in Fig. 6.2h. When the sample lights off at around 316 °C, the gradients of the CO_2 and CO concentration above the sample change dramatically, shown in Fig. 6.2b and e, respectively. When the sample becomes highly active, a prominent CO_2 cloud and a depletion of CO above the sample can be seen in Fig. 6.2c and f, respectively, and they match very well. The CO and CO_2 trends reach a plateau immediately after the ignition of the sample, indicating an MTL reaction. In the MTL regime, the gas composition over the sample differs significantly, as compared to that in the low activity regime, which was modeled by Matera *et al.* [100]. This study shows that a decrease of approximately 70% for the CO concentration close to the sample is measured by PLIF, compared to only approximately 20% measured by the MS. This significant difference is due to the fact that the MS is sampling gases far away from the sample, and suggests that the MS signal measured from the outlet can not accurately reflect the gas composition close to the sample surface.

6.1.2 Model AP-XPS Reactor

In the study of the model AP-XPS reactor, it was also found that the CO_2 concentration in the vicinity of a highly active sample, as measured by PLIF is significantly different from that at the gas outlet, as measured by an MS, similar to the case shown above. In addition, the CO_2 distribution over the sample is strongly dependent on flow rate and chamber pressure. The pressure and flow rate dependence of the CO_2 distribution has been investigated and the results are shown in Fig. 6.3. The images are recorded when the reactions have reached the MTL regime. Figure 6.3a-c show that the gradient of the CO_2 concentration decreases as the gas exchange rate decreases at a total chamber pressure of 150 mbar. A similar tendency can also be found at a total pressure of 50 mbar, as shown in Fig. 6.3d-f. Furthermore, the total pressure is found to have a strong effect on the CO_2 distribution. Figure 6.3b, e and g show that the gradient of the CO_2 concentration decreases as the total pressure decreases while the gas exchange rate is

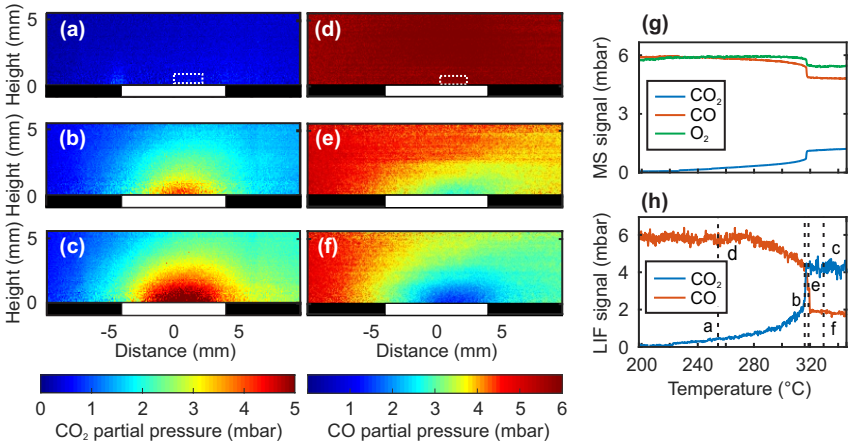

Figure 6.2: CO_2 and CO distribution over a Pd(100) single crystal (*white rectangle*) during CO oxidation. (a-c) 10-shot average CO_2 PLIF images recorded at different temperatures. (d-f) 10-shot average CO PLIF images recorded at different temperatures. (g) MS trends of CO, O_2 and CO_2; (h) Integrated CO_2 and CO PLIF signal from the dashed box in (a) and (d). Note that the shift of the CO_2 and CO cloud to the right of the sample is due to the gas flow.

kept the same. Notably, the CO_2 boundary layer is still present at pressures down to 25 mbar. The presence of the CO_2 boundary layer indicates a substantial depletion of CO above the surface, which probably can explain the missing gas phase CO peak in the AP-XPS spectra in Ref [101]. This is also discussed in Paper II and V.

6.1.3 Stagnation Flow Reactor

Figure 6.4 shows the CO_2 distributions over a Pd(100) sample in the MTL regime at two different flow rates. Both measurements were performed at 300 mbar total pressure and with 1:1 CO/O_2 ratio. It can be seen that the CO_2 boundary layer is more compressed in the case with the higher flow rate. The vertical CO_2 concentration profile in Fig. 6.4a shows a good agreement with the modeling, which is presented in more detail in Paper X. The good agreement indicates that a good stagnation flow can be obtained in the reactor.

One of the advantages of using stagnation flow geometry for studying single crystal samples under *operando* conditions is that we can get a well defined CO_2 signal from the sample surface, which is not interfered by the signal from other parts of the sample, i.e. the sides, as illustrated in Fig. 6.5. During the temperature ramp-up, the PLIF images in Fig. 6.5a-c reveal that the sides of the sample (indicated by the red arrow)

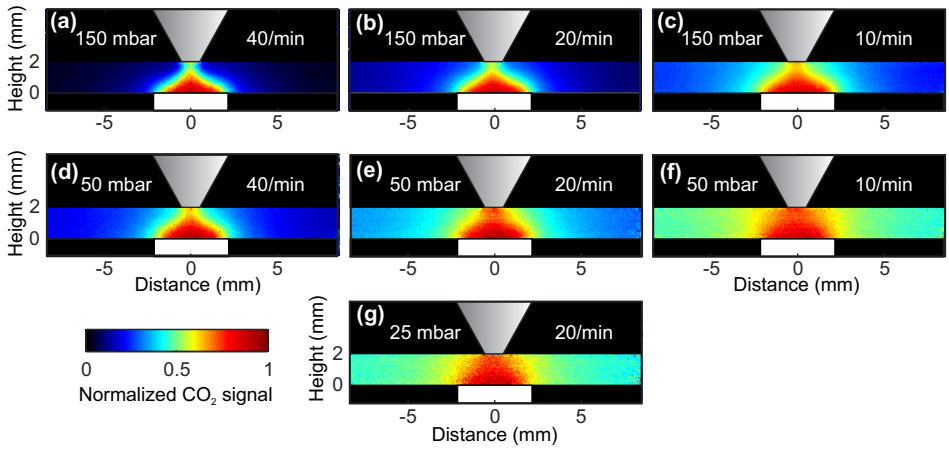

Figure 6.3: Pressure and flow dependence of the CO_2 distribution over a Pd(100) single crystal during CO oxidation in the MTL regime. Note: x mbar and y/min denote the total chamber pressure and the gas exchange rate, respectively. All images are averaged over 1000 shots to improve the signal to noise ratio.

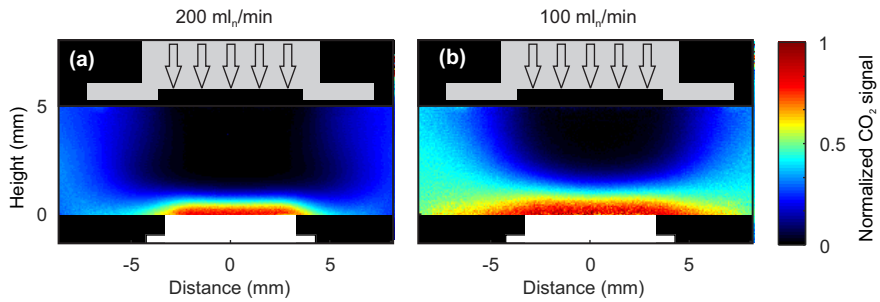

Figure 6.4: CO_2 distribution over a Pd(100) during CO oxidation in MTL regime at different flow rates, (a) 200 ml_n min^{-1} and (b) 100 ml_n min^{-1}, with the same total pressure of 300 mbar. (a) shows a better stagnation flow.

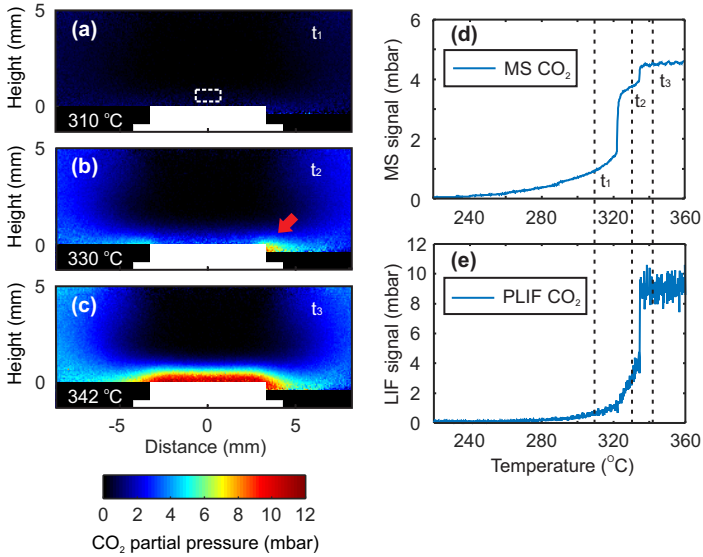

Figure 6.5: The CO_2 distribution over a Pd(100) single crystal during CO oxidation in a stagnation flow. (a)-(c), PLIF 10-shot average images recorded at different time and temperatures during the temperature ramp-up. (d) The MS signal. (e) The integrated PLIF signal 0.5 mm above the sample. The active sides of the sample are indicated by the red arrow in (b).

become active at t_2, earlier than the top surface which becomes active at t_3. Both the MS signal in Fig. 6.5d and the integrated LIF signal in Fig. 6.5e, indicate an MTL reaction after the light-off of the top surface. Importantly, comparing the LIF signal with the MS signal, there is only one step in the LIF trend corresponding to the ignition of the top surface, while there are two distinct steps in the MS trend, corresponding to the ignition of the sides and top of the sample, respectively. This demonstrates that a well-defined CO_2 signal generated only from the top surface can be retrieved from the PLIF signal, which is not or very little interfered by the signal generated from the sides of the sample. This shows the benefits of combining stagnation flow with PLIF measurements for studying single crystal model catalysts under *operando* conditions.

Figure 6.6 shows the CO distributions over the Pd(100) sample during CO oxidation in the MTL regime using a stagnation flow and a prototypical flow geometry, respectively, under the same gas conditions as in Fig. 6.5c. Surprisingly, comparing Fig. 6.5c and Figure 6.6a, the increase of CO_2 partial pressure is much more than the decrease of CO partial pressure, with 9 mbar and 6 mbar, respectively. One would suspect that this discrepancy comes from the uncertainty of the calibration of the PLIF signal. However, a comparison of the CO distribution between two measurements

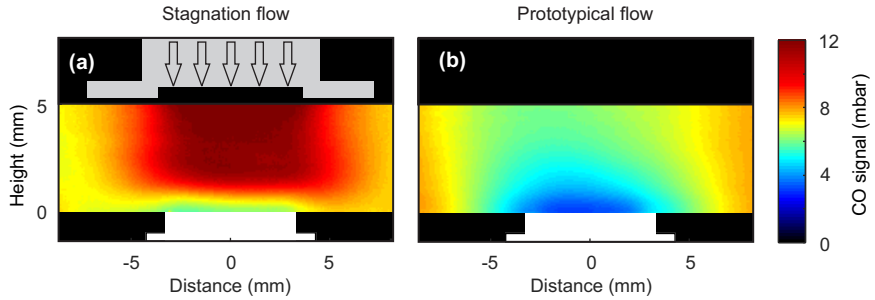

Figure 6.6: CO distribution over a Pd(100) during CO oxidation in the MTL regime using two different flow geometries, (a) stagnation flow and (b) prototypical flow, showing the depletion of CO is much more in (b) than in (a).

with different flow geometries reveals a significant difference in the depletion of CO, regarding to both gradient and partial pressure, as shown in Figure 6.6. This indicates that flow and reactor geometries have a strong impact on the gas composition above the sample surface under realistic conditions.

6.2 Visualization of Activity around Samples

If different parts (microscopically and macroscopically) of a catalyst consist of different surface structures, they will exhibit different catalytic activity, which can be reflected by the gas composition around them under reaction conditions. With its high spatial resolution, PLIF can be used to visualize the gas distribution, i.e. to probe the catalytic activity, around a catalyst. In this way, we can visualize the activity around the sample down to sub-mm scale, limited by the gas diffusion. We demonstrate this with three examples in the following.

6.2.1 Curved Samples

As already described in Chapter 2, a curved crystal sample consists of two sides with different type of steps, A type and B type. We used PLIF to follow the CO_2 distribution over a curved Pd and Pt sample, separately, during CO oxidation. In this way, we can investigate the role of steps on the activation temperature for the curved Pd and Pt samples. The results are shown in Fig. 6.7.

In the experiment with the Pd, the sample is slowly heated from 230 to 330 °C in a total gas flow of 100 ml_n min^{-1}. As the temperature increases, a steady increase of CO_2 can be seen. At 304 °C, the B-type side of the sample becomes highly active, as evidenced by the prominent CO_2 cloud over the B-type side of the sample, as shown

in Fig. 6.7a. As the temperature further increases, and at 310 °C, the A-type side of the sample also becomes highly active, as evidenced by the CO_2 cloud over the entire sample, as shown in Fig. 6.7b. The PLIF images and two integrated LIF trends in Fig. 6.7c, one from each side, clearly reveal that the A-type and B-type side of the Pd sample ignite at different temperatures, with a difference of 6 °C. The difference in activation temperature between these two types of step was supported by Density Function Theory (DFT) calculations, which reveal that the steps have different ability of releasing strain in the mircoterraces, facilitating the CO desorption and initiating the catalytic reaction. More details of the DFT calculations can be found in Paper VI.

In the experiment with the Pt, the sample is heated from from 240 to 350 °C in the same gas conditions as in the case with the Pd. In contrast to the case with the Pd, no obvious difference in the activation temperature can be observed between the A-type and B-type side of the Pt sample. Both sides have the same light-off temperature of 301 °C, as evidenced by the PLIF images recorded just before and after the light-off of the sample with a 0.1 s separation. DFT calculations have not been performed for the Pt crystal, but is of great interest for future work.

6.2.2 Active sides

Single crystal catalysts are widely used for surface science studies. In practice, they are manufactured to have grooves or be hat-shaped for easy-to-hold purposes. This will introduce undefined catalytic surfaces, i.e. sides, which are usually exposed to the same gas environment as the top surface that is studied. If the sides are also active during the experiment, it would be difficult to avoid the resulted interference, leading to not well-defined correlations in structure-activity analysis.

To demonstrate this, the CO_2 distribution over a Pd(111) single crystal (2 mm thick) during CO oxidation was studied with PLIF in the prototypical flow reactor shown in Fig. 6.1a. The results are shown in Fig. 6.8. The PLIF images recorded at different temperatures during the ramp up, as shown in Fig. 6.8a-c (top view), and d-f (side view) reveal that the sides of the sample become active before the top surface of the sample. Compared to the stagnation flow case shown in Fig. 6.5, there are two distinct steps in both the PLIF and MS trends, as shown in 6.1g and h, respectively. The PLIF images in Fig. 6.8b and e, as well as LIF trend (red) in Fig. 6.8g clearly demonstrate that there is a substantial amount of CO_2 that spills over from the active sides to above the top surface. This spill-over effect can be a potential issue when one tries to correlate the catalytic activity with the surface change in *operando* studies, without spatially resolved measurements of the gas phase. To minimize this spill-over effect, one can use the stagnation flow geometry as shown in Fig. 6.1c.

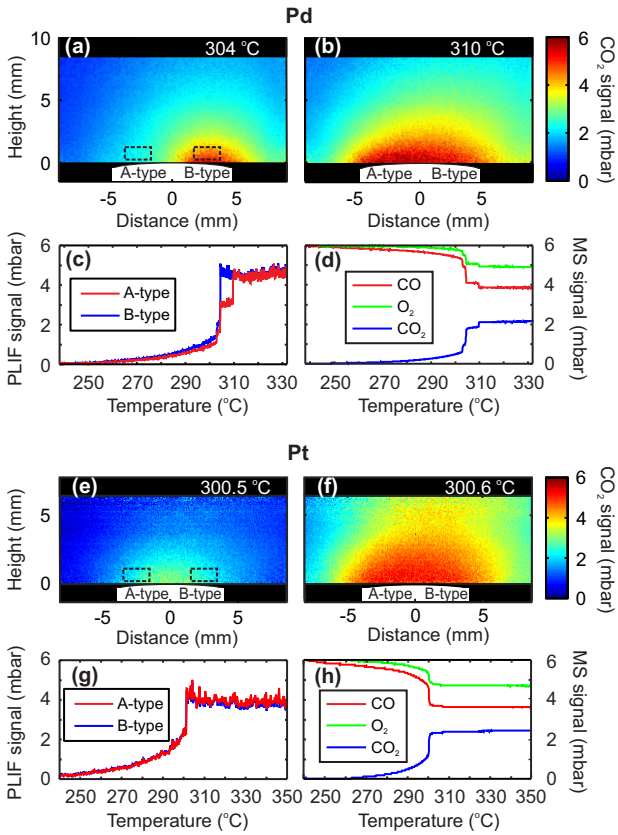

Figure 6.7: PLIF and MS measurements of a curved Pd (a-d), and a curve Pt crystal (e- h), in a gas flow of 4 ml_n min^{-1} CO, 4 ml_n min^{-1} O_2 and 92 ml_n min^{-1} Ar, and at a total chamber pressure of 150 mbar. (a) and (b) show PLIF images recoreded just after the first and the second light-off, respectively. (c) shows the integrated PLIF signal from a small region just above each side of the Pd sample. (d) shows the MS trends of CO, O_2 and CO_2. (e) and (f) show PLIF images recorded just before and after the light-off, respectively. (g) shows the integrated PLIF signal from a small region just above each side of the Pt sample. (h) shows the MS trends of CO, O_2 and CO_2.

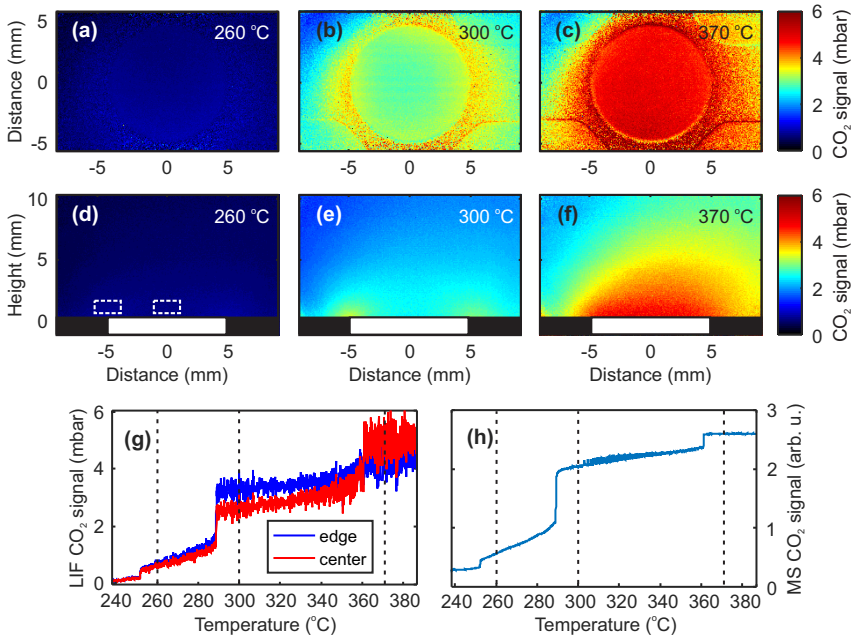

Figure 6.8: The CO_2 distribution over a Pd(111) single crystal during CO oxidation in a prototypical flow geometry. (a)-(c) and (d)-(f) show PLIF 10-shot average images recorded at different time and temperatures during the temperature ramp-up in two separate measurements, from top view and side view, respectively. (g) The PLIF trends integrated from small regions above the center (red) and the edge (blue) of the sample, respectively. The regions are marked by the dashed rectangles in (d). (h) The CO_2 MS signal.

6.2.3 Two Samples

By placing two samples side-by-side in the same reactor, one can directly compare the light-off temperatures of the two samples in the same gas environment. The case with two powder samples has been demonstrated in Paper VII. Here we show an example with two single crystal samples, Pd(553) and Pd(111).

The samples are heated up slowly on the same heating holder. Three PLIF images that were recorded at different temperatures and times, as shown in Fig. 6.9a-c, reveal that the two samples have different light-off temperatures. Figure 6.9a shows that there is a small amount of signal between the two samples at t_1, which can be attributed to the active sides of the samples. In this case, however, we cannot identify which of the samples that is responsible for the active sides because the camera view is not large enough. The LIF trends in Fig. 6.9d clearly show a large difference in activation temperature between the two samples, approx. 60 °C. This result supports the finding with the curved Pd crystal in Fig. 6.7, where the side with steps are more active than the top with extended (111) facet.

6.3 Gas-Surface Correlations in *Operando* Studies

In order to get a better understanding of the gas-surface interaction in heterogeneous catalytic reactions, it is essential to correlate the structural change of the surface to the gas composition close the surface. In this section, we demonstrate the importance of spatially and temporally resolved gas detection in *operando* studies of catalysis, by combining PLIF with surface techniques, SOR and HESXRD, respectively, in CO oxidation over a Pd(100) surface.

6.3.1 Spatial Correlation

From the previous section, we can see that the CO_2 composition across a highly active Pd sample is not homogeneous. To investigate the effect of the gradient in the gas composition on the sample surface, we have combined PLIF and SOR, for simultaneous measurements of the CO_2 distribution above and the optical reflectance of a Pd(100) surface during CO oxidation. We found that when the reaction was in the MTL regime, the inhomogeneity of the gas composition across the sample could lead to an inhomogeneity of the surface reflectivity, which can be attributed to a gradient of oxide thickness and surface roughness [13].

The results are summarized in Fig. 6.10. During the experiment, the Pd(100) sample was kept at 320 °C and 125 mbar, in a total flow of 50 ml_n min^{-1}. The initial partial pressures of O_2, CO and Ar were set to 75 mbar , 5 mbar and 45 mbar, respectively. The reaction was thus under O_2 rich condition with a 15:1 O_2/CO ratio. An

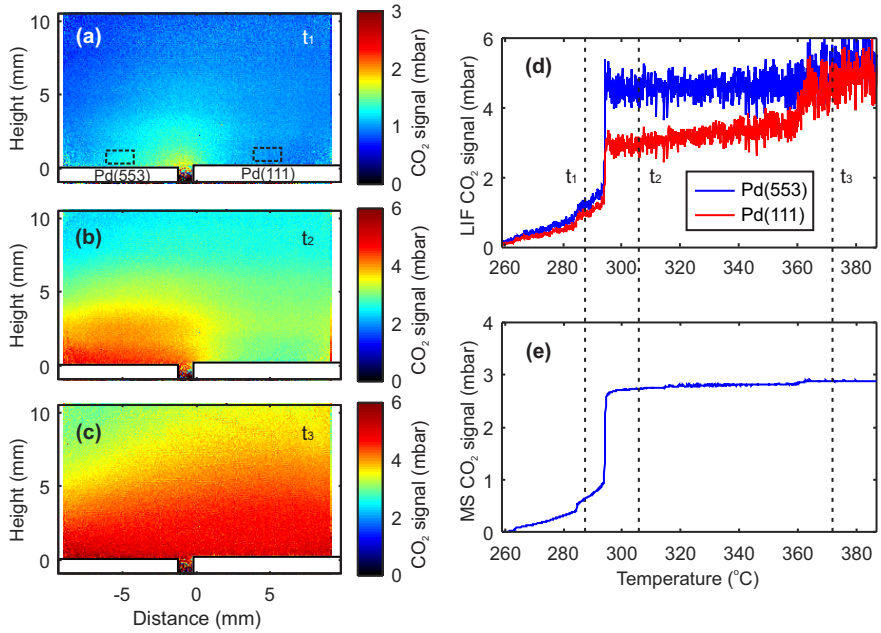

Figure 6.9: The CO_2 distribution over two samples, Pd(553) and Pd(111), during CO oxidation. (a)-(c) PLIF 10-shot average images recorded at different time and temperatures during the temperature ramp-up showing the CO_2 distribution over the two samples. (d) The PLIF trends integrated from small regions above the Pd(553) and Pd(111), respectively. The regions are marked by the dashed rectangles in (a). (e) The MS CO_2 signal.

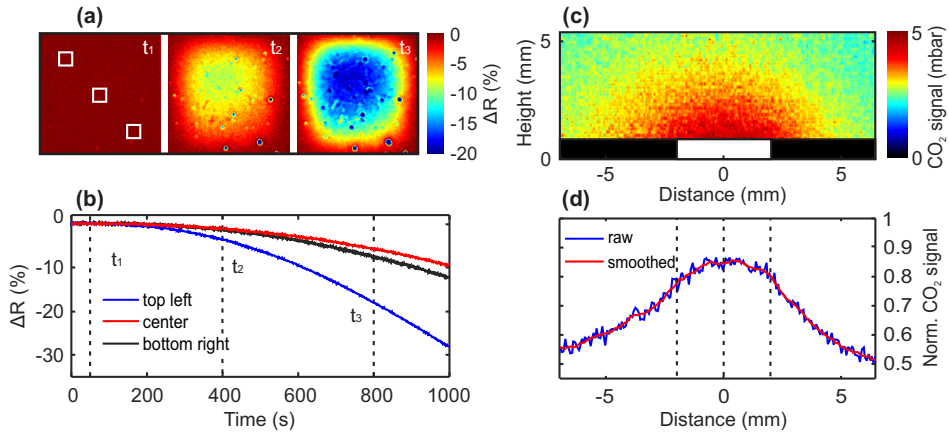

Figure 6.10: Simultaneous measurements of SOR and PLIF during CO oxidation over a Pd(100). (a) SOR images showing the surface reflectance change at t_1 = 50 s, t_2 = 400 s, and t_3 = 800 s. (b) The change of the SOR signal at different regions of the surface marked by the white squares in (a). (c) PLIF image showing the CO_2 distribution above the sample. (d) Normalized CO_2 profiles horizontally at 0.5 mm above the sample. The dashed lines mark the positions of the center and the edges of the sample. $t = 0$ is defined as when the gases were switched from pure Ar to CO and O_2 mixtures.

MS was used to measure the gas composition from the outlet and to ensure that the reaction was in the MTL regime. Fig. 6.10a shows that the SOR signal does not change homogeneously over the entire surface. Instead, the signal decreases much faster at the center of the sample than at the corners of the sample. The corresponding CO_2 gas distribution above the sample is shown in Fig. 6.10c. A normalized horizontal CO_2 profile in Fig. 6.10d, shows that the CO_2 distribution across the sample is not homogeneous but decreases radially from the center of the surface. This suggests that the gas composition has the highest O_2/CO ratio at the center. Combining the results from the PLIF and SOR measurements, the inhomogeneous development of the surface reflectance, which has also been observed in Ref [12], can be attributed to the gradient of the gas composition across the surface, where the higher O_2/CO ratio at the center of the sample causes a faster Pd oxide formation and a quicker roughening, compared to that at the corners of the sample.

6.3.2 Temporal Correlation

We will emphasize the importance of temporal resolution of gas phase detection in *operando* catalysis studies, using a combined PLIF, HESXRD and MS measurement

during CO oxidation over a Pd(100) as showcase. The results are shown in Fig. 6.11. At the start of the experiment, the sample was exposed to 6 mbar of CO and 144 mbar of Ar but no O_2 and at a constant temperature of 200 °C, which resulted in an inactive and CO poisoned sample. This is confirmed by the HESXRD image in Fig. 6.11a, which shows a CTR from the substrate, indicating a metallic surface. At this stage, no CO_2 is detected in the gas phase above the sample surface, as evidenced by the PLIF image in Fig. 6.11e. As the O_2 flow was switched on, the sample became active immediately and the PLIF image in Fig. 6.11f shows a substantial amount of CO_2 above the sample, indicating an ignition of the reaction. Interestingly, at this stage, a metallic surface is still detected in the HESXRD image shown in Fig. 6.11b. About 2.5 s after the ignition, surface oxide rods originating from the $\sqrt{5} \times \sqrt{5} - R27°$ surface oxide appear in the diffraction pattern in Fig. 6.11c. Correspondingly, a prominent boundary layer of CO_2 above the sample is detected with PLIF, as shown in Fig. 6.11g. As the reaction continues in the MTL regime, the prominent boundary layer of CO_2 above the sample remains, shown in Fig. 6.11h and the $\sqrt{5} \times \sqrt{5} - R27°$ surface oxide diffraction pattern intensifies, as shown in Fig. 6.11d.

The most interesting finding from this experiment is that a well-ordered surface oxide structure, to be detectable by HESXRD, is not immediately formed at the early stage in the MTL regime. From Fig. 6.11i we can see that the surface oxide rod signal appears slightly after the jump in the CO_2 PLIF trend but before the change of the CO_2 MS trend. This suggests that an immediate detection of the gas phase with high temporal resolution is important in order to draw an accurate temporal correlation between the gas phase and the surface under *operando* conditions.

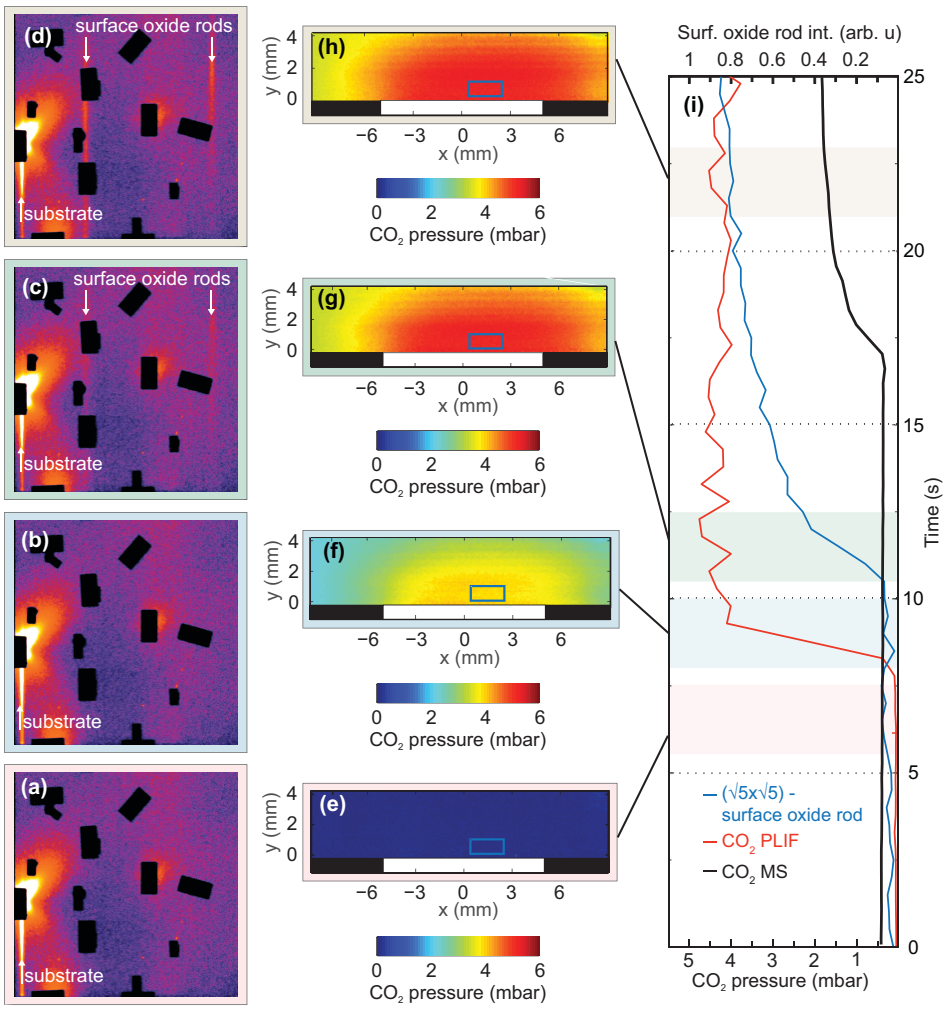

Figure 6.11: Simultaneneous measurements of HESXRD, PLIF and MS during CO oxidation over a Pd(100). (a)-(d) show four HESXRD images acquired at different time, and (e)-(h) show the corresponding PLILF images. Each image (HESXRD and PLIF) is averaged over 2.5 s. (i) the HESXRD, PLIF and MS trends over time. showing the surface oxide rod signal, the CO_2 pressure just above the sample, and the CO_2 pressure at the gas outlet of the reactor, respectively. The data is plotted with an updating frequency of 0.5 s. The black rectangles in the diffraction images shows the positions of tungsten pieces which protect the detector from strong Bragg reflections from the Pd(100) and the sapphire chamber.

Chapter 7

Conclusions and Outlook

Using mainly CO oxidation over a Pd(100) single crystal catalyst as a showcase, we have demonstrated the distinct advantages of using PLIF for gas phase characterization during catalytic reactions. The advantages lie on the properties of PLIF, high spatial and temporal resolution, non-intrusiveness as well as the suitability to be operated at *operando* conditions.

Using the high spatial resolution of PLIF, we can image the gas distribution around an active catalyst, revealing the gas composition close to the surface, which is important for structure-activity analysis in *operando* studies. In addition, we can characterize the gas flow in a catalytic reactor by imaging the gas distribution over a working catalyst. This shows the great potential of using PLIF for characterization of reactors and optimization of reaction conditions, as reactor geometries and flow have a strong effect on the gas phase of model catalysts.

By taking advantage of the high spatial and temporal resolution of PLIF, we can follow the dynamic change of the gas phase and directly compare the catalytic activity of different parts of a sample, or two separate samples, in the same gas environment. Our results show that one should pay attention to the sides/edges of a single crystal sample when it is studied under *operando* conditions, as the activity from the sides/edges might lead to not-well defined structure-activity correlations.

Although PLIF generally requires a complex experimental setup, e.g. the laser system, it has been shown that PLIF is a flexible technique that can be combined with other surface techniques for simultaneous measurements. The results from the simultaneous measurements with PLIF and SOR reveal that an inhomogeneity of the gas phase close to a highly active sample can lead to an inhomogeneity of optical reflectivity of the surface, which strongly indicates a gradient of oxide thickness and/or surface roughness. It therefore suggests that one should pay attention to the probed area of a sample when using surface sensitive techniques. For example, HP-STM only probes a

small region on the surface while SXRD gives an integrated signal along a large footprint on the surface. The results from the simultaneous measurements with PLIF and HESXRD reveal that temporal resolution of the gas phase detection as well as of the surface structure measurements is crucial for making meaningful structure-function correlations.

For future work, it would be of great interest to use PLIF to study other important flow geometries, e.g. a channel flow which is highly relevant to industrial applications where high flow rates are used. The temperature gradient of the gas in the channel flow would be interesting to measure with PLIF as well. The experimental results can then be compared with the model, which would give more insights into the surface chemistry of model catalysts in a channel flow.

CO oxidation has been used as a showcase throughout this thesis to demonstrate the powerful capabilities of PLIF. The applications of PLIF are however definitely not limited to only simple reactions, e.g. CO oxidation where there are only three species involved. In fact, there are a lot of interesting reactions to study, e.g. NO assisted CO oxidation, ammonia oxidation, etc.

There is one distinct advantage of laser-based techniques that has not been demonstrated in this work. That is the ability to detect many radicals of interest, such as OH, CH, Formaldehyde and CH_3, in relevant catalytic reactions. For conventional methods, e.g. MS, it is usually challenging to detect radicals which are very reactive and short-lived. In contrast, laser-based techniques are powerful in detecting radicals, e.g. in flames. For future work, it would be of great interest to detect, for example CH_3 radicals in the gas phase in oxidative coupling of methane (OCM) reactions [102], as the information of CH_3 radicals in the gas phase can provide new insights into the reaction mechanisms [103]. For the detection of CH_3 radicals, photo-fragmentation laser induced fluorescence can be used [104].

It is of great value to combined PLIF with surface sensitive techniques for simultaneous measurements. On one hand, it would be convenient to employ more compact PLIF setups. For example, CW quantum-cascade lasers would be very attractive for CO_2 and CO PLIF [72, 105]. On the other hand, it would also be interesting to combine PLIF with lab-based surface techniques, e.g. PM-IRAS, as synchrotron-based techniques are not easily accessible for daily use.

Last but not the least, IR-DFWM hold great potential in catalysis for quantitative, *in situ* detection of small hydrocarbon molecules, such as CH_4, C_2H_4, C_2H_2 and C_2H_6, in relevant catalytic reactions.

Bibliography

[1] Ertl, G.; Knözinger, H.; Weitkamp, J. Handbook of heterogeneous catalysis; VCH: Weinheim, 2008.

[2] Heck, R. M.; Farrauto, R. J.; Gulati, S. T. Catalytic air pollution control: commercial technology; John Wiley & Sons, 2009.

[3] Ertl, G. Reactions at surfaces: From atoms to complexity. Angewandte Chemie International Edition **2008**, 47, 3524–3535.

[4] Frenken, J.; Groot, I. *Operando* research in heterogeneous catalysis; Springer: Cham, 2017.

[5] Starr, D. E.; Liu, Z.; Havecker, M.; Knop-Gericke, A.; Bluhm, H. Investigation of solid/vapor interfaces using ambient pressure X-ray photoelectron spectroscopy. Chemical Society Reviews **2013**, 42, 5833–5857.

[6] Hendriksen, B. L. M.; Bobaru, S. C.; Frenken, J. W. M. Looking at heterogeneous catalysis at atmospheric pressure using tunnel vision. Topics in Catalysis **2005**, 36, 43–54.

[7] Frenken, J.; Groot, I. In *Operando* research in heterogeneous catalysis; Frenken, J., Groot, I., Eds.; Springer: Cham, 2017; pp 1–30.

[8] Stierle, A.; Molenbroek, A. M. Novel *in situ* probes for nanocatalysis. MRS Bulletin **2007**, 32, 1001–1009.

[9] Ryczkowski, J. IR spectroscopy in catalysis. Catalysis Today **2001**, 68, 263–381.

[10] Gao, F.; McClure, S. M.; Cai, Y.; Gath, K. K.; Wang, Y.; Chen, M. S.; Guo, Q. L.; Goodman, D. W. CO oxidation trends on Pt-group metals from ultrahigh vacuum to near atmospheric pressures: A combined *in situ* PM-IRAS and reaction kinetics study. Surface Science **2009**, 603, 65–70.

[11] Jinschek, J. R. Advances in the environmental transmission electron microscope (ETEM) for nanoscale *in situ* studies of gas-solid interactions. Chemical Communications **2014**, 50, 2696–2706.

[12] Onderwaater, W. G.; Taranovskyy, A.; Bremmer, G. M.; Baarle, G. C. v.; Frenken, J. W. M.; Groot, I. M. N. From dull to shiny: A novel setup for reflectance difference analysis under catalytic conditions. Review of Scientific Instruments **2017**, 88, 023704.

[13] Onderwaater, W. G.; Taranovskyy, A.; van Baarle, G. C.; Frenken, J. W. M.; Groot, I. M. N. *In Situ* optical reflectance difference observations of CO oxidation over Pd(100). The Journal of Physical Chemistry C **2017**, 121, 11407–11415.

[14] Freund, H.-J.; Meijer, G.; Scheffler, M.; Schlögl, R.; Wolf, M. CO oxidation as a prototypical reaction for heterogeneous processes. Angewandte Chemie International Edition **2011**, 50, 10064–10094.

[15] van Spronsen, M. A.; Frenken, J. W. M.; Groot, I. M. N. Surface science under reaction conditions: CO oxidation on Pt and Pd model catalysts. Chemical Society Reviews **2017**, 46, 4347–4374.

[16] Gao, F.; Wang, Y.; Cai, Y.; Goodman, D. W. CO oxidation on Pt-group metals from ultrahigh vacuum to near atmospheric pressures. 2. palladium and platinum. The Journal of Physical Chemistry C **2009**, 113, 174–181.

[17] Gao, F.; Wang, Y.; Goodman, D. W. Reply to "comment on 'CO oxidation on Pt-group metals from ultrahigh vacuum to near atmospheric pressures. 2. palladium and platinum'". The Journal of Physical Chemistry C **2010**, 114, 6874–6874.

[18] van Rijn, R.; Balmes, O.; Resta, A.; Wermeille, D.; Westerström, R.; Gustafson, J.; Felici, R.; Lundgren, E.; Frenken, J. W. M. Surface structure and reactivity of Pd(100) during CO oxidation near ambient pressures. Physical Chemistry Chemical Physics **2011**, 13, 13167–13171.

[19] Gustafson, J.; Balmes, O.; Zhang, C.; Shipilin, M.; Schaefer, A.; Hagman, B.; Merte, L. R.; Martin, N. M.; Carlsson, P.-A.; Jankowski, M.; Crumlin, E. J.; Lundgren, E. The role of oxides in catalytic CO oxidation over rhodium and palladium. ACS Catalysis **2018**, 4438–4445.

[20] Matera, S.; Reuter, K. First-principles approach to heat and mass transfer effects in model catalyst studies. Catalysis Letters **2009**, 133, 156–159.

[21] Matera, S.; Reuter, K. Transport limitations and bistability for *in situ* CO oxidation at $RuO_2(110)$: First-principles based multiscale modeling. Physical Review B **2010**, 82, 085446.

[22] Matera, S.; Reuter, K. When atomic-scale resolution is not enough: Spatial effects on *in situ* model catalyst studies. Journal of Catalysis **2012**, 295, 261–268.

[23] Matera, S.; Maestri, M.; Cuoci, A.; Reuter, K. Predictive-quality surface reaction chemistry in real reactor models: Integrating first-principles kinetic Monte Carlo simulations into computational fluid dynamics. ACS Catalysis **2014**, 4, 4081–4092.

[24] Roos, M.; Kielbassa, S.; Schirling, C.; Häring, T.; Bansmann, J.; Behm, R. J. Scanning mass spectrometer for quantitative reaction studies on catalytically active microstructures. Review of Scientific Instruments **2007**, 78, 084104.

[25] Tan, C. K. C.; Delgass, W. N.; Baertsch, C. D. Spatially resolved *in situ* FTIR analysis of CO adsorption and reaction on Pt/SiO_2 in a silicon microreactor. Applied Catalysis B: Environmental **2009**, 93, 66–74.

[26] Kohse-Höinghaus, K. Laser techniques for the quantitative detection of reactive intermediates in combustion systems. Progress in Energy and Combustion Science **1994**, 20, 203–279.

[27] Eckbreth, A. C. Laser diagnostics for combustion temperature and species; Taylor and Francis: New York, 1996.

[28] Aldén, M.; Bood, J.; Li, Z.; Richter, M. Visualization and understanding of combustion processes using spatially and temporally resolved laser diagnostic techniques. Proceedings of the Combustion Institute **2011**, 33, 69–97.

[29] Rosén, A.; Ljungström, S.; Wahnström, T.; Kasemo, B. Laser diagnostics of radicals in catalytic reactions. Journal of Electron Spectroscopy and Related Phenomena **1986**, 39, 15–25.

[30] Fridell, E.; Westblom, U.; Aldén, M.; Rosén, A. Spatially resolved laser-induced fluorescence imaging of OH produced in the oxidation of hydrogen on platinum. Journal of Catalysis **1991**, 128, 92–98.

[31] Gudmundson, F.; Fridell, E.; Rosén, A.; Kasemo, B. Evaluation of hydroxyl desorption rates from platinum using spatially resolved imaging of laser-induced fluorescence. The Journal of Physical Chemistry **1993**, 97, 12828–12834.

[32] Fridell, E.; Elg, A.; Rosén, A.; Kasemo, B. A laser-induced fluorescence study of OH desorption from Pt(111) during oxidation of hydrogen in O_2 and decomposition of water. The Journal of Chemical Physics **1995**, 102, 5827–5835.

[33] Gudmundson, F.; Persson, J. L.; Försth, M.; Behrendt, F.; Kasemo, B.; Rosén, A. OH gas phase chemistry outside a Pt catalyst. Journal of Catalysis **1998**, 179, 420–430.

[34] Försth, M.; Gudmundson, F.; Persson, J. L.; Rosén, A. The influence of a catalytic surface on the gas-phase combustion of H_2 + O_2. Combustion and Flame **1999**, 119, 144–153.

[35] Försth, M.; Eisert, F.; Gudmundson, F.; Persson, J.; Rosén, A. Analysis of the kinetics for the H_2 + $\frac{1}{2}$ O_2 $\rightleftharpoons$ H_2O reaction on a hot Pt surface in the pressure range 0.10–10 Torr. Catalysis Letters **2000**, 66, 63–69.

[36] Anderson, L. C.; Xu, M.; Mooney, C. E.; Rosynek, M. P.; Lunsford, J. H. Hydroxyl radical formation during the reaction of oxygen with methane or water over basic lanthanide oxide catalysts. Journal of the American Chemical Society **1993**, 115, 6322–6326.

[37] Su, H.; Yeung, E. S. High-throughput screening of heterogeneous catalysts by laser-induced fluorescence imaging. Journal of the American Chemical Society **2000**, 122, 7422–7423.

[38] Kang, W.; Fujita, O.; Ito, K. Visualization of formaldehyde distribution above platinum plate catalyst by using LIF method. Journal of Energy Resources Technology **1996**, 118, 82–87.

[39] Reinke, M.; Mantzaras, J.; Bombach, R.; Schenker, S.; Inauen, A. Gas phase chemistry in catalytic combustion of methane/air mixtures over platinum at pressures of 1 to 16 bar. Combustion and Flame **2005**, 141, 448–468.

[40] Eriksson, S.; Schneider, A.; Mantzaras, J.; Wolf, M.; Jaras, S. Experimental and numerical investigation of supported rhodium catalysts for partial oxidation of methane in exhaust gas diluted reaction mixtures. Chemical Engineering Science **2007**, 62, 3991–4011.

[41] Zetterberg, J.; Blomberg, S.; Gustafson, J.; Sun, Z. W.; Li, Z. S.; Lundgren, E.; Aldén, M. An *in situ* set up for the detection of CO_2 from catalytic CO oxidation by using planar laser-induced fluorescence. Review of Scientific Instruments **2012**, 83, 053104.

[42] Zetterberg, J.; Blomberg, S.; Gustafson, J.; Evertsson, J.; Zhou, J.; Adams, E. C.; Carlsson, P.-A.; Aldén, M.; Lundgren, E. Spatially and temporally resolved gas distributions around heterogeneous catalysts using infrared planar laser-induced fluorescence. Nature Communications **2015**, 6, 7076.

[43] Blomberg, S.; Brackmann, C.; Gustafson, J.; Aldén, M.; Lundgren, E.; Zetterberg, J. Real-time gas-phase imaging over a Pd(110) catalyst during CO oxidation by means of planar laser-induced fluorescence. ACS Catalysis **2015**, 5, 2028–2034.

[44] Zhou, J.; Pfaff, S.; Lundgren, E.; Zetterberg, J. A convenient setup for laser-induced fluorescence imaging of both CO and CO_2 during catalytic CO oxidation. Applied Physics B **2017**, 123, 87.

[45] Zhou, J.; Blomberg, S.; Gustafson, J.; Lundgren, E.; Zetterberg, J. Visualization of gas distribution in a model AP-XPS reactor by PLIF: CO oxidation over a Pd(100) catalyst. Catalysts **2017**, 7, 29.

[46] Zhou, J.; Blomberg, S.; Gustafson, J.; Lundgren, E.; Zetterberg, J. Simultaneous imaging of gas phase over and surface reflectance of a Pd(100) single crystal during CO oxidation. The Journal of Physical Chemistry C **2017**, 121, 23511–23519.

[47] Blomberg, S.; Zhou, J.; Gustafson, J.; Zetterberg, J.; Lundgren, E. 2D and 3D imaging of the gas phase close to an operating model catalyst by planar laser induced fluorescence. Journal of Physics: Condensed Matter **2016**, 28, 453002.

[48] Zellner, A.; Suntz, R.; Deutschmann, O. Two-dimensional spatial resolution of concentration profiles in catalytic reactors by planar laser-induced fluorescence: NO reduction over diesel oxidation catalysts. Angewandte Chemie International Edition **2015**, 54, 2653–2655.

[49] Somorjai, G. A.; Li, Y. Introduction to surface chemistry and catalysis; John Wiley & Sons, 2010.

[50] Orent, T. W.; Bader, S. D. LEED and ELS study of the initial oxidation of Pd(100). Surface Science **1982**, 115, 323–334.

[51] Todorova, M.; Lundgren, E.; Blum, V.; Mikkelsen, A.; Gray, S.; Gustafson, J.; Borg, M.; Rogal, J.; Reuter, K.; Andersen, J. N.; Scheffler, M. The Pd(100)-$(\sqrt{5} \times \sqrt{5})R27°$-O surface oxide revisited. Surface Science **2003**, 541, 101–112.

[52] Kostelník, P.; Seriani, N.; Kresse, G.; Mikkelsen, A.; Lundgren, E.; Blum, V.; Šikola, T.; Varga, P.; Schmid, M. The surface oxide: A LEED, DFT and STM study. Surface Science **2007**, 601, 1574–1581.

[53] Shipilin, M.; Hejral, U.; Lundgren, E.; Merte, L. R.; Zhang, C.; Stierle, A.; Ruett, U.; Gutowski, O.; Skoglundh, M.; Carlsson, P.-A.; Gustafson, J. Quantitative surface structure determination using *in situ* high-energy SXRD: Surface oxide formation on Pd(100) during catalytic CO oxidation. Surface Science **2014**, 630, 229–235.

[54] Shipilin, M.; Stierle, A.; Merte, L. R.; Gustafson, J.; Hejral, U.; Martin, N. M.; Zhang, C.; Franz, D.; Kilic, V.; Lundgren, E. The influence of incommensurability on the long-range periodicity of the Pd(100)-$(\sqrt{5}\times\sqrt{5})R27°$-PdO(101). Surface Science **2017**, 660, 1–8.

[55] Shipilin, M.; Gustafson, J.; Zhang, C.; Merte, L. R.; Stierle, A.; Hejral, U.; Ruett, U.; Gutowski, O.; Skoglundh, M.; Carlsson, P.-A.; Lundgren, E. Transient structures of PdO during CO oxidation over Pd(100). The Journal of Physical Chemistry C **2015**, 119, 15469–15476.

[56] Weaver, J. F. Surface chemistry of late transition metal oxides. Chemical Reviews **2013**, 113, 4164–4215.

[57] Rogal, J.; Reuter, K.; Scheffler, M. Thermodynamic stability of PdO surfaces. Phys. Rev. B **2004**, 69, 075421.

[58] Hendriksen, B. L. M.; Bobaru, S. C.; Frenken, J. W. M. Oscillatory CO oxidation on Pd(100) studied with *in situ* scanning tunneling microscopy. Surface Science **2004**, 552, 229–242.

[59] Onderwaater, W. G.; Balmes, O.; Roobol, S. B.; Van Spronsen, M.; Drnec, J.; Carla, F.; Felici, R.; Frenken, J. W. M. Oxidation of CO on Pd(100): On the structural evolution of the PdO layer during the self sustained oscillation regime. Catalysis, Structure & Reactivity **2017**, 3, 89–94.

[60] Hirvi, J. T.; Kinnunen, T.-J. J.; Suvanto, M.; Pakkanen, T. A.; Nørskov, J. K. CO oxidation on PdO surfaces. The Journal of Chemical Physics **2010**, 133, 084704.

[61] Schüth, F.; Henry, B. E.; Schmidt, L. D. Oscillatory reactions in heterogeneous catalysis. Advances in Catalysis **1993**, 39, 51–127.

[62] Imbihl, R.; Ertl, G. Oscillatory kinetics in heterogeneous catalysis. Chemical Reviews **1995**, 95, 697–733.

[63] Hendriksen, B. L. M.; Ackermann, M. D.; van Rijn, R.; Stoltz, D.; Popa, I.; Balmes, O.; Resta, A.; Wermeille, D.; Felici, R.; Ferrer, S.; Frenken, J. W. M. The role of steps in surface catalysis and reaction oscillations. Nature Chemistry **2010**, 2, 730–734.

[64] Li, Z.; Rupinski, M.; Zetterberg, J.; Alwahabi, Z.; Aldén, M. Mid-infrared polarization spectroscopy of polyatomic molecules: Detection of nascent CO_2 and H_2O in atmospheric pressure flames. Chemical Physics Letters **2005**, 407, 243 – 248.

[65] Karlsson, H. Calibration measurements in a catalysis reaction chamber using thermographic phosphors; Bachelor's Thesis: Lund University, 2015.

[66] van Rijn, R.; Ackermann, M. D.; Balmes, O.; Dufrane, T.; Geluk, A.; Gonzalez, H.; Isern, H.; de Kuyper, E.; Petit, L.; Sole, V. A.; Wermeille, D.; Felici, R.; Frenken, J. W. M. Ultrahigh vacuum/high-pressure flow reactor for surface x-ray diffraction and grazing incidence small angle X-ray scattering studies close to conditions for industrial catalysis. Review of Scientific Instruments **2010**, 81, 014101.

[67] Daily, J. W. Laser induced fluorescence spectroscopy in flames. Progress in Energy and Combustion Science **1997**, 23, 133 – 199.

[68] Dally, B. B.; Masri, A. R.; Barlow, R. S.; Fiechtner, G. J. Two-photon laser-induced fluorescence measurement of CO in turbulent non-premixed bluff body flames. Combustion and Flame **2003**, 132, 272–274.

[69] Brackmann, C.; Bood, J.; Nauclér, J. D.; Konnov, A. A.; Aldén, M. Quantitative picosecond laser-induced fluorescence measurements of nitric oxide in flames. Proceedings of the Combustion Institute **2017**, 36, 4533–4540.

[70] Li, Z. S.; Kiefer, J.; Zetterberg, J.; Linvin, M.; Leipertz, A.; Bai, X. S.; Aldén, M. Development of improved PLIF CH detection using an Alexandrite laser for single-shot investigation of turbulent and lean flames. Proceedings of the Combustion Institute **2007**, 31, 727–735.

[71] Brackmann, C.; Li, Z.; Rupinski, M.; Docquier, N.; Pengloan, G.; Aldén, M. Strategies for formaldehyde detection in flames and engines using a single-mode Nd:YAG/OPO laser system. Applied Spectroscopy **2005**, 59, 763–768.

[72] Goldenstein, C. S.; Miller, V. A.; Hanson, R. K. Infrared planar laser-induced fluorescence with a CW quantum-cascade laser for spatially resolved CO_2 and gas properties. Applied Physics B **2015**, 120, 185–199.

[73] Kirby, B. J.; Hanson, R. K. Linear excitation schemes for IR planar-induced fluorescence imaging of CO and CO_2. Applied Optics **2002**, 41, 1190–1201.

[74] Alwahabi, Z. T.; Zetterberg, J.; Li, Z. S.; Aldén, M. High resolution polarization spectroscopy and laser induced fluorescence of CO_2 around 2 μm. European Physical Journal D **2007**, 42, 41–47.

[75] Kirby, B. J.; Hanson, R. K. Imaging of CO and CO_2 using infrared planar laser-induced fluorescence. Proceedings of the Combustion Institute **2000**, 28, 253–259.

[76] Aldén, M.; Wallin, S.; Wendt, W. Applications of two-photon absorption for detection of CO in combustion gases. Applied Physics B **1984**, 33, 205–208.

[77] Seitzman, J. M.; Haumann, J.; Hanson, R. K. Quantitative two-photon LIF imaging of carbon monoxide in combustion gases. Applied Optics **1987**, 26, 2892–2899.

[78] Brackmann, C.; Sjöholm, J.; Rosell, J.; Richter, M.; Bood, J.; Aldén, M. Picosecond excitation for reduction of photolytic effects in two-photon laser-induced fluorescence of CO. Proceedings of the Combustion Institute **2013**, 34, 3541–3548.

[79] Linow, S.; Dreizler, A.; Janicka, J.; Hassel, E. Comparison of two-photon excitation schemes for CO detection in flames. Applied Physics B **2000**, 71, 689–696.

[80] Loge, G. W.; Tiee, J. J.; Wampler, F. B. Multiphoton induced fluorescence and ionization of carbon monoxide ($B^1\Sigma^+$). The Journal of Chemical Physics **1983**, 79, 196–202.

[81] Abrams, R. L.; Lind, R. C. Degenerate four-wave mixing in absorbing media. Optics Letters **1978**, 2, 94–96.

[82] Abrams, R. L.; Lind, R. C. Degenerate four-wave mixing in absorbing media: errata. Optics Letters **1978**, 3, 205–205.

[83] Kiefer, J.; Ewart, P. Laser diagnostics and minor species detection in combustion using resonant four-wave mixing. Progress in Energy and Combustion Science **2011**, 37, 525–564.

[84] Vander Wal, R. L.; Holmes, B. E.; Jeffries, J. B.; Danehy, P. M.; Farrow, R. L.; Rakestraw, D. J. Detection of HF using infrared degenerate four-wave mixing. Chemical Physics Letters **1992**, 191, 251–258.

[85] Germann, G. J.; Rakestraw, D. J. Multiplex spectroscopy: Determining the transition moments and absolute concentrations of molecular species. Science **1994**, 264, 1750–1753.

[86] Germann, G. J.; Farrow, R. L.; Rakestraw, D. J. Infrared degenerate 4-wave-mixing spectroscopy of polyatomic molecules - CH_4 and C_2H_2. Journal of the Optical Society of America B-Optical Physics **1995**, 12, 25–32.

[87] Richard, K.; Ewart, P. High-resolution infrared polarization spectroscopy and degenerate four wave mixing spectroscopy of methane. Applied Physics B-Lasers and Optics **2009**, 94, 715–723.

[88] Tang, Y.; Reid, S. A. Infrared degenerate four wave mixing spectroscopy of jet-cooled C_2H_2. Chemical Physics Letters **1996**, 248, 476–481.

[89] Sun, Z. W.; Li, Z. S.; Li, B.; Alden, M.; Ewart, P. Detection of C_2H_2 and HCl using mid-infrared degenerate four-wave mixing with stable beam alignment: towards practical in situ sensing of trace molecular species. Applied Physics B **2010**, 98, 593–600.

[90] Sahlberg, A. L.; Zhou, J.; Aldén, M.; Li, Z. S. Non-intrusive *in situ* detection of methyl chloride in hot gas flows using infrared degenerate four-wave mixing. Journal of Raman Spectroscopy **2015**, 46, 695–701.

[91] Sahlberg, A.-L.; Hot, D.; Aldén, M.; Li, Z. S. Non-intrusive, *in situ* detection of ammonia in hot gas flows with mid-infrared degenerate four-wave mixing at 2.3 µm. Journal of Raman Spectroscopy **2016**, 47, 1140–1148.

[92] Reichardt, T. A.; Lucht, R. P. Interaction of closely spaced resonances in degenerate four-wave-mixing spectroscopy. Journal of the Optical Society of America B-Optical Physics **1997**, 14, 2449–2458.

[93] Feidenhans'l, R. Surface structure determination by X-ray diffraction. Surface Science Reports **1989**, 10, 105–188.

[94] Robinson, I. K.; Tweet, D. J. Surface X-ray diffraction. Reports on Progress in Physics **1992**, 55, 599.

[95] Stierle, A.; Gustafson, J.; Lundgren, E. In *Operando* research in heterogeneous catalysis; Frenken, J., Groot, I., Eds.; Springer International Publishing: Cham, 2017; pp 59–87.

[96] Gustafson, J.; Shipilin, M.; Zhang, C.; Stierle, A.; Hejral, U.; Ruett, U.; Gutowski, O.; Carlsson, P.-A.; Skoglundh, M.; Lundgren, E. High-energy surface X-ray diffraction for fast surface structure determination. Science **2014**, 343, 758–761.

[97] Hejral, U.; Müller, P.; Shipilin, M.; Gustafson, J.; Franz, D.; Shayduk, R.; Rütt, U.; Zhang, C.; Merte, L. R.; Lundgren, E.; Vonk, V.; Stierle, A. High-energy x-ray diffraction from surfaces and nanoparticles. Physical Review B **2017**, 96, 195433.

[98] Bluhm, H.; Hävecker, M.; Knop-Gericke, A.; Kiskinova, M.; Schlögl, R.; Salmeron, M. *In Situ* X-ray photoelectron spectroscopy studies of gas-solid interfaces at near-ambient conditions. MRS Bulletin **2007**, 32, 1022–1030.

[99] Zanier, F.; Michelon, N.; Canu,; P., Design and characterization of a stagnation flow reactor for heterogeneous microkinetic studies. Chemical Engineering Journal **2017**, 315, 67 – 82.

[100] Matera, S.; Blomberg, S.; Hoffmann, M. J.; Zetterberg, J.; Gustafson, J.; Lundgren, E.; Reuter, K. Evidence for the active phase of heterogeneous catalysts through *In Situ* reaction product imaging and multiscale modeling. ACS Catalysis **2015**, 5, 4514–4518.

[101] Blomberg, S.; Hoffmann, M. J.; Gustafson, J.; Martin, N. M.; Fernandes, V. R.; Borg, A.; Liu, Z.; Chang, R.; Matera, S.; Reuter, K.; Lundgren, E. *In situ* X-ray photoelectron spectroscopy of model catalysts: At the edge of the gap. Physical Review Letters **2013**, 110, 117601.

[102] Arndt, S.; Laugel, G.; Levchenko, S.; Horn, R.; Baerns, M.; Scheffler, M.; Schlögl, R.; Schomäcker, R. A critical assessment of Li/MgO-based catalysts for the oxidative coupling of methane. Catalysis Reviews **2011**, 53, 424–514.

[103] Luo, L.; Tang, X.; Wang, W.; Wang, Y.; Sun, S.; Qi, F.; Huang, W. Methyl radicals in oxidative coupling of methane directly confirmed by synchrotron VUV photoionization mass spectroscopy. Scientific Reports **2013**, 3, 1625.

[104] Li, B.; Zhang, D.; Yao, M.; Li, Z. Strategy for single-shot CH_3 imaging in premixed methane/air flames using photofragmentation laser-induced fluorescence. Proceedings of the Combustion Institute **2017**, 36, 4487–4495.

[105] Mathews, G. C.; Goldenstein, C. S. Wavelength-modulated planar laser-induced fluorescence for imaging gases. Optics Letters **2017**, 42, 5278–5281.

Summary of Papers

Paper I:
A convenient setup for laser-induced fluorescence imaging of both CO and CO_2 during catalytic CO oxidation

J. Zhou, S. Pfaff, E. Lundgren and J. Zetterberg, Applied Physics B, 2017, 123, 87

In this paper we present a setup for PLIF imaging of both CO and CO_2 during catalytic CO oxidation over a Pd(100) single crystal. The experimental setup consists of a nanosecond YAG-Dye laser system together with a broadband mid-infrared Optical Parametric Oscillator (Mid-IR OPO). With the setup it is convenient to switch PLIF measurements between CO and CO_2.

I planned the experiment and took part in the measurements and data analysis, and wrote the manuscript.

Paper II:
Visualization of gas distribution in a model AP-XPS reactor by PLIF: CO oxidation over a Pd (100) catalyst

J. Zhou, S. Blomberg, J. Gustafson, E. Lundgren and J. Zetterberg, Catalysts 2017, 7, 29

This paper describes a home-built model reactor that can be used to mimic the gas flow in a real one for ambient pressure X-ray photoelectron spectroscopy (AP-XPS). It investigates the flow characteristics in the reactor with PLIF visualizing the CO_2 distribution above a Pd(100) catalyst during CO oxidation. The results show that the CO_2 distribution is strongly dependent on the flow rate and rector geometry.

I planned the experiment and took part in the measurements, and was responsible for the data analysis and manuscript writing.

Paper III:
Simultaneous imaging of gas phase over and surface reflectance of a Pd(100) single crystal during CO oxidation

J. Zhou, S. Blomberg, J. Gustafson, E. Lundgren and J. Zetterberg, The Journal of Physical Chemistry C 2017, 121, 23511-23519

This paper presents simultaneous measurements of the gas phase and the optical surface reflectance of a Pd (100) single crystal during CO Oxidation, and investigates the spatial correlation between the gas phase and the surface reflectance under oxidation conditions. The results show that when the reaction is in the mass transfer limited (MTL) regime, the inhomogeneity of the gas composition across the sample can lead to an inhomogeneity of the surface reflectivity, which indicates a gradient of oxides thickness and surface roughness.

I planned the experiment and took part in the measurements, and was responsible for the data analysis and manuscript writing.

Paper IV:
2D and 3D imaging of the gas phase close to an operating model catalyst by planar laser induced fluorescence

S. Blomberg, J. Zhou, J. Gustafson, J. Zetterberg and E. Lundgren, Journal of Physics: Condensed Matter 2016, 28, 453002

This paper reviews the use of PLIF for imaging the gas phase above model catalysts at work under semi-realistic conditions, e.g. CO_2/CO during CO oxidation, CO_2 during CO_2 hydrogenation, and NH_3 during hydrogen assisted NH_3 oxidation. It highlights the benefits of PLIF with its high spatial and temporal resolution.

I took part in most of the CO_2 PLIF measurements and data analysis.

Paper V:
Comparison of AP-XPS and PLIF measurements during CO oxidation over Pd single crystals

S. Blomberg, J. Zetterberg, J. Gustafson, J. Zhou, C. Brackmann and E. Lundgren, Topics in Catalysis 2016, 59, 478-486

This work investigates the gas phase close to a Pd(100) surface during CO oxidation,

and compares the results obtained from separate AP-XPS and PLIF measurements. The PLIF results show that the prominent CO_2 boundary layer formed over the surface in the MTL regime can inhibit the CO defusing onto the surface resulting in a depletion of CO. This depletion of CO can be used to explain the lack of CO gas phase signal in the AP-XPS spectra.

I took part in the CO_2 PLIF measurements and data analysis.

Paper VI:
Strain dependent light-off temperature in catalysis revealed by planar laser-induced fluorescence

S. Blomberg, J. Zetterberg, J. Zhou, L. R. Merte, J. Gustafson, M. Shipilin, A. Trinchero, L. A. Miccio, A. Magaña, M. Ilyn, F. Schiller, J. E. Ortega, F. Bertram, H. Grönbeck and E. Lundgren, ACS Catalysis 2017, 7, 110-114

This paper shows the advantage of using PLIF in comparing the light-off temperatures between the two sides of a cylindrically shaped Pd single crystal sample with two different step orientations. The results show that the B-type step has a 6 °C lower light-off temperature as compared to the A-type step. The experimental finding is supported by the Density Function Theory (DFT) calculations.

I took part in the PLIF measurements and data analysis.

Paper VII:
Novel *in situ* techniques for studies of model catalysts

E. Lundgren, C. Zhang, L. R. Merte, M. Shipilin, S. Blomberg, U. Hejral, J. Zhou, J. Zetterberg and J. Gustafson, Accounts of Chemical Research 2017, 50, 2326-2333

This paper presents three relatively new yet powerful *in situ* techniques, AP-XPS, PLIF and High Energy Surface X-ray Diffraction (HESXRD) for *operando* studies of model catalysts using CO oxidation over a Pd(100) as an example. The paper discusses the strengths and weaknesses of each experimental technique, and shows that both surface structural knowledge and the composition of the gas phase close to the catalyst surface are essential for a better understanding of the structure-function relationships under semi-realistic gas conditions.

I took part in the CO_2 PLIF measurements and made the data analysis.

Paper VIII:
Spatially and temporally resolved gas distributions around heterogeneous catalysts using infrared planar laser-induced fluorescence

J. Zetterberg, S. Blomberg, J. Gustafson, J. Evertsson, J. Zhou, E.C. Adams, P.A. Carlsson, M. Aldén and E. Lundgren, Nature Communications 2015, 6, 7076

This paper demonstrates the advantages of PLIF in studying the gas phase in heterogeneous catalysis, such as high spatial and temporal resolution. The spatially resolved CO_2 distribution over a highly active catalyst reveals that the gas composition close to the catalyst is significantly different from that measured by a mass spectrometer (MS) located at the gas outlet of the reactor. The paper also demonstrates the potential ability of PLIF for sample screening in catalysis studies. It shows that PLIF can be a powerful complementary tool to conventional ones, e.g. MS, for studying the gas phase over working catalysts

I took part in the calibration measurements for the CO_2 PLIF signal.

Paper IX:
Combining synchrotron light with laser technology in catalysis research

S. Blomberg, J. Zetterberg, J. Gustafson, J. Zhou, M. Shipilin, S. Pfaff, U. Hejral, P. A. Carlsson, O. Gutowski, F. Bertram and E. Lundgren, Journal of Synchrotron Radiation 2018, 25, 1389-1394

This paper presents simultaneous PLIF and HESXRD measurements of CO oxidation over a Pd(100) surface under *operando* conditions. The results show an interesting temporal correlation between the surface oxide rod signal detected by HESXRD and the light-off of a sample, as evidenced by the PLIF visualization of the CO_2 production above the sample. This paper shows the benefit of the sub-second time resolution of the two techniques, allowing for an improved assignment of the correlation between the surface structure and the gas phase composition above the surface.

I took part in both the PLIF and HESXRD measurements and analyzed the PLIF data.

Paper X:
Experimental and modeling studies of the gas phase of model catalysts in a stagnation flow

J. Zhou, S. Matera, S. Pfaff, S. Blomberg, E. Lundgren and J. Zetterberg, Submitted to the Journal of Physical Chemistry C

This paper presents a home-built flow reactor with which we study the CO oxidation over a Pd(100) single crystal catalyst in a stagnation flow. The results show a good agreement between the measured and modeled CO_2 concentration profiles above the sample, which indicates that a good stagnation flow can be achieved with in the reactor. In addition, the measured CO_2 profiles can be used by the model to predict the gas concentrations right at the sample surface.

I was responsible for the PLIF measurements and data analysis, and wrote the majority of the manuscript.

Paper XI:
Combining HESXRD with LED reflectance and PLIF for *operando* catalyst surface characterization

S. Pfaff, J. Zhou, U. Hejral, J. Gustafson, M. Shipilin, S. Albertin, S. Blomberg, O. Gutowski, A. C. Dippel, E. Lundgren and J. Zetterberg, In manuscript

This paper presents simultaneous PLIF, surface optical reflectance (SOR) and HESXRD measurements of CO oxidation over a Pd(100) surface under *operando* conditions. The results show clear temporal and spatial correlations between the oxide signal detected by HESXRD and the reduced surface reflectance measured by SOR, both of which can be related to a highly oxidizing environment close to the sample surface in the MTL regime, as evidenced by the PLIF measurements. This paper demonstrates the importance of performing spatially resolved measurements of both the surface and gas phase macroscopically for a better understanding of the gas-surface correlations.

I took part in the measurements and the analysis of the PLIF and surface optical reflectance data.

Paper XII:
Non-intrusive detection of methanol in gas phase using infrared degenerate four-wave mixing

J. Zhou, A. L. Sahlberg, H. Nilsson, E. Lundgren and J. Zetterberg, Applied Physics B 2015, 121, 123-130

This paper describes a non-intrusive gas detection tool, IR-DFWM for the detection of methanol in gas phase with high spatial and temporal resolution. The paper discusses the potential interference from CH_4 and CO_2, and the results show that interference-free detection of methanol is possible. The results also show the potential of using IR-DFWM to detect methanol in catalytic environments, such as CO_2 hydrogenation and CH_4 oxidation.

I planned the experiment and took part in the measurements and data analysis, and was responsible for the manuscript writing.

Paper I

Appl. Phys. B (2017) 123:87
DOI 10.1007/s00340-017-6681-3

Applied Physics B
Lasers and Optics

A convenient setup for laser-induced fluorescence imaging of both CO and CO_2 during catalytic CO oxidation

Jianfeng Zhou[1] · **S. Pfaff**[1] · **E. Lundgren**[2] · **J. Zetterberg**[1]

Received: 24 November 2016 / Accepted: 20 February 2017 / Published online: 10 March 2017
© The Author(s) 2017. This article is published with open access at Springerlink.com

Abstract In-situ knowledge of the gas composition close to a catalyst is essential for a better understanding of the gas–surface interaction. With planar laser-induced fluorescence (PLIF), the gas distribution around an operating catalyst can be visualized with high spatial and temporal resolution, in a non-intrusive manner. We report on a convenient setup using a nanosecond YAG-Dye laser system together with a broadband mid-infrared optical parametric oscillator (OPO) for imaging both CO and CO_2 over a Pd(100) catalyst during catalytic CO oxidation, compare it to previously used systems, and show examples of its capabilities.

1 Introduction

Catalysis plays an important role in our daily life. Approximately 90% of all chemicals and materials around us are produced using catalysis at one stage or another [1]. In addition to this, catalysis is used to reduce emissions for a more sustainable society. For example, the three-way catalyst is used in almost every gasoline-fueled vehicle to clean the exhaust gases from harmful species such as CO, NO_x, and hydrocarbons. CO oxidation, being an important model reaction, has been studied intensively for many decades [2]. The reaction process is well known under ultra-high vacuum (UHV) conditions where gas flows and gas distribution around a sample are often neglected. However, the number of molecules interacting with the catalyst surface increases significantly at elevated pressures, and as a result, a change in the gas composition close to the surface may lead to a change of the surface structure [3, 4]. Therefore, it is essential to obtain in-situ knowledge of the gas composition close to an operating catalyst to achieve a better understanding of the gas–surface interaction.

Conventional gas analytical tools such as mass spectrometry (MS), gas chromatography (GC), and Fourier transform infrared spectrometry (FTIR) are often used to analyze gases from the outlet of a reactor. These techniques have the benefit of measuring several species simultaneously, but they suffer from a time delay or poor temporal resolution, and are not capable to spatially resolve the gas composition around a sample. Although capillary sampling techniques can provide spatially resolved concentration profiles inside reactors [5], it cannot deliver two-dimensional measurements to follow dynamic changes in the gas phase on a sub-second scale, and the intrusive nature of the probe may introduce errors in data interpretation.

As an in-situ and non-invasive gas detection technique with high spatial and temporal resolution, planar laser-induced fluorescence (PLIF) has been widely used in the combustion community for flame studies [6–8], but much less applied in the catalyst community [9]. In earlier studies during the 1990s, LIF has been used to study the OH formation close to a Pt catalyst during the H_2 oxidation [10–14], the distribution of OH desorbed from a Pt catalyst during catalytic water formation reaction [15], and the formaldehyde distribution above a platinum plate during catalytic combustion of methanol/air mixtures [16]. However, in the 2000s, there were

Electronic supplementary material The online version of this article (doi:10.1007/s00340-017-6681-3) contains supplementary material, which is available to authorized users.

✉ Jianfeng Zhou
Jianfeng.zhou@forbrf.lth.se

[1] Division of Combustion Physics, Lund University, 221 00 Lund, Sweden

[2] Division of Synchrotron Radiation Research, Lund University, 221 00 Lund, Sweden

very limited works related to catalysis studies, two of which are the studies of OH during the gas phase combustion of fuel-lean methane/air pre-mixtures over Pt [17], and formaldehyde over supported Rh catalysts for partial oxidation of methane in exhaust gas diluted reaction mixtures [18]. Over the past few years, applications of the technique have been largely extended to study the distribution of CO_2 and/or CO over model catalysts during CO oxidation [19–25], hydrogen-assisted NH_3 oxidation above a Ag/Al_2O_3 powder catalyst [23], as well as catalytic reduction of NO by hydrogen to ammonia over a Pt/Al_2O_3 catalyst [26]. All of these studies have demonstrated PLIF as a powerful complimentary tool to conventional tools, such as MS, for studies of gas phase in catalysis.

In previous works by Blomberg et al. [20], the detection of CO and CO_2 from CO oxidation was carried out separately using two large laser systems. The CO PLIF was performed using a picosecond laser system consisting of a mode-locked Nd:YAG laser with an external amplifier and an optical parametric generator, yielding a broadband UV beam. And the CO_2 PLIF was performed using a nanosecond laser system consisting of a Nd:YAG laser, a dye laser, and a mixing unit, generating a tunable narrowband infrared laser beam.

Here we report a convenient setup using a nanosecond YAG-Dye laser system together with a broadband mid-infrared optical parametric oscillator (OPO) for imaging both CO and CO_2. CO is detected via the visible-wavelength fluorescence (450–660 nm) of the $B^1\Sigma^+ \rightarrow A^1\Pi$ transition in the Angstrom bands by nanosecond two-photon excitation of the $X^1\Sigma^+ \rightarrow B^1\Sigma^+$ transition at 230.1 nm [27, 28], while CO_2 is detected via the mid-infrared fluorescence from the fundamental band ~4.3 μm by broadband excitation at ~2.7 μm. Excitation at 2.7 μm is chosen as an optimized scheme for the current setup, because it provides relatively strong absorption cross section, while the laser absorption by the air along the beam path is not so severe. Other excitation schemes for CO_2 PLIF detection can be found in [29–33]. As a proof of concept, quantitative measurements of both CO and CO_2 over a Pd catalyst during catalytic CO oxidation have been carried out to demonstrate the high spatial and temporal resolution of the two techniques for studies of gas phase in catalysis. Comparisons between the picosecond and nanosecond excitation approaches for CO detection, and between the narrowband and broadband excitation approaches for CO_2 detection, will be presented. The quenching effect on the signal calibration for both CO and CO_2 will also be discussed.

2 Experiment

2.1 Laser-induced fluorescence

The optical setup to perform measurements of CO and CO_2 is shown in Fig. 1. An injection seeded Nd:YAG laser (Continuum, Powerlite DLS 8010) operating at second harmonic (532 nm, 800 mJ/pulse, 10 Hz) was used to pump the Dye laser (Continuum, Vista) running on R610 dye (Exiton), with ethanol as solvent, which produced laser radiation of around 150 mJ at 587.2 nm with a linewidth specified to 0.05 cm^{-1}. This fundamental dye output was then frequency doubled by a BBO crystal (Continuum, Vista FX) to obtain a UV beam of around 30 mJ/pulse at 293.6 nm. This UV beam was mixed in a second BBO crystal (Continuum, Vista FX) with the residual 1064 nm beam from the Nd:YAG laser, generating laser pulses at 230.1 nm of energy ~9 mJ and pulse width ~5 ns. The 230.1-nm beam was steered by three UV-fused silica prisms, shaped into a thin laser sheet of

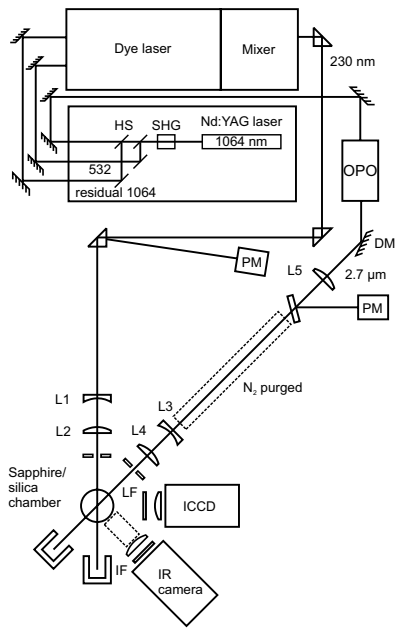

Fig. 1 Schematic of the optical setup. SHG, second harmonic generator; HS, harmonics separators; L1 UVFS lens, $f = -40$ mm; L2 UVFS lens, $f = 150$ mm; L3 CaF_2 lens, $f = -40$ mm; L4 CaF_2 lens, $f = 100$ mm; L5 CaF_2 lens, $f = 500$ mm; *DM* dichroic mirror, *PM* power meter, *IF* interference filter, *LF* long-pass filter; *dashed boxes* indicate the N_2 purged region

~6 mm height by a cylindrical and a spherical lens, $f = -40$ mm and $f = 150$ mm, respectively, and sent through the silica chamber just above the catalyst sample. The laser sheet had energy of ~2.5 mJ in front of the chamber, mainly due to energy losses from the optics and edge cutting by the aperture. The reflected 230.1-nm beam from one of the prisms was measured by a power meter (Gentec-EO, Maestro) to keep track of shot-to-shot variation in the laser pulse energy during measurement.

The CO fluorescence was imaged by an ICCD camera (Princeton Instruments, PIMAX 3) using an objective (Nikkor $f = 50$ mm, f/1.2) with a 31-mm extension ring mounted on the camera. The intensifier gate was set to 250 ns, which is much longer than the collision-free lifetime (68 ns) of the $B^1\Sigma^+$ fluorescence [34]. Images were acquired at a 10-Hz repetition rate. The CCD chip was hardware-binned 2 × 2 to increase the image acquisition rate as well as the signal-to-noise ratio (SNR). A long-pass filter (GG455, Schott) was applied to suppress the scattering and fluorescence from the fused silica chamber below 455 nm.

To switch the laser output from UV to mid-IR for CO_2 detection, the second harmonic generator (SHG) crystal and the harmonics separators (HS) were removed from the YAG laser. The fundamental 1064-nm laser beam with ~350 mJ/pulse from the YAG laser was used to pump an IR-OPO (GWU, versaScan-L 1064), generating a signal beam ~1.7 μm and an idler beam at 2.7 μm, with ~8 mJ/pulse and ~7 mJ/pulse, respectively. Both the signal and idler beams have pulse width of ~5 ns. The idler beam was separated from the signal beam by a dichroic mirror (HR at 2.7 μm), and formed into a thin laser sheet of ~6 mm height by a cylindrical and two spherical lenses, $f = -40$ mm, $f = 100$ mm, and $f = 500$ mm, respectively, and sent through the sapphire chamber just above the catalyst. The idler beam had energy of ~3 mJ in front of the chamber. A CaF_2 window in the beam path was used to reflect ~10% of the laser energy to keep track of shot-to-shot variation with a power meter.

The CO_2 fluorescence was imaged by a liquid-nitrogen-cooled, 256 × 256 InSb IR camera (Santa Barbara Focal Plane, SBF LP134) using a CaF_2 lens ($f = 50$ mm, f/2.3). A cold interference filter inside the camera, centered at 4.26 μm and with FWHM of 200 nm, was used to suppress the strong thermal background. As the radiative lifetime of the IR-transition is rather long ~100 μs [29], the exposure time was set to 30 μs to discriminate background and favor fluorescence signal, and a time delay of 10 μs relative to the Q-switch of the YAG laser was used to avoid scattering from the laser and time jitter. As the thermal background was continuously varying during the experiments, the camera was triggered at 20 Hz, via a pulse generator (BNC, Model 575), with every second exposure measuring the background, which was to be subtracted afterwards. A more detailed description of this detection scheme can be referred to [19]. To reduce laser energy attenuation along the beam path and fluorescence signal loss between the cell and the IR camera, purging of N_2 was applied during measurements.

2.2 Sample and catalysis reactor

The sample investigated was a Pd single crystal with diameter of 8 mm, thickness of 2 mm and a (100) surface orientation. A fused silica cylindrical chamber with diameter of 30 mm and height of 25 mm was used for the CO measurements, while a sapphire one of the same dimensions for the CO_2 measurements. Gases were supplied to the reactor by individual mass flow controllers (Bronkhorst EL-FLOW), and the gas pressure in the reactor was controlled by a digital pressure controller (Bronkhorst EL-PRESS). The gas composition in the reactor was measured by a quadruple mass spectrometer (Pfeiffer, QME 220) connected to the outlet of the reactor with an automated leak valve. The sample was heated by a boralectric heater, the temperature of which was measured by a type D thermocouple. When the sample was heated at a slow speed of ~15 °C/min, the temperature of the sample was assumed to be the same as the sample heater.

3 Results and discussions

To examine the CO and CO_2 absorption behaviors to the corresponding excitation laser sources, excitation scans for both CO and CO_2 have been performed, as shown in Fig. 2. For the CO excitation scan, 4% CO was mixed in Ar at room temperature and a pressure of 150 mbar, while for the CO_2 excitation scan, 4% CO_2 was mixed in Ar at the same temperature and pressure. Before each measurement, the chamber was pumped down to a very low pressure (~1 mbar) and then purged with the measured gases. The purging lasted for long enough time (~5 min) to ensure that there is no or negligible amount of residual gases in the chamber. In Fig. 2, a smoothing of five consecutive data points has been applied to both scans to reduce noise due to shot-to-shot laser energy fluctuation.

As can be seen in Fig. 2a, a high-resolution CO spectrum showing the Q-branch of the $B^1\Sigma^+(v' = 0) \rightarrow A^1\Pi(v'' = 0)$ transition is obtained thanks to the narrowband UV beam. By convoluting a variety of laser profiles (with assumed Gaussian shape) and a simulated CO absorption spectrum (at 296 K and 150 mbar), and comparing the convoluted spectra with the measured CO excitation scan, the full-width of half maximum (FWHM) of the UV laser is estimated to ~0.5 cm^{-1} (0.0026 nm). In contrast to CO, the CO_2 spectrum in Fig. 2 b exhibits a very broad feature due

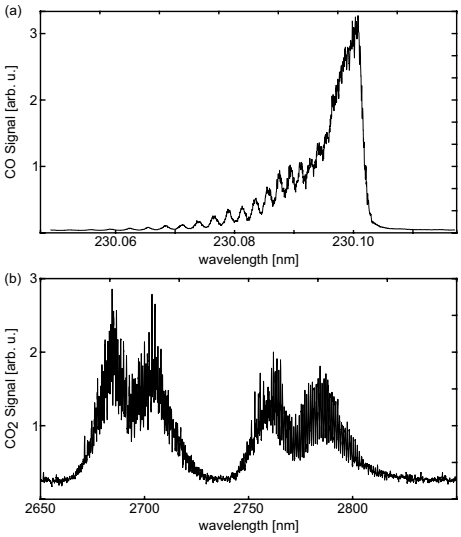

Fig. 2 Excitation spectrum of CO (**a**) and CO_2 (**b**) at room temperature and 150 mbar

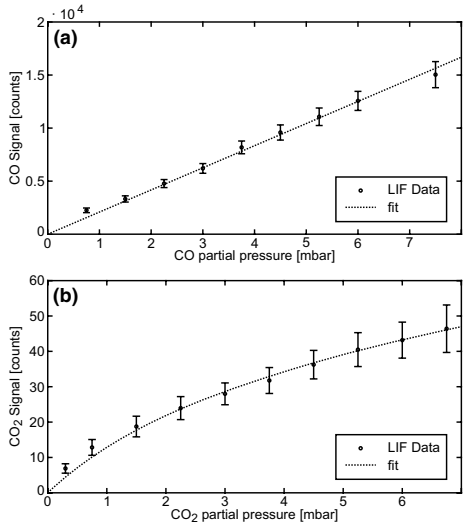

Fig. 3 Concentration dependence of the fluorescence signal for CO (**a**) and CO_2 (**b**), at 300 °C and 150 mbar

to the broadband laser from the IR-OPO. In a similar manner as above, the full-width of half maximum (FWHM) of the IR laser is estimated to ~10 cm^{-1} (7.3 nm). Thus, the linewidth of this laser covers a number of ro-vibrational lines in the $(00^00) \rightarrow (10^001)$ transition of CO_2. It is worth noting that the linewidth of the laser from this IR-OPO has strong wavelength dependence. At wavelength ~3 μm, the linewidth was previously measured to ~5 cm^{-1} using an IR grating and an IR camera [35].

For quantitative PLIF measurements of CO and CO_2, the concentration dependence on the fluorescence signal for both CO and CO_2 was investigated by varying the partial pressure of CO and CO_2 in Ar separately at non-reacting conditions. For non-reacting conditions, the sample was heated at the same total chamber pressure and gas flow rates as for reacting conditions. In this way, the temperature gradient of the gases close to the sample surface will be the same for non-reacting and reacting conditions. Figure 3 shows the concentration dependence of the fluorescence signal for both CO and CO_2, at 300 °C (sample temperature), 150 mbar total chamber pressure, and 100 mL_n/min total flow rate. Each point is an average of 200 laser shots (corresponds to an acquisition time of 20 s), and the standard deviation of the 200 measurements is presented by the error bars. For both CO and CO_2, the laser energies used were non-saturating. The CO signal shows linear concentration dependence. With a linear fitting, the single-shot detection limit of CO is estimated to 0.5 mbar (SNR = 1). In contrast to CO, the CO_2 curve is slightly bent towards higher concentrations due to self-absorption effect inside the chamber. The CO_2 signal is fitted with a function taking into account the self-absorption, and the single-shot detection limit of CO_2 is estimated to 0.1 mbar (SNR = 1).

It is worth noting that the CO_2 measured at reacting conditions is mainly localized in a hemispherical cloud above the sample, and the size of this cloud is much smaller than that of the chamber. Using the Beer–Lambert Law in Eq. (1),

$$\frac{I}{I_0} = \exp\left(-\frac{qPl}{kT}\sigma_\nu\right) = \exp(-Nl\sigma_\nu), \tag{1}$$

where I is the intensity after the path, I_0 is the initial intensity before the path, σ_ν is the IR cross section, q is the mole fraction, P is the pressure, T is the temperature, k is Boltzmann's constant, l is the path length, and N is the number of absorbers; the mass path Nl is estimated to be a factor of 4 smaller for reacting conditions than non-reacting conditions, given that the diameters of the sample and the chamber are 8 and 30 mm, respectively. Furthermore, the maximum partial pressure of CO_2 at reacting conditions is kept below 6 mbar. Therefore, the self-absorption effect is considered negligible for the CO_2 measurements at reacting conditions.

To show the capabilities of the current setup, two separate PLIF measurements were performed during CO oxidation over a Pd(100) single-crystal catalyst, one for CO and the other for CO_2. Figure 4 summarizes the measurement results. The two measurements were performed using similar heating current ramp speed; the current was ramped from 0.65 to 1.15 A for CO, and from 0.6 to 1.2 A for CO_2, both in 600 s. For comparison, the temperature range from 200 to 346 °C is shown. Both measurements were performed at flows of 4 mL_n/min CO, 4 mL_n/min O_2, and 92 mL_n/min Ar at 150 mbar total pressure (corresponding to initial partial pressures of 6 mbar of CO, 6 mbar of O_2, and 138 mbar of Ar). In both cases, the vertical laser sheet was positioned above the sample (indicated by the white rectangle), and a small region (indicated by the dashed box) in the bottom of the laser sheet was averaged to evaluate the LIF signals close to the sample surface. The spatial resolution for CO is 40 µm/pixel, and for CO_2 80 µm/pixel. The temporal resolution for both CO and CO_2 PLIF measurements is 0.1 s, but the PLIF images presented are 10-shot averaged, giving a temporal resolution of 1 s.

At low temperature 253 °C, a homogeneous CO distribution can be seen in Fig. 4a. This corresponds to the CO_2 PLIF image in Fig. 4g showing very little CO_2 produced. Both the CO and CO_2 PLIF images indicate that the sample is inactive. As the temperature increases, the partial pressure of CO drops and the partial pressure of CO_2 increases steadily, as shown in the MS in Fig. 4e and the LIF trends in Fig. 4d, f. When the sample ignites (the highly active phase of the catalytic reaction initiates), the gradient of the CO and CO_2 concentrations above the sample changes significantly, as can be seen in Fig. 4b, h, respectively. When the sample is highly active, a clear depletion of CO and a formation of CO_2 above the sample can be seen in Fig. 4c, i, respectively. From both the MS and LIF trends, the CO and CO_2 concentrations stabilize immediately (less than 1 s) after the ignition of the sample. This indicates that the reaction has reached the mass transfer limited (MTL) regime, i.e., the reaction is mass transfer limited by the ability of CO molecules diffusing and reaching onto the surface. In the MTL regime, the gas distribution over the sample is not homogeneous, and a decrease of ~70% for the CO concentration close to the sample is measured by PLIF, compared to only ~20% observed by the MS located at the gas outlet of the chamber. This significant difference can be explained by the fact that the MS is sampling gases far away from the sample surface, in this case about 30 mm. It is worth pointing out that the shift of the CO and CO_2 cloud to the right of the sample is due to the gas flow.

Since this work presents a detection approach each for CO and CO_2 in catalysis studies, it is interesting to compare them with other approaches used in previous works. For CO detection, the nanosecond excitation approach in this work is compared to the picosecond excitation approach used in [20]. The benefit of using a picosecond pulse is that it can provide high peak power beneficial for the two-photon excitation process, and lower C_2 interference from flames, compared to using a nanosecond pulse [36]. Since C_2 interference is not of concern in this work, it is mostly interesting to compare the CO detection limit and laser

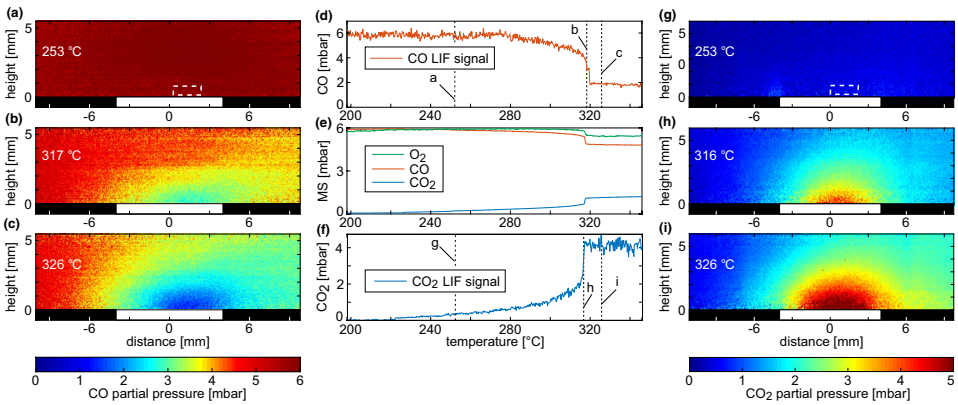

Fig. 4 PLIF imaging of both CO and CO_2 during CO oxidation over a Pd(100) single crystal (*white rectangular*). **a–c** show CO PLIF images; **d** shows the average CO PLIF signal; **e** shows the MS trends of CO, O_2 and CO_2; **f** shows the average CO_2 PLIF signal; **g–i** show CO_2 PLIF images; the *dashed boxes* indicate the region used to evaluate the PLIF signals. All PLIF images are 10 laser shot averaged, representing acquisition time 1 s

Table 1 Comparison of CO PLIF between nanosecond and picosecond excitation approaches

CO PLIF	Excitation wavelength (nm)	Linewidth FWHM (cm^{-1})	Linewidth FWHM (nm)	Pulse Energy (mJ)	Pulse length	Gate (ns)	Spatial resolution (μm)	Temporal resolution (s)
Nanosecond	230.1	0.5	0.0026	9	5 ns	250	40	0.1
Picosecond	230.1	5	0.026	0.4	80 ps	30	60	0.1

Table 2 Comparison of CO_2 PLIF between broadband and narrowband excitation approaches

CO_2 PLIF	Excitation wavelength (μm)	Linewidth FWHM (cm^{-1})	Linewidth FWHM (nm)	Pulse Energy (mJ)	Pulse length (ns)	Gate (μs)	Spatial resolution (μm)	Temporal resolution (s)
Broadband	2.7	10	7.3	7	5	30	80	0.1
Narrowband	2.7	0.025	0.018	4	5	20	70	0.1

shot-to-shot stability. For CO_2 detection, the broadband excitation approach in this work is compared to the narrowband excitation approach used in [23]. The comparison between them will be focused on their CO_2 detection limits. Tables 1 and 2 summarize the key parameters for the comparisons between the nanosecond and the picosecond excitation approaches for CO detection, and between the broadband and the narrowband excitation approaches for CO_2 detection. In each case, the two approaches employed almost the same detection optics (e.g., camera, objective, extension ring, and filter), which makes the comparisons more feasible.

For CO detection, a SNR of 3 with a standard deviation of 34% (for 10 laser shots) was measured for a CO partial pressure of 5 mbar at a total pressure of 100 mbar (in Ar) and 150 °C, using the picosecond excitation approach [20]. Based on the CO concentration dependence study in [20], the single-shot CO detection limit can be estimated to be around 2 mbar. In this work, the nanosecond excitation approach gives a lower single-shot detection limit of 0.5 mbar at similar conditions (150 mbar and 300 °C). Compared to the picosecond approach, the nanosecond excitation approach also gives smaller standard deviation within the same range of time, thus better laser shot-to-shot stability. For CO_2 detection, the detection limit of CO_2 was measured to 0.1 mbar at 300 °C and 150 mbar, using the narrowband excitation approach [23]. In this work, the broadband excitation approach gives a similar detection limit under the same conditions (150 mbar and 300 °C). However, the broadband excitation approach utilizes a small IR-OPO instead of a dye laser and a mixing unit used by the narrowband excitation approach, thus has the advantages of being more compact and convenient to use.

To evaluate the quenching effects on the calibrations of the CO and CO_2 PLIF signal and to compensate for it to a certain extent, the PLIF signals with and without the quencher gases were recorded at room temperature. The results are shown in Table 3, where the values are normalized, i.e., the LIF signal with a quencher gas was divided by the LIF signal without a quencher gas. Note that Ar is not considered as a quencher gas here and was used as a buffer gas to keep the total pressure at 150 mbar, which is similar to the reacting conditions above.

Table 3 Quenching effect on normalized CO and CO_2 PLIF signals. The total pressure is 150 mbar with Ar used as buffer gas

Fluorescing gases	6 mbar CO		3 mbar CO_2	
Quencher gases	6 mbar CO_2	6 mbar O_2	6 mbar CO	6 mbar O_2
22 °C	0.88	0.88	0.75	0.98

As quenching is temperature dependent, the LIF signal at higher temperatures is evaluated using Eq. (2–5),

$$S_{\mathrm{LIF}} = \eta_c E g f(T) \sigma_0 N \phi, \tag{2}$$

$$\phi = \frac{A}{A + \sum_i Q_i} \propto \frac{1}{\sum_i Q_i}, \tag{3}$$

$$Q_i = q_i p_i \propto \frac{\sigma_i^2 p_i}{\sqrt{T}}, \tag{4}$$

$$S_{\mathrm{LIF}} \propto \frac{1}{\sum_i \sigma_i^2 p_i} \sqrt{T} f(T), \tag{5}$$

where S_{LIF} is the fluorescent intensity, η_c is the collection efficiency, E is the laser energy, g is a function that describes the spectral overlap between the laser and the absorption spectral lineshape, $f(T)$ is the Boltzmann distribution, σ_0 is the absorption cross section, N is the number

density of the absorber, ϕ is the fluorescence quantum yield, Q_i is the quenching rate, q_i is the quenching rate coefficient, p_i is the partial pressure for species i, σ_i is the quenching cross section, and Eq. (3) assumes that the spontaneous emission rate is far less than the quenching rate. Assuming the quenching cross sections in Eq. (5) are temperature independent over a small temperature range (300 K) for both CO [37] and CO_2, the normalized PLIF signal will be independent of temperature. This means that the decrease of the LIF signal due to quenching is the same for different temperatures.

From Table 3, it can be seen that for CO, the quenching from O_2 and CO_2 was found to be similar, e.g., 6 mbar of each O_2 and CO_2 decrease the CO signal by 12%. And for CO_2, the quenching from O_2 was found to be very small, e.g., 6 mbar O_2 only decreases the CO_2 signal by 2%, while the quenching from CO was found to be relatively strong, e.g., 6 mbar CO can reduce the CO_2 signal by 25%. To estimate the maximum deviation on the LIF signal calibration in Fig. 4 introduced by quenching, the reaction can be separated into two parts for the discussion, before and after ignition. Before ignition, the majority of gases in the cell (and close to the sample) are CO and O_2. Therefore, the quenching is small for the CO signal and a maximum deviation of 12% is estimated due to the presence of 6 mbar O_2. In contrast, the quenching is much stronger for the CO_2 signal and a maximum deviation of 25% is estimated due to the presence of 6 mbar of each CO and O_2. After ignition, nearly all CO molecules reaching onto the surface are converted into CO_2; thus, the majority of gases close to the sample are CO_2 and O_2. As a result, the quenching for the CO_2 signal close to the sample is considered negligible. In contrast, the quenching for the CO signal close to the sample is much stronger, and has therefore been taken into account. After the correction for quenching, we obtained a good match between the CO and CO_2 profiles close to the sample when the reaction is in the highly active phase, i.e., around 2 mbar of CO and 4 mbar of CO_2.

4 Conclusions

In this work, we have reported a convenient setup for LIF imaging of both CO and CO_2 from catalytic CO oxidation above a Pd(100) single-crystal catalyst. Both approaches for the CO and CO_2 detection are shown to have advantages over the previously used approaches. For CO detection, the nanosecond excitation approach presented in the current work gives lower detection limit and better shot-to-shot stability under similar conditions, compared to the picosecond excitation approach in the literature. For CO_2 detection, the broadband excitation approach with an IR-OPO reported here gives the same detection limit as the narrowband excitation approach used in our previous work, but shows the merit of compactness and convenience. Simultaneous measurement of CO and CO_2 will be worth trying in future work using part of the residual 1064 beam from the YAG laser (another part for the UV mixing) to pump the IR-OPO. This will have distinct advantages over separate measurements for detection of CO and CO_2 in catalytic reactions, where the relation between the CO and CO_2 concentrations is not directly correlated, compared to the case in CO oxidation.

Acknowledgements This work was financially supported by the Knut and Alice Wallenberg Foundation, the Royal Physiographic Society of Lund, and the Swedish Research Council.

Open Access This article is distributed under the terms of the Creative Commons Attribution 4.0 International License (http://creativecommons.org/licenses/by/4.0/), which permits unrestricted use, distribution, and reproduction in any medium, provided you give appropriate credit to the original author(s) and the source, provide a link to the Creative Commons license, and indicate if changes were made.

References

1. M. Bowker, *The basis and applications of heterogeneous catalysis* (Oxford University Press Inc., New York, 1998)
2. G. Ertl, H. Knözinger, J. Weitkamp, *Handbook of heterogeneous catalysis* (VCH, Weinheim, 2008)
3. F. Gao, S.M. McClure, Y. Cai, K.K. Gath, Y. Wang, M.S. Chen, Q.L. Guo, D.W. Goodman, Surf. Sci. **603**, 65 (2009)
4. J. Gustafson, M. Shipilin, C. Zhang, A. Stierle, U. Hejral, U. Ruett, O. Gutowski, P.-A. Carlsson, M. Skoglundh, E. Lundgren, Science **343**, 758 (2014)
5. M. Roos, S. Kielbassa, C. Schirling, T. Häring, J. Bansmann, R.J. Behm, Rev. Sci. Instrum. **78**, 084104 (2007)
6. K. Kohsehoinghaus, Prog. Energy Combust. Sci. **20**, 203 (1994)
7. A.C. Eckbreth, *Laser diagnostics for combustion temperature and species* (Taylor and Francis, New York, 1996)
8. M. Alden, J. Bood, Z. Li, M. Richter, Proc. Combust. Inst. **33**, 69 (2011)
9. J. Zetterberg, S. Blomberg, J. Zhou, J. Gustafson, E. Lundgren, in *Operando Research in Heterogeneous Catalysis* (Springer International Publishing, 2017), p. 131
10. E. Fridell, U. Westblom, M. Alden, A. Rosen, J. Catal. **128**, 92 (1991)
11. E. Fridell, A. Rosen, B. Kasemo, Langmuir **10**, 699 (1994)
12. E. Fridell, A.P. Elg, A. Rosén, B. Kasemo, J. Chem. Phys. **102**, 5827 (1995)
13. F. Gudmundson, J.L. Persson, M. Försth, F. Behrendt, B. Kasemo, A. Rosén, J. Catal. **179**, 420 (1998)
14. M. Försth, F. Gudmundson, J.L. Persson, A. Rosén, Combust. Flame **119**, 144 (1999)
15. F. Gudmundson, E. Fridell, A. Rosen, B. Kasemo, J. Phys. Chem. **97**, 12828 (1993)
16. W. Kang, O. Fujita, K. Ito, J. Energy Res. Technol. **118**, 82 (1996)
17. M. Reinke, J. Mantzaras, R. Bombach, S. Schenker, A. Inauen, Combust. Flame **141**, 448 (2005)
18. S. Eriksson, A. Schneider, J. Mantzaras, M. Wolf, S. Jaras, Chem. Eng. Sci. **62**, 3991 (2007)

19. J. Zetterberg, S. Blomberg, J. Gustafson, Z.W. Sun, Z.S. Li, E. Lundgren, M. Alden, Rev. Sci. Instrum. 83 (2012)
20. S. Blomberg, C. Brackmann, J. Gustafson, M. Aldén, E. Lundgren, J. Zetterberg, ACS Catal. 2028 (2015)
21. J. Zetterberg, S. Blomberg, J. Gustafson, J. Evertsson, J. Zhou, E.C. Adams, P.-A. Carlsson, M. Alden, E. Lundgren, Nat Commun 6 (2015)
22. S. Blomberg, J. Zetterberg, J. Gustafson, J. Zhou, C. Brackmann, E. Lundgren, Topics in Catalysis, 1 (2016)
23. S. Blomberg, J. Zhou, J. Gustafson, J. Zetterberg, E. Lundgren, J. Phys. Condens. Matter **28**, 453002 (2016)
24. S. Matera, S. Blomberg, M.J. Hoffmann, J. Zetterberg, J. Gustafson, E. Lundgren, K. Reuter, ACS Catal. **5**, 4514 (2015)
25. S. Blomberg, J. Zetterberg, J. Zhou, L.R. Merte, J. Gustafson, M. Shipilin, A. Trinchero, L.A. Miccio, A. Magaña, M. Ilyn, F. Schiller, J.E. Ortega, F. Bertram, H. Grönbeck, E. Lundgren, ACS Catal. (2016)
26. A. Zellner, R. Suntz, O. Deutschmann, Angew Chem Int Ed Engl **54**, 2653 (2015)
27. J. Haumann, J.M. Seitzman, R.K. Hanson, Opt. Lett. **11**, 776 (1986)
28. M. Aldén, S. Wallin, W. Wendt, Appl. Phys. B **33**, 205 (1984)
29. B.J. Kirby, R.K. Hanson, Proc. Combust. Inst. **28**, 253 (2000)
30. B.J. Kirby, R.K. Hanson, Appl. Optics **40**, 6136 (2001)
31. B.J. Kirby, R.K. Hanson, Appl. Optics **41**, 1190 (2002)
32. C.S. Goldenstein, V.A. Miller, R.K. Hanson, Appl. Phys. B **120**, 185 (2015)
33. Z.T. Alwahabi, J. Zetterberg, Z.S. Li, M. Alden, European Physical Journal D **42**, 41 (2007)
34. G.W. Loge, J.J. Tiee, F.B. Wampler, J. Chem. Phys. **79**, 196 (1983)
35. A.-L. Sahlberg, J. Kiefer, M. Aldén, Z. Li, Appl Spectrosc **70**, 1034 (2016)
36. C. Brackmann, J. Sjöholm, J. Rosell, M. Richter, J. Bood, M. Aldén, Proc. Combust. Inst. **34**, 3541 (2013)
37. T.B. Settersten, A. Dreizler, R.L. Farrow, J. Chem. Phys. **117**, 3173 (2002)

Paper II

catalysts

MDPI

Article

Visualization of Gas Distribution in a Model AP-XPS Reactor by PLIF: CO Oxidation over a Pd(100) Catalyst

Jianfeng Zhou [1,*], Sara Blomberg [2], Johan Gustafson [2], Edvin Lundgren [2] and Johan Zetterberg [1]

[1] Division of Combustion Physics, Lund University, SE-221 00 Lund, Sweden; johan.zetterberg@forbrf.lth.se
[2] Division of Synchrotron Radiation Research, Lund University, SE-221 00 Lund, Sweden; sara.blomberg@sljus.lu.se (S.B.); johan.gustafson@sljus.lu.se (J.G.); edvin.lundgren@sljus.lu.se (E.L.)
* Correspondence: jianfeng.zhou@forbrf.lth.se; Tel.: +46-46-222-9274

Academic Editor: Juan J. Bravo-Suarez
Received: 24 November 2016; Accepted: 11 January 2017; Published: 17 January 2017

Abstract: In situ knowledge of the gas phase around a catalyst is essential to make an accurate correlation between the catalytic activity and surface structure *in operando* studies. Although ambient pressure X-ray photoelectron spectroscopy (AP-XPS) can provide information on the gas phase as well as the surface structure of a working catalyst, the gas phase detected has not been spatially resolved to date, thus possibly making it ambiguous to interpret the AP-XPS spectra. In this work, planar laser-induced fluorescence (PLIF) is used to visualize the CO_2 distribution in a model AP-XPS reactor, during CO oxidation over a Pd(100) catalyst. The results show that the gas composition in the vicinity of the sample measured by PLIF is significantly different from that measured by a conventional mass spectrometer connected to a nozzle positioned just above the sample. In addition, the gas distribution above the catalytic sample has a strong dependence on the gas flow and total chamber pressure. The technique presented has the potential to increase our knowledge of the gas phase in AP-XPS, as well as to optimize the design and operating conditions of in situ AP-XPS reactors for catalysis studies.

Keywords: AP-XPS; PLIF; boundary layer; CO oxidation

1. Introduction

Catalysis is an essential technology for our society in that around 90% of all chemicals worldwide are produced using it [1]. In addition, environmental sustainability also relies on catalysis, particularly heterogeneous catalysis [2]. Although catalysis has been used and studied for more than a century, a fundamental understanding of the mechanisms behind most catalytic processes is still lacking, which calls for studies of catalysis at an atomic level. One of the most versatile surface-sensitive techniques is X-ray photoelectron spectroscopy (XPS) since it provides quantitative information about the elemental composition and chemical specificity of the surface [3]. Historically, XPS has been used to investigate surfaces under ultra-high vacuum (UHV) conditions, but during the last decades, the technique has been modified to operate under more realistic conditions, which is often referred to as ambient pressure X-ray photoelectron spectroscopy (AP-XPS). With AP-XPS, it is possible to detect both the gas-phase and surface chemical composition in situ, which makes it valuable for catalysis studies [4].

When moving from UHV conditions to elevated pressures, the effect of gas molecules close to the surface increases [5,6]. For example, a change of the gas composition can lead to compositional and structural changes of a working catalyst [7,8], which in turn can change the kinetics of the reaction. Therefore, in situ knowledge of the gas phase around a catalyst is essential to make an accurate correlation between the catalytic activity and surface structure *in operando* catalysis studies [9]. As mentioned above, AP-XPS can provide in situ gas-phase information of a working catalyst; however, the information suffers from poor temporal resolution and, so far, a lack of spatial resolution. As an

additional gas tool for AP-XPS, a mass spectrometer (MS) is often used to analyze gases in an AP-XPS set up. Although a MS has the advantage of measuring several gases simultaneously, it cannot easily spatially resolve and image gases close to a sample, and usually samples the gases with a slight time delay. To overcome these problems, planar laser-induced fluorescence (PLIF) can be used to detect gases in the vicinity of a working catalyst in situ non-intrusively with high spatial and temporal resolution. A number of recent applications of PLIF have demonstrated it as a powerful gas detection tool, complementary to MS in catalysis studies [10–14].

One of the most intensively studied reactions using AP-XPS is CO oxidation, particularly on Pd single-crystal surfaces [15–18]. It is well-known that when the reaction is in the highly active phase, under semi-realistic conditions, it is often mass transfer limited (MTL) by the ability of CO molecules diffusing and reaching onto the surface. In the MTL regime, a CO_2 boundary layer (a sharp gradient of the CO_2 cloud) is often formed at high pressure, which changes the gas composition close to the sample surface [19,20]. Blomberg et al. have recently shown how this is reflected in the AP-XPS gas-phase signal by comparing gas-phase images by PLIF with AP-XPS data [21]. Those PLIF images, however, are obtained from a regular catalytic reactor in the absence of a nozzle close to the sample. It is highly likely that the presence of such a nozzle could change the gas distribution close to a sample significantly. In this work, a model reactor is therefore designed to mimic gas flows in a real AP-XPS reactor. To investigate how the presence of the nozzle affects the gas distribution close the sample surface, PLIF is used to visualize the CO_2 distribution over a Pd(100) catalyst during CO oxidation. We show that the CO_2 concentration in the vicinity of the sample, as measured by PLIF, is significantly different from that at the gas outlet, as measured by a MS. In addition, the CO_2 distribution over the sample is strongly dependent on the flow rate and chamber pressure, as well as the flow configurations.

2. Results

A model reactor with a nozzle as the gas outlet was designed to mimic gas flows in a real AP-XPS reactor. The nozzle has an aperture with a diameter of 1 mm and is located at a normal operating distance, which is twice the diameter of the aperture [22,23]. A schematic of the nozzle and the flow configuration is shown in Figure 1a. A MS connected to the nozzle (as the gas outlet) via a leak valve was used to measure the global gas concentration. In this way, the MS can be seen to sample gases close to the sample, similar to a capillary MS. PLIF was used to image the CO_2 gas distribution over a Pd(100) catalyst during CO oxidation in this model AP-XPS reactor.

2.1. Comparison between PLIF and MS

PLIF and MS were compared in a CO oxidation experiment where the sample was heated by a heating plate from 220 to 380 °C at a constant rate of 16 °C/min, at flows of 4.8 mL_n/min CO, 4.8 mL_n/min O_2 and 110.4 mL_n/min Ar (corresponding to 0 °C and atmospheric pressure), and at a total pressure of 150 mbar (corresponding to initial partial pressures of 6 mbar each of CO and O_2, and 138 mbar of Ar). It can be seen from both LIF and MS traces, in Figure 1b,c, that as the temperature of the catalyst increases, the CO_2 partial pressure increases steadily from zero, and then increases dramatically when the sample ignites at 330 °C. As the temperature continues to increase, the CO_2 partial pressure reaches a plateau, indicating that the activity has reached the MTL regime. Figure 1d–f show three CO_2 PLIF images captured at 300, 330 and 348 °C, respectively. The PLIF images show the CO_2 distribution over the sample with a high spatial resolution, 70 μm/pixel in this case. Focusing on the individual PLIF images, it can be seen that at 300 °C, the PLIF image is almost completely black, showing very little CO_2 produced as the sample is in the low-activity regime. When the sample ignites at 330 °C, a clear increase gradient of the CO_2-related intensity can be seen in the corresponding PLIF image. At 348 °C, the PLIF image shows a clear cloud, or the so-called boundary layer of CO_2 formed above the sample when the reaction has reached the MTL regime.

Comparing the LIF and MS traces, the CO_2 partial pressure in the vicinity of the sample, as measured by PLIF, is significantly different from that at the gas outlet, as measured by the MS.

An even more pronounced difference can be seen at the highly active phase; approximately 5 mbar CO_2 partial pressure is measured by PLIF, compared to around 2 mbar measured by the MS. However, no pronounced time delay (within 1 s) of the MS signal was found in this experiment, due to a short and small-sized tube, used between the MS and the gas outlet of the reactor, and a high flow rate in this experiment. A movie showing the dynamic change of the CO_2 distribution during the reaction can be found in the Supplementary Materials Video S1.

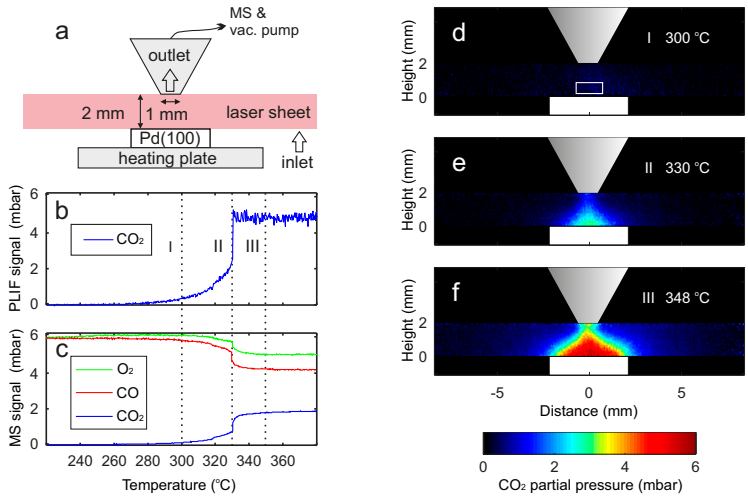

Figure 1. CO_2 distribution over a Pd(100) single-crystal catalyst: (**a**) schematic of the nozzle which is connected to a vacuum pump and a mass spectrometer; (**b**) average CO_2 planar laser-induced fluorescence (PLIF) signal inside the white hollow box above the sample indicated by the white solid box; (**c**) Mass spectrometer (MS) profiles of O_2, CO and CO_2; (**d**–**f**) CO_2 PLIF images (10 laser-shot averaged, representing a time interval of 1 s) recorded at 300, 330 and 348 °C during the temperature ramp at a constant rate of 16 °C/min.

2.2. Pressure and Flow Rate Dependence

To study the pressure and flow dependence of the gas distribution over the sample, the sample was heated using the same temperature ramp at different pressures and flow rates, and the CO_2 signals were measured by both PLIF and the MS. The average PLIF CO_2 signal and the MS CO_2 signal are shown in Figure 2. The CO_2 signals shown are normalized to the initial CO partial pressures for purposes of comparison, since the partial pressures of CO, O_2 and Ar vary for different gas conditions and the ratio of CO and O_2 is kept to 1:1.

The ignition temperature of the sample is not the focus of this work; however, it is still interesting to show how the pressure and flow rate affect the ignition temperature. Under all the gas conditions in Figure 2, the reaction ignites at between 315 and 330 °C. At both 150 and 50 mbar, the sample has a higher light-off temperature at higher flux rates. This is due to the fact that at higher flux rates, the gas in the reactor (and close to the sample surface) is exchanged faster, which also means that the CO/O_2 ratio stays higher until higher temperatures, leading to higher ignition temperatures.

Interestingly, the CO_2 signal close to the sample, as measured by PLIF, does not change noticeably with the flow rates, as shown in Figure 2a,b. However, there is a slight increasing trend of the CO_2 signal measured by the MS with the decreasing flow rate, as shown in Figure 2d,e. This behavior can be explained by the fact that at lower flow rates, the CO molecules stay in the reactor longer and a larger fraction of the molecules are converted into CO_2.

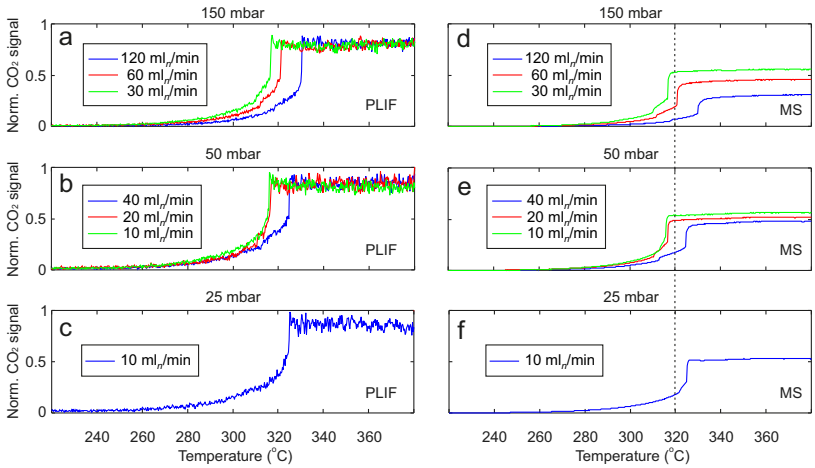

Figure 2. The CO_2 signals (here normalized to the initial CO partial pressures for comparison) measured by (**a**) PLIF at 150 mbar; (**b**) PLIF at 50 mbar; (**c**) PLIF at 25 mbar; (**d**) MS at 150 mbar; (**e**) MS at 50 mbar; (**f**) MS at 25 mbar. For 150 and 50 mbar pressures, three different flow rates are shown for comparison, while for 25 mbar only one flow rate is shown. All reactions are performed using 1:1 ratio of CO and O_2 and the same temperature ramp-up speed. A 4:4:92 ratio of CO, O_2 and Ar is used in 150 mbar with total flow of 120, 60 and 30 mL_n/min, and in 50 mbar with total flow of 40 and 20 mL_n/min. A 5:5:90 ratio of CO, O_2 and Ar is used in 50 mbar with total flow of 10 mL_n/min, and in 25 mbar with total flow of 10 mL_n/min. The dashed line is for guidance in temperature reading.

The CO_2 boundary layer formed over a catalyst in the MTL regime during CO oxidation has been shown to play an important role on the kinetics of the catalytic reaction [24,25]. Therefore, it is of great interest to study the CO_2 distribution over the sample in the MTL regime under different gas conditions. Figure 3 summarizes the investigation of the pressure and flow rate dependence of the CO_2 distribution. The images were recorded when the reactions reached the MTL regime, under the gas conditions shown in Figure 2. Since the reactions stabilize in the MTL regime, all images are averaged over 1000 shots to improve the signal-to-noise ratio.

The gas volumetric exchange rate per reactor volume (hereinafter referred to as the gas exchange rate) is dependent on both the flow rate and chamber pressure, and directly related to the diffusion of the gas. Thus, the gas exchange rate is used to facilitate the comparison of the CO_2 distribution for different pressures. In fact, it is difficult to accurately estimate the gas exchange rate due to the complex geometry of the reactor. The gas exchange rates presented in Figure 3 are, therefore, simply calculated as the total flow rate divided by the chamber volume. However, this simplified calculation is sufficient for qualitative studies.

In a comparison of Figure 3a–c, it can be seen that the gradient of the CO_2 signal intensity decreases as the gas exchange rate decreases from 40/min to 10/min while the total chamber pressure is kept at 150 mbar. A similar tendency can also be seen when the total pressure is at 50 mbar, as shown in Figure 3d–f. This smeared-out effect can be explained by more CO molecules being converted into CO_2 inside the reactor at lower gas exchange rates, hence the stronger CO_2 presence. It is interesting to see that the CO_2 distribution also has a strong dependence on the total pressure. Comparing Figure 3b,e,g, the CO_2 cloud becomes more smeared out as the total pressure decreases while the gas exchange rate is kept the same. This is most likely due to the diffusion effect, which is stronger at lower pressures. However, the CO_2 boundary layer (sharp gradient of the CO_2 cloud) can still be clearly seen at pressures down to 25 mbar.

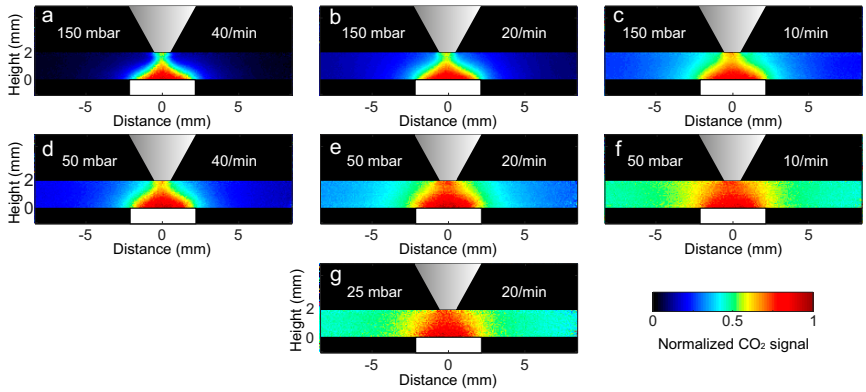

Figure 3. Pressure and flow dependence of the CO_2 distribution over a Pd(100) single-crystal catalyst in the mass transfer limited (MTL) regime: (**a**–**c**) chamber pressure at 150 mbar, gas exchange rate at 40, 20 and 10 per minute, respectively; (**d**–**f**) chamber pressure at 50 mbar, gas exchange rate at 40, 20 and 10 per minute, respectively; (**g**) chamber pressure at 25 mbar, gas exchange rate at 20 per minute. All PLIF images are 1000 laser-shot averaged (acquisition time of 100 s). The nozzle is used as the gas outlet, which is connected to a vacuum pump and a mass spectrometer.

To better illustrate the pressure and flow dependence of the CO_2 distribution above the sample, horizontal CO_2 profiles are plotted in Figure 4. Figure 4a shows the profiles with different gas exchange rates at a fixed total pressure of 150 mbar, while Figure 4b shows the profiles with different total pressures at a fixed gas exchange rate of 20/min. It can be clearly seen that the gradient of the profiles becomes smaller at a lower gas exchange rate and lower total pressure.

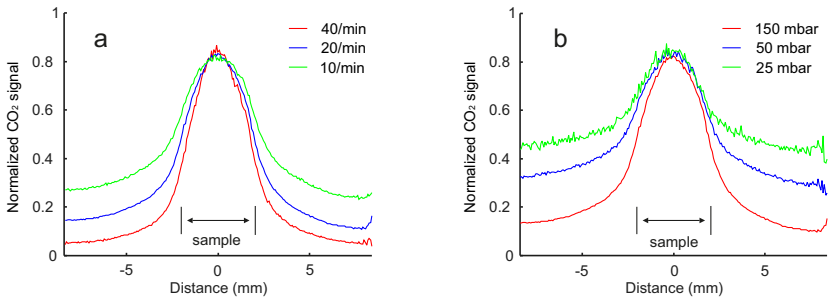

Figure 4. Normalized CO_2 profiles (averaged over five rows) at 0.5 mm above the sample in the MTL regime. (**a**) Chamber pressure at 150 mbar for different gas exchange rates; (**b**) Gas exchange rate of 20 per minute for different chamber pressures.

2.3. Flow Configuration Dependence

Apart from the strong dependence on the chamber pressure and flow rate, the CO_2 gas distribution over an active Pd(100) sample was also found to vary significantly for different flow configurations. Figure 5a shows the model AP-XPS reactor where the nozzle is used as the gas outlet. Figure 5b shows a reactor similar to the model AP-XPS reactor where the nozzle is not used as the gas outlet. Instead, the gas outlet was located below the sample holder. Figure 5c shows a regular reactor without a nozzle. In all configurations, the gas outlet was connected to both the vacuum pump and the MS. All images were recorded when the reactions reached the MTL regime under the same gas conditions.

It can be clearly seen that both the shape and the gradient of the CO_2 cloud in Figure 5a differ considerably, compared to the ones in Figure 5b,c. In addition, the CO_2 partial pressures measured by the MS differ significantly. A higher CO_2 partial pressure is measured by the MS in Figure 5a than in Figure 5b,c. This is probably due to the fact that the CO_2 molecules produced were localized close to the sample, and the gas sampling distance between the gas outlet and the sample surface is much shorter in Figure 5a than in Figure 5b,c. Comparing Figure 5b,c, there is a small difference in the CO_2 partial pressures measured by the MS between these two configurations, which could be due to the disturbance of the gas flow around the sample by the nozzle or the volume change of the reactor with the presence of the nozzle in Figure 5b. However, for all the flow configurations, the CO_2 partial pressures close to the sample measured by PLIF were approximately the same. For a comparison of the cases with the nozzle and without the nozzle, a movie showing the dynamic change of the CO_2 distribution can be found in the Supplementary Materials Video S2.

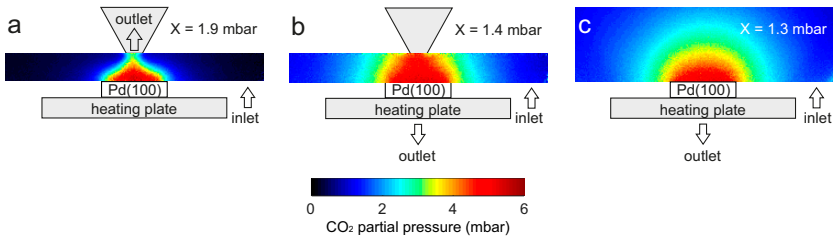

Figure 5. CO_2 distribution in the MTL regime for different flow configurations: (**a**) model ambient pressure X-ray photoelectron spectroscopy (AP-XPS) reactor where the nozzle is used as the gas outlet; (**b**) reactor with a nozzle but the gas outlet is located approximately 3 cm below the sample holder; (**c**) reactor without a nozzle, and the gas outlet is also located below the sample holder. All images are recorded under the same gas conditions, i.e., 6 mbar each of CO and O_2 and 138 mbar of Ar (total flow of 120 mL_n/min). All images are 1000 laser-shot averaged. In all configurations, the gas outlet is connected to both the vacuum pump and the MS. *X* denotes the CO_2 partial pressures measured by the MS.

3. Discussion

PLIF makes it possible to spatially resolve gases close to the sample with a sufficient temporal resolution, to follow dynamic changes in the gas phase during catalytic reactions. In this study, a model AP-XPS reactor with a nozzle positioned just above the sample and connected to a vacuum pump and a MS was designed to mimic the gas flows in a real AP-XPS reactor. The study shows that the CO_2 concentration in the vicinity of the sample, as measured by PLIF, was found to be different from the overall CO_2 concentration measured by the MS. An even more pronounced difference could be seen when the reaction reached the MTL regime. As gas molecules close to the sample interact directly with the catalyst surface, in situ knowledge of the gas composition close to the sample is essential to make an accurate correlation between the catalytic activity and surface structure *in operando* studies of catalysis. Therefore, PLIF has the advantage of providing more accurate information of the gas phase close to the sample. Since MS has the benefit of measuring several gases simultaneously, a combination of PLIF and MS can provide an even more complete picture of the gas phase during catalytic reactions.

The gas distribution over a highly active sample was found to have a strong dependence on the flow rate and the total chamber pressure, as well as the flow configuration. This finding can be useful to obtain better knowledge of the gas phase in AP-XPS, as well as to optimize the design and operating conditions of in situ AP-XPS reactors. The common upper limit of the operating pressure of AP-XPS is a few mbar [26]. In this work, the minimum total chamber pressure investigated was 25 mbar (partial pressures of 1.25 mbar CO, 1.25 mbar O_2 and 22.5 mbar Ar), limited by the pumping efficiency with a total flow of 10 mL_n/min. However, the results showed a tendency where the gas distribution above

the sample became more homogeneous at lower pressures and lower flow rates. From this tendency, it was estimated that a boundary layer of CO_2 above the sample in the MTL regime could still be present at a 10 mbar chamber pressure and a 10 mL_n/min flow rate, or at lower chamber pressures with higher flow rates. Within such a boundary layer, the CO_2 partial pressure decreases radially from the center of the sample, and the CO and O_2 partial pressures decrease radially towards the center of the sample. When surface structures are to be determined, the gas composition over the sample should ideally be homogeneous. We found in this study that the gas composition over the sample was not homogeneous due to the formation of the boundary layer. Lower pressures and flow rates would promote a more homogeneous gas distribution above the sample. However, higher pressures and flow rates are usually needed to mimic more realistic conditions in catalysis applications. The boundary layer is, therefore, of practical interest in catalysis studies.

Although the dependence of the gas distribution as a function of the distance between the nozzle and the sample surface was not investigated in this study, it is interesting to discuss it as a short working distance of an analyzer is preferred in most AP-XPS experiments [27,28]. At shorter distances, it is likely that the nozzle will have a stronger impact on the gas flow close to the sample surface, as gases close to the surface are pumped away more efficiently. Therefore, it can be inferred that the CO_2 gas cloud over the sample would be more distorted at shorter working distances.

As the technique of AP-XPS is being developed towards higher and higher operating pressures in an effort to bridge the so-called pressure gap in catalysis studies, gas phase–related phenomena become increasingly important. As a powerful gas detection tool, PLIF has great potential to promote a better understanding of the gas-surface interaction during catalytic reactions.

4. Materials and Methods

4.1. Sample and Reactor

The sample investigated was a Pd(100) single crystal of dimension 4 × 4 mm^2. The cleaning procedure of the sample can be referred to [14]. The sample was heated by a boralectric heater, the temperature of which was measured by a type D thermocouple. A cubical chamber of volume 23 cm^3 with CaF_2 windows was used for CO_2 PLIF measurements. A cone-shaped nozzle of aperture diameter of 1 mm is located 2 mm above of the sample and acted as gas outlet. Gases (from AGA Gas AB, Lidingö, Sweden, the purities of CO, O_2 and Ar are 99.97%, 99.9996% and 99.997%, respectively) were supplied to the reactor by individual mass flow controllers (Bronkhorst EL-FLOW, Bronkhorst High-Tech B.V., Ruurlo, The Netherlands), and the gas pressure in the reactor was regulated by a digital pressure controller (Bronkhorst EL-PRESS, Bronkhorst High-Tech B.V.). A carbonyl trap was used to remove nickel carbonyl present in the CO gas. The gas composition in the reactor was measured by a quadrupole mass spectrometer (Pfeiffer, QME 220, Pfeiffer Vacuum GmbH, Asslar, Germany) connected to the outlet of the reactor by a 70 cm long gas tube (d = 1/16 in.) and with a leak valve which kept the pressure in the MS at 5 × 10^{-6} mbar. The MS signal is converted into mbar by normalizing the MS CO and O_2 signal to the known initial partial pressures, and the CO_2 signal was scaled to match the observed conversion of CO. A schematic of the reaction system can be found in the Supplementary Materials Figure S1.

4.2. PLIF

The detection of CO_2 was realized by a broadband excitation of the $(00^00) \rightarrow (10^001)$ combination band at ~2.7 μm and collecting fluorescence from the fundamental band at ~4.3 μm. The fundamental 1064 nm laser beam with ~350 mJ/pulse from a single-mode seeded Nd:YAG (neodymium-doped yttrium aluminium garnet) laser operating at 10 Hz, was used to pump an IR OPO (GWU, versaScan-L 1064, Erftstadt, Germany), generating a signal beam at ~1.7 μm and an idler beam at ~2.7 μm, with ~8 and ~7 mJ/pulse, respectively. The idler beam was shaped into a thin laser sheet of 2 mm height by a set of focusing lens and then sent through the reactor just above the catalyst. The CO_2 fluorescence

was imaged by a liquid-nitrogen-cooled, 256 × 256 InSb IR camera (Santa Barbara Focal Plane, SBF LP134, Goleta, CA, USA). A cold interference filter inside the camera, centered at 4.26 μm, was used to suppress the strong thermal background. The exposure time was set to 30 μs to suppress background and favor fluorescence signal. Purging of N_2 was applied during measurements to reduce laser energy attenuation along the beam path and fluorescence signal loss between the cell and the IR camera. A detailed description of the detection scheme and the evaluation of PLIF signal can be found in [10,29].

Supplementary Materials: The following are available online at: www.mdpi.com/2073-4344/7/1/29/s1, Figure S1: Schematic of the reaction system, Video S1: Movie_reactor with a nozzle, Video S2: Movie_reactor without a nozzle.

Acknowledgments: This work was financially supported by the Knut & Alice Wallenberg Foundation, the Swedish Research Council and the Royal Physiographic Society of Lund.

Author Contributions: Jianfeng Zhou, Sara Blomberg and Johan Zetterberg designed the experiments; Jianfeng Zhou and Sara Blomberg performed the experiments; Jianfeng Zhou analyzed the data and wrote the manuscript; Sara Blomberg, Johan Gustafson, Johan Zetterberg and Edvin Lundgren improved the manuscript; Johan Zetterberg and Edvin Lundgren supervised the project.

Conflicts of Interest: The authors declare no conflict of interest.

References

1. Bowker, M. *The Basis and Applications of Heterogeneous Catalysis*; Oxford University Press Inc.: New York, NY, USA, 1998.
2. Ertl, G.; Knözinger, H.; Weitkamp, J. *Handbook of Heterogeneous Catalysis*; Wiley-VCH: Weinheim, Germany, 2008.
3. Hüfner, S. *Photoelectron Spectroscopy*; Springer: Berlin, Germany, 1995.
4. Starr, D.E.; Liu, Z.; Havecker, M.; Knop-Gericke, A.; Bluhm, H. Investigation of solid/vapor interfaces using ambient pressure X-ray photoelectron spectroscopy. *Chem. Soc. Rev.* **2013**, *42*, 5833–5857. [CrossRef] [PubMed]
5. Gao, F.; McClure, S.M.; Cai, Y.; Gath, K.K.; Wang, Y.; Chen, M.S.; Guo, Q.L.; Goodman, D.W. CO oxidation trends on Pt-group metals from ultrahigh vacuum to near atmospheric pressures: A combined in situ PM-IRAS and reaction kinetics study. *Surf. Sci.* **2009**, *603*, 65–70. [CrossRef]
6. Rupprechter, G.; Weilach, C. Mind the gap! Spectroscopy of catalytically active phases. *Nano Today* **2007**, *2*, 20–29. [CrossRef]
7. Hendriksen, B.L.M.; Bobaru, S.C.; Frenken, J.W.M. Oscillatory CO oxidation on Pd(100) studied with in situ scanning tunneling microscopy. *Surf. Sci.* **2004**, *552*, 229–242. [CrossRef]
8. Gustafson, J.; Shipilin, M.; Zhang, C.; Stierle, A.; Hejral, U.; Ruett, U.; Gutowski, O.; Carlsson, P.-A.; Skoglundh, M.; Lundgren, E. High-energy surface X-ray diffraction for fast surface structure determination. *Science* **2014**, *343*, 758–761. [CrossRef] [PubMed]
9. Bañares, M.A. Operando methodology: Combination of in situ spectroscopy and simultaneous activity measurements under catalytic reaction conditions. *Catal. Today* **2005**, *100*, 71–77. [CrossRef]
10. Blomberg, S.; Zhou, J.; Gustafson, J.; Zetterberg, J.; Lundgren, E. 2D and 3D imaging of the gas phase close to an operating model catalyst by planar laser induced fluorescence. *J. Phys. Condens. Matter* **2016**, *28*, 453002. [CrossRef] [PubMed]
11. Zellner, A.; Suntz, R.; Deutschmann, O. Two-dimensional spatial resolution of concentration profiles in catalytic reactors by planar laser-induced fluorescence: NO reduction over diesel oxidation catalysts. *Angew. Chem. Int. Ed.* **2015**, *54*, 2653–2655. [CrossRef] [PubMed]
12. Blomberg, S.; Zetterberg, J.; Zhou, J.; Merte, L.R.; Gustafson, J.; Shipilin, M.; Trinchero, A.; Miccio, L.A.; Magaña, A.; Ilyn, M.; et al. Strain dependent light-off temperature in catalysis revealed by planar laser-induced fluorescence. *ACS Catal.* **2016**, 110–114. [CrossRef]
13. Zetterberg, J.; Blomberg, S.; Gustafson, J.; Evertsson, J.; Zhou, J.; Adams, E.C.; Carlsson, P.-A.; Aldén, M.; Lundgren, E. Spatially and temporally resolved gas distributions around heterogeneous catalysts using infrared planar laser-induced fluorescence. *Nat. Commun.* **2015**, *6*, 7076. [CrossRef] [PubMed]

14. Blomberg, S.; Brackmann, C.; Gustafson, J.; Aldén, M.; Lundgren, E.; Zetterberg, J. Real-time gas-phase imaging over a Pd(110) catalyst during CO oxidation by means of planar laser-induced fluorescence. *ACS Catal.* **2015**, *5*, 2028–2034. [CrossRef] [PubMed]
15. Toyoshima, R.; Yoshida, M.; Monya, Y.; Kousa, Y.; Suzuki, K.; Abe, H.; Mun, B.S.; Mase, K.; Amemiya, K.; Kondoh, H. In situ ambient pressure XPS study of CO oxidation reaction on Pd(111) surfaces. *J. Phys. Chem. C* **2012**, *116*, 18691–18697. [CrossRef]
16. Blomberg, S.; Hoffmann, M.J.; Gustafson, J.; Martin, N.M.; Fernandes, V.R.; Borg, A.; Liu, Z.; Chang, R.; Matera, S.; Reuter, K.; et al. In-situ X-ray photoelectron spectroscopy of model catalysts: At the edge of the gap. *Phys. Rev. Lett.* **2013**, *110*, 117601. [CrossRef] [PubMed]
17. Toyoshima, R.; Yoshida, M.; Monya, Y.; Suzuki, K.; Mun, B.S.; Amemiya, K.; Mase, K.; Kondoh, H. Active surface oxygen for catalytic CO oxidation on Pd(100) proceeding under near ambient pressure conditions. *J. Phys. Chem. Lett.* **2012**, *3*, 3182–3187. [CrossRef] [PubMed]
18. Toyoshima, R.; Yoshida, M.; Monya, Y.; Suzuki, K.; Amemiya, K.; Mase, K.; Mun, B.S.; Kondoh, H. In situ photoemission observation of catalytic CO oxidation reaction on Pd(110) under near-ambient pressure conditions: Evidence for the Langmuir–Hinshelwood mechanism. *J. Phys. Chem. C* **2013**, *117*, 20617–20624. [CrossRef]
19. Matera, S.; Reuter, K. Transport limitations and bistability for in situ CO oxidation at RuO_2(110): First-principles based multiscale modeling. *Phys. Rev. B* **2010**, *82*, 085446. [CrossRef]
20. Matera, S.; Blomberg, S.; Hoffmann, M.J.; Zetterberg, J.; Gustafson, J.; Lundgren, E.; Reuter, K. Evidence for the active phase of heterogeneous catalysts through in situ reaction product imaging and multiscale modeling. *ACS Catal.* **2015**, *5*, 4514–4518. [CrossRef]
21. Blomberg, S.; Zetterberg, J.; Gustafson, J.; Zhou, J.; Brackmann, C.; Lundgren, E. Comparison of AP-XPS and PLIF measurements during CO oxidation over Pd single crystals. *Top. Catal.* **2016**, *59*, 478–486. [CrossRef]
22. Bluhm, H.; Hävecker, M.; Knop-Gericke, A.; Kiskinova, M.; Schlögl, R.; Salmeron, M. In situ X-ray photoelectron spectroscopy studies of gas-solid interfaces at near-ambient conditions. *MRS Bull.* **2007**, *32*, 1022–1030. [CrossRef]
23. Kahk, J.M.; Villar-Garcia, I.J.; Grechy, L.; Bruce, P.J.K.; Vincent, P.E.; Eriksson, S.K.; Rensmo, H.; Hahlin, M.; Åhlund, J.; Edwards, M.O.M.; et al. A study of the pressure profiles near the first pumping aperture in a high pressure photoelectron spectrometer. *J. Electron Spectrosc. Relat. Phenom.* **2015**, *205*, 57–65. [CrossRef]
24. Matera, S.; Reuter, K. When atomic-scale resolution is not enough: Spatial effects on in situ model catalyst studies. *J. Catal.* **2012**, *295*, 261–268. [CrossRef]
25. Matera, S.; Maestri, M.; Cuoci, A.; Reuter, K. Predictive-quality surface reaction chemistry in real reactor models: Integrating first-principles kinetic monte carlo simulations into computational fluid dynamics. *ACS Catal.* **2014**, *4*, 4081–4092. [CrossRef]
26. Schnadt, J.; Knudsen, J.; Andersen, J.N.; Siegbahn, H.; Pietzsch, A.; Hennies, F.; Johansson, N.; Martensson, N.; Ohrwall, G.; Bahr, S.; et al. The new ambient-pressure X-ray photoelectron spectroscopy instrument at MAX-lab. *J. Synchrotron Radiat.* **2012**, *19*, 701–704. [CrossRef] [PubMed]
27. Maibach, J.; Xu, C.; Eriksson, S.K.; Åhlund, J.; Gustafsson, T.; Siegbahn, H.; Rensmo, H.; Edström, K.; Hahlin, M. A high pressure X-ray photoelectron spectroscopy experimental method for characterization of solid-liquid interfaces demonstrated with a Li-ion battery system. *Rev. Sci. Instrum.* **2015**, *86*, 044101. [CrossRef] [PubMed]
28. Takagi, Y.; Wang, H.; Uemura, Y.; Ikenaga, E.; Sekizawa, O.; Uruga, T.; Ohashi, H.; Senba, Y.; Yumoto, H.; Yamazaki, H.; et al. In situ study of an oxidation reaction on a Pt/C electrode by ambient pressure hard X-ray photoelectron spectroscopy. *Appl. Phys. Lett.* **2014**, *105*, 131602. [CrossRef]
29. Zetterberg, J.; Blomberg, S.; Gustafson, J.; Sun, Z.W.; Li, Z.S.; Lundgren, E.; Aldén, M. An in situ set up for the detection of CO_2 from catalytic CO oxidation by using planar laser-induced fluorescence. *Rev. Sci. Instrum.* **2012**, *83*, 053104. [CrossRef] [PubMed]

© 2017 by the authors; licensee MDPI, Basel, Switzerland. This article is an open access article distributed under the terms and conditions of the Creative Commons Attribution (CC-BY) license (http://creativecommons.org/licenses/by/4.0/).

Paper III

THE JOURNAL OF PHYSICAL CHEMISTRY C

Article

Cite This: J. Phys. Chem. C 2017, 121, 23511-23519

pubs.acs.org/JPCC

Simultaneous Imaging of Gas Phase over and Surface Reflectance of a Pd(100) Single Crystal during CO Oxidation

Jianfeng Zhou,[†] Sara Blomberg,[‡] Johan Gustafson,[‡] Edvin Lundgren,[‡] and Johan Zetterberg*[,†]

[†]Division of Combustion Physics and [‡]Division of Synchrotron Radiation Research, Lund University, SE-221 00 Lund, Sweden

Supporting Information

ABSTRACT: A direct correlation between the reaction activity and the surface structure of a catalyst is generally needed to better understand the mechanisms behind the heterogeneous catalysis process. In this work, we employed planar laser-induced fluorescence (PLIF) to spatially resolve the CO_2 distribution just above a Pd(100) surface, and simultaneously monitored the optical reflectance of the surface, during CO oxidation. We show that when the reaction is in the mass transfer limited regime, the inhomogeneity of the gas composition over the sample can lead to an inhomogeneity of the surface reflectance change arising from oxide formation and surface roughening. The combination of PLIF and surface reflectance also makes it possible to spatially resolve and simultaneously follow the dynamics of the gas phase and the surface on a subsecond time scale during self-sustained reaction oscillations of a Pd(100) surface, providing insights into the gas−surface interaction.

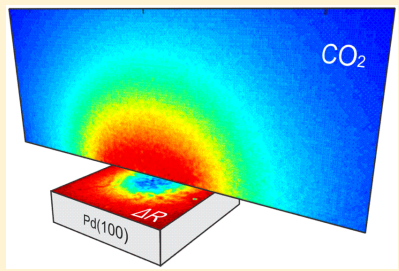

INTRODUCTION

For a fundamental understanding of the mechanisms behind heterogeneous catalysis, a direct correlation between the reaction activity and the surface structure of a catalyst is generally needed, which calls for the so-called *operando* studies of catalysis.[1,2] The past decades have seen a growing number of spatially revolved techniques developed for gas and/or surface characterization of heterogeneously catalyzed reactions.[3] CO oxidation catalyzed by Pd single crystals, being one of the most common model systems, has been studied for a long time.[4,5] In recent years, a number of in situ surface-sensitive techniques have been developed to study the model system, particularly at increased pressures, for example, high-pressure scanning tunneling microscopy/atomic force microscopy (HPSTM/AFM),[6,7] polarization-modulated infrared absorbance spectroscopy (PM-IRAS),[8,9] ambient-pressure X-ray photoelectron spectroscopy (AP-XPS),[10−12] and surface X-ray diffraction (SXRD).[13−15] Studies[6,10,14−18] have shown that a palladium oxide may be formed on a Pd(100) surface under CO oxidation, depending on the temperature, total pressure, and O_2/CO ratio. Because of the oxide formation, an increase of the surface roughness has been found.[15,16]

Onderwaater et al. have recently developed a reflectometer to study the optical reflectance change of a Pd(100) surface during CO oxidation.[19] They have shown that the surface reflectance of the Pd(100) sample decreases during reaction and attribute this to the formation of a palladium oxide layer on the surface. In a more recent paper,[20] with modeling and experimental results, Onderwaater et al. conclude that the decrease of reflectance results both from the formation of a palladium oxide layer and an increase of the surface roughness and is dominated by the latter under CO oxidation reaction.

In their first paper,[19] a decrease of the reflectance is observed to start from the center of the sample surface and spread radially across almost the entire sample, which is attributed to a temperature gradient over the sample due to the heating. In their experiment, the reaction was in the so-called mass transfer limited (MTL) regime, where the reaction rate is mass transfer limited by one of the reactants impinging onto the surface. It has been shown both theoretically and experimentally that when the reaction is in the MTL regime, the gas composition above the surface changes significantly, compared to that in the non-MTL regime.[21−23] This could in turn change the surface structure since it is sensitive to the gas composition.

Here we have developed a surface reflectance setup similar to that reported in refs 19 and 20 and report successful oxidation and reduction experiments with the corresponding changes in surface reflectance of a Pd(100) surface. To move forward, we combine the surface reflectance with planar laser-induced fluorescence (PLIF), a gas detection technique that can spatially resolve gases close to a sample surface in real time. PLIF has been shown to be able to detect gases close to a catalyst sample with high spatial and temporal resolution.[24−27] During CO oxidation, we find that the change of the surface reflectance is closely related to the CO_2 concentration above the surface, which is highest at the center of the active model catalyst from where the surface reflectance change starts. Since

Received: August 14, 2017
Revised: September 29, 2017
Published: September 30, 2017

ACS Publications © 2017 American Chemical Society

DOI: 10.1021/acs.jpcc.7b08108
J. Phys. Chem. C 2017, 121, 23511−23519

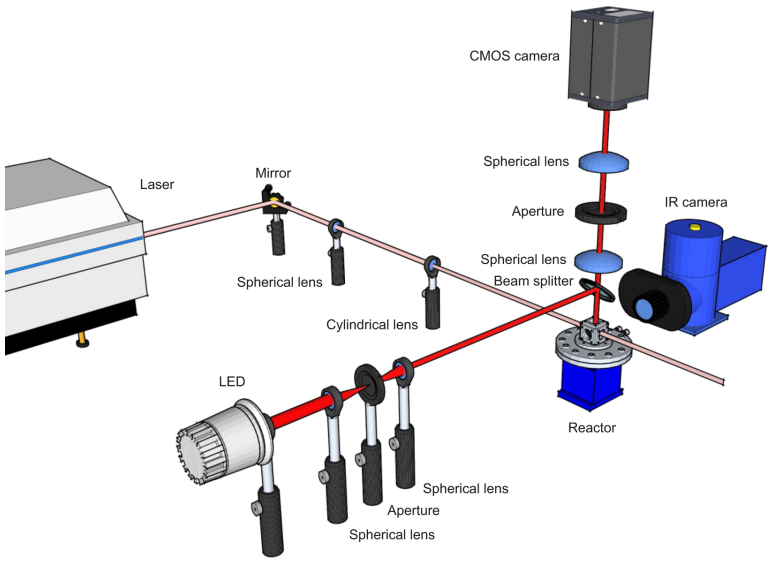

Figure 1. Schematic illustration of the experimental setup for simultaneous measurements of PLIF and surface reflectance of a Pd(100) sample during CO oxidation.

a high CO_2 concentration corresponds to a high O_2/CO ratio and therefore a more oxidizing environment in the MTL regime, we conclude that the change of the gas phase due to the activity of the catalyst is responsible for the radial dynamics of the change of the surface reflectance.

In addition, we have used the combination of surface reflectance and PLIF to study self-sustained reaction oscillations of CO oxidation over the Pd(100) surface. Self-sustained reaction oscillations have been studied in catalytic reactions for many years.[28,29] Previously, Hendriksen et al. have proposed that these reaction oscillations involve two main processes on the surface, roughening and smoothening.[30,31] Recently, Onderwaater et al. from the same group have revisited the reaction oscillations and showed that there are fast and intermediate oscillations superimposed on the regular ones, adding a new aspect to the scenario.[32] As surface reflectance is sensitive to the palladium oxide formation and surface roughness, and since PLIF and surface reflectance provide similarly high spatial and temporal resolutions, the catalytic activity and the surface morphology can be correlated during the oscillation process.

METHODS

Sample and Reactor. The sample under investigation is a Pd(100) single crystal with dimensions of 4 × 4 mm^2 and a thickness of 2 mm. The cleaning procedure of the sample can be found in ref 23. The sample was heated by a boralectric heater, also used as the sample holder, the temperature of which was measured by a type-D thermocouple. The dependence of the surface reflectance on the sample temperature can be found in the Supporting Information.

A schematic picture of the setup is shown in Figure 1. A cubical chamber of volume 23 cm^3 with four windows for optical access was used for PLIF and surface reflectance measurements. Gases were supplied to the reactor by individual mass flow controllers (Bronkhorst EL-FLOW), and the gas pressure in the reactor was regulated by a digital pressure controller (Bronkhorst EL-PRESS) at the gas outlet. The gas composition in the reactor was monitored by a quadruple mass spectrometer (Pfeiffer, QME 220), which was connected to the outlet of the reactor by a 70 cm long gas tube (D = 1/16 in.). An automatic leak valve was used to control the amount of gas from the outlet leaking into the mass spectrometer for analysis and to keep the pressure in the mass spectrometer stable at 5 × 10^{-6} mbar. A more complete description of the gas system can be found in ref 23. The mass spectrometry (MS) signal is calibrated by normalizing the MS CO signal to a known initial partial pressure, and the CO_2 signal is scaled to match the observed conversion of CO.

PLIF. The experimental setup and detection scheme for the CO_2 PLIF have been described in detail previously.[33,34] The detection of CO_2 was realized by exciting the (00°0) → (10°1) combination band at ∼2.7 μm and collecting the fluorescence from the fundamental band at ∼4.3 μm. The fundamental 1064 nm laser beam with ∼350 mJ/pulse from an injection seeded single-mode Nd:YAG laser was used to pump a broad-band infrared optical parametric oscillator (IR OPO; GWU, versaScan-L 1064), generating a signal beam at ∼1.7 μm and an idler beam at ∼2.7 μm, with ∼8 and ∼7 mJ/pulse, respectively, both operating at 10 Hz. As shown in Figure 1, the idler beam was shaped into a thin laser sheet of ∼5 mm height by a spherical lens (f = +500 mm) and a cylindrical lens (f = +100 mm) and then sent through the reactor just above the catalyst. The full width at half-maximum (FWHM) of the idler beam is around ∼10 cm^{-1}, which is broad enough to cover a number of rovibrational lines in the (00°0) → (10°1) transition

DOI: 10.1021/acs.jpcc.7b08108
J. Phys. Chem. C 2017, 121, 23511−23519

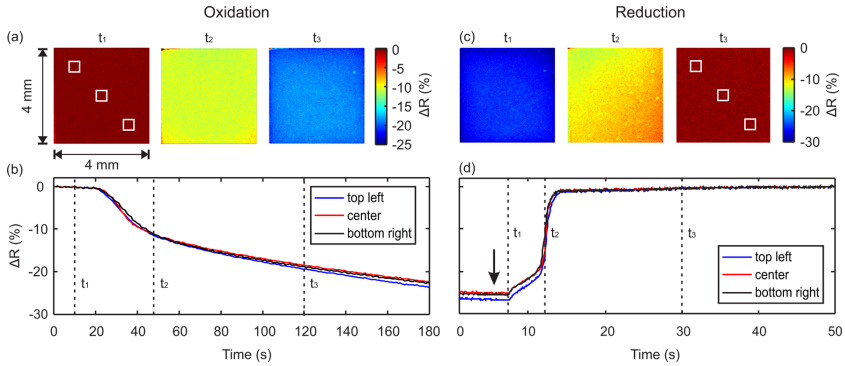

Figure 2. Surface reflectance changes of the sample during the oxidation and reduction processes in pure O_2 and CO, respectively. (a) Snapshots of the surface reflectance at t_1 = 10 s, t_2 = 48 s, and t_3 = 120 s during oxidation of the surface. (b) Change of the surface reflectance at different regions of the surface indicated by the white squares in (a). (c) Snapshots of the surface reflectance at t_1 = 7 s, t_2 = 12 s, and t_3 = 30 s during reduction of the surface. (d) Change of the surface reflectance at different regions of the surface indicated by the white rectangles in (c). The arrow in (d) indicates when the gases are switched from pure O_2 to pure CO.

of CO_2. The CO_2 fluorescence was then imaged by a liquid nitrogen cooled IR camera (Santa Barbara Focal Plane, SBF LP134). An interference filter inside the camera, centered at 4.26 μm, was used to suppress the strong thermal background. The exposure time was set to 30 μs to minimize the background and favor the fluorescence signal. Quantification of the detected PLIF signal is achieved by calibration measurements with known CO_2 partial pressures at corresponding temperatures and total chamber pressures to real measurements.

Surface Reflectance. As illustrated in Figure 1, light from a light-emitting diode (LED; Thorlabs M625L3) is first collimated and spatially filtered by two spherical lenses (f = +100 mm) and a small pinhole (diameter 100 μm) and then sent to a beam splitter above the reactor. The splitter reflects 50% of the collimated beam onto the sample and transmits 50% of the beam reflected by the sample toward a complementary metal oxide semiconductor (CMOS) camera (Andor Zyla). Another pair of spherical lenses (f = +200 mm) and an aperture were used for imaging the sample surface with a bright-field 4f configuration. The camera can be operated at a repetition rate up to 200 Hz, limited by the transfer rate of the data. In this study, the repetition rates were chosen according to the nature of the reaction processes, i.e., a lower rate for the oxidation process and a higher rate for the reduction process.

RESULTS AND DISCUSSION

Oxidation and Reduction. We have performed an oxidation and reduction experiment similar to that by Onderwaater et al.[20] Our results are qualitatively very similar, and we use the results for the more complex CO oxidation experiments described below. The oxidation experiment was performed using a sample temperature of 320 °C and a total pressure of 125 mbar with flows of 4 mL_n/min of O_2 and 36 mL_n/min of Ar (corresponding to initial partial pressures of 12.5 mbar of O_2 and 112.5 mbar of Ar). The reduction experiment was initiated after the oxidation experiment by switching the gas flow to 4 mL_n/min of CO and 36 mL_n/min of Ar (corresponding to initial partial pressures of 12.5 mbar of CO and 112.5 mbar of Ar). Hereinafter, the reflectance change ΔR is defined as $(I - I_0)/I_0$, where I_0 is the reflected intensity at the start of the experiment and I the subsequently measured intensity. Prior to the oxidation experiment, the sample was exposed to a pure CO environment to ensure that the surface was oxide free. The results from the oxidation and reduction experiments are shown in Figure 2. Figure 2a shows how the reflectance changes at t_1 = 10 s, t_2 = 48 s, and t_3 = 120 s during the oxidation process (t = 0 defined as when O_2 was introduced). The change of the surface reflectance as a function of the oxidation time from three different regions (marked by white rectangles) is shown in Figure 2b. Between t_1 = 10 s and t_2 = 48 s, the reflectance decreases at a greater speed, while, after t_2 = 48 s, the decrease of the reflectance is much slower. Our results agree very well with those of Onderwaater et al.[20] According to their model, the decreased reflectance can be attributed to a combination of the formation of a surface oxide and an increased surface roughness. They conclude that an increase of the oxide thickness is mainly responsible for the faster decrease of reflectance and self-terminated after a certain thickness, followed by a roughening process which is responsible for the slower decrease of reflectance. As can be seen from Figure 2b, no significant difference in the surface reflectance, at the different regions of the surface, can be observed during the oxidation in pure oxygen.

Turning to the reduction process shown in Figure 2c,d, the surface reflectance increases rapidly after the introduction of CO (indicated by the arrow) and almost restores its original value after t_3 = 30 s. Interestingly, we can also see the trace of switching the flow in the middle image in Figure 2c; i.e., the gas flows from the bottom right corner to the top left corner of the sample surface. See also Movies M1 and M2 showing the oxidation and reduction measurements, respectively, in the Supporting Information.

CO Oxidation and Gas-Phase Dependence. As mentioned above, the surface chemical composition is sensitive to the gas composition close to the surface, and any spatial inhomogeneity of the gas composition could lead to an inhomogeneity of the surface. We have shown in previous studies that the CO and CO_2 distributions across the Pd surface vary significantly in the MTL reaction region.[26] We therefore

DOI: 10.1021/acs.jpcc.7b08108
J. Phys. Chem. C 2017, 121, 23511−23519

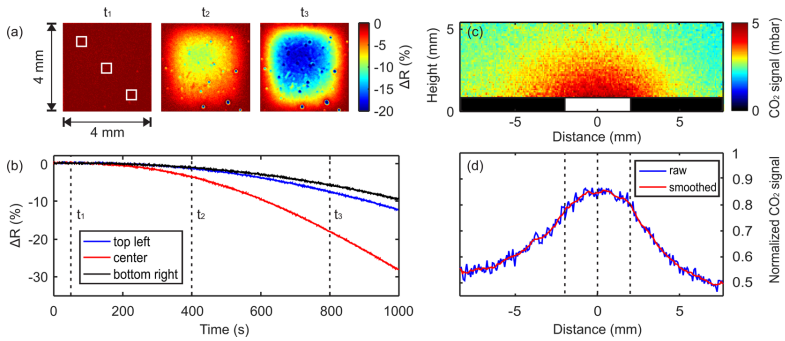

Figure 3. Surface reflectance changes of the sample and CO_2 distribution above the surface during CO oxidation under O_2-rich conditions (15:1 O_2/CO ratio). (a) Snapshots of the surface reflectance change at t_1 = 50 s, t_2 = 400 s, and t_3 = 800 s. (b) Change of the surface reflectance at different regions of the surface indicated by the white rectangles in (a). (c) A 10-shot averaged PLIF image showing the CO_2 distribution over the sample surface, acquired over 1 s. (d) Normalized horizontal CO_2 profile 0.5 mm above the sample. The dashed lines show the positions of the center and the edges of the sample.

investigated the oxidation of the Pd(100) surface under the reaction conditions, particularly in the MTL regime, by measuring the gas composition close to the surface using PLIF and the surface reflectance simultaneously. The results are shown in Figure 3. In the experiment, the sample was kept at 320 °C and 125 mbar, with flows of 30 mL_n/min of O_2, 2 mL_n/min of CO, and 18 mL_n/min of Ar. This corresponds to initial partial pressures of 75 mbar of O_2, 5 mbar of CO, and 45 mbar of Ar, with a 15:1 O_2/CO ratio, meaning that the reaction is under the O_2-rich condition. A mass spectrometer was used to monitor the global gas concentration and to ensure that the reaction was in the MTL regime. Figure 3a, b shows how the surface reflectance changes at t_1 = 50 s, t_2 = 400 s, and t_3 = 800 s during the oxidation process (t = 0 is defined as the time at which the gases were switched from pure Ar to CO and O_2 mixtures). As can be clearly seen, the reflectance change on the sample surface is not homogeneous. Instead, the reflectance at the center of the sample decreases at a much greater speed, compared to that at the corners of the sample. This is emphasized by the trends in Figure 3b, which shows how the reflectivity changes in each of the three squares in Figure 3a. The corresponding CO_2 gas distribution is shown in Figure 3c by a 10-shot averaged PLIF image recorded at t = 50 s, visualizing the CO_2 distribution above the sample, which does not change significantly during the reaction process. A CO_2 boundary layer over the surface can clearly be seen. A normalized (to the initial CO partial pressure, 5 mbar) horizontal CO_2 profile at 0.5 mm above the sample is plotted in Figure 3d. Both parts c and d of Figure 3 clearly show that the CO_2 distribution above the sample is not homogeneous, but decreases radially from the center of the surface. This also means that the O_2/CO ratio is the highest at the center of the surface and decreases radially toward the edges. Combining the results from surface reflectance and gas-phase measurements, we attribute the inhomogeneous development of the surface reflectance to the inhomogeneity of the gas composition above the surface. According to ref 20, the decrease of reflectance is a result of both surface oxide formation and increased surface roughness, and is dominated by the latter. The higher O_2/CO ratio at the center of the sample results in a faster palladium oxide formation and a quicker roughening compared to that at the corners of the sample, explaining the radial dynamic development of the surface reflectance signal from the surface. A small difference in the reflectance change between the two edges of the sample (top left and bottom right), as can be seen in Figure 3a, is due to the gas flow, which results in slightly different gas compositions over the two edges.

It is worth noting that the spots present in Figure 3a are not artifacts from the imaging system, but instead real objects present on the surface. They are not present from the start of the oxidation/roughening process during the reaction, but gradually appear as a decrease of the surface reflectance during the process at a much greater speed than the rest of the surface. Interestingly, they become significantly more pronounced under the reaction conditions, compared to the pure O_2 condition. We speculate that these spots are areas with a high density of steps on the surface, which become oxidized/rougher more easily under the reaction conditions, and are difficult to reduce completely in a pure CO environment, due to the formation of a highly stable PdO surface such as the oxygen-terminated PdO(100).[35]

Surprisingly, as mentioned above, the CO_2 PLIF profile close to the surface does not change considerably during the inhomogeneous oxidation/roughening process of the surface (see the Supporting Information). As the surface clearly simultaneously consists of a number of different oxygen-rich phases during the oxidation/roughening process, it is difficult to isolate a single phase responsible for the high activity and the nonchanging CO_2 distribution detected by PLIF. It is possible that only small areas of the surface with, for instance, chemisorbed oxygen are able to maintain the high activity.[36] It may also be that specific orientations of the PdO, such as the PdO(101) with coordinately oxygen unsaturated sites, is responsible for the high activity.[18]

To further demonstrate the sensitivity of the surface structure to the gas composition, we performed the oxidation and reduction experiments at different O_2/CO ratios. The oxidation experiment was performed at a 4:1 O_2/CO ratio, with flows of 4 mL_n/min of O_2, 1 mL_n/min of CO, and 45 mL_n/min of Ar (corresponding to initial partial pressures of 10 mbar of O_2, 2.5 mbar of CO, and 112.5 mbar of Ar). The reduction experiment was performed at a 1:4 O_2/CO ratio, with flows of

DOI: 10.1021/acs.jpcc.7b08108
J. Phys. Chem. C 2017, 121, 23511−23519

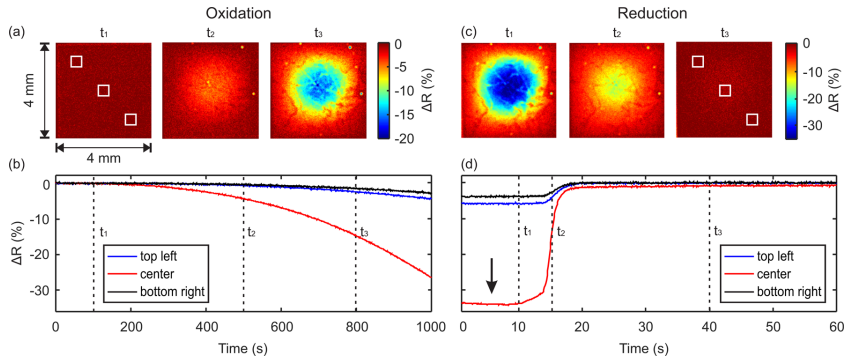

Figure 4. Surface reflectance changes of the sample during the oxidation and reduction process at 4:1 and 1:4 O_2/CO ratios, respectively. (a) Snapshots of the surface reflectance changes during oxidation at t_1 = 100 s, t_2 = 500 s, and t_3 = 800 s. (b) Change of the surface reflectance at different regions of the surface indicated by the white rectangles in (a). (c) Snapshots of the surface reflectance during reduction at t_1 = 10 s, t_2 = 15 s, and t_3 = 40 s. (d) Change of the surface reflectance at different regions of the surface, indicated by the white rectangles in (c). The arrow in (d) indicates when the gases are switched to reduction conditions.

1 mL_n/min of O_2, 4 mL_n/min of CO, and 45 mL_n/min of Ar (corresponding to initial partial pressures of 2.5 mbar of O_2, 10 mbar of CO, and 112.5 mbar of Ar). In both experiments, the sample was kept at 320 °C and 125 mbar and in the highly active phase. The results are summarized in Figure 4. Similar to Figure 3a, Figure 4a shows the inhomogeneous reflectance change on the surface during the oxidation process, but with a difference in shape and size, comparing snapshots at t_3 = 800 s. Comparing the trends between Figures 3b and 4b, it is clear that the reflectance decreases at similar rates at the center of the surface, while at very different rates at the edges of the surface, i.e., much slower in Figure 4b. When the gas is switched from the O_2-rich to the CO-rich condition, the palladium oxide is reduced. As shown in Figure 4c,d, during the reduction process, the surface reflectance increases and returns almost to the initial state after 60 s. See also Movies M3 and M4 in the Supporting Information.

To explain the difference in reflectance change between the two oxidation processes in Figures 3a and 4a, we compare the gas composition just above the sample surface between the two cases, as shown in Figure 5. The horizontal CO_2 partial pressure profile (blue) in Figure 5a,b is obtained by integrating the CO_2 PLIF signal 0.5 mm above the sample surface, similar to Figure 3b. Given the known initial O_2/CO ratio in the gas mixture, the corresponding CO and O_2 profiles just above the surface above the active catalyst can be calculated, assuming that two CO_2 molecules correspond to two CO molecules and one O_2 molecule, as shown in Figure 5a,b. With the calculated CO and O_2 profiles, the O_2/CO ratio profile just above the active catalyst can also be calculated, as plotted in Figure 5c. The cross sections of the reflectance image acquired at t = 800 s during the oxidation process for the two cases have been plotted in Figure 5d to show the correlation with the corresponding gas composition (O_2/CO ratio). In each ease, the gradients of the gas composition and the reflectance change match very well with each other; i.e., a higher O_2/CO ratio yields a lower reflectance over the surface. By comparing the two cases, it can be observed that the O_2/CO ratio profile above the surface is much larger in the 15:1 O_2/CO ratio case than in the 4:1 O_2/CO ratio case, resulting in an overall larger decease in the reflectance over the entire surface. As a result, we can see a more spread out reflectance decrease over the surface in Figure 3 than in Figure 4. However, the dependence of the reflectance change on the O_2/CO ratio does not seem to be linear. Therefore, the large difference in the O_2/CO ratio between the two cases does not result in a large difference in the reflectance change at the center of the surface, but a much more obvious difference at the edges.

Self-Sustained Reaction Oscillations. It has been proposed by Hendriksen et al. that self-sustained reaction oscillations above a Pd(100) during CO oxidation involve two main processes on the surface, roughening and smoothening.[31] We have demonstrated above, using the same approach as Onderwaater,[19,20] how the change of the surface reflectance can be related to the oxidation (roughening) and reduction (smoothening) processes, which in turn are affected by the gas composition close to the surface depending on the initial O_2/CO ratios and the activity of the catalyst. Here, we combine the surface reflectance with PLIF to correlate the surface roughness/oxidation to the gas-phase composition close to the surface during self-sustained reaction oscillations. The results are summarized in Figure 6. The experiment was performed by supplying a constant heating current, which heated the sample to around 240 °C. The total chamber pressure was kept at 150 mbar with flows of 4 mL_n/min of CO, 80 mL_n/min of O_2, and 16 mL_n/min of Ar (corresponding to initial partial pressures of 6 mbar of CO, 120 mbar of O_2, and 24 mbar of Ar), resulting in a 20:1 O_2/CO ratio. Both the PLIF trend in Figure 6a and the MS trends in Figure 6b show an alternating change of the gas phase, indicating that the sample is undergoing self-sustained reaction oscillations. Figure 6c shows the alternating changes in the surface reflectance, which correlate perfectly to the observed gas-phase changes. Due to the exothermic nature of the reaction, the sample temperature is also oscillating, as can be seen in Figure 6d. See also the Supporting Information.

It can be seen from the CO_2 PLIF image in Figure 6e that a very small amount of CO_2 is detected in the case of an almost inactive catalyst at time t_1. As a consequence, a large amount of CO is present close to and on the surface, and the reflectance image in Figure 6h shows that the surface is smooth. Using an

DOI: 10.1021/acs.jpcc.7b08108
J. Phys. Chem. C 2017, 121, 23511−23519

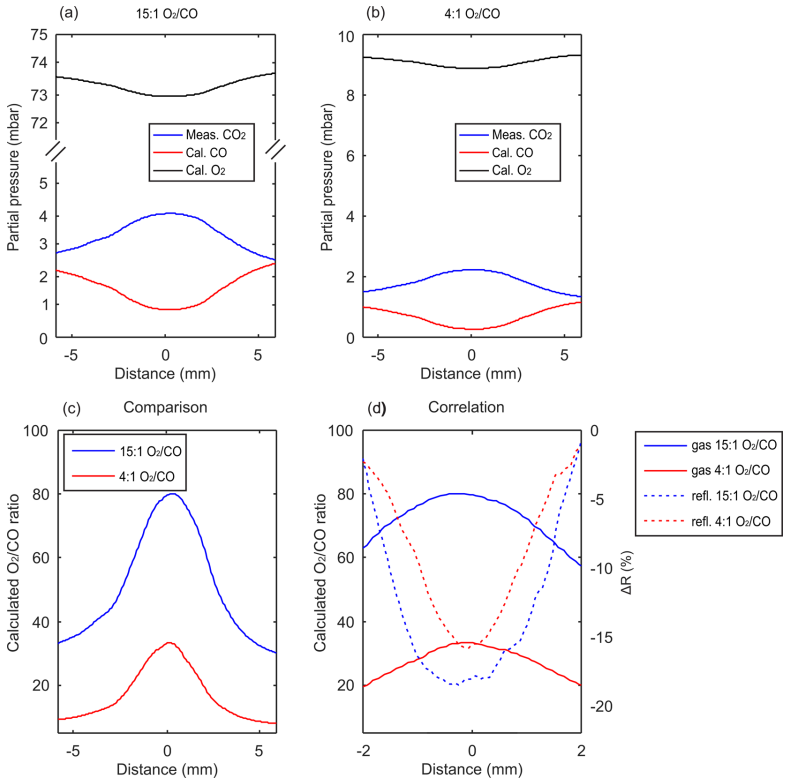

Figure 5. Measured CO_2 and calculated CO and O_2 partial pressure profiles (smoothed) at 0.5 mm above the sample surface for (a) the 15:1 O_2/CO ratio case and for (b) the 4:1 O_2/CO ratio case. (c) Comparison of calculated O_2/CO ratio profiles above the sample surface between the two cases. (d) Correlation between the gas composition and the reflectance change over the sample surface for the two cases, where a higher O_2/CO ratio yields a lower reflectance over the surface for the same condition.

image recorded from a reduced Pd sample as a reference, the reflectance change is zero over the entire surface. We therefore conclude that the surface is metallic, smooth, and nearly saturated with CO at t_1. As the surface becomes active, as evidenced by the PLIF trace in Figure 6a, there is a sudden decrease of the surface reflectance trace as shown in Figure 6c. We attribute this sudden decease of the reflectance to the formation of a thin palladium oxide layer, which is consistent with the observation by Onderwaater et al.,[20] supported by STM and SXRD experiments.[16,17] When the reaction reaches the MTL regime, there is a large amount of CO_2 produced close to the surface, as evidenced by the PLIF images in Figure 6f,g. This results in an increase of the O_2/CO ratio, and as described above, the sample becomes increasingly oxidized/roughened in the MTL regime. As can be seen from the surface reflectance trace from the center of the sample (red) in Figure 6c, there is a decreasing trend from t_2 to t_3, demonstrating that the surface roughness/oxidation increases when the reaction is in the MTL regime. However, as was also described above, the roughening/oxidation process is not homogeneous over the entire surface, as can be seen from the images in Figure 6i,j. The observation further confirms that the gas-phase inhomogeneity results in a surface oxide/roughness inhomogeneity. As the entire sample becomes increasingly rough and oxidized, at a critical point, the surface suddenly becomes inactive, supporting the previous observations by Hendriksen et al.[31] At this point, the amount of CO is increasing, reducing and smoothening the surface, and the process repeats itself. See also Movie M5 in the Supporting Information.

It is worth noting that the changes of the surface reflectance are very small (around 0.4%) in this experiment compared to the experiments shown above (about 30%). This is because the sample was heated to a much lower temperature (around 240 °C) in the oscillation experiment; thus, it is more difficult for the surface to get oxidized/roughened. To enhance the signal-to-noise ratio, 40 images acquired over 20 s are therefore averaged to obtain Figure 6h–j. It is also interesting to see that the center of the surface reflectance change is slightly shifted from the center of the sample. This is due to the flow of the gas, as illustrated by the top view CO_2 PLIF image in Figure 6k, which was recorded from a separate measurement but with the same sample environment.

DOI: 10.1021/acs.jpcc.7b08108
J. Phys. Chem. C 2017, 121, 23511−23519

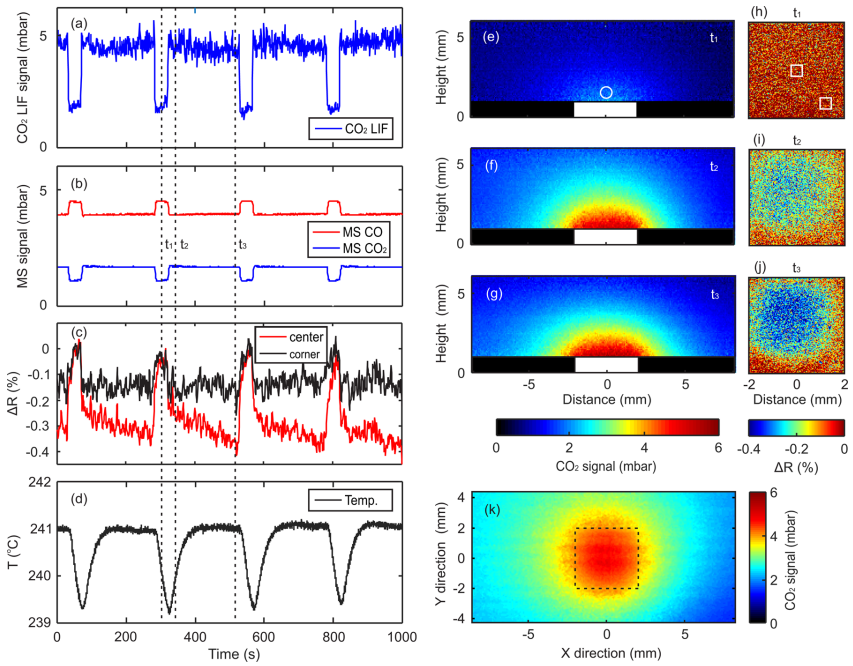

Figure 6. Simultaneous CO_2 PLIF and surface reflectance measurements during oscillations of a Pd(100) sample in CO oxidation. (a) PLIF trend integrating a small region (indicated by the white circle in (e)) just above the sample surface. (b) MS signals of CO and CO_2. (c) Two trends showing the reflectance changes of the center and corner of the sample (indicated by white squares in (h)), respectively. (d) Temperature of the sample holder recorded by a thermal couple. (e–g) Three CO_2 PLIF images recorded at t_1, t_2, and t_3, respectively. (h–j) Three images showing the reflectance change of the surface at t_1, t_2, and t_3, respectively. (k) A CO_2 PLIF image from the top view recorded from a separate measurement but with the same sample environment. The dashed rectangle marks the position of the sample.

SUMMARY AND OUTLOOK

In this work, we have combined measurements of the surface reflectance and PLIF to investigate the Pd(100) surface during CO oxidation. When the reaction is in the MTL regime, the surface exhibits an inhomogeneous surface reflectance change and the gas distribution close to the surface is also inhomogeneous. We attribute the inhomogeneity in the surface reflectance to the inhomogeneity in the gas phase and interpret that, with a higher O_2/CO ratio at the center of the sample, the surface oxide grows faster and as a consequence is roughened by the reaction more quickly, compared to that at the edges of the sample. Such an inhomogeneity of the surface and the gas phase also implies that care should be taken when we are comparing surfaces under the reaction conditions using traditional surface-sensitive techniques, where either a small surface area is probed as in AP-XPS and STM or a large area is probed as in SXRD. From our previous work, the gas distribution can strongly depend on the gas flows, total pressures, and even reactor geometries.[37] Therefore, it would be interesting to investigate how the surface reflectance changes with these parameters. In the oscillation experiment, the simultaneously collected information on the gas phase and the surface reflectance clearly illustrates the roughening and smoothening processes involved in the oscillations. Both the PLIF and surface reflectance techniques provide high spatial (on a macroscopic scale) and temporal resolutions, making it possible to directly correlate the gas phase and surface both spatially and temporally. As the surface reflectance is a relatively simple technique, it would in principle not be difficult to integrate it with diffraction-based techniques, such as SXRD for evaluation of its sensitivity to surface oxides and surface roughness.

ASSOCIATED CONTENT

Supporting Information

The Supporting Information is available free of charge on the ACS Publications website at DOI: 10.1021/acs.jpcc.7b08108.

Temperature dependence of the surface reflectance and PLIF and MS trends during the oxidation process (PDF)

Movie M1 showing the surface reflectance change during oxidation in pure O_2 (AVI)

Movie M2 showing the surface reflectance change during reduction in pure CO (AVI)

Movie M3 showing the surface reflectance change during oxidation under O_2-rich conditions (AVI)

Movie M4 showing the surface reflectance change during reduction under CO-rich reaction conditions (AVI)

Movie M5 showing the simultaneous measurement of PLIF and surface reflectance during oscillations (AVI)

DOI: 10.1021/acs.jpcc.7b08108
J. Phys. Chem. C 2017, 121, 23511–23519

AUTHOR INFORMATION

Corresponding Author

*E-mail: johan.zetterberg@forbrf.lth.se. Phone: +46 (0) 46 222 7728.

ORCID

Jianfeng Zhou: 0000-0003-0862-7951
Sara Blomberg: 0000-0002-6475-013X
Edvin Lundgren: 0000-0002-3692-6142
Johan Zetterberg: 0000-0002-0882-1482

Notes

The authors declare no competing financial interest.

ACKNOWLEDGMENTS

We thank the Knut & Alice Wallenberg Foundation and the Swedish Research Council for financially supporting this work.

REFERENCES

(1) Bañares, M. A. Operando methodology: Combination of In Situ Spectroscopy and Simultaneous Activity Measurements under Catalytic Reaction Conditions. *Catal. Today* **2005**, *100*, 71−77.

(2) *Operando Research in Heterogeneous Catalysis*; Frenken, J., Groot, I., Eds.; Springer: Cham, Switzerland, 2017.

(3) Morgan, K.; Touitou, J.; Choi, J. S.; Coney, C.; Hardacre, C.; Pihl, J. A.; Stere, C. E.; Kim, M. Y.; Stewart, C.; Goguet, A.; et al. Evolution and Enabling Capabilities of Spatially Resolved Techniques for the Characterization of Heterogeneously Catalyzed Reactions. *ACS Catal.* **2016**, *6*, 1356−1381.

(4) Freund, H. J.; Meijer, G.; Scheffler, M.; Schlögl, R.; Wolf, M. CO Oxidation as a Prototypical Reaction for Heterogeneous Processes. *Angew. Chem., Int. Ed.* **2011**, *50*, 10064−10094.

(5) van Spronsen, M. A.; Frenken, J. W. M.; Groot, I. M. N. Surface Science under Reaction Conditions: CO Oxidation on Pt and Pd Model Catalysts. *Chem. Soc. Rev.* **2017**, *46*, 4347−4374.

(6) Hendriksen, B. L. M.; Bobaru, S. C.; Frenken, J. W. M. Looking at Heterogeneous Catalysis at Atmospheric Pressure Using Tunnel Vision. *Top. Catal.* **2005**, *36*, 43−54.

(7) Frenken, J.; Groot, I. In *Operando Research in Heterogeneous Catalysis*; Frenken, J., Groot, I., Eds.; Springer: Cham, Switzerland, 2017; pp 1−30.

(8) Ryczkowski, J. IR Spectroscopy in Catalysis. *Catal. Today* **2001**, *68*, 263−381.

(9) Gao, F.; McClure, S. M.; Cai, Y.; Gath, K. K.; Wang, Y.; Chen, M. S.; Guo, Q. L.; Goodman, D. W. CO Oxidation Trends on Pt-Group Metals from Ultrahigh Vacuum to Near Atmospheric Pressures: A Combined In Situ PM-IRAS and Reaction Kinetics Study. *Surf. Sci.* **2009**, *603*, 65−70.

(10) Toyoshima, R.; Yoshida, M.; Monya, Y.; Suzuki, K.; Mun, B. S.; Amemiya, K.; Mase, K.; Kondoh, H. Active Surface Oxygen for Catalytic CO Oxidation on Pd(100) Proceeding under Near Ambient Pressure Conditions. *J. Phys. Chem. Lett.* **2012**, *3*, 3182−3187.

(11) Blomberg, S.; Hoffmann, M. J.; Gustafson, J.; Martin, N. M.; Fernandes, V. R.; Borg, A.; Liu, Z.; Chang, R.; Matera, S.; Reuter, K.; et al. In-Situ X-Ray Photoelectron Spectroscopy of Model Catalysts: At the Edge of the Gap. *Phys. Rev. Lett.* **2013**, *110*, 117601.

(12) Karslıoğlu, O.; Bluhm, H. In *Operando Research in Heterogeneous Catalysis*; Frenken, J., Groot, I., Eds.; Springer: Cham, Switzerland, 2017; pp 31−57.

(13) Stierle, A.; Molenbroek, A. M. Novel In Situ Probes for Nanocatalysis. *MRS Bull.* **2007**, *32*, 1001−1009.

(14) Gustafson, J.; Shipilin, M.; Zhang, C.; Stierle, A.; Hejral, U.; Ruett, U.; Gutowski, O.; Carlsson, P.-A.; Skoglundh, M.; Lundgren, E. High-Energy Surface X-ray Diffraction for Fast Surface Structure Determination. *Science* **2014**, *343*, 758−761.

(15) Shipilin, M.; Gustafson, J.; Zhang, C.; Merte, L. R.; Stierle, A.; Hejral, U.; Ruett, U.; Gutowski, O.; Skoglundh, M.; Carlsson, P. A.; et al. Transient Structures of PdO during CO Oxidation over Pd(100). *J. Phys. Chem. C* **2015**, *119*, 15469−15476.

(16) Hendriksen, B. L. M.; Bobaru, S. C.; Frenken, J. W. M. Oscillatory CO Oxidation on Pd(1 0 0) Studied with In Situ Scanning Tunneling Microscopy. *Surf. Sci.* **2004**, *552*, 229−242.

(17) Lundgren, E.; Gustafson, J.; Mikkelsen, A.; Andersen, J. N.; Stierle, A.; Dosch, H.; Todorova, M.; Rogal, J.; Reuter, K.; Scheffler, M. Kinetic Hindrance during the Initial Oxidation of Pd(100) at Ambient Pressures. *Phys. Rev. Lett.* **2004**, *92*, 046101.

(18) van Rijn, R.; Balmes, O.; Resta, A.; Wermeille, D.; Westerstrom, R.; Gustafson, J.; Felici, R.; Lundgren, E.; Frenken, J. W. M. Surface Structure and Reactivity of Pd(100) during CO Oxidation near Ambient Pressures. *Phys. Chem. Chem. Phys.* **2011**, *13*, 13167−13171.

(19) Onderwaater, W. G.; Taranovskyy, A.; Bremmer, G. M.; van Baarle, G. C.; Frenken, J. W. M.; Groot, I. M. N. From dull to shiny: A Novel Setup for Reflectance Difference Analysis under Catalytic Conditions. *Rev. Sci. Instrum.* **2017**, *88*, 023704.

(20) Onderwaater, W. G.; Taranovskyy, A.; van Baarle, G. C.; Frenken, J. W. M.; Groot, I. M. N. In Situ Optical Reflectance Difference Observations of CO Oxidation over Pd(100). *J. Phys. Chem. C* **2017**, *121*, 11407−11415.

(21) Matera, S.; Maestri, M.; Cuoci, A.; Reuter, K. Predictive-Quality Surface Reaction Chemistry in Real Reactor Models: Integrating First-Principles Kinetic Monte Carlo Simulations into Computational Fluid Dynamics. *ACS Catal.* **2014**, *4*, 4081−4092.

(22) Matera, S.; Reuter, K. When Atomic-Scale Resolution is Not Enough: Spatial Effects on In Situ Model Catalyst Studies. *J. Catal.* **2012**, *295*, 261−268.

(23) Blomberg, S.; Brackmann, C.; Gustafson, J.; Aldén, M.; Lundgren, E.; Zetterberg, J. Real-Time Gas-Phase Imaging over a Pd(110) Catalyst during CO Oxidation by Means of Planar Laser-Induced Fluorescence. *ACS Catal.* **2015**, *5*, 2028−2034.

(24) Zetterberg, J.; Blomberg, S.; Gustafson, J.; Evertsson, J.; Zhou, J.; Adams, E. C.; Carlsson, P. A.; Alden, M.; Lundgren, E. Spatially and Temporally Resolved Gas Distributions around Heterogeneous Catalysts Using Infrared Planar Laser-Induced Fluorescence. *Nat. Commun.* **2015**, *6*, 7076.

(25) Zellner, A.; Suntz, R.; Deutschmann, O. Two-Dimensional Spatial Resolution of Concentration Profiles in Catalytic Reactors by Planar Laser-Induced Fluorescence: NO Reduction over Diesel Oxidation Catalysts. *Angew. Chem., Int. Ed.* **2015**, *54*, 2653−2655.

(26) Blomberg, S.; Zhou, J.; Gustafson, J.; Zetterberg, J.; Lundgren, E. 2D and 3D Imaging of the Gas Phase close to an Operating Model Catalyst by Planar Laser Induced Fluorescence. *J. Phys.: Condens. Matter* **2016**, *28*, 453002.

(27) Blomberg, S.; Zetterberg, J.; Zhou, J.; Merte, L. R.; Gustafson, J.; Shipilin, M.; Trinchero, A.; Miccio, L. A.; Magaña, A.; Ilyn, M.; et al. Strain Dependent Light-Off Temperature in Catalysis Revealed by Planar Laser-Induced Fluorescence. *ACS Catal.* **2017**, *7*, 110−114.

(28) Imbihl, R.; Ertl, G. Oscillatory Kinetics in Heterogeneous Catalysis. *Chem. Rev.* **1995**, *95*, 697−733.

(29) Schüth, F.; Henry, B. E.; Schmidt, L. D. Oscillatory Reactions in Heterogeneous Catalysis. *Adv. Catal.* **1993**, *39*, 51−127.

(30) Hendriksen, B. L. M.; Bobaru, S. C.; Frenken, J. W. M. Bistability and Oscillations in CO Oxidation Studied with Scanning Tunnelling Microscopy inside a Reactor. *Catal. Today* **2005**, *105*, 234−243.

(31) Hendriksen, B. L. M.; Ackermann, M. D.; van Rijn, R.; Stoltz, D.; Popa, I.; Balmes, O.; Resta, A.; Wermeille, D.; Felici, R.; Ferrer, S.; et al. The Role of Steps in Surface Catalysis and Reaction Oscillations. *Nat. Chem.* **2010**, *2*, 730−734.

(32) Onderwaater, W. G.; Balmes, O.; Roobol, S. B.; Van Spronsen, M.; Drnec, J.; Carla, F.; Felici, R.; Frenken, J. W. M. Oxidation of CO on Pd(1 0 0): On the Structural Evolution of the PdO Layer during the Self Sustained Oscillation Regime. *Catal., Struct. & React.* **2017**, *3*, 89−94.

(33) Zetterberg, J.; Blomberg, S.; Gustafson, J.; Sun, Z. W.; Li, Z. S.; Lundgren, E.; Aldén, M. An In Situ Set Up for the Detection of CO_2

DOI: 10.1021/acs.jpcc.7b08108
J. Phys. Chem. C 2017, 121, 23511−23519

from Catalytic CO Oxidation by Using Planar Laser-Induced Fluorescence. *Rev. Sci. Instrum.* **2012**, *83*, 053104.
(34) Zhou, J.; Pfaff, S.; Lundgren, E.; Zetterberg, J. A Convenient Setup for Laser-Induced Fluorescence Imaging of both CO and CO_2 during Catalytic CO Oxidation. *Appl. Phys. B: Lasers Opt.* **2017**, *123*, 87.
(35) Rogal, J.; Reuter, K.; Scheffler, M. Thermodynamic Stability of PdO Surfaces. *Phys. Rev. B: Condens. Matter Mater. Phys.* **2004**, *69*, 075421.
(36) Gao, F.; Wang, Y.; Cai, Y.; Goodman, D. W. CO Oxidation on Pt-Group Metals from Ultrahigh Vacuum to Near Atmospheric Pressures. 2. Palladium and Platinum. *J. Phys. Chem. C* **2009**, *113*, 174−181.
(37) Zhou, J.; Blomberg, S.; Gustafson, J.; Lundgren, E.; Zetterberg, J. Visualization of Gas Distribution in a Model AP-XPS Reactor by PLIF: CO Oxidation over a Pd(100) Catalyst. *Catalysts* **2017**, *7*, 29.

DOI: 10.1021/acs.jpcc.7b08108
J. Phys. Chem. C 2017, 121, 23511−23519

Simultaneous Imaging of Gas Phase over and Surface Reflectance of a Pd(100) Single Crystal during CO Oxidation

Jianfeng Zhou [1], Sara Blomberg [2], Johan Gustafson [2], Edvin Lundgren [2] and Johan Zetterberg [1]*

AUTHOR ADDRESS

[1] Division of Combustion Physics, Lund University, SE-221 00 Lund, Sweden

[2] Division of Synchrotron Radiation Research, Lund University, SE-221 00 Lund, Sweden

The surface reflectance change can be induced purely by temperature change of the surface, as also observed by Onderwaater et al.[1]. We have investigated the temperature dependence of the surface reflectance under pure Ar environment, and found that the surface reflectance changes linearly with sample temperature, as shown in Figure S1. The result shows that 150 °C change of the sample temperature corresponds to about 1% change of the surface reflectance. In the oscillation experiment, the surface temperature measurements have not been performed due to the complexity of the optical setup. Instead, the temperature of the sample holder was measured by a thermocouple, as shown in Figure 5 (d). Since we performed the experiment under the same sample environment as in [2], where an IR camera was used to measure the surface temperature, we can refer to that result and conclude that the temperature difference of the sample surface between low and highly active phases is about 5 °C. Based on the linear dependence, this would

only attribute to less than 0.04 % of the change of surface reflectance. Therefore, we can conclude that the change of the surface reflectance is mainly due to the formation of surface oxide and surface roughening.

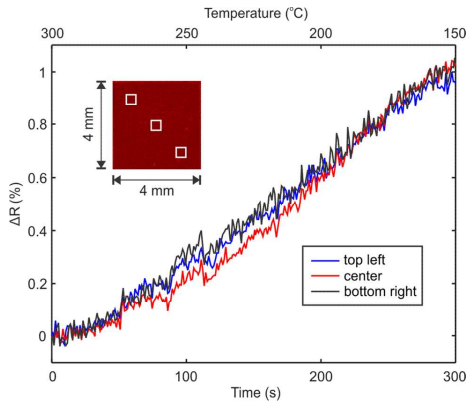

Figure S1 Temperature dependence of surface reflectance in pure Ar.

We have simultaneously measured the surface reflectance and the CO_2 distribution above the surface under O_2 rich (15:1 O_2/CO ratio) reaction condition, as shown in Figure 3 and S2, respectively. However, from both the PLIF and MS CO_2 signal in Figure S2 (a), we have not observed any obvious change of the gas composition close to the surface. Both normalized horizontal CO_2 profiles at 0.5 mm above the surface and snapshots of PLIF image at t_1 = 50 s, t_2 = 400 s and t_3 = 800 s, as shown in S2 (b) and (c-e) respectively, also indicate no significant change of the gas composition above the surface. It is worth noting that the PLIF images look quite different from the ones in Figure 6 because of different gas flows and total chamber pressures, which strongly affect the gradient of the CO_2 partial pressure close to the surface [3].

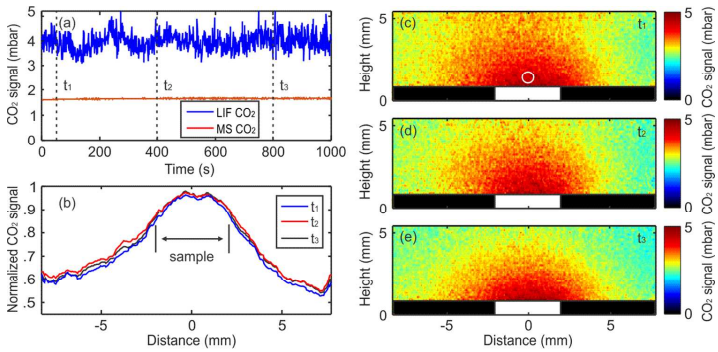

Figure S2 CO_2 distribution over a Pd(100) sample under reaction at 320 °C and 125 mbar. (a) CO_2 PLIF and MS trends; (b) normalized horizontal CO_2 profiles at 0.5 mm above the surface at t_1, t_2 and t_3; (c-e) PLIF images recorded at t_1, t_2 and t_3, showing the CO_2 distribution close to the surface. The white circle in (c) indicates the region used to integrate the PLIF trend in (a).

References

1. Onderwaater, W. G.; Taranovskyy, A.; van Baarle, G. C.; Frenken, J. W. M.; Groot, I. M. N., In Situ Optical Reflectance Difference Observations of CO Oxidation over Pd(100). *J. Phys. Chem. C* **2017,** *121*, 11407-11415.

2. Blomberg, S.; Zhou, J.; Gustafson, J.; Zetterberg, J.; Lundgren, E., 2D and 3D Imaging of the Gas Phase close to an Operating Model Catalyst by Planar Laser Induced Fluorescence. *J. Phys.: Condens. Matter* **2016,** *28*, 453002.

3. Zhou, J.; Blomberg, S.; Gustafson, J.; Lundgren, E.; Zetterberg, J., Visualization of Gas Distribution in a Model AP-XPS Reactor by PLIF: CO Oxidation over a Pd(100) Catalyst. *Catalysts* **2017,** *7*, 29.

Paper IV

OPEN ACCESS
IOP Publishing
Journal of Physics: Condensed Matter
J. Phys.: Condens. Matter **28** (2016) 453002 (16pp)
doi:10.1088/0953-8984/28/45/453002

Topical Review

2D and 3D imaging of the gas phase close to an operating model catalyst by planar laser induced fluorescence

Sara Blomberg[1], Jianfeng Zhou[2], Johan Gustafson[1], Johan Zetterberg[2] and Edvin Lundgren[1]

[1] Division of Synchrotron Radiation Research, Lund University, Box 118, S-221 00, Sweden
[2] Divsion of Combustion Physics, Lund University, Box 118, S-221 00, Sweden

E-mail: sara.blomberg@sljus.lu.se

Received 7 August 2015, revised 18 August 2016
Accepted for publication 22 August 2016
Published 13 September 2016

Abstract

In recent years, efforts have been made in catalysis related surface science studies to explore the possibilities to perform experiments at conditions closer to those of a technical catalyst, in particular at increased pressures. Techniques such as high pressure scanning tunneling/atomic force microscopy (HPSTM/AFM), near ambient pressure x-ray photoemission spectroscopy (NAPXPS), surface x-ray diffraction (SXRD) and polarization-modulation infrared reflection absorption spectroscopy (PM-IRAS) at semi-realistic conditions have been used to study the surface structure of model catalysts under reaction conditions, combined with simultaneous mass spectrometry (MS). These studies have provided an increased understanding of the surface dynamics and the structure of the active phase of surfaces and nano particles as a reaction occurs, providing novel information on the structure/activity relationship. However, the surface structure detected during the reaction is sensitive to the composition of the gas phase close to the catalyst surface. Therefore, the catalytic activity of the sample itself will act as a gas-source or gas-sink, and will affect the surface structure, which in turn may complicate the assignment of the active phase. For this reason, we have applied planar laser induced fluorescence (PLIF) to the gas phase in the vicinity of an active model catalysts. Our measurements demonstrate that the gas composition differs significantly close to the catalyst and at the position of the MS, which indeed should have a profound effect on the surface structure. However, PLIF applied to catalytic reactions presents several beneficial properties in addition to investigate the effect of the catalyst on the effective gas composition close to the model catalyst. The high spatial and temporal resolution of PLIF provides a unique tool to visualize the on-set of catalytic reactions and to compare different model catalysts in the same reactive environment. The technique can be applied to a large number of molecules thanks to the technical development of lasers and detectors over the last decades, and is a complementary and visual alternative to traditional MS to be used in environments difficult to asses with MS. In this article we will review general considerations when performing PLIF experiments, our experimental set-up for PLIF and discuss relevant examples of PLIF applied to catalysis.

Original content from this work may be used under the terms of the Creative Commons Attribution 3.0 licence. Any further distribution of this work must maintain attribution to the author(s) and the title of the work, journal citation and DOI.

 © 2016 IOP Publishing Ltd Printed in the UK

Keywords: PLIF, catalysis, CO oxidation

Online supplementary data available from stacks.iop.org/JPhysCM/28/453002/mmedia

(Some figures may appear in colour only in the online journal)

1. Introduction

Heterogeneous catalysis is one of the major motivations for the interest in gas-surface interaction with metal surfaces. As applied catalysis is based on a trial and error approach due to the complexity of a technical catalyst, model systems such as low-index single crystal surfaces under ultra high vacuum (UHV) conditions and careful control of the reactant gas abundance on the surface has promoted the understanding of adsorbate-adsorbate and adsorbate-substrate interactions [1, 2]. For instance, CO oxidation on transition metal surfaces, which is an important model system for oxidation catalysis [3], has been extensively studied for many years, but despite the apparent simplicity of the reaction, the details of the reaction pathway is still unclear. While a number of investigations suggests that a surface with chemisorbed oxygen is the most active phase [4, 5], other studies have proposed that the oxidized form of the surface is the most active phase under the pressure and temperature conditions appropriate for real-world catalytic oxidation reactions [6–8] or at the border between a thin oxide and the metal [9]. The details are still under discussion [10–12].

Because of these issues and the need for fundamental knowledge, there is a rapid technical development expanding the literature based on *in situ* techniques under realistic conditions during catalytic reactions [13–30] as well as novel theoretical approaches [31–35] using model catalysts and semi-realistic conditions.

At the same time, there is an increasing awareness that the details of the reactor geometry is essential for the resulting activity and the resulting structure at the surface. There have been a number of different reactors used for different *in situ* techniques, and the most common setup is a stainless steel vessel that may reach high vacuum (HV 10^{-3}–10^{-6} mbar) or even ultra high vacuum (UHV 10^{-10} mbar) and operated in a flow or batch mode. In general, it is in principle easy to simulate the gas flows through a vessel using finite element approaches, however the situation becomes significantly more complicated as a catalyst becomes active inside the vacuum vessel, changing the gas composition and flows significantly. There has been some pioneering attempts to simulate this situation [36, 37]. In some cases, the experimental setup is further complicated by the introduction of a differentially pumped electron analyzer close to the sample, as in the NAPXPS set-up.

To this end, we have use planar laser induce fluorescence (PLIF) to investigate the 2D gas distribution with the focus on CO_2 and CO in the CO oxidation reaction to investigate the actual gas composition close to the model catalyst surface in a semi-realistic environment as the model catalyst becomes active [19, 36, 38–41]. PLIF is a commonly used technique in combustion related research to investigate the gas composition during combustion such as in a flame and a number of other research fields [42, 43], but has only been limited used in catalysis related research [44–51], and in particular very little work has been done on CO, CO_2 and small hydrocarbons. The reason for the limited number of experiments is that these molecules have no or not easily accessible transitions in the UV-visible spectral range, making both excitations and detection more difficult, and has only become feasible in the last decade. In the present review, we explain the experimental facilities needed to perform PLIF and the physical processes involved in the measurements. Our measurements show that for CO oxidation the gas phase composition of CO and CO_2 is significantly different close to the active model catalyst surface compared to the composition measured by MS far away from the active catalyst. We show that the gas distribution can also be imaged in 3D.

Furthermore, the spatial resolution of PLIF provides an excellent opportunity to compare different catalysts in the same reactant environment. We present measurements with high spatial and temporal resolution from a 'curved' Pd single crystal, revealing differences in the activation temperatures at different parts of the crystal. Also differences in the activation temperature between two different catalysts in the same reactor is presented clearly showing differences between the activation of the two catalysts with different materials composition. Further, we present an experimental solution to how gaseous cross-talk between catalysts can be avoided by placing catalyst in tubes and monitoring the exhaust inside a vacuum vessel, indicating how several catalysts may be tested simultaneously in the same environment

In addition, the high time resolution of PLIF directly demonstrate the activation or light-off of a catalyst as the temperature is ramped to the ignition temperature. Therefore, the PLIF technique is an excellent tool to visualize gas phase changes during catalysis, also for fundamental studies. To demonstrate this, we present the appearance of the 2D CO_2 distribution during self-sustained reaction oscillations over a Pd(1 0 0) model catalyst, and propose a model for the changes of the catalyst surface during these oscillations.

As the reactor geometry is important for the gas distribution in the reactor, the technique can also be used to characterize the gas-flow properties in reactors of different designs, as illustrated by the visualization of the 2D CO_2 distribution in a stagnation flow reactor as well as in a reactor designed to mimic a common NAPXPS setup.

We also show that the technique can be extended to other reactions and gases relevant for catalysis such as CO and NH_3.

2. PLIF

In laser-induced fluorescence (LIF) a laser beam excites the molecule of interest, the excited molecule relaxes by emitting a photon, i.e. fluoresces, and the fluorescence light is then detected. The process is highly selective, meaning that the technique is species specific, targeting a specific molecule. It is also a relatively strong process, allowing for short gate times (ns-μs depending on wavelength region and molecule) and high repetition rates (limited by the laser pulse energy and molecule) but also means that it can be extended to 2D by forming the laser beam into a sheet of light and by detecting the ensuing fluorescence with a 2D detector. When LIF is implemented in a 2D fashion it is often referred to planar laser-induced fluorescence (PLIF), and is then highly spatially resolved along all three dimensions (down to 50 μm), i.e. it yields a cross section of the sought after species. The expression for the LIF signal S_{LIF} in the linear excitation regime is given by

$$S_{\mathrm{LIF}} = \eta_c E g f(T) \sigma_0 \chi_{\mathrm{abs}} \frac{P}{k_{\mathrm{B}} T} \phi. \quad (1)$$

where η_c is the experimental collection efficiency, E is the laser energy, g is a function that describes the spectral overlap between the laser and the absorption spectral lineshape, $f(T)$ is the Boltzmann fraction, σ_0 is the absorption cross section of the detected species, χ_{abs} is the molefraction of the detected species that together with $P/k_{\mathrm{B}}T$ gives the number density of the same species and ϕ is the fluorescence quantum yield. The fluorescence quantum yield represents the excited-state emission rates and the collisional interaction and energy transfer between the CO_2 and the carrier gas. The expression shows that the detected LIF signal is linearly dependent on the gas density and the fraction of molecules in the state from which the laser excites the molecule, $f(T)$. This implies that if the signal is carefully analyzed it can be calibrated into partial pressures. The signal is strongly dependent on the number density of molecules which is also taken into account in the analysis process. The number density of molecules N, can be described by

$$N = \frac{PV}{(k_{\mathrm{B}} T)} \quad (2)$$

where P is the total pressure, V is the volume, k_{B} the Boltzmann coefficient and T the temperature of the gas. This shows that the number density of molecules and thus the PLIF signal will decrease with the temperature. This is illustrated in figure 1. Figure 1(a) shows how the CO_2 PLIF signal 0.5 mm above an active sample changes as the temperature of the sample is ramped up. After the activation of the catalyst identified by a sudden 'jump' in the signal, the signal is expected to be constant but a significant decrease of the signal with the temperature is observed. The temperature dependency of the PLIF signal is illustrated in figure 1(b). The PLIF signal plotted is detected at a constant CO_2 molefraction and the decrease of the signal is only due to the increase in temperature, affecting both the number density and the population of the probed energy level, which follows the Boltzmann distribution. This temperature dependency is used to analyze the raw PLIF signal shown in figure 1(a) and the resulting corrected PLIF signal is shown in figure 1(c). In the present work we detect CO_2, CO and NH_3 during catalytic reactions, either as a reactant or a product. Each molecule requires a different experimental set-up due to differences in excitation energies and detection wavelengths. In table 1 we have summarized some of the parameters which needs to be taken into account for each molecule.

3. CO_2

In CO oxidation the product is CO_2. The CO_2 molecule lacks accessible transitions in the UV/visible spectral range, but can be reached through ro-vibrational transitions in the mid-infrared. There are several transitions that can be used in the mid-infrared, e.g. the overtone and combination band at around 2.0 μm ($12°1 \rightarrow 00°0$), the combination band at 2.7 μm ($00°0) \rightarrow (10°1$) [52] and the fundamental band at around 4.3 μm [53] (figure 2(a)). The overtone and combination band at around 2.0 μm is a weak transition compared to 2.7 and 4.3 μm, limiting the sensitivity. For the fundamental band at 4.3 μm, which was recently demonstrated, the high cross section becomes tricky in larger setups, since the laser beam is strongly attenuated in the ambient air. Owing to these reasons, the combination band at 2.7 μm was chosen in this study, it is stronger than the 2.0 μm band (around 45 times) but still weak enough so as not attenuate the laser radiation too much along the beam path. Throughout our experiments, a laser system operated at 10 Hz generated the IR-laser light by difference-frequency mixing the output from a dye laser (PRSC-D-18, Sirah) at 763 nm with the fundamental frequency from a Nd:YAG laser (PRO 290-10, Spectra Physics) at 1064 nm in a $LiNbO_3$ crystal. The resulting 2.7 μm laser beam had a pulse energy of 4 mJ, a pulse length of 5 ns and an estimated linewidth of 0.025 cm^{-1}. The 2.7 μm laser beam was formed into a laser sheet using sheet forming optics and was used to excite a ro-vibrational transition of the $(00°0) \rightarrow (10°1)$ of CO_2. The CO_2 fluorescence was detected by a LN_2 cooled, InSb focal plane array (Santa Barbara Focal Plane, SBF-134). Calibration measurements under similar conditions (pressure, flow, temperature and CO_2 partial pressures) as in the CO oxidation experiments but at known CO_2 partial pressures were carried out for converting the signal to partial pressures, a calibration curve at 150 mbar and room temperature is shown in figure 2(b)). Due to mostly re-absorption of the CO_2 fluorescence signal the curve bends downwards at around 10 mbar CO_2 partial pressure, however up to around 4 mbar the curve is close to linear. The CO partial pressure of the incoming gas is therefore kept well below 10 mbar when the PLIF signal should be calibrated to partial pressures. The bending of the calibration curve may result in higher noise level at higher CO_2 partial pressures. The calibration curve will change with both total pressure and temperature, however at 150 mbar and room temperature the detection limit of CO_2 with the present set-up is about 0.04 mbar, at the same pressure and at 300 °C the detection limit changes to about 0.1 mbar. The calibration

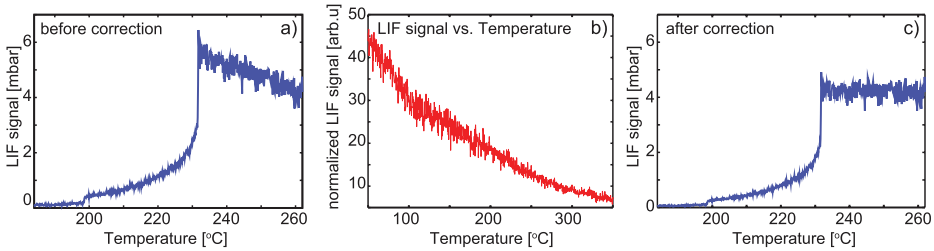

Figure 1. (a) The raw PLIF signal detected over a catalyst is plotted as a function of the catalyst temperature. (b) The PLIF signal decreases with $1/T$. (c) The raw data shown in (a) corrected for the decreasing number of gas molecules due to the temperature increase.

Table 1. Summary of the important experimental parameters used for the molecules investigated in the present manuscript.

Molecule	Spatial resolution (μm)	Temporal resolution (Hz)	Integration time	Excitation wavelength	Detection Wavelength
CO_2	70	10	20 μs	2.7 μm	4.26 μm
CO	300	10	30 ns	230.1 nm	450–660 nm
NH_3	100	10	100 ns	305 nm	565 nm

measurement allows for good estimation of the CO_2 partial pressure produced by the active catalyst but quenching as well as slight re-absorption of the fluorescence in the CO_2 gas between the interrogated region and the camera are not fully compensated for. This does not affect the signal significantly in the present measurements, since relatively low total pressures are used (<150 mbar). The CO_2 fluorescence signal at 4.3 μm is absorbed by the air between the cell and camera and to increase the signal, the path of the fluorescence light can be purged with a non adsorbing gas such as N_2.

3.1. Imaging CO_2

The CO_2 fluorescence, originating from the fundamental band at 4.26 μm, was imaged perpendicular to the laser sheet onto a 2D focal plane array (FPA) (SBF LP134, Santa Barbara Focal Plane) through an interference filter centered around 4.26 μm to discriminate background. To further discriminate the thermal background, an inherent difficulty when working in the mid-infrared regime, the FPA was triggered at 20 Hz, thus taking an extra image between every laser shot, making subtraction of the thermal background possible. The integration for each frame was 15 μs and chosen for efficient collection of the CO_2 fluorescence signal, which is more than 100 μs long at these pressures, while avoiding detector saturation by the thermal background. The temperature of the gas molecules are gradually decreasing with the distance from the sample and an image of the laser sheet at several temperatures was therefore taken. This allows for compensation of the temperature fluctuations in the CO_2 images as well as for steady inhomogeneities in the laser sheet. The CO_2 fluorescence images, with a spatial resolution of 70 μm along all three dimensions (limited by the thickness of the laser sheet), visualized the distribution of CO_2 in the reaction chamber. The experimental set-up is illustrated in figure 3(a). The laser beam was split up and about 10% of the light was led through a reference cell with a known CO_2 concentration. The fluorescence from the reference cell was then detected to compensate for shot-to-shot fluctuations and wavelength jitter. The global gas composition was measured with a mass spectrometer connected via a 70 cm long tube (diameter of 1/8″) at the outlet of the reactor and the temperature with a type D thermocouple connected to the sample holder.

3.2. Single crystals

Real catalysis is a complicated process, and to gain fundamental information on catalytic processes on the atomic scale to understand surface mediated reaction mechanisms, model systems are used. Single crystal surfaces are the most common model catalysts in surface science since they mimic the extended facets on a catalyst nano particle. It is well known that the surface gas interaction is essential for the surface atomic structure on the active catalyst surface. In contrast, the gas phase close to the surface of an active catalyst at semi-realistic conditions has not been studied in detail, and should reveal information about the actual gas composition interacting with the surface in the presence of the active catalyst. In figures 4(a) and (b) the CO_2 production over a Pd(1 0 0) single crystal is visualized using PLIF, in a gas mixture of 6 mbar CO, 6 mbar O_2 and 138 mbar Ar. At the start of the experiment, the temperature of the crystal is too low (<100 °C) and the catalyst not active, and as a result no CO_2 signal is detected with PLIF or with MS. As the temperature is increased (figure 4(d) a small increase in the CO_2 production is detected with PLIF (figure 4(c)) and MS (figure 4(d)), indicating a CO poisoned surface [20, 54], inhibiting the oxygen molecule to dissociate on the surface and enable an efficient reaction. The small increase of the CO_2 signal can be explained by a statistical increase of the CO desorption as the temperature is increasing, leaving free surface areas where O_2 can adsorb dissociatively and react. However at a temperature of approximately 270 °C

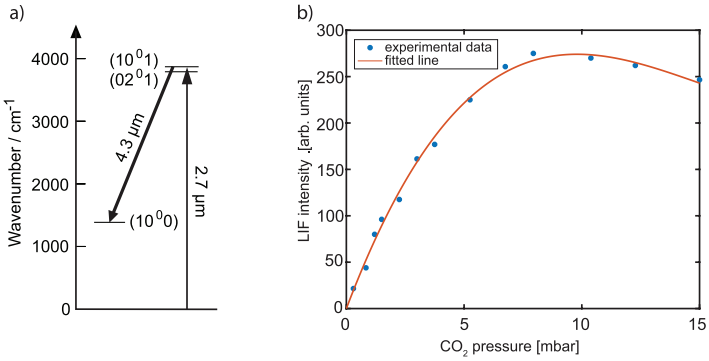

Figure 2. (a) CO_2 energy level diagram showing the excitation at 2.7 μm that generate fluorescence emissions at 4.3 μm that is detected to image the CO_2 distribution in the reactor. (b) Calibration curve measured at a total pressure of 150 mbar and room temperature.

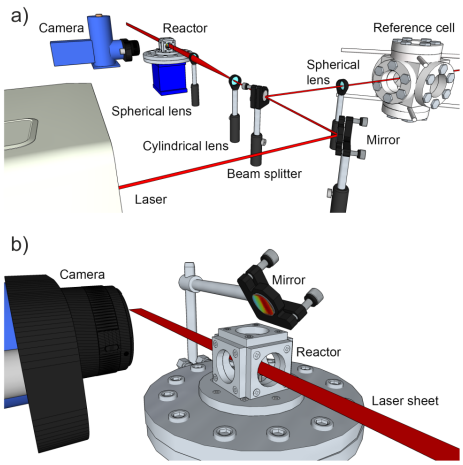

Figure 3. The PLIF experimental set-up. (a) The laser beam is shaped into a laser sheet with a cylindrical and spherical lens. The laser sheet can then interact with the CO_2 gas molecules in the chamber and by detecting the fluorescence light with a camera, an image of the CO_2 gas distribution is achieved. In this figure a reference cell is used with a constant gas pressure to calibrate for fluctuations in the fluorescence signal. (b) To generate the top view images, the laser sheet was rotated 90 °C to be horizontally oriented across the sample. A mirror positioned at the top of the chamber reflects the fluorescence onto the camera creating an image.

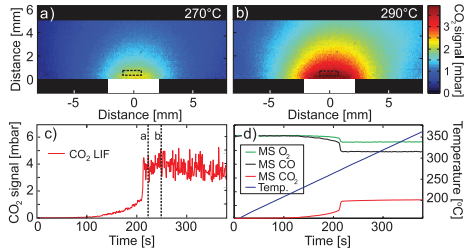

Figure 4. CO oxidation using Pd(1 0 0) as a catalyst. The PLIF images showing the CO_2 distribution over the surface at two different temperatures 270 °C (at light-off) (a) and 290 °C (b), respectively. (c) PLIF CO_2 signal extracted from the black rectangle shown in (a). (d) The MS signal measured at the outlet of the reactor together with the temperature of the sample (see also supplementary movie 1 (stacks.iop.org/JPhysCM/28/453002/mmedia)).

the CO_2 production increases tremendously, demonstrating that light-off has occurred. This means that the CO coverage is low enough, and the O coverage high enough, for the rate of CO removal (through desorption and reaction) to be higher than the adsorption rate. The result is a sudden lifting of the CO poisoning and an activation of the catalyst. After the light-off, the sample is highly active and a saturation of the CO_2 signal is reached. The images of the CO_2 in figures 4(a) and (b) show a cloud of CO_2 close to the surface with a gradually decreasing CO_2 concentration with the distance from the surface. The CO_2 cloud can be observed at temperatures below light-off, but becomes significantly more visible after light-off. After light-off, the temperature is increased further but the CO_2 production is unchanged indicating that the reaction has reached a mass transfer limited (MTL) regime. In this regime the process is limited by the CO diffusion to the surface and not by the intrinsic activity of the sample. The detected cloud of CO_2 is often referred to as the boundary layer of CO_2 that hinders the CO molecules to reach the surface [36, 37]. At the conditions applied in the experiment shown in figure 4 the CO_2 concentration is significantly higher in a sphere with the radius of approximately 5 mm around the surface. This implies that the gas composition is significantly different within this sphere as compared to the gas inlet or outlet where the partial pressures of the gases present in the chamber is measured. The difference becomes apparent by comparing the partial pressure of CO_2 measured by PLIF just above the surface (black rectangle in figure 4(a)) and the MS sampling the gas at the outlet of the reactor. The result is shown in figures 4(c) and (d) where a maximum of 4 mbar CO_2 is detected by PLIF (figure

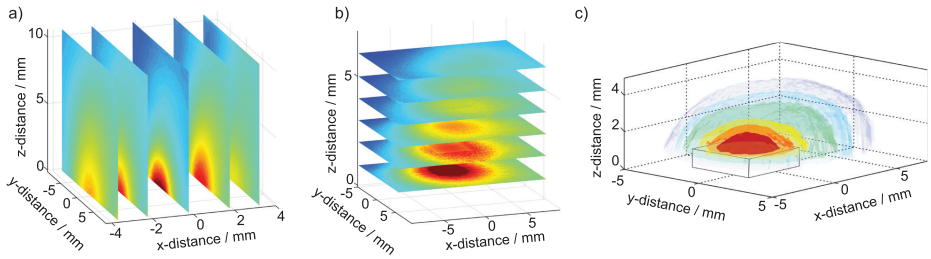

Figure 5. Producing 3D images of the CO_2 gas phase in MTL regime by (a) slicing perpendicular to the surface (b) slicing parallel to the surface (c) The resulting 3D reconstruction of the CO_2 sphere.

4(c)) and the corresponding number measured with MS is 1.5 mbar (figure 4(d)). The PLIF results highlight the necessity of studying the gas phase composition close to the active surface when a reaction experiment under semi-realistic conditions is performed.

3.3. 3D mapping of the gas phase

Two different experimental set-up geometries for excitation and detection were utilized in this study, one where the laser sheet was vertical and the fluorescence light was imaged through the side window, the other with the laser sheet incident in a horizontal fashion, and the fluorescence light collected through the top window, reflected on a mirror positioned as close as possible to the window and again imaged onto the FPA (figure 3(b)). Both geometries used the same optics (a spherical lens with $f = +200$ mm and a cylindrical lens with $f = -40$ mm), the only difference being that the cylindrical lens was rotated 90°. The possibility of imaging the gas phase from two directions permits to construct a 3D image of the CO_2 gas cloud that surrounds the surface when the sample is highly active and in the MTL regime. In this regime the CO_2 production reach a steady state and do not change significantly in time or with temperature. Several PLIF images can therefore be recorded at this steady state regime without a significant change in the gas distribution over the surface. By moving the laser sheet 1 mm for each image in the vertical (figure 5(a)) and subsequently in the horizontal direction (figure 5(b)), it is possible to generate a 3D representation of the CO_2 cloud surrounding the catalyst surface, see figure 5(c). The 3D image visualize the CO_2 gas close to the surface and it is evident that in a cubical shaped reactor as used in this experiment, the CO_2 concentration is gradually decreasing with the radius from the center of the surface resulting in CO_2 sphere surrounding the surface. The 3D images also reveal a small asymmetry in the fringe of the gas sphere which is a result of the gas flow going from left to right in the figure.

3.4. Self-sustained reaction oscillations

Self-sustained reaction oscillations have been observed in catalytic reactions for many years [55, 56]. Surprisingly, the oscillations in the reactivity appears to occur under fixed temperature and flow conditions and are therefore termed 'self-sustained'. In the case of CO oxidation, the oscillation has also been correlated to the simultaneous changes in the surface roughness, and as a consequence the number of steps on the surface [15].

To study the oscillation during CO oxidation, a technique which allows for *in situ* measurement in semi-realistic conditions is required. As demonstrated above, the gas phase is highly important for experiments carried out at semi-realistic conditions. We have visualized the oscillating CO_2 production over a Pd(1 0 0) single crystal during CO oxidation from both side and top view. The experiments were performed in a constant oxygen rich gas mixture of 4 ml_n min^{-1} CO, 80 ml_n min^{-1} O_2 and 16 ml_n min^{-1} Ar (ml_n min^{-1}—where n refers to 0 °C and atmospheric pressure) at a total pressure of 150 mbar at a temperature of 240 °C. In an image sequence of 1200 s, as shown in figure 6, the CO_2 production drops and rises twice, demonstrating that the sample is switching between high and low activity. This occurs in steady state conditions and the switching displays a periodic oscillating pattern. The PLIF images in figures 6(a) and (d) show the CO_2 distribution over a low active sample, and the images clearly show that the CO_2 production do not drop to zero but the activity of the sample is lower in this part. The rate of CO conversion is increasing with time in the low active part of the oscillations which is more clear when the PLIF trend is plotted in figure 6(g). The PLIF trend is extracted just above the surface and the partial pressure of CO_2 above the sample increase from approximately 1.5–2.3 mbar in the low activity part. The behavior is similar to the CO poisoned situation described above before light-off, with the difference that the temperature is not observed to be increasing. Figures 6(b) and (e) show the light-off where the catalyst switch to the highly active phase, indicating that CO desorbs from the surface allowing O_2 to dissociate on the surface. As described above, this leads to an increased activity and the sphere of CO_2 is already observed around the surface before the light-off, but is even more pronounced in figures 6(c) and (f) in which the CO_2 distribution in the highly active phase is shown. In the highly active phase the sphere of CO_2 indicates that the sample is in the MTL regime as discussed above. The PLIF trend also shows an almost 100% CO conversion which support the interpretation that the reaction is in MTL by the CO diffusion. The oscillations could also be detected with the MS (figure 6(h)) and the temperature variation of the sample surface (figure 6(i)) of around 5 °C

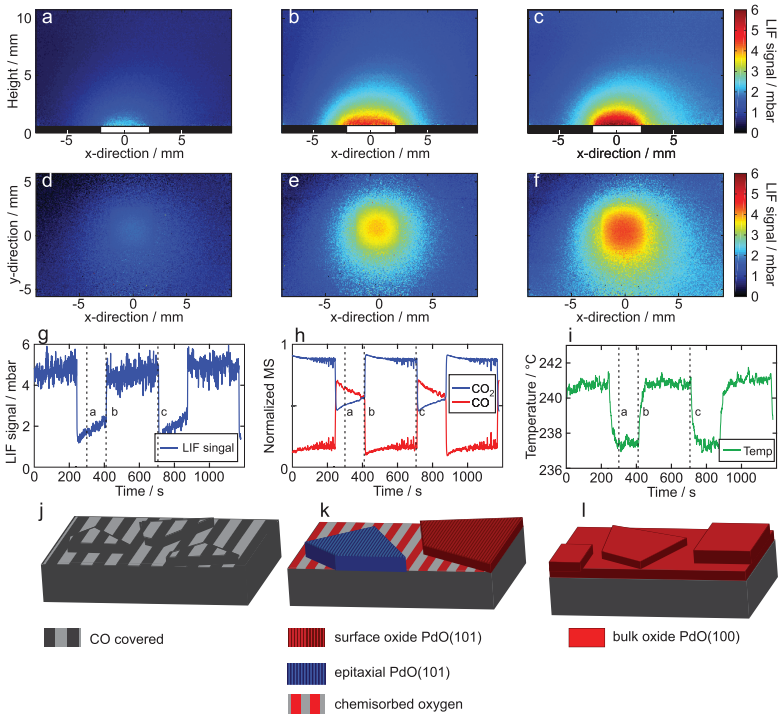

Figure 6. Self sustained reaction oscillations over Pd(1 0 0) side view and top view (see also supplementary movie 2 and supplementary movie 3) (a) and (d) very low activity (b) and (e) at light-off (c) and (f) very high activity and in mass transfer limited regime. (g) The PLIF trend as detected just above the samples. a–c indicates the corresponding PLIF images. (h) The MS signal. a–c indicates the corresponding PLIF images. (i) IR-camera recording of the sample temperature. a–c indicates the corresponding PLIF images. (j)–(l) Possible mechanism behind the oscillations. (j) CO binds to the metallic surface, especially at steps, poisoning the catalytic reaction. With time the surface becomes flatter and the poisoning effect is reduced until the reaction lights-off. (k) At light-off, almost all CO close to the surface is removed, and the surface is exposed to an oxidizing environment resulting in chemisorbed oxygen or a surface oxide on the surface. (l) In the mass transfer limited state, the surface continue to form a thicker oxide, which becomes inactive with the formation of the most stable PdO surface, the PdO(1 0 0). With the lower activity, the CO concentration near the surface increases, which reduces the oxide and leaves the surface in a CO poisoned metallic phase with a large density of steps, and the process starts over.

of the sample surface between the low and high activity was observed due to the exothermal CO oxidation reaction.

Although we have no information on the surface composition, we may speculate on how the nature of the surface may contribute to the self-sustained reaction oscillations. The low activity phase is similar to that observed above, associated with a CO poisoned phase on which the reaction follows the Langmuir-Hinshelwood kinetics (see figure 6(j)). In contrast to the example above, however, the temperature is in this case essentially constant and another mechanism is needed in order to explain the switch to high activity. In accordance with ref [15], we believe that the surface starts in a relatively rough state, with lots of steps. These bind CO harder than flat areas. With time, however, the surface becomes flatter, the CO bonds becomes weaker, and the CO coverage decreases. This leads to more adsorbed oxygen and an increased activity. At a critical point, the activity is high enough for all the adsorbed CO to react to CO_2 and we reach light-off. Clearly, in the vicinity of the surface the gas phase is at this point significantly more oxidizing than prior to light-off. Under such conditions a PdO(1 0 1) surface oxide and even an epitaxial PdO(1 0 1) thin film [21, 22, 57] may form. These are all surface structures which are regarded to be beneficial for the CO oxidation reaction, also in UHV conditions [58–60]. The PdO(1 0 1) surface contain undercoordinated Pd atoms necessary for CO adsorption. However, as time progress, the oxide grows thicker due to the oxidizing gas phase, and may eventually break up and transform into small crystallites with PdO(1 0 0) figure 6(l), the most stable PdO surface [61]. The reaction rate immediately switches to the low-activity regime, the sample temperature decrease, and the increased CO concentration near the surface leads to a reduction of PdO(1 0 0) via defects. More metal surface is exposed, which now is covered by CO, in particular at steps and the oscillating cycle repeats. The novelty in

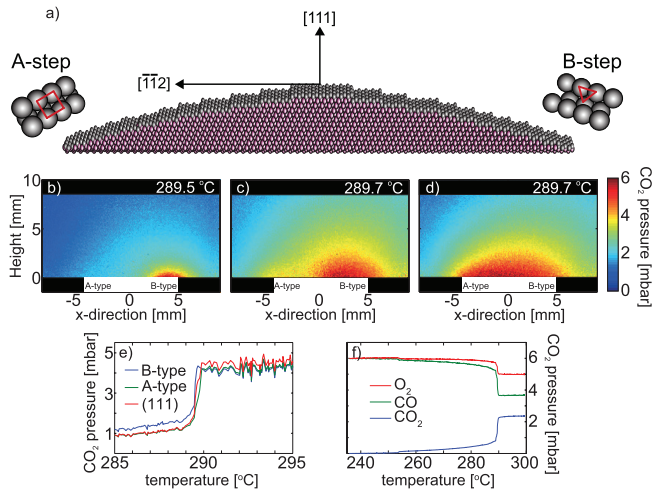

Figure 7. CO oxidation over a curved Pd(1 1 1) crystal (a) Schematic model of the cylindrical shaped Pd(1 1 1) crystal where the orientation of the A- and B-type steps are illustrated. (b)–(d) PLIF images of the light-off of the B-type step side at 289.5 °C and the A- type side at 289.7 °C. (e) PLIF trend extracted 0.5 mm from the surface on each side as well as the top of the crystal. (f) The MS signals showing the gas composition at the outlet of the reactor.

this model lies in the change from an active oxide surface (the PdO(1 0 1)) to an inactive oxide surface PdO(1 0 0). Obviously more measurements are needed to confirm the model, and the difficulties lies in observing a change in a surface structure sensitive signal from small nano-crystallites as the surface switches between active PdO(1 0 1) to inactive PdO(1 0 0).

3.5. Curved crystal

As briefly discussed above in the context of the PdO(1 0 1), under-coordinated sites have been considered to be essential for the reactivity and activity in a number of catalytic reactions [62–64]. Vicinal surfaces have, because of the high step density, been studied intensively to increase the knowledge about the role of under-coordinated sites and steps in chemical reactions [23, 27, 65–72]. On surfaces vicinal to the (1 1 1) the orientation of the steps can be either A-type ((1 1 1) oriented) or B-type ((1 0 0) oriented), and since the step-atoms have different coordination numbers, a difference in the reactivity has been observed [73, 74]. However, a direct comparison of the differences between different step orientations during a catalytic reaction at semi-realistic conditions have not been performed previously due to the limited number of techniques that fulfill the requirements needed to perform such experiments. PLIF hold the spatial and temporal resolution required to make an *in situ* comparison study during a catalytic reaction. In order to compare the different step orientations, we have studied CO oxidation over a cylindrical shaped Pd(1 1 1) crystal using PLIF. The cylindrical shaped crystal [75–77] expose A- and B type steps, respectively, see figure 7(a). In a gas mixture of 6 mbar CO, 6 mbar O_2 and 138 mbar Ar when the temperature of the crystal is slowly ramped, the PLIF images reveal that the B-type step have a lower light-off temperature than the A-type step. The PLIF images in figures 7(b)–(d) show the light-off of the two sides respectively. The temperature difference of the light-offs is extremely narrow but by looking at the CO_2 images it is evident that the B-type has the lowest light-off temperature. We also used the advantage of the possibility to extract data locally 0.5 mm above each side and the top of the crystal and the CO_2 trends are plotted in figure 7(e). The plotted trends only show a temperature range of 10 °C corresponding to the light-off sequence of the three different parts of the crystal. The trends clearly show that the reaction is in the MTL regime after light-off but the visualization of the CO_2 distribution over the crystal is a great advantage when the light-off should be determined. The lack of spatial resolution with MS makes it impossible to distinguish from where on the surface the CO_2 originates (figure 7(f)). This is an example illustrating the advantage with the spatial resolution of the gas phase.

As discussed above, the light-off temperature depends on the CO desorption temperature, allowing for oxygen dissociation on the surface. Therefore, it is surprising to find that the stepped parts of the curved crystal has a lower light-off temperature than the extended (1 1 1) surface at the center, since the CO binding would be expected to be stronger at the steps than at the (1 1 1) terraces, and thus a higher desorption temperature. At least, similar light-off temperatures could be expected, since the desorption temperature from the extended (1 1 1) is expected to be similar to the (1 1 1) micro terraces between steps (figure 8(a)). To explain the experimental observations, we rely on Density Functional Theory (DFT) calculations. It is known that the (1 1 1) Pd surface is under tensile stress, and the DFT calculations shows that the (1 1 1) micro

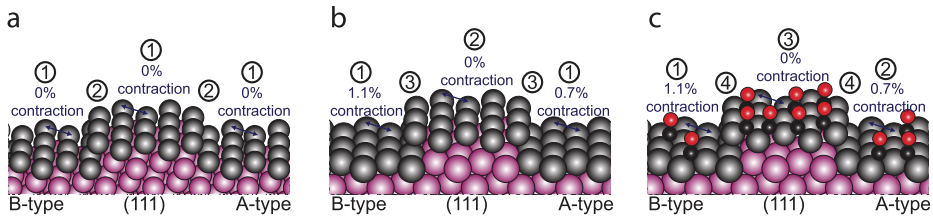

Figure 8. Schematic models of the cylindrical shaped Pd(1 1 1) crystal illustrating the light-off of the reaction according to theory in three situations. The numbers, one to four, indicate the light-off where one is the lowest light-off temperature. (a) An unrelaxed surface should generate the same light-off temperature for terraces on both sides as well at the top of the crystal. The steps is expected to have a slightly higher light-off temperature thus, the extended (1 1 1) terrace at the top of the crystal should have a lower light-off temperature than the steps. (b) Both the A- and B- type steps generate a relaxed surface which lower the light-off temperature at the terraces. (c) The CO coverage of the relaxed surfaces will affect the desorption temperature differently on the A- and B-type steps respectively, which explains the lower light-off temperature on the B-type side of the crystal.

terraces on (2 2 3) and (5 5 3) surfaces may relax the stress by decreasing the in-plane lattice constant slightly. This relaxation does not occur on extended (1 1 1) terraces in the absence of steps. Surprisingly, the difference in relaxation capabilities on extended and micro (1 1 1) terraces affects the CO desorption temperature, explaining why the stepped parts of the curved crystals have a lower light-off temperature. However, this would result in that the stepped parts of the curved crystal would have the same light-off temperature, both lower than on the extended (1 1 1) surface (figure 8(b)). This is not observed experimentally, since we find that the part of the curved crystal with B-type steps (e.g. (5 5 3)-oriented facet) has a lower light-off temperature than the part with A-type steps (e.g. (2 2 3)-oriented facet). To explain this discrepancy, the DFT calculations indicate that the B-type side has a stronger CO adsorption energy dependence than the A-type step. At 0.6 ML the CO differential adsorption energy is 1.13 eV for the A-type side while 1.01 eV for the B-type side. Assuming a linear coverage dependence of the differential adsorption energy the repulsion between the adsorbed CO molecules destabilize the CO layer faster on the (5 5 3) than on the (2 2 3) surfaces. This explains why the light-off is lower for the (5 5 3) surface, (figure 8(c)).

The conceptual implications of the above described model are significant for the understanding of catalytic CO oxidation and other oxidation reactions using nano particles. It is already known that the reactivity, for instance in dissociation processes [62, 78], is higher at steps or the corresponding edges between terraces on a nano particle. However, in the case of CO oxidation the O_2 dissociation will not happen unless the CO has desorbed, and the desorption temperature will depend on the ability of the nano particle terrace to relax, which in turn depends on the size of the nano particle facet.

3.6. Two powder samples simultaneously

To further demonstrate the spatial resolution and illustrate the versatility of PLIF, figure 9 shows the CO_2 distribution over two powder catalyst samples, measured simultaneously in 18 ml_n min^{-1} CO, 18 ml_n min^{-1} O_2, and 36 ml_n min^{-1} Ar at a total pressure of 105 mbar. The samples consist of 2%Pd/CeO_2 (hereafter called the Pd-sample) and 2%Pt1%Pd/CeO_2 (hereafter called the Pt-Pd-sample) pressed powder pellets which are placed 8 mm apart from each other in the reactor. The temperature of the samples are ramped up and down and the PLIF images show that it is possible to distinguish the CO_2 distribution around each sample. In the beginning of the experiment (figure 9(a)) none of the samples show any notable CO conversion. At a temperature of 170 °C (figure 9(b)) the light-off of the Pd-sample is observed, resulting in the formation of a CO_2 cloud around that sample. As the temperature is further increased, the Pt-Pd sample is observed to become active at about 220 °C (figure 9(c)) and a much larger total cloud of CO_2 is now visible. However, the spatial resolution of the experimental set-up is clearly high enough to spatially distinguish which of the two samples that becomes active first. At 250 °C (figure 9(d)), both samples are in the MTL regime indicated by the constant CO_2 production even though the temperature is increased further. When the temperature is decreasing, the Pt-Pd sample becomes inactive first (figure 9(e)) and soon followed by the extinction of the Pd-sample (figure 9(f)). The ignition/extinction events for both samples give rise to the corresponding signatures in the PLIF trend, MS signal and temperature data (figures 9(g)–(i)). Obviously the MS signal does not distinguish which catalyst activates first. The PLIF trend, extracted in the area marked with a rectangle over each sample in figure 9(a), clearly show that the Pd sample is highly active in a wider temperature range compared to the Pt-Pd sample. However, the trends also show a gaseous cross-talk between the two catalysts that result in a different gas composition over the Pt-Pd sample, which can have an influence on the light-off temperatures or influencing activation energies extracted from the data. The gaseous cross-talk between the samples demonstrated here with PLIF should be taken into account when performing experiments with several samples in the reactor simultaneously. This experiment shows the potential of having 2D, spatially resolved, non-intrusive measurements of the gas distribution, opening up for simultaneous characterization of more than one sample at a time and direct *in situ* comparisons. The approach could be beneficial e.g. when studying systems where more than one active

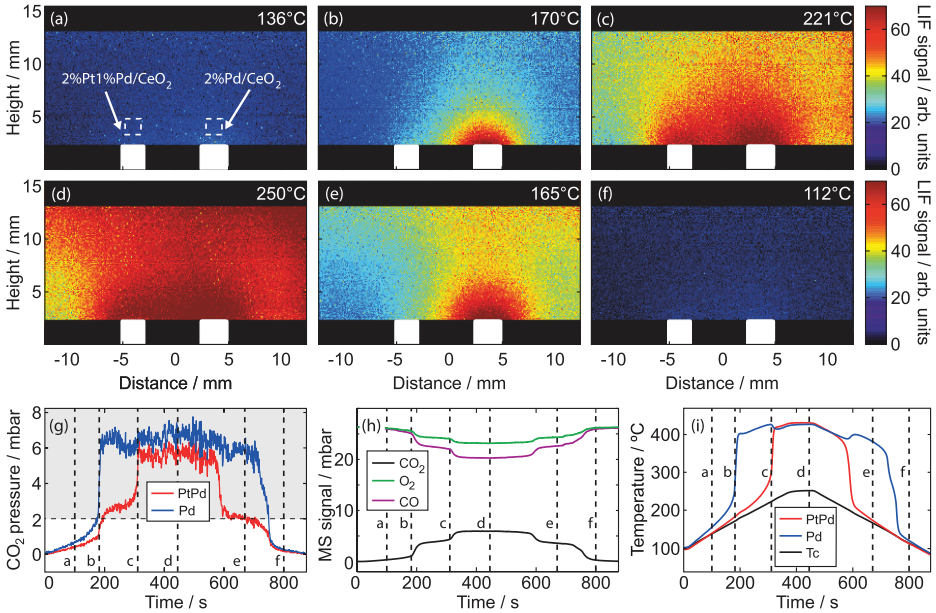

Figure 9. The CO_2 distribution over two samples simultaneously, (a)–(f), IR PLIF single-shot images during the reaction showing the CO_2 distribution over a Pt-Pd sample and Pd powder catalyst surfaces at different times and temperatures and at 105 mbar of total pressure. (g) The fluorescence signal 0.7 mm above each sample (red and blue). (h) The MS signal. (i) The temperature of the sample surfaces (red and blue) measured by an IR camera together with the temperature of the sample holder, measured by a thermocouple (Tc) (see also supplementary movie 4).

catalyst is needed to drive different reactions, and how the presence of one catalyst affects the other.

3.7. Three exhaust tubes

Because of the possible interaction of the samples as demonstrated above, we designed a reactor where the samples are separated in three glass tubes to avoid gaseous cross-talk. This could be important if the activity of several samples should be evaluated in a correct way. If several samples can be studied simultaneously and by a direct comparison determine the most active catalyst or the catalyst with the lowest activation/light-off temperature, it could be of interest to catalyst production industry. In the experiment shown in figure 10 we probe the CO_2 production originating from three separate samples simultaneously, and in parallel, by placing the samples into three separated flow tubes. The tubes end inside the middle of the vacuum chamber where the laser sheet was placed as close as possible (<1 mm) to the exits of the tubes, see (figure 10(a)). In this way the gas originating from each individual tube could be probed simultaneously by the laser. Three different catalysts were placed in the tubes, each containing Pd/CeO_2, Pt/CeO_2 and Pt/Al_2O_3, respectively. The experiment was performed in a 1:1 ratio of CO and O_2 at a total pressure of 1 bar which is approximately ten times higher total pressure than in the experiment described in section 3.6. This addresses the possibility of performing experiments in a wide pressure range using PLIF. PLIF, MS and temperature of the samples, measured by a thermocouple, was monitored while the temperature of the samples were increased. At temperatures below 70 °C no PLIF signal was visible indicating that all samples are inactive. A temperatures above 170 °C the tube with the Pd/CeO_2 sample show a CO_2 signal (figure 10(b)) indication catalytic activity. At 100 °C higher temperature the Pt/CeO_2 sample (figure 10(c)) becomes active as evidenced by the detection a CO_2 production from the corresponding tube. The Pt/Al_2O_3 clearly shows the highest activation temperature of 345 °C (figure 10(d)). In this set-up it is also clear that the low flow is directed towards the bottom of the reactor where the outlet is situated, making the detected signal appearing to be not centered in the tubes. The MS signal, as discussed in the experiments shown above, is not able to distinguish from which sample the CO_2 signal is originating from (figure 10(e)). The individual CO_2 PLIF trends that can be extracted from each of the samples (figure 10(f)) provides the opportunity to extract quantitative data for the individual catalysts. Three Arrhenius plots (figure 10(g)) can be produced by combining the temperature data and the reaction rate. Activation energy of 0.25 eV, 0.53 eV and 1.05 eV are found for the Pd/CeO_2, Pt/CeO_2 and Pt/Al_2O_3 samples, in good agreement with values reported in the literature [79, 80]. To extract the activation energy using the MS is more

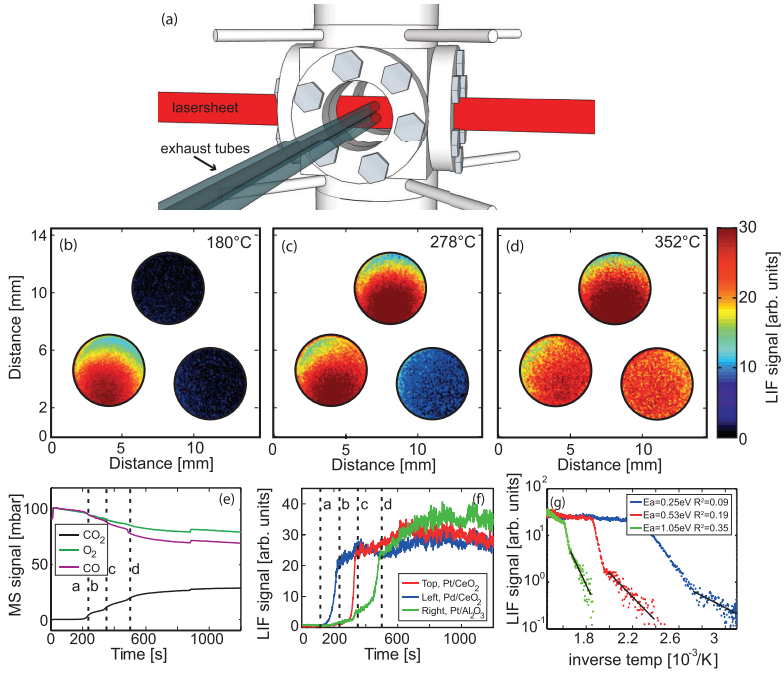

Figure 10. The CO_2 signal from three different samples in three separate exhaust tubes. (a) A schematic illustration of the experimental set-up. (b)–(d) The CO_2 signal from the gas exiting the three tube ends are shown in the top panel. e) shows the MS signal during the experiment and (f) shows the averaged PLIF signal exiting each tube, and the corresponding three Arrhenius plots are shown in (g) (see also supplementary movie 5).

complicated due to the overlapping CO_2 MS signals inhibiting the extraction of the individual reaction rates for each of the three catalysts.

3.8. CO_2 hydrogenation

PLIF can also be used to visualize the consumption of CO_2 when CO_2 is used as a reactant in a chemical reaction. Figure 11 shows the hydrogenation of CO_2 which also demonstrate that PLIF is a powerful technique when small changes in the gas composition should be detected. In the experiment 1% CO_2, 5% H_2 and 94% Ar is used with a total flow of 200 ml_n min^{-1} and a total pressure of 300 mbar resulting in a maximum CO_2 partial pressure of 3 mbar when the experiment start. The sample used in the experiment was a pressed powder pellet that consists of 3% Rh supported by CeO_2. At the time when the temperature is 100 °C no activity of the Rh/CeO_2 catalyst can be observed with PLIF (figure 11(a)) or with MS. As the temperature is increased the catalyst start to consume CO_2 and at 400 °C the lack of signal in the PLIF image is clear (figure 11(b)). The depletion of CO_2 is significant close to the surface and the CO_2 concentration is increasing with the distance from the surface. This shows that also for this reaction, the gas phase close to the surface has a different

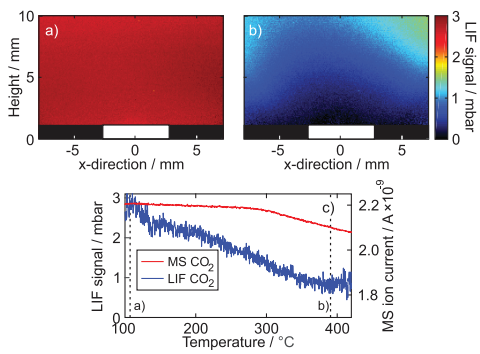

Figure 11. CO_2 hydrogenation over a Rh catalyst. a() CO_2 PLIF image with an inactive sample. (b) CO_2 PLIF image over a highly active sample. (c) The PLIF trend and CO_2 MS signal plotted against the temperature of the sample. The dashed lines indicate the corresponding PLIF image taken at this temperature during the reaction. The PLIF trend shows that the partial pressure of CO_2 just above the surface decrease from 3 mbar to below 1 mbar.

gas composition within a region similar as for the CO oxidation as was shown above. The CO_2 hydrogenation reaction is

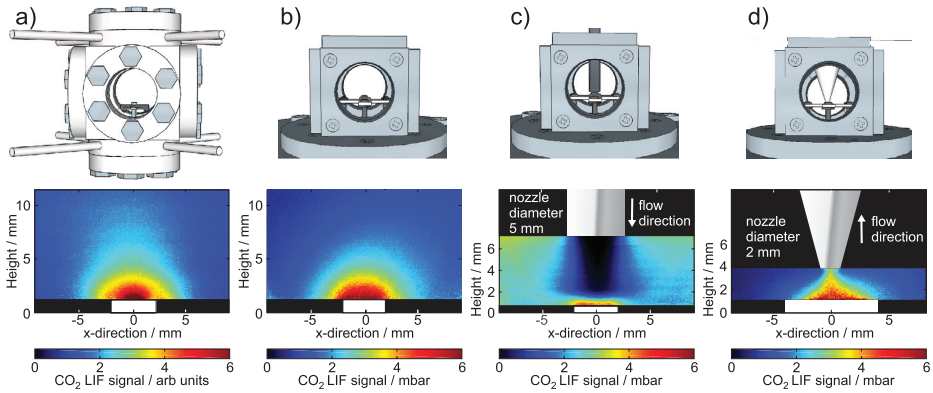

Figure 12. CO_2 gas distribution in the MTL regime in two different reactors and for three different flow configurations, (a) a 240 ml reactor flowing 45 mbar each of CO and O_2 in 90 mbar of Ar with a total pressure of 180 mbar (total flow of 72 ml_n min^{-1}), (b) a 23 ml reactor flowing 6 mbar each of CO and O_2 in 138 mbar of Ar (total flow of 100 ml_n min^{-1}), (c) a 23 ml reactor with a stagnation flow configuration flowing 6 mbar each of CO and O_2 in 138 mbar of Ar (total flow of 100 ml_n min^{-1}), (d) a 23 ml reactor where the outlet is pumped through a 2 mm in diameter cone simulating an APXPS analyzer nozzle and flowing 6 mbar each of CO and O_2 in 138 mbar of Ar (total flow of 100 ml_n min^{-1}).

not as efficient as the CO oxidation but the images demonstrate that a cloud with a different gas composition appears close to the surface in this reaction as well. The CO_2 partial pressure close to the surface can be analyzed in more detail and the PLIF signal extracted just above the surface is plotted together with the MS CO_2 signal in figure 11(c)). The PLIF trend shows that the partial pressure of CO_2 decrease to below 1 mbar, indicating that the catalyst is active in consuming CO_2 in a CO_2 hydrogenation reaction. Further, the CO_2 MS signal is decreasing insignificantly, since only the CO_2 signal far from the active sample is detected. Concerning the reaction products, several species could be formed, such as methanol and methane. In the present set-up none of the products could be detected by the MS at the outlet. Experiments in which the product is probed by PLIF is planned for the future since PLIF could distinguish between different product species and could contribute to novel information on activity and selectivity for the CO_2 hydrogenation using different catalysts.

3.9. Using PLIF for studies of the gas distribution in model reactors

The gas molecules interacting with the surface play an important role for the catalytic activity of the surface and it is therefore of great interest to increase the knowledge about the gas phase in the vicinity to the catalyst surface [81]. We have studied the CO oxidation reaction in four different set-ups where the design of the reactors are similar to the ones used when single crystals are studied as model catalysts. These reactors have a geometry that results in a gas flow around the sample and not through it, as opposed to when a powder catalyst is investigated in a fixed-bed reactor. The results do not reveal the optimal experimental reactor but our studies clearly demonstrate that the gas composition in the reactor is truly dependent on the flow and the geometry of the reactor. The results may also act as a guidance when new reactors are developed. In figure 12 images of the CO_2 distribution when the reaction is mass transfer limited by CO, from all four reactors are shown. The images of the CO_2 gas phase show that the gas composition is significantly different locally above the catalyst surface as compared to the rest of the chamber. The reactor in figures 12(a) and (b) have a cubical shape with a volume of 240 ml and 23 ml, respectively. Both reactors have a gas- inlet and outlet positioned far away from the sample surface where the mass spectrometer is measuring the global composition in the reactor. The images show a similar CO_2 distribution in both reactors with a spherical shaped cloud around the surface with a decreasing gradient of CO_2 with the radius of the sphere. Figure 12(c) shows a stagnation flow set-up which flattens the sphere of CO_2. This is because the tube positioned approximately 5 mm above the surface is used as a the gas inlet with a gas flow of 100 ml_n min^{-1}. The opposite is detected in figure 12(d) when a cone positioned 2 mm from the surface is used as the gas outlet. The images show that the CO_2 molecules is flowing through the cone which reshape the sphere significantly. This set-up mimic the flow in a NAPXPS set-up when the nozzle to the XPS analyzer is positioned only a couple of mm from the surface. In NAPXPS experiments, and all other *in situ* techniques that allows for higher pressure investigation, the most interesting, from a surface science point of view, is the gas molecules interacting with the surface. The high temporal resolution (for each image) as well as high frequency of the images allows for an immediately detection of small changes in the gas phase interacting with the catalyst surface. This information is not easily achieved with other gas phase detecting techniques such as MS, which is often located at the outlet of the chamber and thereby measure the global gas composition in the chamber and not locally over the sample. Capillary MS can be used to measure locally over the surface but a probe might disturb the flow in the chamber.

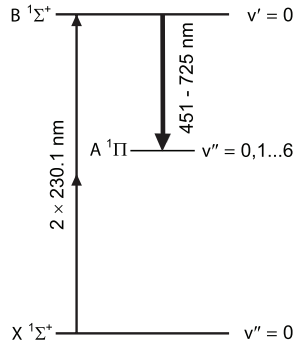

Figure 13. CO energy level diagram. By using a two-photon excitation process with a wavelength of 230 nm the $X^1\sum^+(0,0) \rightarrow B^1\sum^+$ transition can be accessed and the fluorescence is detected in the 450–660 nm range as the molecule relax.

From the images of the different set-ups we can conclude that in the MTL regime of CO oxidation the CO_2 concentration closest to the surface is similar for all set-ups but the shape of the boundary layer formed is dependent on the flow, pressure and geometry of the chamber.

4. CO

CO is one of the reactants together with O_2 in the CO oxidation reaction. To probe CO, an electronic transition in the vacuum ultraviolet region needs to be reached. The absorption in the ambient air induces a strong attenuation of the laser beam at these wavelengths. To overcome this problem, a two-photon excitation with a wavelength of 230 nm can be used to reach the $X^1\sum^+(0,0) \rightarrow B^1\sum^+$ transition. This is called the Hopfield–Birge band in the CO molecule. Fluorescence in the visible region with the wavelength between 450–660 nm is emitted when the molecule relaxes and the A state is populated as illustrated in figure 13. The two-photon process implies that the fluorescence signal shows a linear to quadratic laser power dependence instead of pure linear as described for the CO_2 signal shown above. In the experiment shown in here we used a picosecond laser system consisting of a mode-locked Nd:YAG laser (PL2143C, Ekspla) with external amplifier (APL70-1100, Ekspla). The Nd:YAG third harmonic at 355 nm pumps an Optical Parametric Generator (PG 401-P80-SH, Ekspla), tuned to 230 nm. The laser line width at 230 nm was specified to be 5 cm^{-1} with a pulse energy of typically 0.4 mJ. The repetition rate was 10 Hz and the 80 ps pulse duration provides high peak power, highly beneficial for the two-photon excitation process. The use of a picosecond laser together with the low partial pressure of CO used in the experiments shown in here, reduces the interference of stimulated emission which is considered to be negligible. Calibration measurements were carried out at known partial pressures and at 150 °C. A linear dependency was observed and together with laser pulse energy compensation, the signal in the images was calibrated into partial pressures.

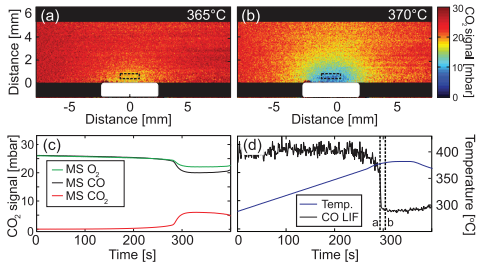

Figure 14. CO oxidation over Pd(1 1 0) probing CO with PLIF. (a) shows the 2D PLIF image as the reaction is igniting and (b) the 2D PLIF image at MTL. (c) shows the MS data of CO, O_2 and CO_2. (d) shows the temperature ramp (blue) and the PLIF CO signal extracted in the area indicated by the rectangle in (a) and (b) (see also supplementary movie 6).

4.1. Imaging CO

The CO fluorescence was imaged perpendicular to the laser sheet onto an ICCD camera (PIMAX 3, Princeton Instruments) using an $f = 50$ mm objective (Nikkor f/1.2) with a 36 mm extension tube mounted on the camera. Images were acquired at a 10 Hz repetition rate with the intensifier gate set to 30 ns. A long-pass filter (GG395, Schott) was used to suppress scattering and fluorescence from surfaces in the reactor. The laser sheet thickness was estimated to 300 μm, which also set the spatial resolution in the image. Laser sheet profiles were recorded at different temperatures for compensation of the thermal gradient in the CO images as well as for steady inhomogeneity in the laser sheet.

4.2. CO oxidation

The work described so far has focused on detecting CO_2 during CO oxidation and the CO_2 gas phase has been imaged and studied in detail. To understand the gas phase interaction with the catalyst surface in a more complete picture, the CO gas phase has also been visualized during CO oxidation over a Pd catalyst. In figure 14 the CO gas phase was imaged while the Pd(1 1 0) single crystal was heated in a gas mixture of 1:1 ratio of CO and O_2. The partial pressures were 26.5 mbar, 26.5 mbar and 53 mbar for CO, O_2 and Ar, respectively, resulting in a total pressure of 106 mbar. At the start of the experiment the sample was inactive due to the lack of available sites for O_2 dissociation on a CO covered surface. As the temperature was linearly increased as shown in figure 14(d), the rate of the reaction was also increasing with the temperature. At 365 °C a drastic drop was detected in the CO concentration, which indicates the light-off of the reaction and the Pd crystal is highly active. As discussed previously, this occurs when CO desorbs from the surface leaving sites accessible for dissociation of O_2. Figure 14(a) shows the CO distribution over the surface at the light-off. A locally lower CO concentration in a

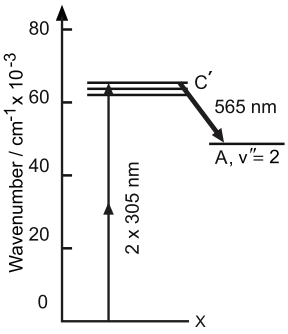

Figure 15. NH_3 energy level diagram. The $X \rightarrow C'$ can be reached by using a two-photon excitation process with a wavelength of 305 nm, and the fluorescence can be detected at 565 nm.

volume in the vicinity of the surface is observed immediately when the crystal switch to the highly active regime. The MS in figure 14(c) shows a global decrease of CO in the chamber and a simultaneous increase in the CO_2 signal confirms that CO is being oxidized. After the light-off the reaction is mass transfer limited by the CO and the CO image in figure 14(b) shows that the volume with significantly lower CO concentration close to the surface is larger than at light-off. The significant consumption of CO at the surface in the MTL regime results in a depletion region of CO locally over the surface. This volume has a similar spherical shape as the CO_2 cloud detected with PLIF in the CO oxidation reaction. The CO PLIF signal extracted in this region, indicated with a black rectangle in figures 14(a) and (b), shows that the CO signal drops 80% from the initial CO partial pressure which can be compared to a 20–30% decrease measured at the outlet with the MS. The CO measurements presented here show the expected opposite behavior with respect to CO_2 in terms of concentration, and also explains the lack of detectable gas phase CO in NAPXPS during MTL conditions [20, 41].

5. NH_3

As for CO, two-photon excitation is used to access the NH_3 molecule. The problem with strong absorption in air of single photon excitation in the vacuum ultraviolet regime, where electronic resonances of the NH_3 is probed, can be avoided by simultaneous absorption of two laser photons. The transition between $X \rightarrow C'$ can therefore be probed by two-photon at 305 nm, followed by population in the A state via fluorescence emissions band at 565 nm, illustrated in figure 15. To generate the 305 nm photons a combined Nd:YAG (Quanta-Ray PRO 250-10, Spectra Physics) and dye laser (Cobra Stretch-G-2400, Sirah) system operating at 10 Hz repetition rate and with 8 ns pulse duration was used. The fundamental wavelength of 610 nm was then frequency doubled to 305 nm using a BBO (beta barium borate) crystal which had a maximum output pulse energy of 35 mJ. A detailed description about the experimental set-up can be found in [82].

5.1. Imaging NH_3

The fluorescence at 565 nm was imaged with an intensified CCD camera (PI-MAX3, Princeton Instruments) with an $f = 50$ mm objective (Nikkor *f*/1.2) or an $f = 150$ mm UV lens (B. Halle *f*/2) was mounted on the camera. While continuous background was efficiently suppressed using CCD gates of 100 ns or less, scattered laser radiation was filtered using longpass filters (Schott).

5.2. Hydrogen assisted NH_3 oxidation above a Ag/Al_2O_3 powder catalyst

One important task in the exhaust cleaning of vehicles using diesel engines is the reduction of NO_x emissions in the exhaust gases. A three-way catalyst used to oxidize CO and hydrocarbons is not efficient to reduce the NO_x due to the oxygen rich conditions. However, several alternatives can be used to reduce the NO_x such as traps, hydrocarbon-assisted selective catalytic reduction (HC-SCR) and ammonia-assisted selective catalytic reduction (NH_3-SCR). In the NH_3-SCR process the NH_3 should ideally react with O_2 and NO to form N_2 and H_2O. It has also been shown that H_2 has a promoting effect on the low temperature activity when Ag particles supported by Al_2O_3 are used as the catalyst for the NH_3-SCR process. The role of the H_2 in the reaction mechanism is still under debate and several suggestions have been discussed in the literature such as influence of the chemical state of silver [83–85], removal of reaction inhibitors from the catalyst surface [84, 86] or partial oxidation of the reducing agent [85, 87]. In figure 16 we visualize the promoting effect of H_2 in the oxidation of NH_3 over a Ag/Al_2O_3 powder catalyst by probing the NH_3 with PLIF. In the experiment the temperature of the catalyst is kept to 160 °C and a constant flow of 3.6% NH_3, 90% O_2 with pulses 6%Ar or H_2 at a total pressure of 310 mbar. Figure 16(a) shows a homogenous NH_3 distribution in the image, indicating an inactive catalyst at these conditions. A more interesting result is achieved when H_2 is introduced in the reactor and the reaction and consumption of NH_3 is suddenly initiated. To keep the total pressure constant, the partial pressure of Ar is reduced when H_2 is pulsed into the reactor. The local reduction of NH_3 over the catalyst is clear in the PLIF image shown in figure 16(b). The depletion of NH_3 is significant close to the surface and the MS signals in figure 16(c) show simultaneously an increase of H_2O (green curve) and N_2 (red curve) in the reactor. Figure 16(c) also shows a temperature increase of the sample when H_2 is present in the reactor (pink regions) which is yet another indication of an active catalyst. Together with the MS and temperature the PLIF NH_3 signal is plotted and it is clear that the H_2 effect is reversible in the sense that the NH_3 signal increases again when H_2 is not present in the reactor. These H_2 switches can be repeated several times and the catalyst activity is similar each time.

6. Summary and outlook

In the present review we have shown that it is possible to image different gases in the close vicinity to an active catalyst by the use of PLIF. Recent development of laser and detector technology has enabled this capability. The experiments can be done

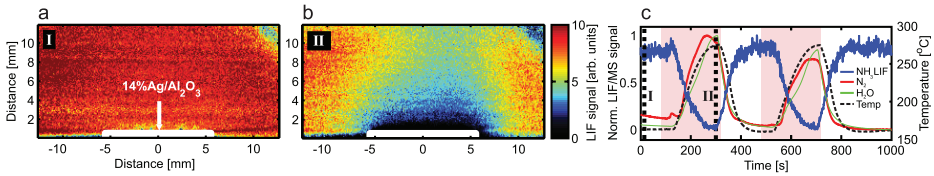

Figure 16. (a) NH_3 PLIF image above an inactive Ag/Al_2O_3 catalyst. (b) NH_3 distribution above the catalyst when H_2 is present in the reactor. The heavily reduced NH_3 area above the surface indicate the promoting effect of H_2 on the reaction. (c) The MS signal from masses representing N_2 and H_2O together with the temperature as well as the NH_3 PLIF signal is plotted. The pink regions represent when H_2 is present in the reactor (see also supplementary movie 7).

by the correct combination of lasers, detector and reactor set-up, and it is clear that a combination of expertise is needed for successful measurements. It is essential to combine expertise in laser based techniques with expertise in catalysis or catalytic surface science. By PLIF, the change of the 2D gas distribution can be observed on a timescale better than 0.4 s and with a spatial resolution of 0.1 mm. In this way we can visualize the ignition of the catalyst and the formation of a CO_2 cloud or boundary layer in the MTL region around the catalyst. We show that the CO_2 cloud may also be imaged in 3D by slicing the CO_2 cloud in sheets at different locations by the laser.

The present results were initiated by the need to visualize the gas phase in the proximity of an active CO oxidation catalyst, to demonstrate the change of the gas phase close to the catalyst surface. Such knowledge is needed if a meaningful structure/activity connection is to be made by other techniques available for *in situ* studies such as HPSTM, SXRD, PM-IRAS, and NAPXPS. At present there is a debate in the catalytic surface science community concerning the active phase of the late transition metals during CO oxidation, and the measurements presented here demonstrate a significant change in the gas composition which undoubtedly will affect the surface structure, making any structure/activity correlation less obvious. We illustrate the technique by imaging spontaneous reaction oscillations above a Pd(1 0 0) surface.

The spatial resolution of PLIF can be used in several different ways. In the present review, we show how different parts of a curved crystal have different ignition temperatures. An explanation is provided based on DFT calculations indicates different CO desorption temperatures at the (5 5 3), (2 2 3) and (1 1 1) parts of the curved crystal, due to differences in the ability to relax in plane stress and differences in CO coverage. We also show that in the present set-up it is straight forward to differentiate between completely different catalysts placed simultaneously in the same reactor, simply by observing their ignition temperature. By designing a special set-up consisting of tubes, it is possible to reduce gaseous cross talk between catalysts, making individual concentration determinations possible.

During the years that we have developed PLIF for catalysis, we have realized that the method is useful to visualize differences in gas flows for different reactors. In particular we illustrate how the CO_2 gas distribution changes when using a cubic reactor, a stagnation flow reactor and a reactor mimicking the more complex NAPXPS reactor.

By choosing the right laser and detector system, gases other than CO_2 can in a straightforward manner be visualized. We show this by imaging CO during a CO oxidation reaction and by imaging NH_3 in the SCR of NOx by a silver based catalyst. Therefore, it is clear that a large number of molecules can be imaged during catalytic reactions, much of the know-how already exist in the laser using combustion community.

The present review underlines the potential capacity of PLIF as a technique to visualize catalytic reaction with high spatial and time resolution. However, no information about the chemical or structural composition at the surface is available by PLIF. Therefore, combining other *in situ* techniques such as PM-IRAS and SXRD with PLIF is an attractive future direction. This approach could yield simultaneous surface structural and gas distribution information, in particular with spatial information.

Since PLIF is sensitive only to the gas phase, it should be interesting to study catalytic reactions which not only depends on the catalytic surface, but also on reactions in the gas phase by radicals. One reaction in which CH_3 (methyl) radicals are believed to take part by gas phase reactions is the oxidative coupling of methane. Here methane and oxygen are transformed into ethane or ethene/ethylene and water, but via gas phase reactions with methyl. Imaging methyl close to the catalyst surface during this reaction can possibly only be performed by PLIF.

Acknowledgments

This work was financially supported by the Knut and Alice Wallenberg Foundation and the Swedish Research Council.

References

[1] Duke C B and Plummer E W (ed) 2001 Frontiers in surface and interface science *Surf. Sci.* **500** 1
[2] Ertl G, Knözinger H and Weitkamp J 1997 *Handbook of Heterogeneous Catalysis* (New York: Wiley)
[3] Freund H J, Meijer G, Scheffler M, Schlögl R and Wolf M 2011 *Angew. Chem., Int. Ed.* **50** 10064
[4] Gao F, Wang Y, Cai Y and Goodman D W 2009 *J. Phys. Chem. C* **113** 174
[5] Chen M, Zheng Y and Wan H 2013 *Top. Catal.* **56** 1299
[6] Hendriksen B L M and Frenken J W M 2002 *Phys. Rev. Lett.* **89** 046101
[7] Hendriksen B L M and Frenken J W M 2004 *Surf. Sci.* **552** 229
[8] Ackermann M D *et al* 2005 *Phys. Rev. Lett.* **95** 255505
[9] Westerström R *et al* 2008 *J. Phys.: Condens. Matter* **20** 184018

[10] Rupprechter G and Weilach C 2007 *Nano Today* **2007** 2
[11] van Rijn R *et al* 2010 *J. Phys. Chem.* C **114** 6875
[12] Gustafson J, Westerström R, Balmes O, Resta A, van Rijn R, Torrelles X, Herbschleb C T, Frenken J W M and Lundgren E 2010 *J. Phys. Chem.* C **114** 22372
[13] Stierle A and Molenbroek A M 2007 *MRS Bull.* **32** 1001
[14] Gustafson J, Westerström R, Mikkelsen A, Torrelles X, Balmes O, Andersen J N, Baddeley C J and Lundgren E 2008 *Phys. Rev.* B **78** 045423
[15] Hendriksen B L M, Ackermann M D, van Rijn R, Stoltz D, Popa I, Balmes O, Resta A, Wermeille D, Felici R, Ferrer S and Frenken J W M 2010 *Nat. Chem.* **2** 730
[16] Over H, Balmes O and Lundgren E 2009 *Catal. Today* **145** 236
[17] Farkas A, Zalewska-Wierzbicka K, Bachmann C, Goritzka J, Langsdorf D, Balmes O, Janek J and Over H 2013 *J. Phys. Chem.* C **117** 9932
[18] Toyoshima R, Yoshida M, Monya Y, Suzuki K, Mun B S, Amemiya K, Mase K and Kondoh H 2012 *J. Phys. Chem. Lett.* **3** 3182
[19] Zetterberg J, Blomberg S, Gustafson J, Sun Z W, Li Z S, Lundgren E and Aldén M 2012 *Rev. Sci. Instrum.* **83** 053104
[20] Blomberg S *et al* 2013 *Phys Rev Lett* **110** 117601
[21] Gustafson J, Shipilin M, Zhang C, Stierle A, Hejral U, Ruett U, Gutowski O, Carlsson P A, Skoglundh M and Lundgren E 2014 *Science* **343** 758
[22] Shipilin M *et al* 2014 *Surf. Sci.* **630** 229
[23] Shipilin M *et al* 2015 *J. Phys. Chem.* C **119** 15469
[24] Duke A S, Galhenage R P, Tenney S A, Sutter P and Chen D A 2015 *J. Phys. Chem.* C **119** 381
[25] Shipilin M, Gustafson J, Zhang C, Merte L R and Lundgren E 2016 *Phys. Chem. Chem. Phys.* **18** 20312
[26] Zhang C, Lundgren E, Carlsson P-A, Balmes O, Hellman A, Merte L R, Shipilin M, Onderwaater W and Gustafson J 2015 *J. Phys. Chem.* C **119** 11646
[27] Balmes O, Prevot G, Torrelles X, Lundgren E and Ferrer S 2016 *ACS Catal.* **6** 1285
[28] Rotermund H H 1997 *Surf. Sci. Rep.* **29** 265
[29] Rotermund H H, Haas G, Franz R U, Tromp R M and Ertl G 1995 *Science* **270** 608
[30] Bertram M, Beta C, Rotermund H H and Ertl G 2003 *J. Phys. Chem.* B **107** 9610
[31] Reuter K, Frenkel D and Scheffler M 2004 *Phys. Rev. Lett.* **93** 116105
[32] Rogal J, Reuter K and Scheffler M 2007 *Phys. Rev. Lett.* **98** 046101
[33] Reuter K 2016 *Catal. Lett.* **146** 541
[34] van den Bossche M and Grönbeck H 2015 *J. Am. Chem. Soc.* **137** 12035
[35] Taylor C D, Wasileski S A, Filhol J-S and Neurock M 2006 *Phys. Rev.* B **73** 165402
[36] Matera S and Reuter K 2009 *Catal. Lett.* **133** 156
[37] Matera S and Reuter K 2010 *Phys. Rev.* B **82** 085446
[38] Blomberg S, Brackmann C, Zetterberg J, Gustafson J, Aldén M and Lundgren E 2015 *ACS catal.* **5** 2028
[39] Matera S, Blomberg S, Hoffmann M J, Zetterberg J, Gustafson J, Lundgren E and Reuter K 2015 *ACS Catal.* **5** 4514
[40] Zetterberg J, Blomberg S, Gustafson J, Evertsson J, Adams E C, Carlsson P A, Aldén M and Lundgren E 2015 *Nat. Commun.* **6** 7076
[41] Blomberg S, Zetterberg J, Gustafson J, Zhou J, Brackmann C and Lundgren E 2016 *Top. Catal.* **59** 478
[42] Svanberg S 1987 *Phys. Scr. T* **19b** 469
[43] Aldén M, Wallin S and Wendt W 1984 *Appl. Phys. B* **33** 205
[44] Fridell E, Westblom U, Aldén M and Rosén A 1991 *J. Catal.* **128** 92
[45] Fridell E, Elg A P, Rosén A and Kasemo B 1995 *J. Chem. Phys.* **102** 5827
[46] Fridell E, Rosén A and Kasemo B 1994 *Langmuir* **10** 699
[47] Gudmundson F, Persson J L, Forsth M, Behrendt F, Kasemo B and Rosén A 1998 *J. Catal.* **179** 420
[48] Kang W, Fujita O and Ito K 1996 *J. Energy Resour. Technol.* **118** 82
[49] Gudmundson F, Fridell E, Rosén A and Kasemo B 1993 *J. Phys. Chem.* **97** 12828
[50] Su H and Yeung E S 2000 *J. Am. Chem. Soc.* **122** 7422
[51] Anderson L C, Xu M, Mooney C E, Rosynek M P and Lunsford J H 1993 *J. Am. Chem. Soc.* **115** 6322
[52] Kirby B J and Hanson R K 2002 *Appl. Opt.* **41** 1190
[53] Goldenstein C S, Miller V A and Hanson R K 2015 *Appl. Phys. B: Lasers Opt.* **120** 185
[54] Burrows M G T and Stockmayer W H 1940 *Proc. R. Soc. Lond.* A **176** 474
[55] Schuth F, Henry B E and Schmidt L D 1993 *Adv. Catal.* **39** 51
[56] Imbihl R and Ertl G 1995 *Chem. Rev.* **95** 697
[57] van Rijn R, Balmes O, Resta A, Wermeille D, Westerström R, Gustafson J, Felici R, Lundgren E and Frenken J W M 2011 *Phys. Chem. Chem. Phys.* **13** 13167
[58] Hinojosa J A, Kan H H and Weaver J F 2008 *J. Phys. Chem.* C **112** 8324
[59] Zhang F, Li T, Pan L, Asthagiri A and Weaver J F 2014 *Catal. Sci. Technol.* **4** 3826
[60] Weaver J F, Zhang F, Pan L, Li T and Asthagiri A 2015 *Acc. Chem. Res.* **48** 1515
[61] Rogal J, Reuter K and Scheffler M 2004 *Phys. Rev.* B **69** 075421
[62] Zambelli T, Wintterlin J, Trost J and Ertl G 1996 *Science* **273** 1688
[63] Over H 2012 *Chem. Rev.* **112** 3356
[64] Weaver J F 2013 *Chem. Rev.* **113** 4164
[65] Lang B, Joyner R W and Somorjai G A 1972 *Surf. Sci.* **30** 454
[66] Castner G and Somorjai G A 1979 *Surf. Sci.* **83** 60
[67] Hoogers D and King D A 1993 *Surf. Sci.* **286** 306
[68] Hammer B, Nielsen O H and Nørskov J K 1997 *Catal. Lett.* **46** 31
[69] Hammer B 1999 *Phys. Rev. Lett.* **83** 3681
[70] Gustafson J *et al* 2006 *Phys. Rev.* B **74** 035401
[71] Westerström R *et al* 2007 *Phys. Rev.* B **76** 155410
[72] Somorjai G A and Li Y 2010 *Introduction to Surface Chemistry and Catalysis* 2nd edn (Hoboken, NJ: Wiley)
[73] Wang J *et al* 2005 *Phys. Rev. Lett.* **95** 256102
[74] Tao F *et al* 2010 *Science* **327** 850
[75] Corso M, Schiller F, Fernandez L, Cordon J and Ortega J E J 2009 *Phys. Condens. Matter* **21** 353001
[76] Mom R V, Hahn C, Jacobsen L and Juurlink L B 2013 *Surf. Sci.* **613** 15
[77] Walter A L *et al* 2015 *Nat. Commun.* **6** 8903
[78] Dahl S, Logadottir A, Egeberg R C, Larsen J H, Chorkendorff I, Törnqvist E and Nørskov J K 1999 *Phys. Rev. Lett.* **83** 1814
[79] Bourane A and Bianchi D 2001 *J. Catal.* **202** 34
[80] Oran U and Uner D 2004 *Appl. Catal. B: Environ.* **54** 183
[81] Matera S, Maestri M, Cuoci A and Reuter K 2014 *ACS Catal.* **4** 4081
[82] Brackmann C, Hole O, Zhou B, Li Z S and Aldén M 2014 *Appl. Phys.* B **115** 25
[83] Richter M, Bentrup U, Eckelt R, Schneider M, Pohl M M and Fricke R 2004 *Appl. Catal.* B **51** 261
[84] Brosius R, Arve K, Groothaert M H and Martens J A 2005 *J. Catal.* **231** 344
[85] Shimuzu K, Tsuzuki M, Kato K, Yokota S, Okumura K and Satsuma A 2007 *J. Phys. Chem.* C **111** 950
[86] Kannisto H, Ingelsten H H and Skoglundh M 2009 *Top. Catal.* **52** 1817
[87] Sazama P, Capek L, Drobna H, Sobalik Z, Dedecek J, Arve K and Wicterlova B 2005 *J. Catal.* **232** 302

Paper V

Top Catal (2016) 59:478–486
DOI 10.1007/s11244-015-0524-4

ORIGINAL PAPER

Comparison of AP-XPS and PLIF Measurements During CO Oxidation Over Pd Single Crystals

S. Blomberg[1] · J. Zetterberg[2] · J. Gustafson[1] · J. Zhou[2] · C. Brackmann[2] · E. Lundgren[1]

Published online: 4 January 2016
© The Author(s) 2016. This article is published with open access at Springerlink.com

Abstract The interaction between the gas-phase molecules and a catalyst surface is crucial for the surface structure and are therefore important to consider when the active phase of a catalyst is studied. In this study we have used two different techniques to study the gas phase during CO oxidation over Pd single crystals. Gas-phase imaging by planar laser-induced fluorescence (PLIF) shows that a spherical boundary layer with a decreasing gradient of CO_2 concentration out from the surface, is present close to the surface when the Pd crystal is highly active. Within this boundary layer the gas composition is completely different than that detected at the outlet of the chamber. The PLIF images of the gas-phase distribution are used to achieve a better understanding of the gas composition between the surface and the detector of a set-up for ambient pressure X-ray photoelectron spectroscopy (AP-XPS), a common technique for surface structure determination of model catalysts. The results show that also the gas-phase peaks present in the AP-XPS spectra truly represent the gas closest to the surface, which facilitates the interpretation of the AP-XPS spectra and thereby also the understanding of the mechanism behind the reaction process.

Keywords Ambient pressure X-ray photoelectron spectroscopy · Planar laser-induced fluorescence · Pd(100) · Pd(110) · Gas-phase

✉ S. Blomberg
sara.blomberg@sljus.lu.se

[1] Division of Synchrotron Radiation Research, Lund University, Box 118, 221 00 Lund, Sweden

[2] Division of Combustion Physics, Lund University, Box 118, 221 00 Lund, Sweden

1 Introduction

CO oxidation, where a CO molecule interacts with an oxygen molecule to form CO_2, is one of many reactions that occur in an automotive catalyst to clean the exhaust gases from the toxic CO molecules. Due to its simplicity, the reaction is often used as a model reaction [1] and because its wide application the reaction has been studied in great detail for many decades [2]. The reaction process is well-known under ultra-high vacuum (UHV) conditions but less is known about the surface structure and reaction mechanism under more realistic operating conditions for the catalyst. More realistic conditions in turn involve higher pressure, which implies that the number of molecules interacting with the surface increases significantly. The gas molecules interacting with the catalyst surface are essential for the surface structure and a change in the gas composition close to the surface may result in a change of the surface composition [3, 4]. It is therefore important to perform catalysis experiments in situ where knowledge of the gas molecules interacting with the surface can be achieved and used to understand the active surface structure of a catalyst in a better way [5].

There is a limited number of available techniques for probing the gas phase close to the surface of a model catalyst, and traditionally the gas composition has been analyzed using a mass spectrometer (MS) positioned at the reactor outlet. The MS data will therefore not reveal any direct information about the gas interacting with the surface and the actual connection between the MS signal and the gas distribution close to the surface is not clear. However, the development of traditional electron-based surface science techniques, enabling operation at higher pressures, has allowed for extraction of chemical information not only from the surface but also from the gas

phase. Ambient pressure X-ray photoelectron spectroscopy (AP-XPS) [6, 7] is an example of a high-pressure set-up, common for catalysis studies, which is capable of monitoring surface reconstruction in situ as well as the gas phase close to the surface.

Oxidation of CO over transition metals is often mass transfer limited (MTL) by the minority reactants [8, 9] in the highly active regime of the catalyst. This means that the reaction is not kinetically controlled but, limited by the number of minority reactants that can penetrate a boundary layer of the product to reach the surface. The reaction is therefore completely controlled by diffusion of the reactants, which makes the gas-phase composition highly important for the catalytic process. Gas-phase studies using AP-XPS have been performed and reported in the literature [10–12], but very few have been performed for a highly active catalyst during CO oxidation [13–16]. As mentioned previously, the formation of a CO_2 boundary layer changes the gas composition close to the sample surface, but how this is reflected in the AP-XPS gas-phase signal is not obvious. Planar laser-induced fluorescence (PLIF) has been shown to be capable of imaging the gas-phase distribution above an active catalyst surface with high spatial resolution [17–20]. The imaged gas-phase region is similar as the one probed by AP-XPS and can therefore contribute to an improved understanding of the AP-XPS spectra and, as a consequence, a better understanding of the details of the catalytic processes on the surface.

This contribution presents a comparison of the gas phase composition detected by AP-XPS and PLIF close to a highly active Pd catalyst surface exposed to a 1:1 mixture of CO and O_2. By comparing the ratios of CO and CO_2 for the two techniques, we show that AP-XPS probes the gas composition in the vicinity of the surface, and therefore provides a considerably better estimation of the gas composition as compared to an MS located at the outlet of the reactor.

2 Experimental

All experiments were performed in mixtures having a 1:1 ratio of CO and O_2, but at different total pressures. In the AP-XPS experiment the total pressure was varied from 0.013 to 1.3 mbar [13]. The PLIF experiments performed for CO and CO_2 detection were carried out at a total pressure of 106 and 150 mbar, respectively, where a pressure controller at the outlet was used to keep the pressure constant in the chamber. The partial pressures in the CO experiment were set to 26.5 mbar (18 ml_n/min) each for CO and O_2, and to 53 mbar (36 ml_n/min) for Ar whereas 6 mbar (4 ml_n/min) each of CO and O_2 and 138 mbar (92 ml_n/min) of Ar were used in the CO_2 experiment. This results in a gas residence time in the chamber of 20 s for the CO experiment while in the CO_2 experiment the gas residence time is only 2 s. For the XPS experiment the inlet flow was controlled via a leak valve and the partial pressure of each gas was measured. No pressure controller was used and the inlet and outlet flow was constant throughout the whole experiment. In all experiments a standard BN heater [21, 22] was used to ramp the temperature of the crystal in order to start with an inactive crystal and then monitor the gas phase when the catalytic activity of the sample increases and reaches the highly active regime, in which the reaction is mass transfer limited.

2.1 Ambient Pressure X-Ray Photoelectron Spectroscopy

The AP-XPS measurements were carried out at beamline 9.3.2 at the ALS in Berkeley [10], CA, USA where differential pumping stages combined with electrostatic lenses enables reaction experiments in situ at pressures up to approximately 10 mbar. The sample was mounted on a special-made holder for catalysis experiments and a thermocouple was attached to the heating plate close to the single crystal. The set-up consists of two chambers between which the sample can be transferred without being exposed to air. This allows for sample preparation, such as sputtering, before transfer into the analysis chamber, where a hemispherical analyzer is attached. The gas pressures were controlled by individual leak valves. The only outlet from the analysis chamber is via the nozzle to the detector and in order to maintain the pressure at the surface to at least 98 % of the inlet pressure at room temperature, the working distance between the sample and nozzle should be larger than twice the diameter of the aperture at the first pumping stage [10]. To achieve this for the present beamline set-up, the working distance was approximately 2 mm, which is also the focus of the detector and implies that the number of detected electrons from the surface is optimized.

The C 1s spectra were measured with a photon energy of 435 eV and the energy was calibrated to the Fermi level. The decomposition of the spectra was made using a Doniach and Sunjic [23] lineshape convoluted with a Gaussian lineshape and subtraction of a linear background.

2.2 Planar Laser-Induced Fluorescence

PLIF allows for species-specific detection in the gas phase with high sensitivity and two-dimensional imaging. The technique is commonly employed for combustion diagnostics, but less used in the field of catalysis [22, 24]. Here, we have used PLIF to visualize the gas-phase CO and CO_2 above two different Pd single crystals. Two different laser

systems and reactors were used for probing CO and CO_2 respectively, but the layout of the experimental set-up was the same in both experiments and is shown in Fig. 1. In both set-ups an MS was attached to the gas outlet of the chamber for analysis of the overall gas composition. The Pd(100) crystal used for the CO_2 experiment was the same as used in the AP-XPS experiments but when CO was probed a Pd(110) crystal, with the same size, was used. In these studies, thin lasersheets arranged perpendicular to the crystal surface probed CO and CO_2 across the center of the crystals with wavelengths of 230 nm and 2.7 μm, respectively. The resulting fluorescence emission at 440–660 nm for CO and 4.26 μm for CO_2 was detected with a CCD camera and focal plane array detector, respectively, and images of an area of approximately 5 × 16 mm^2 of the specific gas distribution were obtained. The PLIF detection limit is at ppm levels and a spatial resolution better than 0.4 and 0.07 mm for the CO and CO_2 measurements, respectively, were achieved in the presented measurements. The laser repetition rate was 10 Hz, also representing the number of images taken every second. However, for noise reduction, the images shown in Fig. 4, are averaged over ten acquired images generating a timescale of 1 image/s. The analysis process for the PLIF images, which for instance includes temperature corrections and calibrations, is described in detail in [22].

2.3 Sample Preparation

Pd single crystals with surface orientation (100) and (110) were used as model catalysts. In the AP-XPS measurements the Pd(100) crystal was cleaned by sputtering and oxygen treatment in the preparation chamber. The crystal was then transferred into the analysis chamber without being exposed to air. The cleanness of the surface was then checked with AP-XPS before the reaction experiments were performed. In the PLIF experiments, the crystals were cleaned in the same way, with sputtering and oxygen treatment, but in this set-up there is no transfer system between the preparation chamber and the reactor, and the crystal was exposed to air before it was mounted in the reactor. To reduce contaminations on the surface the crystal temperature was ramped up and down in a CO and O_2 environment before the reaction experiments were performed.

3 Results

In Fig. 2, the C 1s spectra are shown, acquired during CO oxidation using a 1:1 ratio of CO and O_2 at different total pressures [13] with a Pd(100) single crystal used as a model catalyst. The O 1s and Pd $3d_{5/2}$ core levels were also measured but are not shown here. Starting with the experiment at a total pressure of 1.3 mbar (Fig. 2a), the sample is inactive at low temperature and CO in the gas phase is clearly observed at approximately 290 eV. CO adsorbed in a bridge site on the Pd(100) surface is also detected at 286 eV [25]. The temperature of the crystal is then stepwise increased and when a temperature of 340 °C is reached the sample is highly active and CO desorbs instantaneously from the surface simultaneously as the CO gas-phase peak disappears. In the spectrum measured at 340 °C a single peak, corresponding to CO_2 in the gas phase, is observed, showing that the sample is highly active. When the temperature is increased further, no obvious increase in the CO_2 gas-phase peak can be seen which shows that under these conditions, the reaction reaches its maximum conversion of CO to CO_2 immediately after ignition. The conclusion is then that after ignition the reaction is not kinetically controlled but mass transfer limited by the CO diffusion. However, a highly

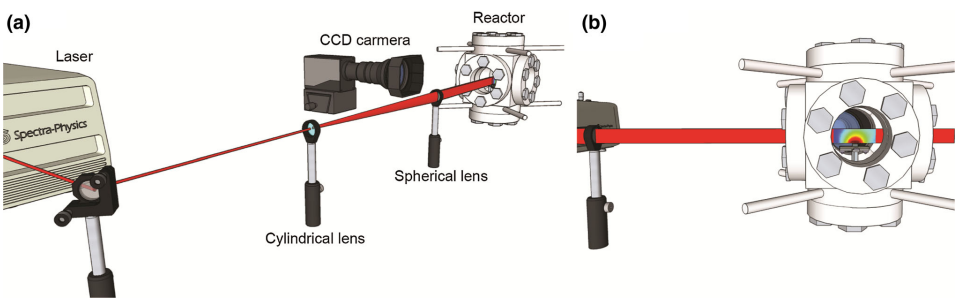

Fig. 1 An overview of the PLIF experimental set-up. **a** The laser-beam is shaped into a thin lasersheet by passing a cylindrical and spherical lens before it enters the reactor. The lasersheet can then probe the gas in two dimensions. **b** The fluorescence is detected by a CCD camera perpendicular to the lasersheet and a PLIF image of the gas distribution over the Pd crystal can be detected

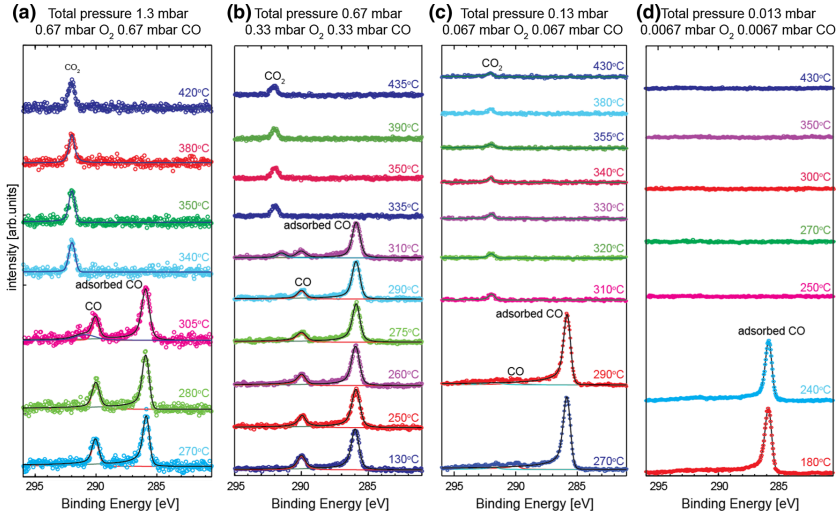

Fig. 2 AP-XPS C 1s spectra from CO oxidation using Pd(100) catalyst in 1:1 CO and O_2 atmospheres at different total pressures **a** 1.3 mbar, **b** 0.67 mbar, **c** 0.13 mbar, **d** 0.013 mbar. CO_2 and CO gas-phase peaks are observed as well as CO adsorbed on the surface

active sample producing a significant amount of CO_2 should still have CO in the gas phase close to the surface to maintain its high activity. Surprisingly, no trace of CO can be is seen in the spectra after ignition. When the total pressure is reduced to 0.67 mbar, shown in Fig. 2b, a similar behavior can be observed. CO is adsorbed on the surface until the ignition temperature is reached and after ignition, which occurs at slightly lower temperature compared with the higher pressure (1.3 mbar), only gas-phase CO_2 can be seen in the C 1s spectra. Interestingly, at 310 °C both a CO_2 and a CO gas-phase peak can be detected together with a peak originating from CO adsorbed on the surface, indicating that a complete MTL has not yet been reached, which in turn implies that only parts of the surface is fully active. We know from our previous studies [13] that chemisorbed oxygen starts to occupy the surface at this moment, but the exact nature of the surface is obviously still beyond our reach. To speculate, we could suggest that the surface consist of islands of atomic oxygen bordered by islands of CO, and the CO_2 production occurs at the border between the islands and/or at vacancies within the oxygen islands. Furthermore, it can also be seen that the CO_2 peak is shifting towards higher energy as the surface goes from partly to fully active. The reason is the change in the surface work function [26, 27] as the CO desorbs fully from the surface and the oxygen fully adsorb on the surface. Decreasing the total pressure even further to 0.13 mbar (Fig. 2c) the ignition temperature is decreased to 310 °C, but the CO-trend is still the same. It is also clear that the ratio between peaks of adsorbed CO and gas-phase CO is increasing with decreasing pressure, even though a similar CO coverage of the surface is expected for the different total pressures. This is simply because the number of molecules in the gas phase decreases when the pressure is reduced. The spread of the raw data (circles in Fig. 2) is also lower when the pressure is reduced, which results in more well-defined spectra. However, at an even lower total pressure of 0.013 mbar (Fig. 2d), the partial pressures of CO and CO_2 are too low to be detected and no gas-phase peaks in the C 1s spectra can be observed. Still, the ignition temperature is concluded to be around 250 °C, due to the absence of the peak corresponding to adsorbed CO at this temperature. In fact, the absence of a peak corresponding to CO adsorbed on the surface demonstrates a very low coverage suggesting that the reaction is extremely fast, and that all CO reaching the surface instantaneously is converted to CO_2.

To investigate the changes in the gas phase in more detail the areas of the CO and CO_2 gas-phase peaks are extracted from the C 1s spectra and plotted in Fig. 3. The advantage of extracting the CO and CO_2 peak areas from the same spectrum is that difficulties such as compensation for background and number-of-sweeps, are reduced. In addition, the cross sections for CO and CO_2 in the gas phase are similar [28], making it possible to compare the integrated intensities of the peaks. In the plots, the peak

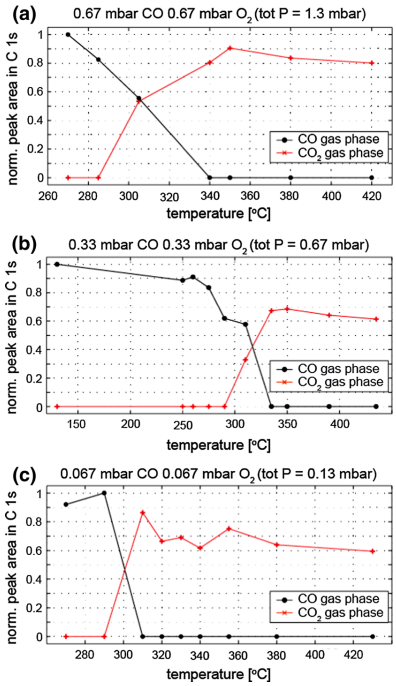

Fig. 3 Normalized CO and CO_2 gas-phase peak areas, evaluated from the AP-XPS C 1s spectra, plotted versus catalyst temperature for different total pressures **a** 1.3 mbar, **b** 0.67 mbar, **c** 0.13 mbar. *Lines* have been inserted between the measurement points for guidance

areas are normalized to the area of the CO peak in the beginning of the experiment but similar results are achieved by plotting the ratios between the gas-phase peaks and the Pd substrate peak. The error of the data can be estimated to be ±5 %, based on the statistical error between consecutive scans. Figure 3a shows results for a total pressure of 1.3 mbar, where the area of the CO gas-phase peak (black points) decreases when the temperature is increased while the CO_2 peak is not detectable until after ignition. At ignition the CO peak decreases to zero and the CO_2 peak area increases (red crosses) to an approximately constant level confirming that the MTL regime is reached. Figure 3b and c show the peak areas at the lower total pressures of 0.67 and 0.13 mbar. No obvious difference can be seen between the three plots, suggesting that the gas composition close to the surface is similar for all three total pressures. The absence of the CO gas-phase peak after ignition could be interpreted as no CO molecules are present in the gas phase close to the surface after ignition but instead immediately converted into CO_2. However, for none of the three experiments in which the gas phase is detected, the CO_2 peak area reaches the same peak area as the CO prior to ignition (it only reaches 60–80 % of the CO peak). This would then suggest that CO is still present in the gas phase but below the detection limit of the AP-XPS set-up, however, the interpretation of the data is still not obvious. It is of particular interest to know how the gas-phase peaks observed in the AP-XPS spectra are related to the actual gas composition close to the surface. In an attempt to answer this question we have investigated the composition of the gas-phase more thoroughly using PLIF.

PLIF images of CO and CO_2 acquired at three different temperatures, respectively, during the temperature ramp, are shown in Fig. 4. The images represent the gas composition of an inactive sample (image I), at ignition (image II), and a highly active sample (image III). Due to the different ignition temperatures of the crystals [365 °C for Pd(110) and 270 °C for the Pd(100)] the temperature of the samples when the images were acquired are different for the CO and CO_2 cases. Starting with images acquired at the lowest temperatures, the lack of CO_2 PLIF signal and the homogenous partial pressure of CO clearly indicates that the samples are inactive at these temperatures (image I). When the ignition temperatures of the samples are reached, local changes in the gas composition close to the surface are observed (image II). Immediately after ignition, a spherically shaped region with increased CO_2 concentration is formed around the surface (image III) which stays unchanged even if the temperature is increased further. This is a visualization of the boundary layer of the CO_2 that hinders CO from reaching the surface in the MTL regime, consistent with the reduced CO signal detected in the corresponding region. The images show that after the boundary layer is formed, the changes in the gas composition close to the surface are small, indicating steady state conditions in the gas phase. It is also clear that the gas-phase evolution during the reaction is comparable for both crystals and that the surface structure does not affect the gas phase significantly, which is in agreement with the results reported by Toyoshima et al. [14, 15]. They also report a lower ignition temperature for Pd(110) compared to the Pd(100), which is not observed in the PLIF studies, possibly because different chambers with different gas flow properties were used for the two experiments. The partial pressures of CO and O_2 are also higher (26.5 mbar) in the experiment where the Pd(110) was used compared to the partial pressures used when the Pd(100) crystal was investigated (6 mbar). This may also contribute to a higher ignition temperature for the Pd(110) compared with the Pd(100) crystal.

Figure 5a shows MS data recorded during CO oxidation over Pd(110). When the sample temperature reaches

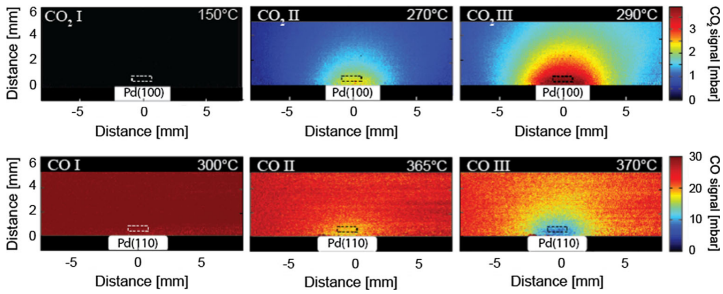

Fig. 4 PLIF images of CO_2 (*upper panel*) and CO (*lower panel*) gas-phase distributions over Pd single crystals during CO oxidation in a 1:1 ratio of CO and O_2. The gas flow is in the direction from *left to right* in all images. The *white filled rectangles* represent the single crystals samples and the *dashed rectangles* above show the areas where the PLIF signals plotted in Fig. 5 are evaluated. The *Roman numerals* are correlated to time points and temperatures in Fig. 5

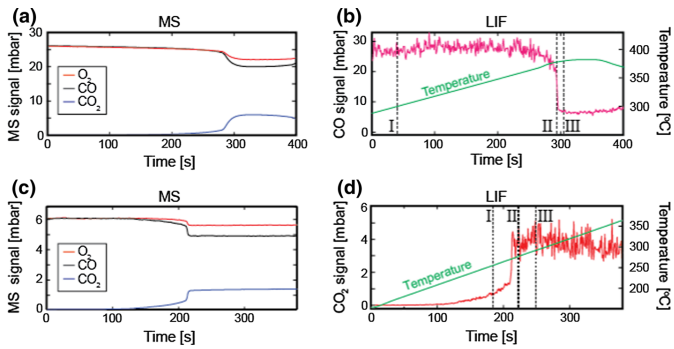

Fig. 5 Comparison of the MS and PLIF signals, **a** MS signal detected during CO oxidation over Pd(110). **b** Corresponding CO PLIF trend extracted 0.5 mm from surface and sample temperature. **c** MS signal detected during CO oxidation over Pd(100). **d** Corresponding CO_2 PLIF trend extracted 0.5 mm from surface and sample temperature

ignition the CO signal decreases simultaneously as the CO_2 signal increases and both signals reach constant levels, even though the temperature is increased further. This is, as discussed above, a clear indication of an MTL reaction. In this regime the MS CO partial pressure detected at the outlet of the chamber has decreased by approximately 25 %. This can be compared to the CO PLIF signal plotted in Fig. 5b, extracted 0.5 mm from the surface (the dashed rectangle in the images in Fig. 4 shows the area where the signal is extracted) where the CO signal decreases by approximately 80 %. The Roman numerals in the plot indicate time points for the corresponding image of the gas-phase distribution shown in Fig. 4. Similar divergence is also observed between the MS and CO_2 PLIF signal shown in Fig. 5c and d, respectively. The results from the MS and PLIF can in turn be compared to the C 1s peak areas plotted in Fig. 3. The C 1s peak areas show, just as the PLIF data, a higher ratio between the reactant and the product signal as compared to the MS signal. The reason for the different ratios detected by the different techniques can be understood by studying the PLIF images. The images reveal a completely different gas composition in the MTL regime, close to the surface where the AP-XPS and PLIF signals are extracted, which is not detected by the MS.

4 Discussion

The gas molecules interacting with the surface are obviously important for the surface composition, and the determination of an active site or phase of the catalyst. It is

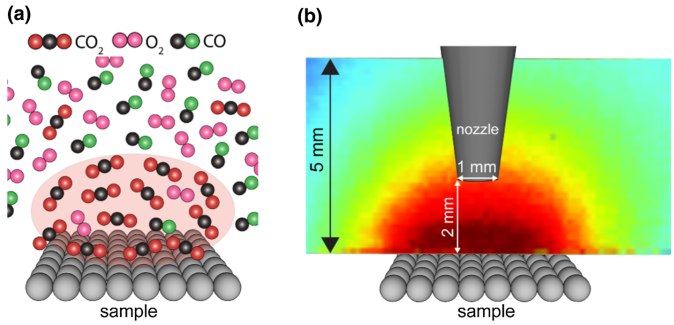

Fig. 6 Illustration of the boundary layer of CO_2 during CO oxidation over a highly active surface. **a** Model showing the high CO_2 and low CO concentration within the boundary layer. **b** Schematic view of the highly active sample surface with PLIF image showing the CO_2 distribution above the catalyst. The AP-XPS nozzle is located at normal operating distance, which is approximately twice the diameter of the nozzle aperture. Electrons with a take-off angle of 23° will reach the detector

therefore important to gain knowledge about the gas distribution around the catalyst in order to understand to which extent relevant information can be deduced from gas-phase AP-XPS spectra. Due to the differences in the experimental set-ups, the extent and size of the gas phase distribution at MTL may be influenced by the different flow and conditions of the different set-ups, but as our results demonstrate, the main contribution to the gas-phase peaks at MTL in AP-XPS originates from the seriously CO-depleted zone, often referred to in the literature as the boundary layer. The very high conversion of CO that is observed in both the AP-XPS and in the PLIF signal is within this boundary layer. We do not observe any indication that the catalytic behavior at MTL is different because of the different experimental set-ups.

Both PLIF and AP-XPS show consistently a significantly different gas composition above the single crystal surfaces compared to the rest of the chamber when the MTL regime is reached, as illustrated in Fig. 6a. This behavior is observed for both the Pd(110) and Pd(100) crystals and is expected to follow for any highly active transition metal during CO oxidation, at least in the case of a single crystal positioned in a reactor in a similar way as in the present experiments. The concentration gradient of CO and CO_2 within the boundary layer is dependent on the gas exchange in the chamber and the activity of the sample. The gas flow in the AP-XPS set-up is complex due to the large volume of the reactor with the only outlet being the nozzle of the analyzer. The distance between the aperture of the nozzle and the surface is about 2 mm resulting in a semi-flow type of reactor, and the rate of the gas exchange and the gas composition above the surface are difficult to estimate.

Comparing ratios of the CO and CO_2 peak areas in the AP-XPS C 1s spectra, measured during the temperature ramp, as well as PLIF and MS signals, shows that AP-XPS data are in considerably better agreement with PLIF data than with MS data. The peak areas, however, differ compared with ratios of the gas-phase peak heights shown in the AP-XPS spectra (Fig. 2). The reason for the larger area of the CO peak is the larger splitting of the vibrational fine structure in CO as compared with CO_2 [29, 30], which gives a broadening of the peak and generates a larger area for the CO peak. The stronger scattering of the electrons of the CO_2 molecules might also modify the peak area, but this contribution is relatively small and will not affect the high ratio between CO and CO_2 signals in the MTL regime. This observation indicates that most of the gas-phase molecules detected in the AP-XPS measurements originate from a region with a comparable relation between the CO and CO_2 concentrations as inside the boundary layer imaged in the PLIF experiments, and that the aperture of the AP-XPS detector nozzle is located at a distance from the surface where the gas-phase concentration gradient has not changed significantly but reveal a similar CO and CO_2 ratio as that close to the surface, schematically illustrated in Fig. 6b. Furthermore, the AP-XPS measurements are averaged over a volume above the surface. As a consequence, if the gas-phase distribution or the boundary layer were to be measured by AP-XPS, it is likely to appear smeared out as compared to the distribution observed by PLIF. This drastic reduction would result in a CO level just below the detection limit for AP-XPS, explaining the absence of the CO gas-phase peak for the highly active sample. It could be argued that the CO should still be detected in the AP-XPS measurements for the highest pressure, 0.13 mbar (20 % of 0.67 mbar). However, 0.13 mbar is close to the general detection limit of AP-XPS ($\sim$0.05 mbar) [31], which is further affected by the photoelectron kinetic energy, the photoelectron cross-section, and the types of gases used in the experiments. The PLIF

measurements, however, confirm that CO is still present in the gas-phase above the crystal but the concentration decreases by approximately 80 % compared to the initial CO level. This is interpreted as the fast build-up of the boundary layer of CO_2 after ignition that hinders CO to reach the surface which decreases the CO concentration close to the surface significantly in the MTL regime.

5 Conclusions

The PLIF images of CO and CO_2 display a boundary layer with a spherical shape around the surface when the MTL is reached during CO oxidation. This boundary layer has a significantly different gas composition than that measured at the chamber gas inlet or outlet, with a CO concentration below the detection limit of the AP-XPS. By studying the gas-phase peak areas extracted from the C 1s AP-XPS spectra and compare with the PLIF and MS results, we confirm that the ratio of CO and CO_2 concentrations detected by AP-XPS is comparable with the gas ratio inside the boundary layer. The results indicate that the gas-phase peaks in the AP-XPS spectra represent the gas phase interacting with the surface, and that the aperture of the nozzle is located at a distance from the surface where the CO and CO_2 concentrations are still similar as within the boundary layer. AP-XPS is therefore one of few techniques able to probe the gas phase just above the catalyst surface. This makes AP-XPS suitable for in situ catalysis studies where the spectra can provide information about the gas phase molecules relevant for the surface structure determination of a highly active catalyst.

Altogether, the presence of a boundary layer in the highly active phase of the catalyst implies that in situ studies are important when CO oxidation is investigated in order to achieve a representative picture of the surface structure and the gas molecules interacting with the surface.

Acknowledgments The authors gratefully acknowledge financial support from the Knut and Alice Wallenberg Foundation and the Swedish Research Council.

Open Access This article is distributed under the terms of the Creative Commons Attribution 4.0 International License (http://creativecommons.org/licenses/by/4.0/), which permits unrestricted use, distribution, and reproduction in any medium, provided you give appropriate credit to the original author(s) and the source, provide a link to the Creative Commons license, and indicate if changes were made.

References

1. Freund HJ, Meijer G, Scheffler M, Schlogl R, Wolf M (2011) CO oxidation as a prototypical reaction for heterogeneous processes. Angew Chem Int Edit 50:10064–10094
2. Ertl G, Knozinger H, Weitkamp J (2008) Handbook of heterogeneous catalysis, 2nd edn. Wiley-VCH, Weinheim
3. Gustafson J, Shipilin M, Zhang C, Stierle A, Hejral U, Ruett U, Gutowski O, Carlsson PA, Skoglundh M, Lundgren E (2014) High-energy surface X-ray diffraction for fast surface structure determination. Science 343:758–761
4. Gao F, Wang Y, Cai Y, Goodman DW (2009) CO oxidation on Pt-group metals from ultrahigh vacuum to near atmospheric pressures. 2. Palladium and platinum. J Phys Chem C 113:174–181
5. Hendriksen BLM, Bobaru SC, Frenken JWM (2004) Oscillatory CO oxidation on Pd(100) studied with in situ scanning tunneling microscopy. Surf Sci 552:229–242
6. Grass ME, Zhang YW, Butcher DR, Park JY, Li YM, Bluhm H, Bratlie KM, Zhang TF, Somorjai GA (2008) A reactive oxide overlayer on rhodium nanoparticles during CO oxidation and its size dependence studied by in situ ambient-pressure X-ray photoelectron spectroscopy. Angew Chem Int Ed 47:8893–8896
7. Bluhm H, Havecker M, Knop-Gericke A, Kiskinova M, Schlogl R, Salmeron M (2007) In situ x-ray photoelectron spectroscopy studies of gas-solid interfaces at near-ambient conditions. MRS Bull 32:1022–1030
8. Matera S, Reuter K (2009) First-principles approach to heat and mass transfer effects in model catalyst studies. Catal Lett 133:156–159
9. Duprat F (2002) Light-off curve of catalytic reaction and kinetics. Chem Eng Sci 57:901–911
10. Grass ME, Karlsson PG, Aksoy F, Lundqvist M, Wannberg B, Mun BS, Hussain Z, Liu Z (2010) New ambient pressure photoemission endstation at advanced light source beamline 9.3.2. Rev Sci Instrum 81(5):053106
11. Bluhm H (2010) Photoelectron spectroscopy of surfaces under humid conditions. J Electron Spectrosc 177:71–84
12. Siegbahn K (1969) ESCA applied to free molecules. North-Holland Publishing, Amsterdam
13. Blomberg S, Hoffmann MJ, Gustafson J, Martin NM, Fernandes VR, Borg A, Liu Z, Chang R, Matera S, Reuter K, Lundgren E (2013) In situ X-ray photoelectron spectroscopy of model catalysts: at the edge of the gap. Phys Rev Lett 110:117601
14. Toyoshima R, Yoshida M, Monya Y, Suzuki K, Mun BS, Amemiya K, Mase K, Kondoh H (2012) Active surface oxygen for catalytic CO oxidation on Pd(100) proceeding under near ambient pressure conditions. J Phys Chem Lett 3:3182–3187
15. Toyoshima R, Yoshida M, Monya Y, Suzuki K, Amemiya K, Mase K, Mun BS, Kondoh H (2013) In situ photoemission observation of catalytic CO oxidation reaction on Pd(110) under near-ambient pressure conditions: evidence for the langmuir-hinshelwood mechanism. J Phys Chem C 117:20617–20624
16. Toyoshima R, Yoshida M, Monya Y, Kousa Y, Suzuki K, Abe H, Mun BS, Mase K, Amemiya K, Kondoh H (2012) In situ ambient pressure XPS study of CO oxidation reaction on Pd(111) surfaces. J Phys Chem C 116:18691–18697
17. Zellner A, Suntz R, Deutschmann O (2015) Two-dimensional spatial resolution of concentration profiles in catalytic reactors by planar laser-induced fluorescence: NO reduction over diesel oxidation catalysts. Angew Chem Int Ed 54:2653–2655
18. Appel C, Mantzaras J, Schaeren R, Bombach R, Kaeppeli B, Inauen A (2002) An experimental and numerical investigation of turbulent catalytically stabilized channel flow combustion of hydrogen/air mixtures over platinum. P Combust Inst 29:1031–1038
19. Blomberg S, Brackmann C, Gustafson J, Aldén M, Lundgren E, Zetterberg J (2015) Real-time gas-phase imaging over a Pd(110) catalyst during CO oxidation by means of planar laser-induced fluorescence. ACS Catal 5(4):2028–2034
20. Zetterberg J, Blomberg S, Gustafson J, Evertsson J, Zhou J, Adams CE, Carlsson PA, Aldén M, Lundgren E (2015) Spatially

and temporally resolved gas distributions around heterogeneous catalysts using infrared planar laser-induced fluorescence. Nat Commun 6:7076
21. Chang R, Hong YP, Axnanda S, Mao BH, Jabeen N, Wang SD, Tai RZ, Liu Z (2012) In-situ photoelectron spectroscopy with online activity measurement for catalysis research. Curr Appl Phys 12:1292–1296
22. Zetterberg J, Blomberg S, Gustafson J, Sun ZW, Li ZS, Lundgren E, Alden M (2012) An in situ set up for the detection of CO_2 from catalytic CO oxidation by using planar laser-induced fluorescence. Rev Sci Instrum 83:053104
23. Doniach S, Šunjić M (1970) Many-electron singularity in X-ray photoemission and X-ray line spectra from metals. J Phys Part C Solid 3:285–291
24. Eckbreth AC (1988) Laser diagnostics for combustion temperature and species. Energy and engineering science series, vol 7. Abacus Press, Tunbridge Wells, Kent; Cambridge, Mass
25. Andersen JN, Qvarford M, Nyholm R, Sorensen SL, Wigren C (1991) Surface core-level shifts as a probe of the local overlayer structure—Co on Pd(100). Phys Rev Lett 67:2822–2825
26. Siegbahn H (1985) Electron-spectroscopy for chemical-analysis of liquids and solutions. J Phys Chem 89:897–909
27. Axnanda S, Scheele M, Crumlin E, Mao BH, Chang R, Rani S, Faiz M, Wang SD, Alivisatos AP, Liu Z (2013) Direct work function measurement by gas phase photoelectron spectroscopy and its application on PbS nanoparticles. Nano Lett 13: 6176–6182
28. Shirley DA, Kobrin PH, Truesdale CM, Lindle DW, Ferrett TA, Heimann PA, Becker U, Kerkhoff HG, Southworth SH (1984). Gas-phase photoemission with soft X-Rays: Cross sections and angulardistributions. Proc. SPIE 0447:150–156
29. Neeb M, Kempgens B, Kivimaki A, Koppe HM, Maier K, Hergenhahn U, Piancastelli MN, Rudel A, Bradshaw AM (1998) Vibrational fine structure on the core level photoelectron lines of small polyatomic molecules. J Electron Spectrosc 88:19–27
30. Kempgens B, Maier K, Kivimaki A, Koppe HM, Neeb M (1997) Vibrational excitation in C 1s and O 1s photoionization of CO. J Phys B 30:L741–L747
31. Crumlin EJ, Bluhm H, Liu Z (2013) In situ investigation of electrochemical devices using ambient pressure photoelectron spectroscopy. J Electron Spectrosc 190:84–92

Paper VI

ACS Catalysis

Research Article

pubs.acs.org/acscatalysis

Strain Dependent Light-off Temperature in Catalysis Revealed by Planar Laser-Induced Fluorescence

Sara Blomberg,*[,†] Johan Zetterberg,[‡] Jianfeng Zhou,[‡] Lindsay R. Merte,[†] Johan Gustafson,[†] Mikhail Shipilin,[†] Adriana Trinchero,[§] Luis A. Miccio,[∥] Ana Magaña,[⊥] Maxim Ilyn,[#] Frederik Schiller,[#] J. Enrique Ortega,[⊥,∥,#] Florian Bertram,[&] Henrik Grönbeck,[§] and Edvin Lundgren[†]

[†]Synchrotron Radiation Research, Lund University, Box 118, SE-221 00 Lund, Sweden

[‡]Combustion Physics, Lund University, Box 118, SE-221 00 Lund, Sweden

[§]Competence Centre for Catalysis, Chalmers University of Technology, SE-412 96, Gothenburg, Sweden

[∥]Donostia International Physics Center DIPC, 20018 San Sebastian, Spain

[⊥]Departamento de Física Aplicada I, Universidad del Pais Vasco, 20018 San Sebastian, Spain

[#]Centro de Física de Materiales CSIC/UPV-EHU Materials Physics Center, 20018 San Sebastian, Spain

[&]DESY Photon Science, Notkestraße 85, 22607 Hamburg, Germany

Supporting Information

ABSTRACT: Understanding how specific atom sites on metal surfaces lower the energy barrier for chemical reactions is vital in catalysis. Studies on simplified model systems have shown that atoms arranged as steps on the surface play an important role in catalytic reactions, but a direct comparison of how the light-off temperature is affected by the atom orientation on the step has not yet been possible due to methodological constraints. Here we report in situ spatially resolved measurements of the CO_2 production over a cylindrical-shaped Pd catalyst and show that the light-off temperature at different parts of the crystal depends on the step orientation of the two types of steps (named A and B). Our finding is supported by density functional theory calculations, revealing that the steps, in contrast to what has been previously reported in the literature, are not directly involved in the reaction onset but have the role of releasing stress.

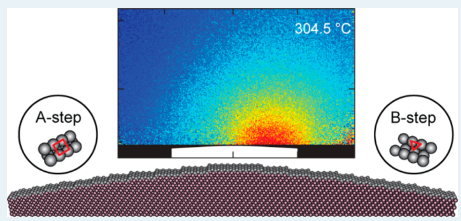

KEYWORDS: *CO oxidation, planar laser-induced fluorescence, density functional theory, cylindrical crystal, steps*

INTRODUCTION

Catalysts are vital for a wide range of applications in exhaust gas cleaning, in the chemical industry, and in energy production because they reduce the energy barrier of chemical reactions, in turn increasing the rates by which these reactions occur. Because of their prevalence, it is of significant interest, from both fundamental scientific and industrial points of view, to identify, characterize, and understand processes promoting catalytic reactions.[1,2]

Simplified model catalysts based on vicinal surfaces have previously been used to study the reactivity properties of specific sites of a crystal under well-controlled conditions. Results from these studies indicate that steps and defects have different reactivities in comparison to flat terraces which are caused by undercoordinated atoms.[3−9] This has implications for the catalytic properties of the surface. For example, catalytic reactions occur with lower conversion efficiency on single-crystal surfaces than on nanoclusters that hold a high density of steps and defects.[10−13] Undercoordinated atoms related to steps and defects are considered to be the most important active sites of a catalyst in many reactions. It has also been shown that catalytic reaction rates are influenced by the specific orientation of the steps[12] and suggested theoretically that terrace atoms subjected to different degrees of strain may alter the reactivity.[14] Despite these previous studies, it is still not well understood how steps, and their orientation, influence the transition of the catalyst on going from low to high activity, the so-called light-off. This is because of the lack of experimental techniques that have the temporal and spatial resolution required to perform side-by-side comparisons of the catalytic reactions of different step orientations at operating conditions.

Here we report the first experimental in situ side-by-side comparison of the role of step orientation (A and B types, shown in Figure 1A) in CO oxidation and demonstrate explicitly, using high temporal and spatial resolution, that the catalytic reaction around the B-type steps has a lower light-off temperature (by 6 °C) than that around the A-type steps. Our side-by-side comparison was made possible by using a

Received: August 26, 2016
Revised: November 9, 2016
Published: November 15, 2016

 © 2016 American Chemical Society

DOI: 10.1021/acscatal.6b02440
ACS Catal. 2017, 7, 110−114

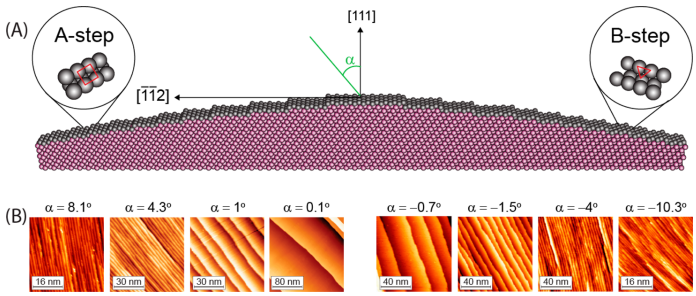

Figure 1. Surface of the curved Pd(111) crystal contains two types of steps. (A) Schematic illustration of the curved crystal indicating a decreasing width of adjacent terraces with increasing miscut angle α. The miscut of the crystal generates A- and B-type steps; insets show their geometries. (B) Scanning tunneling microscopy images taken at different locations on the sample surface, marked by the angle α. The terrace width of the vicinal surfaces decreases with the marked angle.

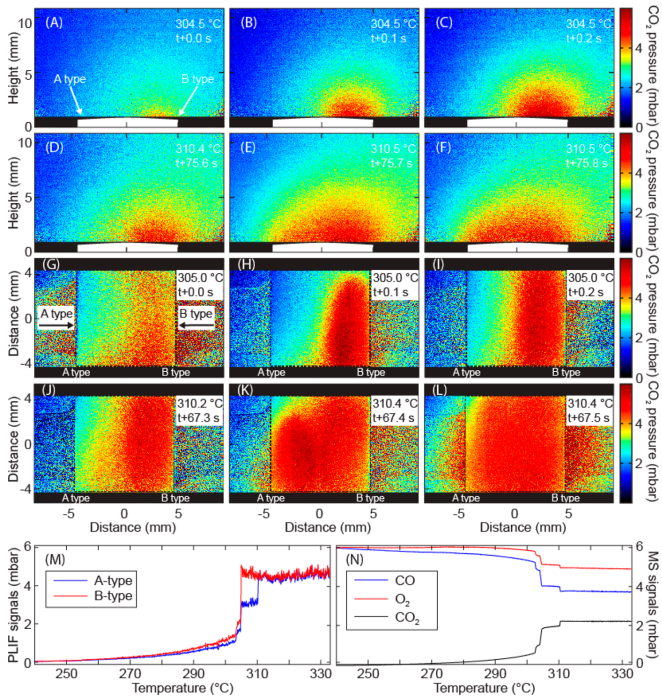

Figure 2. PLIF measurements revealing 6 °C lower CO_2 light-off temperature over the B-type side of the crystal in comparison to the corresponding A-type, in a 1:1 gas mixture of CO and O_2. PLIF images of the CO_2 catalytic reaction are collected over time as the temperature is increased by 0.05 °C/s. (A)−(F) Side view measurements where the white box at the bottom illustrates the position of the sample. (G)−(L) Top view measurements where the edges of the sample are marked with black lines. The temperature and time difference between each image are indicated in the top right corner of the images. (M) PLIF intensity extracted 0.5 mm over the B-type (red) and A-type (blue) side of the crystal, respectively, showing that light-off occurs earlier over the B-type side in comparison to the A-step side. (N) Mass spectrometry signals of CO, O_2, and CO_2, respectively, detected at the outlet of the reactor. See also movie M1 (side view) and movie M2 (top view) in the Supporting Information.

cylindrically shaped Pd crystal, where the curvature of the surface results in a smooth transition between a series of vicinal surfaces with the A- and B-step orientations separated by (111) terraces on each side of the crystal,[15−17] in conjunction with planar laser-induced fluorescence (PLIF)[18,19] (see sections 1 and 2 in the Supporting Information). Density functional theory (DFT) calculations support our findings and show, in contrast to what has been previously reported in the literature,

DOI: 10.1021/acscatal.6b02440
ACS Catal. 2017, 7, 110−114

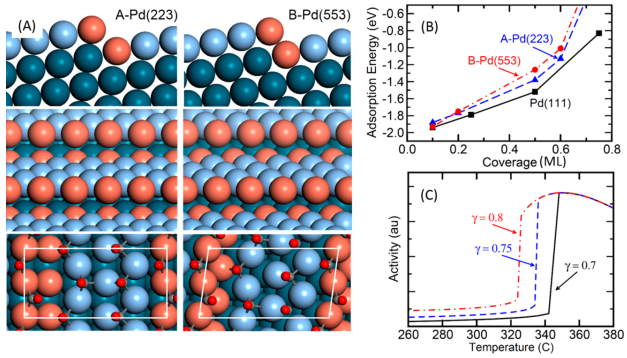

Figure 3. DFT calculations revealing different light-off temperatures for the central (111) facet and the A- and B-steps, respectively. (A) Structural models for the stepped surfaces. Pd(223) and Pd(553) were used as model surfaces for A- and B-steps, respectively. Two different side views are shown, and the surface cells are indicated by white lines in the top view. The structure for a CO coverage of 0.6 ML are reported at the bottom. The atoms at the steps, (111) microterraces, and bulk are shown in bronze, light blue, and dark blue, respectively. (B) Coverage dependence of the differential adsorption energy. (C) Reaction activity as a function of temperature. The light-off temperature depends critically on the coverage dependence of the CO desorption energy, given by the parameter γ. The desorption energy at low coverage (E^{d}_{CO}) is at higher coverage scaled according to $E^{d}_{CO}(1 - \gamma\theta)$.

that steps only have a secondary effect on the light-off temperature in CO oxidation and that strained microterraces are the primary areas at which the light-off occurs. Our results can be applied to industrial catalysts made up of nanoparticles that also consist of strained microterraces of varying sizes.

RESULTS

Cylindrical Pd Crystal and Its Characteristics. In our study we cut and polished a cylindrical Pd(111) crystal along the [111] symmetry direction with a total angle of $\alpha = \pm 15°$. The miscut introduced vicinal surfaces in the $[\bar{1}\bar{1}2]$ direction. These vicinal surfaces consist of (111) terraces, with stepwise decreasing widths, separated by {100}-like steps, hereafter denoted A-type steps, and {111}-like steps in the $[11\bar{2}]$ direction, hereafter denoted B-type steps (Figure 1A). This means that a cylindrically curved crystal provides all vicinal directions. Scanning tunneling microscopy characterization (Figure 1B) shows that, on both sides of the crystal, the step density increases with increasing angle, confirming the structural model. The smooth transition between adjacent vicinal surfaces is also confirmed by low-energy electron diffraction and X-ray diffraction (see sections 3–5 in the Supporting Information).

Planar Laser-Induced Fluorescence To Probe the Activity. We used PLIF to probe the catalytic light-off of the sample in situ during CO oxidation, and performed a side-by-side comparison of the activity around the different types of steps (see sections 1 and 2 in the Supporting Information for a description of PLIF). This method enables imaging of the CO_2 distribution over the curved surface with high spatial (70 μm) and temporal resolution (each measurement takes 15 μs with a repetition rate of 10 Hz). We conducted two separate experiments to obtain side (Figure. 2A–F) and top views (Figure. 2G–L) of the development of the catalytic activity over time with increasing temperature. The experiments were performed in the gas mixture of 4 mL_n/min each of CO and O_2, and 92 mL_n/min of the carrier gas Ar, at a total pressure of 150 mbar. The temperature was ramped at a rate of 0.05 °C/s, and images were acquired with an update frequency of 10 Hz.

We found that the catalytic reaction light-off occurs at 6 °C lower temperature for the B-type steps. At 304.5 °C the catalytic reaction over the B-type steps ignited (Figure 2A,G and movies M1 and M2 in the Supporting Information) and a CO_2 cloud was formed above it, reaching a steady state within approximately 0.2 s (Figure 2A–C,G–I). This indicates that the reaction becomes locally mass transfer limited by CO and an almost complete conversion of CO is detected over the B-type side. Simultaneously as the B-type side ignites a small increase in CO_2 signal is also observed over the A-type side, which is due to cross-talk from the highly active B-type side. The cross-talk could possibly affect the light-off temperature for the A-type side; however, our previous studies using one or two samples in the reactor during the CO oxidation reaction demonstrate that the light-off for one sample does not differ significantly even if a second sample is placed in the vicinity of the first. The size of the CO_2 cloud close to the B-type surface did not change noticeably for ~75.5 s, which corresponded to a temperature increase of 6 °C. At a temperature of 310.5 °C the A-type step side, as well as the central part of the crystal, became active, which is manifested by an increase in CO_2 concentration with a spherical shape close to the crystal surface (Figure 2D–F,J–L and movies M1 and M2 in the Supporting Information). The earlier light-off temperature of the B-side of the crystal is further seen in the CO_2 production plots extracted from the PLIF measurements 0.5 mm above each side of the crystal (Figure 2M) and the global gas composition in the chamber monitored by a mass spectrometer at the gas outlet (Figure 2N). While the mass spectrometer signals also show stepwise change of the gas composition that is related to the different light-off temperature of the two sides of the crystal, this method lacks in spatial resolution, meaning that it is not possible to correlate the signal to the specific step orientation of the crystal where the catalytic reaction occurs.

Both top and side view experiments indicate the same difference in light-off temperature, thus verifying the reprodu-

DOI: 10.1021/acscatal.6b02440
ACS Catal. 2017, 7, 110–114

cibility of the results. To rule out that the observed temperature differences of the two sides are not due to the direction of the gas flow, we further performed similar PLIF experiments on a sample rotated by 180°. The results from these experiments confirm a lower light-off temperature on the B-type side of the crystal.

DFT Calculations To Support and Explain Experimental Findings. To understand the observed difference in light-off temperatures between the two types of surface steps, we performed DFT calculations of CO adsorption on Pd(111) and two models of the A- and B-steps (Figure 3A). In particular, we calculated CO adsorption energies at different coverages because the CO adsorption energies are directly related to the desorption temperatures, which in turn determine the light-off temperatures of the reaction for the CO-saturated surface.[20] This approach may appear questionable, since CO-induced reconstructions of stepped surfaces have been observed previously for Pt and Cu vicinal surfaces.[21] However, no such CO-induced reconstructions have been observed for vicinal Pd surfaces,[22] and therefore we use unreconstructed Pd vicinal surfaces for our modeling.

The results and analysis reveal several important points. First, they show that steps are not necessarily and directly involved in the catalytic reaction onset but indirectly by releasing stress. At low CO coverages, the adsorption energy on the (111) microterraces and steps are within 0.03 eV for all three surfaces (see Figure 3B). At higher coverages, the CO adsorption energy on the (111) microterraces is lower than that of Pd(111). This is surprising, given that the local geometry of the preferred hollow adsorption sites is the same. However, the difference can be understood from tensile stress release of the (111) microterraces due to the presence of the steps,[16] but not at the extended (111) terrace at the center of the curved crystal. The contraction of the metal−metal bond distance in the surface layer at the (111) microterraces (∼1%) has clear effects on the electronic structure of the metal, which could be observed in the d-band center, which is a descriptor of the CO adsorption energy.[23,24] The d-band center with respect to the Fermi energy is −1.72 eV for Pd(111), whereas it is −1.89 eV for the two stepped surfaces. This result highlights the importance of strain effects in heterogeneous catalysis, because it indicates that the (111) microterraces of the stepped surfaces determine the light-off temperature, which has not been considered previously. Thus, the results show that steps can have a role other than simply providing undercoordinated sites, since here the steps have the role of releasing the stress but are not directly involved in the reaction onset.

The difference in light-off temperatures between the A and B step types can in turn be understood from the slight differences in coverage dependence of the CO adsorption energy, with the B-step having a stronger coverage dependence in comparison to the A-step (Figure 3B). At a coverage of 0.6 ML, the differential CO adsorption energy is 1.13 eV for the A-step, whereas it is 1.01 eV for the B-step. The reported adsorption energy of CO is overestimated due to the use of the PBE functional. However, the differences in adsorption energy among Pd(111) and A-type and B-type stepped surfaces are weakly dependent on exchange-correlation functional. With increasing CO coverage, the CO layer destabilizes because of the intermolecular repulsion, and assuming a linear coverage dependence of the differential adsorption energy ($E^{d}_{CO}(1 - \gamma\theta)$; see section 7 in the Supporting Information), the destabilization as a function of coverage occurs more quickly on the B-step than on the A-step, resulting in a lower light-off temperature on the B-step (Figure 3C). These theoretical observations are confirmed by X-ray photoelectron spectroscopy, in which a lower CO saturation coverage is found on the B- than on the A-step, which in turn has a lower coverage than the (111) facet in the center of the crystal (see section 6 in the Supporting Information).

The well-characterized surface of the crystal allows for a correlation between the step orientation and light-off temperatures but cannot reveal information about the most active step orientation after light-off, since the reaction is mass transfer limited by CO within 0.2 s after light-off on both sides. This is also supported by theory, as illustrated by the 2D volcano plot in Figure 7 in the Supporting Information. The two different surfaces representing the two different step orientations on the curved crystal are within the highest activity region where no obvious difference in activity is expected.

DISCUSSION

CO oxidation has been studied intensely, both experimentally and theoretically, for many decades, but a complete understanding of how the steps and their orientation affect the light-off temperature has not yet been reached. In this study, we have uncovered an important and unexpected role of the steps, which has not been considered before, that affects the light-off temperature in CO oxidation. The findings have been possible to achieve due to the use of PLIF, which provides the spatial and temporal resolution required to accomplish a direct comparison of the step orientations, and we combined our experimental observations with DFT. Our in situ comparison of A- and B-type steps, where the CO_2 production over a cylindrically shaped Pd crystal is probed by PLIF, reveals that the B-type steps have a 6 °C lower light-off temperature than the A-type steps. To our surprise, it also reveals that the stepped parts of the crystal, which is expected to be more reactive and thus have a higher CO desorption temperature, have a lower light-off temperature than the extended (111) surface at the center of the crystal. The DFT calculations suggest that the steps release the strain on the surfaces by decreasing the in-plane lattice constant, which is the reason for the lower light-off temperature on the stepped part of the crystal. The relaxation in turn affects the CO coverage differently on the A- and B-type stepped surfaces and explains why the B-type step part of the crystal reveals the lowest light-off temperature.

We propose the following new interpretation of the role of the steps, that CO oxidation does not start at the step edges as is often suggested in the literature but at the (111) terraces and that the role of the steps is to release strain in the (111) microterraces, facilitating the CO desorption and initiating the catalytic reaction. Although supported nanoparticles in an industrial catalyst are more complex systems and other factors are also influential, the present investigation on stepped surfaces provides fundamental knowledge of the light-off mechanism that can contribute to bridging the gap between model catalyst systems and industrial particles. When they are viewed in a greater perspective, the results may influence the understanding of the light-off temperatures of active facets of nanoparticles used as industrial catalysts or in electrochemical reactions where nanoelectrodes are used for oxygen and hydrogen production, especially in different energy applications. The light-off temperature depends on the ability of the

DOI: 10.1021/acscatal.6b02440
ACS Catal. 2017, 7, 110−114

nanoparticle terrace to relax, which in turn depends on the size of the nanoparticle facet.

The results cannot reveal information about the most active step orientation after light-off, since the reaction is mass transfer limited by CO. Therefore, it would be of great interest to explore the role of the steps after light-off but when the reaction is not mass transfer limited. We can furthermore speculate if the steps have similar effects in other reactions. It is already known that the reactivity, for instance in dissociation processes,[5] is higher at steps or at the corresponding edges between terraces on nanoparticles. In the meantime, our findings that the B-type stepped surface has a lower light-off temperature in CO oxidation provides strong support to look beyond the traditional view of the role of the steps in a catalytic reaction.

■ ASSOCIATED CONTENT

Supporting Information

The Supporting Information is available free of charge on the ACS Publications website at DOI: 10.1021/acscatal.6b02440.

Catalytic reaction light-off (AVI)
Methods (PLIF, STM, LEED, XRD, XPS) and theory (PDF)
Catalytic reaction light-off (AVI)

■ AUTHOR INFORMATION

Corresponding Author

*E-mail for S.B.: sara.blomberg@sljus.lu.se.

ORCID

Sara Blomberg: 0000-0002-6475-013X
Frederik Schiller: 0000-0003-1727-3542

Author Contributions

S.B., J.Zetterberg, J.G., J.E.O., and E.L. conceived and designed the experiments. S.B., J.Zetterberg, J.Zhou, L.R.M., J.G., M.S., L.A.M., A.M., M.I., F.S., F.B., and E.L. performed the experiments. S.B., J.Zetterberg, J.Zhou, L.R.M., L.A.M., and A.M. analyzed the data. A.T. and H.G. performed the theoretical calculations. S.B., J.Zetterberg, J.E.O., H.G., and E.L. cowrote the paper.

Notes

The authors declare no competing financial interest.

■ ACKNOWLEDGMENTS

The authors thank the Knut and Alice Wallenberg Foundation, the Swedish Research Council, the Swedish Foundation for Strategic Research, and the Crafoord Foundation. Support by the MAX IV staff is gratefully acknowledged. The calculations were performed at C3SE through a SNIC grant. J.E.O. acknowledges support from the Spanish Ministry of Economy (MAT2013-46593-C6-4-P) and the Basque Government (IT621-13).

■ REFERENCES

(1) Ertl, G. *Reactions at solid surfaces*; Wiley: Hoboken, NJ, 2009.
(2) Somorjai, G. A.; Li, Y. M. *Proc. Natl. Acad. Sci. U. S. A.* **2011**, *108*, 917−924.
(3) Hendriksen, B. L. M.; Ackermann, M. D.; van Rijn, R.; Stoltz, D.; Popa, I.; Balmes, O.; Resta, A.; Wermeille, D.; Felici, R.; Ferrer, S.; Frenken, J. W. M. *Nat. Chem.* **2010**, *2*, 730−734.
(4) Lang, B.; Joyner, R. W.; Somorjai, G. A. *Surf. Sci.* **1972**, *30*, 454−474.
(5) Zambelli, T.; Wintterlin, J.; Trost, J.; Ertl, G. *Science* **1996**, *273*, 1688−1690.
(6) Dahl, S.; Logadottir, A.; Egeberg, R. C.; Larsen, J. H.; Chorkendorff, I.; Tornqvist, E.; Norskov, J. K. *Phys. Rev. Lett.* **1999**, *83*, 1814−1817.
(7) Hammer, B.; Nielsen, O. H.; Norskov, J. K. *Catal. Lett.* **1997**, *46*, 31−35.
(8) Hammer, B. *Top. Catal.* **2006**, *37*, 3−16.
(9) Egeberg, R. C.; Dahl, S.; Logadottir, A.; Larsen, J. H.; Norskov, J. K.; Chorkendorff, I. *Surf. Sci.* **2001**, *491*, 183−194.
(10) Mavrikakis, M.; Stoltze, P.; Norskov, J. K. *Catal. Lett.* **2000**, *64*, 101−106.
(11) Valden, M.; Lai, X.; Goodman, D. W. *Science* **1998**, *281*, 1647−1650.
(12) Honkala, K.; Hellman, A.; Remediakis, I. N.; Logadottir, A.; Carlsson, A.; Dahl, S.; Christensen, C. H.; Norskov, J. K. *Science* **2005**, *307*, 555−558.
(13) Behrens, M.; Studt, F.; Kasatkin, I.; Kuhl, S.; Havecker, M.; Abild-Pedersen, F.; Zander, S.; Girgsdies, F.; Kurr, P.; Kniep, B. L.; Tovar, M.; Fischer, R. W.; Norskov, J. K.; Schlogl, R. *Science* **2012**, *336*, 893−897.
(14) Mavrikakis, M.; Hammer, B.; Norskov, J. K. *Phys. Rev. Lett.* **1998**, *81*, 2819−2822.
(15) Besocke, K.; Krahlurban, B.; Wagner, H. *Surf. Sci.* **1977**, *68*, 39−46.
(16) Walter, A. L.; Schiller, F.; Corso, M.; Merte, L. R.; Bertram, F.; Lobo-Checa, J.; Shipilin, M.; Gustafson, J.; Lundgren, E.; Brion-Rios, A. X.; Cabrera-Sanfelix, P.; Sanchez-Portal, D.; Ortega, J. E. *Nat. Commun.* **2015**, *6*, 8903.
(17) Janlamool, J.; Bashlakov, D.; Berg, O.; Praserthdam, P.; Jongsomjit, B.; Juurlink, L. B. F. *Molecules* **2014**, *19*, 10845−10862.
(18) Zetterberg, J.; Blomberg, S.; Gustafson, J.; Evertsson, J.; Zhou, J.; Adams, C. E.; Carlsson, P. A.; Aldén, M.; Lundgren, E. *Nat. Commun.* **2015**, *6*, 7076.
(19) Blomberg, S.; Brackmann, C.; Gustafson, J.; Alden, M.; Lundgren, E.; Zetterberg, J. *ACS Catal.* **2015**, *5*, 2028−2034.
(20) Burrows, M. G. T.; Stockmayer, W. H. *Proc. R. Soc. London, Ser. A* **1940**, *176*, 474−483.
(21) Tao, F.; Dag, S.; Wang, L. W.; Liu, Z.; Butcher, D. R.; Bluhm, H.; Salmeron, M.; Somorjai, G. A. *Science* **2010**, *327*, 850−853.
(22) Shipilin, M.; Gustafson, J.; Zhang, C.; Merte, L. R.; Lundgren, E. *Phys. Chem. Chem. Phys.* **2016**, *18*, 20312−20320.
(23) Hammer, B.; Norskov, J. K. *Surf. Sci.* **1995**, *343*, 211−220.
(24) Hammer, B.; Morikawa, Y.; Norskov, J. K. *Phys. Rev. Lett.* **1996**, *76*, 2141−2144.

DOI: 10.1021/acscatal.6b02440
ACS Catal. 2017, 7, 110−114

Supporting information

Strain dependent light-off temperature in catalysis revealed by planar laser-induced fluorescence

Sara Blomberg[1], Johan Zetterberg[2], Jianfeng Zhou[2], Lindsay R. Merte[1], Johan Gustafson[1], Mikhail Shipilin[1], Adriana Trinchero[3], Luis A. Miccio[5], Ana Magaña[4], Maxim Ilyn[6], Frederik Schiller[6], J. Enrique Ortega[4,5,6], Florian Bertram[7], Henrik Grönbeck[3] and Edvin Lundgren[1]*

[1] *Synchrotron Radiation Research, Lund University, Box 118, SE-221 00 Lund, Sweden*
[2] *Combustion Physics, Lund University, Box 118, SE-221 00 Lund, Sweden*
[3] *Competence Centre for Catalysis, Chalmers University of Technology, SE-412 96, Gothenburg, Sweden*
[4]*Departamento de Física Aplicada I, Universidad del Pais Vasco, 20018-San Sebastian, Spain*
[5]*Donostia International Physics Center DIPC, 20018- San Sebastian, Spain*
[6]*Centro de Física de Materiales CSIC/UPV-EHU Materials Physics Center, 20018-San Sebastian, Spain*
[7]*DESY Photon Science, Notkestr. 85, 22607 Hamburg, Germany*

Corresponding author: sara.blomberg@sljus.lu.se

Methods

S1. Planar laser-induced fluorescence, PLIF

In laser-induced fluorescence (LIF) a laser beam excites the molecule of interest, the excited molecule relaxes by emitting a photon, i.e. fluoresces, and the fluorescence light is then detected. The process is highly selective, meaning that the technique is species specific, targeting a specific molecule. It is also a relatively strong process, allowing for short gate times (ns-µs depending on wavelength region and molecule) and high repetition rates (limited by the laser pulse energy and molecule) but also means that it can be extended to 2D by forming the laser beam into a sheet of light and by detecting the ensuing fluorescence with a 2D detector. When LIF is implemented in a 2D fashion it is often referred to planar laser-induced fluorescence (PLIF), and is then highly spatially resolved along all three dimensions (down to 50 µm), i.e. it yields a cross section of the sought after species. In our experiments the target molecule was CO_2, the product molecule in CO oxidation. The CO_2 molecule lacks accessible transitions in the UV/visible spectral range, but can be reached through ro-vibrational transitions in the mid-infrared. There are several transitions that can be used in the mid-infrared, e.g. the overtone and combination band at around 2.0 µm ($12^01 \rightarrow 00^00$) (1), the combination band at 2.7 µm (00^00) $\rightarrow$ (10^001) (2, 3) and the fundamental band at around 4.3 µm (4). The overtone and combination band at around 2.0 µm is a weak transition compared to 2.7 and 4.3 µm, limiting the sensitivity. For the fundamental band at 4.3

μm, which was recently demonstrated, the high cross section becomes tricky in larger setups, since the laser beam is strongly attenuated in the ambient air. Owing to these reasons, the combination band at 2.7 μm was chosen in this study, it is stronger than the 2.0 μm band (around 45 times) but still weak enough so as not attenuate the laser radiation too much along the beam path.

Throughout our experiments, a laser system operated at 10 Hz generated the IR-laser light by difference-frequency mixing the output from a dye laser (PRSC-D-18, Sirah) at 763 nm with the fundamental frequency from a Nd:YAG laser (PRO 290-10, Spectra Physics) at 1064 nm in a $LiNbO_3$ crystal. The resulting 2.7 μm laser beam had a pulse energy of ~4 mJ, a pulse length of 5 ns and an estimated linewidth of 0.025 cm^{-1}. The 2.7 μm laser beam was formed into a laser sheet using sheet forming optics and was used to excite the P(18) line of the $(00^00) \rightarrow (10^001)$ of CO_2. The CO_2 fluorescence, originating from the fundamental band at 4.26 μm, was then imaged perpendicular to the lasersheet onto a 2D focal plane array (FPA) (SBF LP134, Santa Barbara Focal Plane) through an interference filter centered around 4.26 μm to discriminate background. To further discriminate the thermal background, an inherent difficulty when working in the mid-infrared regime, the FPA was triggered at 20 Hz, thus taking an extra image between every laser shot, making subtraction of the thermal background possible. The integration for each frame was 15 μs and chosen for efficient collection of the CO_2 fluorescence signal, which is more than 100 μs long at these pressures, while avoiding detector saturation by the thermal background. The CO_2 fluorescence images, with a spatial resolution of ~70 μm along all three dimensions (limited by the thickness of the lasersheet), visualized the distribution of CO_2 in the reaction chamber. The experimental set up is illustrated in Fig S1.

To minimize shot-to-shot fluctuations of the CO_2 fluorescence, the laser beam was split up and about 10 % of the light led through a reference cell. The reference cell was filled with a known CO_2 concentration at the same total pressure as in the experiments, ensuring that the width of the lines are the same as in the experiments. The CO_2 fluorescence was detected by a LN_2 cooled, InSb photovoltaic infrared detector (Judson, J10D). By doing this, the fluorescence signal can be compensated for shot-to-shot fluctuations of the laser energy and for slight wavelength instabilities, both on a shot-to-shot basis and over longer time.

Two different geometries for excitation and detection were utilized in this study, one where the laser sheet was vertical and the fluorescence light was imaged through the side window onto the FPA. The other with the laser sheet was incident in a horizontal fashion, Fig S1B. In this case the fluorescence light was collected through the top window, reflected on a mirror as close as possible to the window and again imaged onto the FPA. Both geometries used the same optics (a spherical lens with f = +200 mm and a cylindrical lens with f = -40 mm), the only difference being that the cylindrical lens was tilted 90°.

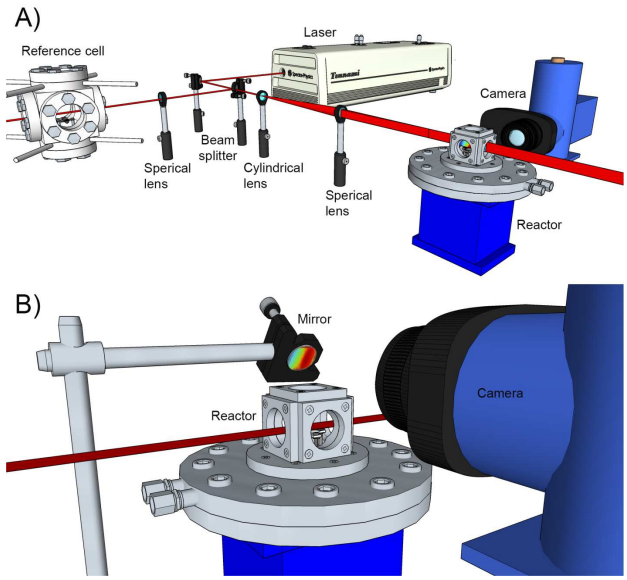

Fig S1. The PLIF experimental setup. A) The laser beam is shaped into a laser sheet with a cylindrical and spherical lens. The laser sheet can then interact with the CO_2 gas molecules in the chamber and by detecting the fluorescence light with a camera, an image of the CO_2 gas molecules is achieved. B) To generate the top view images, the laser sheet was flipped to be horizontal instead. A mirror positioned at the top of the chamber reflected the image onto the camera.

S2. The reactor and gas supply system

The PLIF measurements were performed in a stainless steel reactor with a cubic geometry and a volume of 23.5 ml. CaF_2 windows the with diameter of 25 mm (17 mm optical access), sealed with Viton O-rings, are installed on three sides and the top of the reactor, allowing for the IR-laser light to go through the reactor and interact with the CO_2 gas molecules close to the sample surface and for the fluorescence to reach the detector. To avoid reflections from the fourth side, a black stainless steel plate is covering the fifths side of the cube.

The bottom part of the reactor is attached to a base where the gases are introduced via a 1/8″ Swagelok connection in the reactor. The gas flows are regulated via five individual mass flow controllers (Bronkhorst EL-FLOW) with a capacity to individually flow up to 200 ml_n/min. A pressure controller (Bronkhorst EL-PRESS) is attached to the outlet to keep the pressure constant throughout the experiments. The gas composition in the reactor was measured with a quadruple mass spectrometer (Pfeiffer PrismaPlus QMG220, lowest partial pressure $4x10^{-12}$ mbar). The MS was connected to the outlet of the reactor via a 20 cm (d=1/16″) gas tube. The temporal resolution of the mass spectrometer is approximately 0.4 s for the individual gases. The sample is positioned on a Boron nitride heating cross, which is heated via a DC current. The temperature is measured on the heating cross with a type D thermocouple. A correlation between the sample temperature and the heating cross is done and the sample temperature can be determined. In addition an IR-camera (FLIRP620) was monitoring the temperature of the crystal from the top for the side view

measurements, and a 10 degree increase of the temperature could be observed upon light-off. The base for the reactor is equipped with a water cooling system in order to avoid temperature fluctuations of the reactor when heating the sample.

S3. STM

STM images have been systematically recorded at 300 K using a variable temperature STM setup (Omicron). The coarse movement of the STM piezos allows us to access different Pd surface orientations on the curved crystal. Large area scans indicate homogeneous, defect free, arrays of monatomic steps at all miscut angles in both A-type and B-type steps. We have performed a thorough analysis of individual frames with sizes between 40×40 and 300×300 nm^2, depending on the terrace width, using the WSXM software (5). The STM analysis is always limited to surface areas exhibiting homogeneous step arrays in the μm scale, which is generally the case of surface areas with $\alpha > 1.5^\circ$ values. STM images are automatically processed, and a probability histogram is then produced, which renders the mean terrace width d_m. Fig S2 shows the intensity plot built with all the terrace width histograms across the curved surface, and represented against d_m. We mark with a line the $d_m = d$ function namely the expected maximum for the symmetric distribution that characterizes strongly interacting steps (6). We note that the maxima in all histograms coincides with such line, except for the largest terrace widths d_m >10 nm (small miscut deviations), at which the maximum shifts to the left side of $d_m = d$ and the distribution becomes asymmetric. This means that elastic repulsive interactions between steps in both A-type and B-type steps in stepped Pd(111) appear to be stronger than in the case of stepped Pt(111), where probability maxima in the histograms depart from the $d_m = d$ line for d_m <10 nm (6).

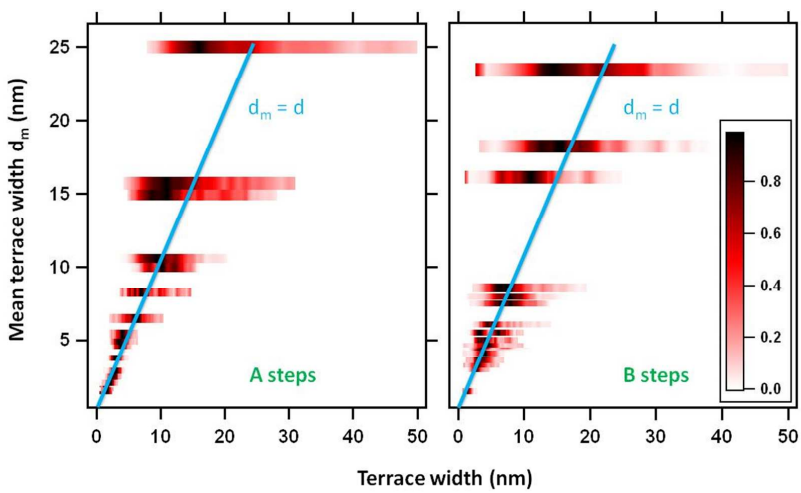

Figure S2. General STM analysis of the curved Pd surface. Image plot of the curved surface built with all the probability histograms at different mean terrace d_m values. Histograms are individually normalized to the maximum probability. This maximum follows the d_m=d line up to almost d_m=10 nm.

4. LEED

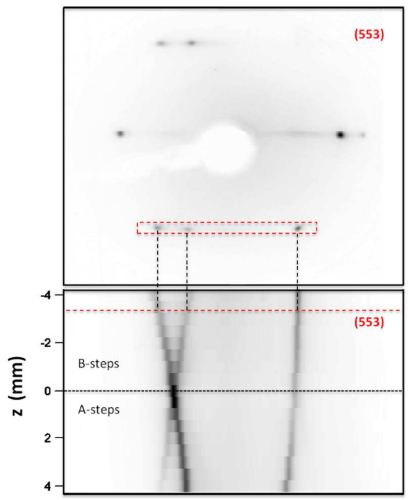

Figure S3 Top, Low Energy Electron Diffraction (LEED) pattern measured at the (553) plane of the Pd curved surface. The dotted rectangle marks the width utilized to integrate the line profile along the (0,-1)-(1,-1) spots shown in the bottom panel as a function of z. Bottom, image built with (0,-1)-(1,-1) LEED line scans taken across the curved sample in Δz=0.5 mm steps. The dotted line marks the line scan for the (553) surface on top, and the solid line the (111) direction.

For Low Energy Electron Diffraction (LEED) experiments, we move the sample position laterally ("z" scale in Fig. S3) to directly probe the different surface planes with a 0.2 mm broad, 82.7 eV electron beam. The standard LEED pattern of Fig. S3 (top) corresponds to the (553) surface, and exhibits the characteristic splitting of the diffracted beams observed in stepped surfaces. The dotted, red rectangle indicates a selected line over this LEED pattern, crossing the (0,-1) and (1,-1) spots. The "collage" image below is then built with individual (0,-1)-(1,-1)line profiles acquired in Δz = 0.5 mm-steps across the curved surface. The resulting image reflects the linear variation of the spot splitting at both sides of the crystal, demonstrating that the Pd(111) curved surface is microscopically defined by monatomic step arrays with smoothly varying step density and negligible step bunching or faceting.

5. XRD

The measurements were carried out at beamline P07 of PETRA III at Deutsches Elektronen-Synchrotron (DESY), which is designed for materials studies with hard X-ray radiation. The X-ray beam had a photon energy of 85 keV and an incident angle of 0.04°, close to the critical angle for total external reflection of Pd(100). The scattered X-rays were detected using a large area Perkin-Elmer detector. To create the desired environment for catalytic reactions we used a specially designed UHV chamber/reactor, similar to the one reported in Ref. (7). It allows

pressures in the 10^{10} Torr range for surface preparation as well as a controlled gas pressure up to 1 atmosphere in the reactor chamber.

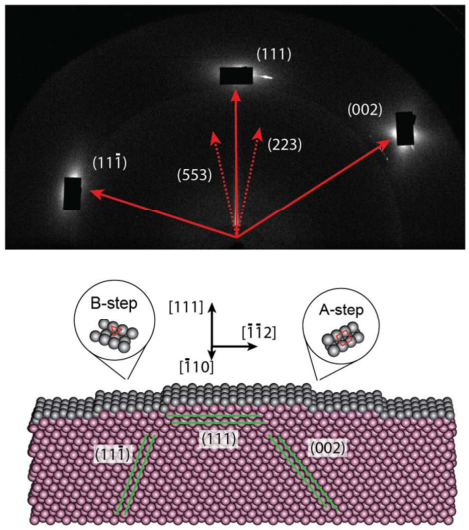

Figure S4. Top: Grazing-incidence X-ray diffraction pattern of the curved crystal to determine the orientation of the steps, obtained with the incident beam parallel to the axis of curvature. Metal blocks cover the intense Bragg reflections, but the bright tails of the (111), (11-1) and (002) reflections are visible. Bottom: Model of the Pd crystal orientation as determined by XRD, with lattice planes corresponding to Bragg reflections indicated. Inclination of the surface normal toward the (002) produces A-type steps while inclination toward the (11-1) produces B-type steps.

S6. XPS

XPS measurements were performed at the spectroscopy endstation of the I311 beamline at the MAX-IV Laboratory, Lund, Sweden (8). This undulator beamline employs a Zeiss SX-700 monchromator with 1200 l/mm grating providing X-ray radiation over a range of ~50–1500 eV. Spectra were collected using a Scienta SES200 analyzer. XPS spectra were collected in normal emission geometry using a photon energy of 650 eV and 400 eV for excitation of O 1s, Pd 3d and C1s core levels, respectively. The same set of spectra were recorded for three different positions on the sample which allowed for measurements on the A-type and B-type steps as well as the (111) facet on the surface. The sample was mounted in such a way that only the Z-direction was changed with an mm-screw in order to move between the different positions.

For XPS measurements, the sample was mounted between tungsten wires through which a DC current was passed for heating, and the temperature was measured by a type K thermocouple welded to the rear of the curved crystal.

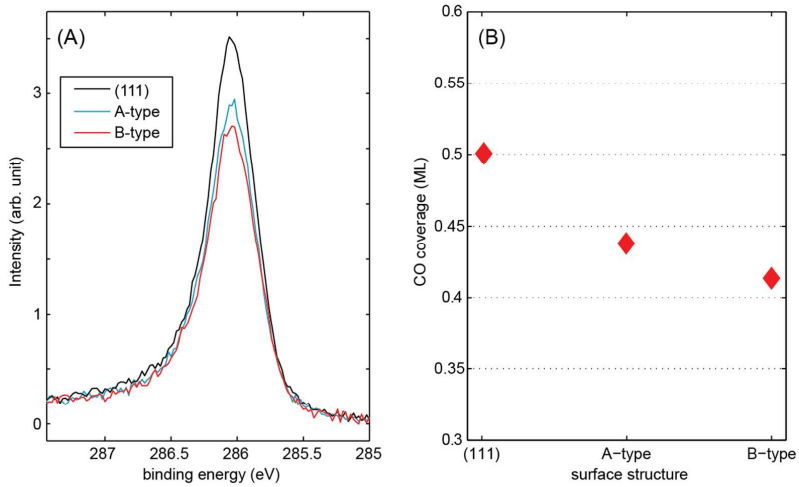

Figure S5. The CO coverage on the cylindrical crystal after 100L CO exposure at room temperature. A) The C1s spectra normalized to the background where the area of the peak indicates the CO coverage. The three C1s spectra represent the CO coverage at (111) (black), A-type side (green) and B-type side (red) positions of the crystal. B) The area is converted into CO coverage and the plot indicates that the lowest CO coverage is observed on the B-type side.

In Figure S5, the C1s spectra recorded after 100L (solid line) CO exposure are shown. The relative intensity between the difference positions on the surface, black (111) green A-type side, red B-type side shows a decreasing coverage where the highest intensity is observed for the (111) followed by the A-type side and B-type side.

The indicated CO coverage presented on all surfaces in here is referred to percentage of monolayer on the Pd(111) surface. The formation of a c(4×2) structure on the (111) surface has previous been observed to reach the saturation coverage of 0.5 ML at 300 K and exposure of a minimum of 3 L CO. We therefore conclude that at 100 L CO the (111) surface has a CO coverage of 0.5 ML which is correlated to the intensity of the C 1s spectra recorded on the (111) position of the crystal. In the evaluation procedure the C1s spectrum recorded at the (111) position are set as a reference to estimate the CO coverage on all three positions, shown in Fig S5. The spectra are normalized to the raw data background before a linear background is fitted and subtracted in order to achieve the area of the C 1s spectra. A linear dependency between the area and CO coverage is assumed and applied in the conversion from area to ML procedure.

S7. Theory

Density Functional Theory/DFT) was applied using the gradient corrected exchange correlation functional according to Perdew, Burke, and Ernzerhof (PBE) (9). The single-electron Kohn-Sham orbitals were expanded in a local numerical basis set (10, 11). In particular, a double numerical basis set was used together with polarization functions. A semicore pseudopotential was used to describe the interaction between the valence electrons ($4s^2 4p^6 4d^{10}$) and the core for Pd. The Kohn-Sham equations were solved self-consistently using an integration technique based on weighted overlapping spheres centered at each atom. In all calculations, repeated slabs including

five Pd-layers were separated by at least 12 Å. Reciprocal space integration over the Brillouin zone was approximated with finite sampling using the Monkhorst-Pack scheme. The Pd(111) surfaces were modelled in *p*(4×4), (4×2√3)rect and *p*(3×3) surface cells respectively. The k-point mesh was (3×3×1) for the smaller cell, whereas a (2×2×1) mesh was used for *p*(4×4) and (4×2√3)rect. The Pd(223) and Pd(553) surfaces were treated in *p*(2×1) surface cells. The *k*-point sampling was in these cases done with a (5x2x1) mesh. Geometry optimization was performed with the two bottom layers fixed to the bulk coordinates and the structures were regarded to be optimized when convergence criteria of 0.02 eV/Å, 0.0002 eV, and 0.002 Å were met for the largest gradient, total energy, and largest change in coordinates, respectively.

All unique adsorption sites for CO were considered for the low coverage case, *i.e.* one CO molecule in the *p*(3×3) surface cell of Pd(111) or the *p*(2×1) surface cell of Pd(223) and Pd(553). The 0.5 ML and 0.75 ML coverage situation for Pd(111) were modelled with the experimentally proposed structures. The 0.5 ML coverage has a *c*(4×2) surface cell (12, 13) which was modelled in a (4×2√3)rect surface cell whereas the 0.75 ML coverage has a *p*(2×2) structure (14) modelled in a p(4×4) surface cell. The higher coverage situations for the stepped surfaces were modelled by evaluating about 60 possible configurations. The differential adsorption energy for a specific coverage was modelled by removing one CO molecule from the surface cell.

The micro-kinetic modelling of the light-off was based on the conventional Langmuir-Hinshelwood mechanism for CO oxidation (15):

$CO + * \leftrightarrow CO*$ (R1)

$O_2 + 2* \leftrightarrow 2O*$ (R2)

$O* + CO* \leftrightarrow CO_2 + 2*$ (R3)

Free surface sites are denoted *, *i.e.* X* corresponds to an adsorbate X bonded to a surface site. The corresponding rate equations are:

$$\frac{d\theta_{CO}}{dt} = s_{CO}^{0}(1-\theta_{CO}^{2})\,p_{CO}k_{CO}^{a} - k_{CO}^{d}\theta_{CO} - k^{r}\theta_{CO}\theta_{O}$$

$$\frac{d\theta_{O}}{dt} = 2s_{O}^{0}(1-\theta_{CO}-\theta_{O})^{2}\,p_{O_2}k_{O_2}^{a} - k_{O_2}^{d}\theta_{O}^{2} - k^{r}\theta_{CO}\theta_{O}$$

Here, θ_{CO} and θ_{O} are the coverages, p_{CO} and p_{O_2} are the pressures, and s_{CO}^{0} and $s_{O_2}^{0}$ the initial sticking coefficients. The rate constants are given by:

$$k_{CO}^{d} = \nu_{CO}^{d} e^{-E_{CO}^{d}(1-\gamma\theta_{CO})/k_B T}$$

$$k_{O_2}^{d} = \nu_{O_2}^{d} e^{-E_{O_2}^{d}(1-\gamma\theta_{O})/k_B T}$$

$$k^{r} = \nu^{r} e^{-E^{r}(1-\beta\theta_{CO})/k_B T}$$

$k_X^a = 1/N_0\sqrt{(2\pi M k_B T)}$

T is the temperature, k_B is the Boltzmann constant, M is the mass of the molecule, and N_0 is the number of sites per area. A linear coverage dependence is introduced for the adsorption energies (E_X^d) and the barrier. Desorption of O_2 is included for completeness, it does not affect the reaction kinetics. The pre-exponential factors are in the modelling of the light–off set to $\nu_{CO}^d = 10^{17}$ and $\nu^r = 10^{14}$, respectively. The sticking coefficients of CO and O_2 has been measured to be structure insensitive over Pd surfaces (see Ref.(16) for a compilation) and both sticking coefficients were set to 0.9. In addition to the light-off simulations, the steady state activity for the three different surfaces were modelled assuming (R3) to be the rate limiting step and the other steps in quasi-equilibrium (17). The reaction barrier was in the simulations calculated from the CO and O adsorption energies according using the scaling relation put forth in Ref.(17).

One interesting finding is that CO at low coverage does not show any clear preference for adsorption at Pd(223) and Pd(553) step sites. This is related to the fact that CO preferentially adsorbs in the fcc three-fold hollow position. Pd(223) has four different fcc sites. The two sites at the (111) micro-facet are calculated to have adsorption energies of 1.89 and 1.86 eV, respectively. The hollow site above the step is for Pd(223) of hcp type and the adsorption energy for this site is calculated to be 1.88 eV, whereas adsorption in a bridge position at the step has an adsorption energy of 1.87 eV. The adsorption energy at the fcc site below the step is 1.71 eV. For Pd(553), the hollow site just above the step is an fcc site with an adsorption energy of 1.93 eV. The sites on the (111) micro-facets have in this case adsorption energies of 1.91 and 1.88 eV, respectively. The fcc site just below the step has an adsorption energy of 1.69 eV, whereas the bridge site at the step is calculated to have an adsorption energy of 1.78 eV. The low adsorption energy of this site is connected to the (111)/(111) character of this step. On Pd(111), the bridge site is calculated to be 0.15 eV less stable than the fcc site.

The lower adsorption energies of CO on the micro (111) facets of Pd(553) and Pd(223) as compared to Pd(111) is related to relaxation of in-plane strain owing to the presence of the step. It is well known that stress may influence the reactivity of metal surfaces, see e.g. Ref. (18).

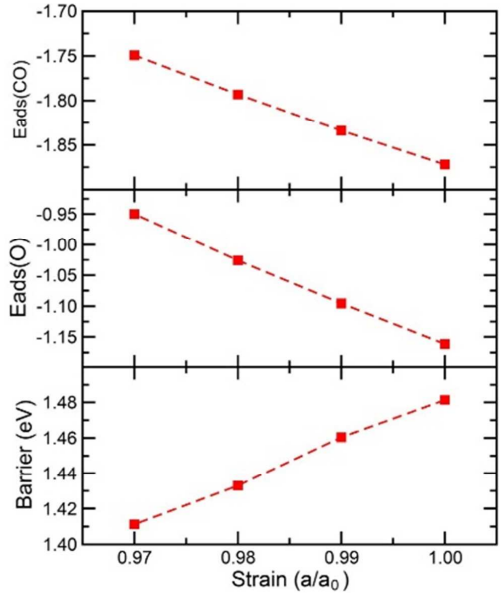

Figure S6. CO and O adsorption energy on Pd(111) as a function of strain. a_0 denotes the equilibrium lattice constant.

In Figure S6 we show how the adsorption of CO and oxygen together with the CO oxidation barrier change on Pd(111) as a function of compressive strain. The adsorption energies and also the barrier scale linearly with the strain. In the light-off experiments, it is the reduction of the CO adsorption energy that is crucial. The linear scaling could be understood within the *d*-band model as the center of the *d*-band shifts to lower energies with respect to the Fermi energy upon compressive strain.

At higher CO coverage, the molecular interactions could be affected by van der Waals interactions. We have investigated this by applying the Tkatchenko-Scheffler (TS) method (19, 20). The coverage dependence with the TS-scheme is compared to the PBE calculations for Pd(111) in Figure S7. The inclusion of vdW-corrections is merely found to stabilize adsorption energies by 0.2-0.3 eV.
We have chosen to focus on the PBE-results because of the too strong bonding of CO to palladium in the TS-scheme. Also PBE is overestimating the adsorption energy which is experimentally is about 1.5 eV at 0.25 ML coverage (21). Because of this, we have performed some calculations with the RPBE functional (22). The results are collected in Table S1. Here we focus on higher coverage as this is important for the light-off temperature. Although the adsorption energy is reduced with RPBE we find that the differences between Pd(223), Pd(553) and Pd(111) are weakly dependent on functional.

	Pd(553)(0.6 ML)	Pd(223)(0.6 ML)	Pd(111)(0.5 ML)	Pd(111)(0.25ML)
RPBE	-1.14	-1.19	-1.33	-1.45
PBE	-1.54	-1.58	-1.74	-1.86

VDW	-1.76	-1.79	-1.97	-2.06

Table S1: Adsorption energy (eV) for CO on Pd(553), Pd(223), Pd(111). The coverage is 0.6 ML for the stepped surfaces, whereas the coverages 0.5 ML and 0.25 ML is shown for Pd(111).

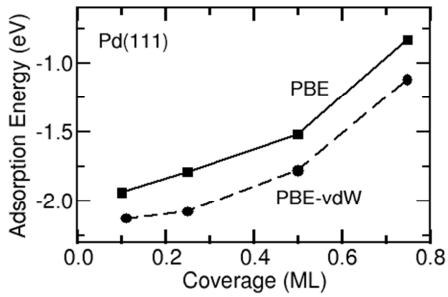

Figure S7. Differential adsorption energy of CO within the PBE+TS scheme. Note that the differential adsorption energy is reported in the main text.

Once the temperature is high enough for CO to desorb all three surfaces Pd(111), Pd(223) and Pd(553) are highly active for CO oxidation. Following the scaling between adsorption energies and reaction barriers for CO(23), the activities at steady state were evaluated at put in context by calculating the volcano plot for a range of CO and O adsorption energies, see Figure S8. The three surface are all close the top of the volcano.

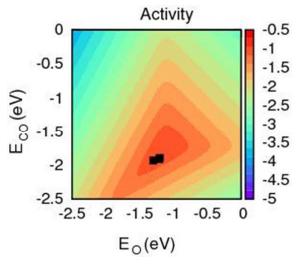

Figure S8. Activity for CO oxidation reaction as a function of CO and O adsorption energies.

References

(1) Alwahabi, Z. T.; Zetterberg, J.; Li, Z. S.;Alden, M., *Eur Phys J D* **2007**, *42,* 41-47.

(2) Zetterberg, J.; Blomberg, S.; Gustafson, J.; Sun, Z. W.; Li, Z. S.; Lundgren, E.;Alden, M., *Rev Sci Instrum* **2012**, *83,* 053104.

(3) Kirby, B. J.;Hanson, R. K., *Appl Optics* **2002**, *41,* 1190-1201.

(4) Goldenstein, C. S.; Miller, V. A.;Hanson, R. K., *Appl Phys B-Lasers O* **2015**, *120,* 185-199.

(5) Horcas, I.; Fernandez, R.; Gomez-Rodriguez, J. M.; Colchero, J.; Gomez-Herrero, J.;Baro, A. M., *Rev Sci Instrum* **2007**, *78,* 013705.

(6) Walter, A. L.; Schiller, F.; Corso, M.; Merte, L. R.; Bertram, F.; Lobo-Checa, J.; Shipilin, M.; Gustafson, J.; Lundgren, E.; Brion-Rios, A. X.; Cabrera-Sanfelix, P.; Sanchez-Portal, D.;Ortega, J. E., *Nat Commun* **2015**, *6,* 8903.

(7) van Rijn, R.; Ackermann, M. D.; Balmes, O.; Dufrane, T.; Geluk, A.; Gonzalez, H.; Isern, H.; de Kuyper, E.; Petit, L.; Sole, V. A.; Wermeille, D.; Felici, R.;Frenken, J. W. M., *Rev Sci Instrum* **2010**, *81,* 014101.

(8) Nyholm, R.; Andersen, J. N.; Johansson, U.; Jensen, B. N.;Lindau, I., *Nucl Instrum Meth A* **2001**, *467,* 520-524.

(9) Perdew, J. P.; Burke, K.;Ernzerhof, M., *Phys Rev Lett* **1996**, *77,* 3865-3868.

(10) Delley, B., *J Chem Phys* **1990**, *92,* 508-517.

(11) Delley, B., *J Chem Phys* **2000**, *113,* 7756-7764.

(12) Giessel, T.; Schaff, O.; Hirschmugl, C. J.; Fernandez, V.; Schindler, K. M.; Theobald, A.; Bao, S.; Lindsay, R.; Berndt, W.; Bradshaw, A. M.; Baddeley, C.; Lee, A. F.; Lambert, R. M.;Woodruff, D. P., *Surf Sci* **1998**, *406,* 90-102.

(13) Rose, M. K.; Mitsui, T.; Dunphy, J.; Borg, A.; Ogletree, D. F.; Salmeron, M.;Sautet, P., *Surf Sci* **2002**, *512,* 48-60.

(14) Kuhn, W. K.; Szanyi, J.;Goodman, D. W., *Surf Sci* **1992**, *274,* L611-L618.

(15) Carlsson, P. A.; Skoglundh, M.; Thormahlen, P.;Andersson, B., *Top Catal* **2004**, *30-1,* 375-381.

(16) Vogel, D.; Spiel, C.; Suchorski, Y.; Trinchero, A.; Schlogl, R.; Gronbeck, H.;Rupprechter, G., *Angew Chem Int Edit* **2012**, *51,* 10041-10044.

(17) Chorkendorff, I.;Niemantsverdriet, J. W., *Concepts of modern catalysis and kinetics*, Wiley-VCH, Weinheim Germany, **2003**.

(18) Jiang, T.; Mowbray, D. J.; Dobrin, S.; Falsig, H.; Hvolbaek, B.; Bligaard, T.;Norskov, J. K., *J Phys Chem C* **2009**, *113,* 10548-10553.

(19) Tkatchenko, A.;Scheffler, M., *Phys Rev Lett* **2009**, *102,* 073005.

(20) McNellis, E. R.; Meyer, J.;Reuter, K., *Phys Rev B* **2009**, *80,* 205414.

(21) Wellendorff, J.; Silbaugh, T. L.; Garcia-Pintos, D.; Norskov, J. K.; Bligaard, T.; Studt, F.;Campbell, C. T., *Surf Sci* **2015**, *640,* 36-44.

(22) Hammer, B.; Hansen, L. B.;Norskov, J. K., *Phys Rev B* **1999**, *59,* 7413-7421.

(23) Mavrikakis, M.; Hammer, B.;Norskov, J. K., *Phys Rev Lett* **1998**, *81,* 2819-2822.

Paper VII

ACCOUNTS of chemical research

Article

pubs.acs.org/accounts

Novel in Situ Techniques for Studies of Model Catalysts

Edvin Lundgren,*[,†] Chu Zhang,[†] Lindsay R. Merte,[†] Mikhail Shipilin,[†] Sara Blomberg,[†] Uta Hejral,[†] Jianfeng Zhou,[‡] Johan Zetterberg,[‡] and Johan Gustafson[†]

[†]Division of Synchrotron Radiation Research, Lund University, Box 118, Lund S-221 00, Sweden

[‡]Division of Combustion Physics, Lund University, Box 118, Lund S-221 00, Sweden

CONSPECTUS: Motivated mainly by catalysis, gas−surface interaction between single crystal surfaces and molecules has been studied for decades. Most of these studies have been performed in well-controlled environments and have been instrumental for the present day understanding of catalysis, providing information on surface structures, adsorption sites, and adsorption and desorption energies relevant for catalysis. However, the approach has been criticized for being too far from a catalyst operating under industrial conditions at high temperatures and pressures. To this end, a significant amount of effort over the years has been used to develop methods to investigate catalysts at more realistic conditions under operating conditions. One result from this effort is a vivid and sometimes heated discussion concerning the active phase for the seemingly simple CO oxidation reaction over the Pt-group metals in the literature.

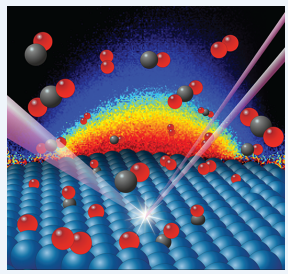

In recent years, we have explored the possibilities to perform experiments at conditions closer to those of a technical catalyst, in particular at increased pressures and temperatures. In this contribution, results from catalytic CO oxidation over a Pd(100) single crystal surface using Near Ambient Pressure X-ray Photo emission Spectroscopy (NAPXPS), Planar Laser-Induced Fluorescence (PLIF), and High Energy Surface X-ray Diffraction (HESXRD) are presented, and the strengths and weaknesses of the experimental techniques are discussed. Armed with structural knowledge from ultrahigh vacuum experiments, the presence of adsorbed molecules and gas-phase induced surface structures can be identified and related to changes in the reactivity or to reaction induced gas-flow limitations. In particular, the application of PLIF to catalysis allows one to visualize how the catalyst itself changes the gas composition close to the model catalyst surface upon ignition, and relate this to the observed surface structures. The effect obscures a straightforward relation between the active phase and the activity, since in the case of CO oxidation, the gas-phase close to the model catalyst surface is shown to be significantly more oxidizing than far away from the catalyst. We show that surface structural knowledge from UHV experiments and the composition of the gas phase close to the catalyst surface are crucial to understand structure−function relationships at semirealistic conditions. In the particular case of Pd, we argue that the surface structure of the PdO(101) has a significant influence on the activity, due to the presence of Coordinatively Unsaturated Sites (CUS) Pd atoms, similar to undercoordinated Ru and Ir atoms found for RuO_2(110) and IrO_2(110), respectively.

1. INTRODUCTION

Heterogeneous catalysis, in which the catalyst (solid) is in another phase than the reactants (gas), is of significant importance for the development of modern society. A catalytic material speeds up an otherwise slow chemical reaction or changes the selectivity without being consumed by the process, making chemical products cheaper to produce, enhancing food production by enabling artificial and effective fertilizers and cleaning unwanted exhaust gases from vehicles.[1] However, since the active material of an industrial catalyst often consists of metallic nanoparticles that are supported on an amorphous or crystalline insulating oxide, and since the catalytic reaction takes place at the surface of such nanoparticles at several hundreds of degrees Celsius and at gas pressures of several bar, the atomic scale process governing the catalytic reaction is notoriously difficult to study. It is therefore understandable that the technical development of new and improved catalysts has been performed using a trial-and-error approach, an approach that has been extremely successful, most notably the improvement of the air quality in densely populated areas due to the development of more efficient catalysts for vehicles[2] but also for numerous other applications.

Nevertheless, the quest for a deeper understanding of the atomic scale process has been pursued for many decades, and the observation that the facets of nanoparticles can be mimicked by extended single crystal surfaces[1] or supported nanoparticles[3] greatly facilitates investigations of the catalytic properties of surfaces and gives rise to the so-called model catalyst. Further, the use of ultrahigh vacuum (UHV) has enabled controlled studies of gas−surface interactions and surface reactions. This development produced the foundation of modern surface science with catalysis as an application, a considerable part of the field of surface science.

The surface science approach has been and still is extremely successful and has provided useful information on adsorption sites, dissociation processes, surface reactions, and surface structures

Received: June 2, 2017
Published: September 7, 2017

ACS Publications © 2017 American Chemical Society

DOI: 10.1021/acs.accounts.7b00281
Acc. Chem. Res. 2017, 50, 2326−2333

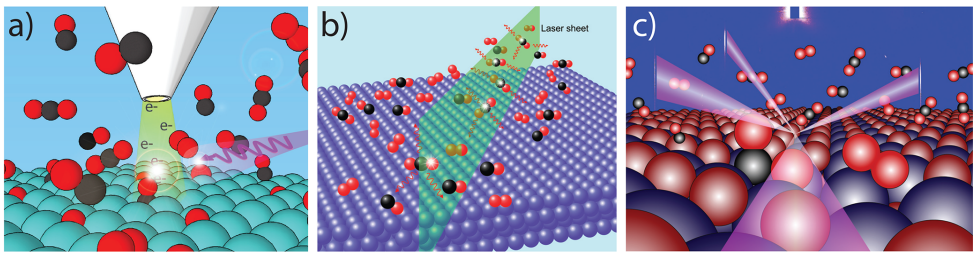

Figure 1. (a) An artist's view of the NAPXPS experiment performed in this Account. An incoming photon with an energy of a few 100 eV creates a core electron by photoemission, which is detected by an electron analyzer. Due to differential pumping of the analyzer, a maximum pressure of 1 mbar has been used in the NAPXPS data presented here. (b) An artist's view of PLIF applied to catalysis. A laser sheet with an appropriate energy excites a rotational−vibrational level in the probed molecule, and the resulting fluorescence is detected by a 2D-detector. The experiments reported in this Account use total pressures up to 200 mbar. (c) An artist's view of HESXRD. Photons with an energy of 85 keV impinge grazing on a surface, giving rise, due to elastic scattering and interference, to a forward oriented diffraction pattern originating from the arrangement of the surface atoms. The diffraction pattern is detected on a large 2D detector. Using this approach total pressures up to 200 mbar were used, although ambient pressures can be used in a straightforward way. Simultaneous mass spectrometry (MS) measurements were performed during the HESXRD and PLIF measurements, while the gas-phase composition was probed by the core electrons from the gas-phase molecules in the NAPXPS measurements.

being involved in a catalytic process. This information has facilitated the understanding of observations using the trial-and-error approach, enabling a more intellectual developmental approach.[4] A significant recognition for the approach came with the Nobel prize awarded to G. Ertl in 2007.[5]

However, simultaneously as the concept of an extended model catalyst and controlled environments was developed, criticism arose arguing that the approach is too far away from the industrial situation and might even obscure the real underlying processes during operation of the catalyst in industrial environments. It is essential to realize that the combination of the environment (gas or liquid) and the active material will determine the atomistic processes governing the activity or properties of the combined system. It can therefore be argued that it is not enough to perform ex situ studies. The discussion introduced the concepts of pressure and materials gaps between fundamental research and applications and inspired research attempting to bridge these gaps.[6−9]

In the past decade, a number of techniques have been developed for in situ studies of catalytic reactions at semirealistic conditions using model catalysts. For many years, Polarization Modulation-Infrared Reflection Absorption Spectroscopy (PM-IRAS),[10,11] X-ray Absorption Spectroscopy (XAS)[12] and Sum Frequency Generation (SFG)[13] were the state-of-the art techniques that allowed for in situ studies of well-defined surfaces. Recent experimental advances have produced Near-Ambient Pressure X-ray Photoelectron Spectroscopy (NAPXPS),[14−16] High-Pressure Scanning Tunneling Microscopy (HP-STM),[17] in situ Surface X-ray Diffraction (SXRD)[18] and Environmental Transmission Electron Microscopy (E-TEM)[19] resulting in an extension of the in situ experimental toolbox.[7]

Our contribution in this rapid development has been in the development of High-Energy Surface X-ray Diffraction at ultrahigh X-ray energies (HESXRD)[20−24] and of Planar Laser-Induced Fluorescence (PLIF)[25−33] applied to catalysis, providing new experimental approaches for in situ measurements.

In most studies at semirealistic conditions, the focus has been to determine the active phase during the catalytic reaction of CO to CO_2. The reaction is important since CO is toxic, is a result of the incomplete combustion of hydrocarbon fuels, and should be removed from exhausts from engines based on hydrocarbons by purification with catalyst. Further, CO is a potent poison for certain oxidation reactions and must therefore also be removed from the reactants.[34] Interestingly, the studies of the CO oxidation reaction at semirealistic conditions encountered almost immediately a controversy concerning the active phase, which remains today. A number of scientists favored chemisorbed oxygen on the catalytic surface as the active agent,[35] while others favored a thin oxide.[36]

Here we will present results from the seemingly simple catalytic CO oxidation, which have served as a benchmark system in UHV surface science for gas−solid interactions,[37] over a Pd(100) surface. Our goal is not to reveal the nature of the active phase during CO oxidation but rather to illustrate the capability and potential of NAPXPS, PLIF, and HESXRD to gain a deeper understanding of catalytic processes under semirealistic conditions, allowing for a comparison between behavior in UHV and semirealistic conditions. The combination of these techniques provides new information on the reaction, and combined with results from other workers, the active phase will be discussed. We will show that surface structural knowledge from UHV experiments is absolutely necessary, as is the exact composition of the gas phase close to the catalyst surface, to understand structure−function relationships at semirealistic conditions. The strengths and weaknesses of the experimental techniques will be discussed and an outlook for future developments and applications will be given.

2. CO AND O_2 INDUCED STRUCTURES ON PD(100)

2.1. CO Induced Structures

The CO adsorption on Pd(100) had been studied intensively[38−41] with a range of experimental techniques, and its adsorption has been determined to be in bridge sites for all coverages. The ordered structures that have been observed are $c(2\sqrt{2} \times \sqrt{2})R45°$ (0.5 ML), $c(3\sqrt{2} \times \sqrt{2})R45°$ (0.67 ML), and $c(4\sqrt{2} \times \sqrt{2})R45°$ (0.75 ML). The structures formed above the 0.5 ML $c(2\sqrt{2} \times \sqrt{2})R45°$ structure are associated with the insertion of denser CO lines between domains of $c(2\sqrt{2} \times \sqrt{2})R45°$.[42,43]

2.2. O_2 Induced Structures

Similar to CO adsorption, oxygen adsorption on Pd(100) has been studied for a long time.[21,24,44−46] Here, two surface structures, the

DOI: 10.1021/acs.accounts.7b00281
Acc. Chem. Res. 2017, 50, 2326−2333

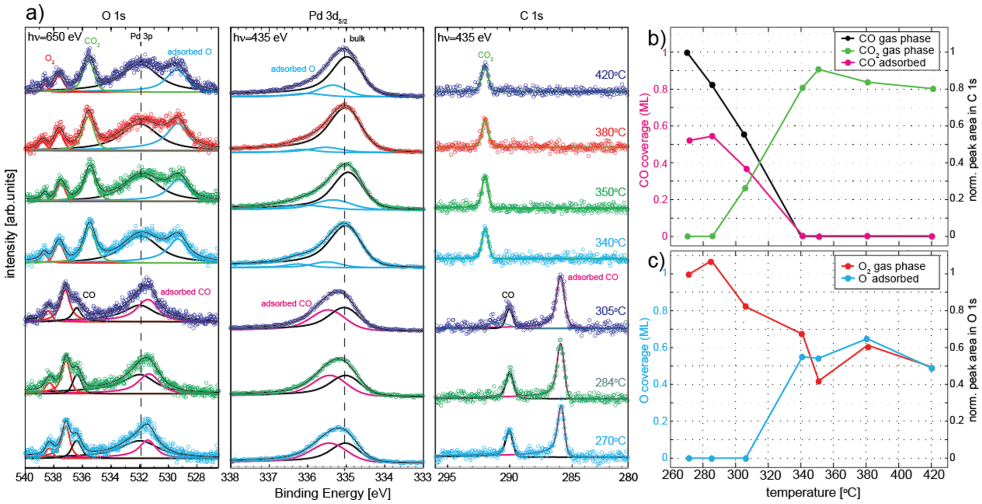

Figure 2. (a) NAPXPS spectra during CO oxidation over a Pd(100) surface using 0.67 mbar CO and 0.67 mbar O_2, as the temperature is increased from bottom to top. (right) C 1s spectra in which emission from the CO adsorbed on the surface and from the gas-phase, as well as emission from the carbon in the CO_2, are indicated. (middle) the Pd $3d_{5/2}$ core level region, the deconvolution indicating if CO or chemisorbed oxygen is adsorbed on the surface. (left) O 1s binding energy region in which the emission from CO, CO_2, and O_2 are indicated. The emission from the Pd 3p core level is also indicated. (b) The CO (black) and CO_2 integrated area normalized to the initial CO gas phase and the amount of adsorbed CO assuming an initial coverage of 0.5 ML. (c) The O_2 gas phase integrated area normalized to the initial area and the oxygen coverage estimated from the Pd 3p/O 1s ratio, see text.

p(2 × 2) (0.25 ML) and the c(2 × 2) (0.5 ML), are the results of dissociative adsorption around room temperature via adsorption of O_2 molecules in the hollow sites. At higher exposures and temperatures also a $p(5 \times 5)$ (0.64 ML) and a $(\sqrt{5} \times \sqrt{5})R27°$ (0.8 ML) have been observed. While the structure for the former is unknown, the latter consists of a single PdO(101) plane on the Pd(100) surface. The oxygen in this structure is therefore more similar to Pd oxide in its chemical properties as compared to the lower coverage structures.

3. EXPERIMENTAL METHODS

The NAPXPS measurements reported here were carried out at beamline 9.3.2 at the Advanced Light Source (ALS) in Berkeley, USA.[47] All spectra were collected in normal emission with photon energies of 435 eV for Pd $3d_{5/2}$ and C 1s, and 650 eV for O 1s. More details on the experimental setup and the experimental procedures can be found in ref 48. In these measurements, the gas-phase composition was measured directly by using the gas-phase photoemission intensities. An artistic illustration of the experiments is shown in Figure 1a.

We have used PLIF[25−33] to visualize the concentration or the distribution of gas phase CO and CO_2 above two different Pd single crystals. Two different laser systems and reactors were used for probing CO and CO_2, but the layout of the experimental setup was the same in both experiments.[33] In these studies, thin laser sheets arranged perpendicular to the crystal surface probed CO and CO_2 across the center of the crystals with wavelengths of 230 nm and 2.7 μm, respectively. The resulting fluorescence emission between 440 and 660 nm for CO and 4.26 μm for CO_2 was detected with an ICCD (intensified CCD) camera and an InSb IR camera, respectively. More details on the experimental setup and experimental procedures can be found in refs 30 and 33. An artistic illustration of the measurements is shown in Figure 1b.

The HESXRD measurements were performed at beamline P07 at PETRAIII, Deutsches Elektronen-Synchrotron (DESY) in Hamburg, Germany, using synchrotron radiation with an energy of 85 keV. The incident angle was set to 0.04° close to the critical angle of total external reflection for palladium at this energy. An artistic illustration of the experiment is shown in Figure 1c. The sample was placed in a chamber,[49] combining an UHV chamber for sample preparation with a gas flow reactor to be used in total pressure of up to 1 bar. More details on the experimental setup and the experimental procedures can be found in refs 20−23.

4. RESULTS

4.1. NAPXPS

In Figure 2a, NAPXPS spectra from O 1s, Pd $3d_{5/2}$, and C 1s are shown as the temperature of the Pd(100) sample is increased from 270 to 420 °C in a gas mixture of 0.67 mbar O_2 and 0.67 mbar CO.

Starting with the C 1s at low temperatures, we find CO adsorbed on the Pd(100) surface in bridge sites with a coverage of approximately 0.5 ML (as judged from the corresponding Pd $3d_{5/2}$ spectrum[41]), as well as a gas-phase peak. As the temperature is increased to 284 °C, the chemisorbed CO is practically the same, while a small decrease is observed in the CO gas-phase intensity. At a temperature of 305 °C, the adsorbed CO decreases slightly and a small CO_2 gas-phase peak can be observed in the vicinity of the CO gas-phase peak. Upon increase of the temperature to 340 °C, no chemisorbed CO or even gas-phase CO can be detected; however a clear CO_2 gas-phase peak is now observed. The shift of the CO_2 gas-phase peak binding energy is

DOI: 10.1021/acs.accounts.7b00281
Acc. Chem. Res. 2017, 50, 2326−2333

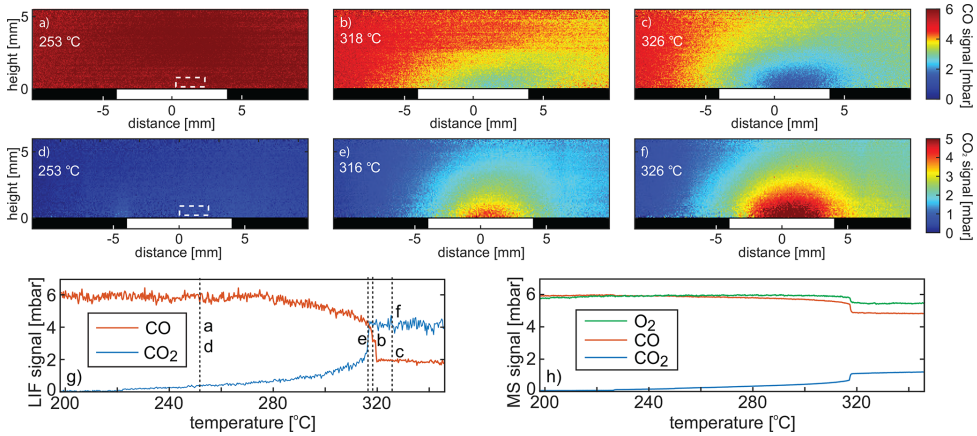

Figure 3. PLIF images of the CO close to the Pd(100) surface using initial partial pressures of 6 mbar CO, 6 mbar O_2, and 138 mbar Ar at different temperatures: (a) 253 °C, (b) 318 °C, (c) 326 °C. The corresponding fluorescence from CO_2 in a measurement performed directly after the CO measurements: (d) 253 °C, (e) 316 °C, (f) 326 °C. (bottom, left) The integrated intensities from the CO and CO_2 signals in the dashed, white rectangle shown in panels a and d just above the sample versus temperature. (bottom, right) The MS signal at the outlet of the reactor.

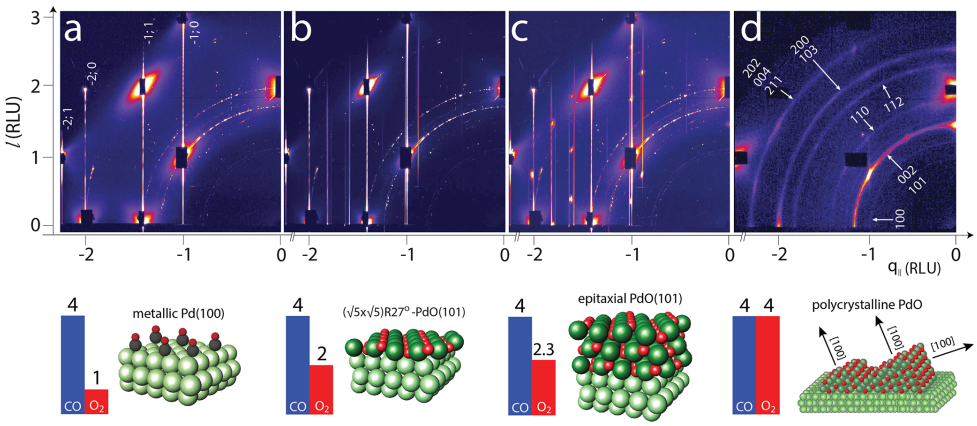

Figure 4. Structural information during CO oxidation obtained from HESXRD measurements. A summation of detector images from a 90° rotation from the indicated CO/O_2 ratios demonstrating the presence of (a) an unreconstructed Pd(100) surface, (b) the $(\sqrt{5}\times\sqrt{5})R27°$ surface oxide, (c) an epitaxial PdO(101) layer coexisting with the $(\sqrt{5}\times\sqrt{5})R27°$, (d) a bulk PdO powder diffraction pattern.

due to a change of the sample work-function.[50] At temperatures above 340 °C, only the CO_2 gas phase peak is observed, having an almost constant value despite an increase in temperature, indicating that the reaction is mass transfer limited (MTL) by the diffusion of CO to the surface. The integrated intensities are shown in Figure 2 b).

Turning to the O 1s region, a similar behavior as in the C 1s can be observed. At low temperatures, CO is observed adsorbed on the surface (although obscured by the Pd 3p level) and in the gas phase. Also an O_2 gas phase peak can be detected, but no chemisorbed oxygen. The amount of CO adsorbed on the surface does not change in any observable way up to a temperature of 305 °C, while the CO and O_2 gas phase peaks are decreasing slightly. At 340 °C, the CO gas phase and surface emission is gone; instead a CO_2 gas phase peak is observed while the O_2 peak is still there, but with lower intensity. Moreover, a new component at a binding energy of 529.5 eV corresponding to chemisorbed oxygen can be observed. The spectra do not change significantly at higher temperatures. The O 1s integrated intensities from the gas phase O_2 and chemisorbed oxygen are plotted in Figure 2c). The chemisorbed oxygen coverage was estimated by comparing the ratio of the Pd 3p and the chemisorbed oxygen component with measurements from known chemisorbed oxygen coverages under UHV conditions.

Finally, in the Pd $3d_{5/2}$, we observe peaks related to adsorbed CO at low temperatures and chemisorbed O at higher temperatures,

DOI: 10.1021/acs.accounts.7b00281
Acc. Chem. Res. 2017, 50, 2326−2333

but we do not observe any $(\sqrt{5}\times\sqrt{5})R27°$ related components. However, using higher oxygen partial pressures, the $(\sqrt{5}\times\sqrt{5})R27°$ may also be observed in the MTL reaction regime.[48] The behavior of the Pd $3d_{5/2}$ is in good agreement with the O 1s and C 1s levels.

4.2. PLIF

One of the more surprising observations in the NAPXPS investigation is the complete removal of the C 1s emission from the CO adsorbed on the surface and in the gas phase, despite the production of CO_2. In order to shed more light on this result, we performed PLIF measurements of the gas phase in the vicinity of the Pd(100) surface during the catalytic reaction by probing CO and CO_2.[33] Both measurements were performed at flows of 4 mL_n/min CO, 4 mL_n/min O_2, and 92 mL_n/min Ar at 150 mbar total pressure (corresponding to initial partial pressures of 6 mbar CO, 6 mbar O_2 and 138 mbar Ar). In both cases, the laser sheet was positioned just above the sample (indicated by the white rectangle in Figure 3a,d. In Figure 3a,b,c, three images from different temperatures from the CO fluorescence are shown as the model catalyst becomes active. At 253 °C, an evenly distributed CO emission can be observed. However, at 318 °C, the fluorescence is decreasing close to the sample, and at 326 °C, the intensity is at a minimum for these conditions and does not decrease further although the temperature is increased, again indicating a MTL reaction. In Figure 3d,e,f, the corresponding CO_2 fluorescence is shown, clearly showing an impressive CO_2 distribution forming a boundary layer in the vicinity of the Pd(100) as the reaction ignites. The PLIF traces just above the sample from CO and CO_2 are shown in Figure 3, bottom left, and the MS in Figure 3, bottom right. From these measurements, it is clear that the gas composition in the vicinity of the sample is different from the composition measured by the MS.[27] The gas composition detected by the NAPXPS described above reflects the gas composition in the immediate vicinity of the surface.[32] The PLIF results therefore explain the low amount of CO detected in the MTL region in the NAPXPS C 1s spectra in the MTL reaction situation at temperatures of 340 °C and above.

4.3. HESXRD

Direct in situ surface structural information during the catalytic CO oxidation over Pd(100) comes from HESXRD[20−24] and is shown in Figure 4. Panels a−d present the reciprocal space maps corresponding to the CO/O_2 ratio as shown below the images. At temperatures below ignition, the signature of the Pd(100) surface can be observed, while MS reveals a low CO_2 production, indicating CO poisoning, as illustrated by the model at the bottom of Figure 4a. At temperatures above ignition, MTL is reached as ignition occurs, and successively more oxygen-rich structures are observed with increasing oxygen partial pressures. Figure 4b,c,d correspond to the signatures of the $(\sqrt{5}\times\sqrt{5})R27°$, epitaxially grown bulk PdO(101),[51,52] and powder bulk PdO, respectively. The models are shown at the bottom of Figure 4.

5. DISCUSSION

The NAPXPS measurements contain information on all the involved molecules and surface structures during the catalytic CO oxidation over Pd(100). It is therefore a unique technique to study catalytic reactions under operating conditions. If previous structural studies have been performed under controlled UHV conditions, the core level components observed during the NAPXPS reaction conditions can be related via a fingerprinting approach to specific adsorption structures, oxides, and gas phase compositions. This is a significant advantage over most other techniques. A major drawback is the limited pressure that can be reached, due to the short mean free path of the photoelectrons. For reasonable measuring times, our NAPXPS measurements limit the maximum pressure to 1 mbar, a questionable pressure to be called "realistic conditions". Another drawback is that insulating samples are difficult to measure due to charging effects, but combined gas exposures in the millibar range and heating may remove charging effects at an insulating surface.[53]

The PLIF measurements only detect the gas phase, but the 2D visualization of the gas phase is a unique way to explore the effects of the model catalyst on the gas phase composition, in particular as the catalyst ignites. PLIF contains no information on the surface structure but may be combined, for example, with HESXRD or with simple reflectivity from the catalyst surface to detect changes in the roughness due to, for instance, oxidation.[54] In principle, a significant number of small hydrocarbons and other molecules relevant for catalysis can be detected by PLIF during catalytic reactions; however, in each case a unique combination of lasers and detectors is needed. Also the sensitivity of the technique is unique for each molecule: CO and CO_2 as probed in the present paper have a detection limit of around 0.1 mbar, but other molecules may be more or less difficult to detect depending on absorption cross section and fluorescence quantum yield. Finally, PLIF can also detect gas-phase radicals and may offer a unique capability for characterizing catalytic systems in which radical desorption is thought to be important, for example, high temperature processes. This is a potentially huge benefit of PLIF as radical detection is generally challenging.

HESXRD provides crystallographic information on a sub-angstrom level and can in principle be obtained without any prior knowledge of the surface structure. In practice, due to the complexity of the surface structures, most structural information is needed before operando HESXRD experiments. HESXRD has very little sensitivity to adsorbed molecules such as CO or atomic oxygen since the scattering strength scales with Z^2, although CO induced structures can be measured by conventional SXRD.[55] The strengths of the technique lie in recording a large part of reciprocal space in a short time, without any pressure restrictions. A major drawback is the very low incident angle used to be close to the critical angle, limiting the heating of the sample since this will misalign the sample.

A significant observation in the present studies, is the effect of the active sample on the surrounding gas phase, which has been predicted theoretically[56,57] for similar sample reactors. Although the disappearance of the CO gas phase peak C 1s is suggestive, it is not until the gas composition is visualized in 2D by PLIF that a much deeper understanding of the implications for the surface structure is obtained. In previous publications, we have investigated this effect extensively, and we have shown that the CO concentration close to the center of the surface is less than 20% of the concentration measured by a MS at the outlet of the reactor. The result is that in the MTL regime of the reaction, the gas phase in the vicinity of the sample is oxidizing, resulting in oxygen-rich surface structures.

Concerning the structure−function relationship of the Pd(100) during CO oxidation, we rarely observe CO−oxygen coadsorbed structures in our studies at elevated pressures. In the NAPXPS measurements, we occasionally detect such structures, but even at the relatively low pressures of NAPXPS, coadsorbed structures quickly disappear as the MTL regime is reached or the surface is CO poisoned. In NAPXPS, we also observe chemisorbed oxygen structures, as was shown above, clearly

DOI: 10.1021/acs.accounts.7b00281
Acc. Chem. Res. 2017, 50, 2326−2333

demonstrating that the chemisorbed oxygen is capable of a reaction rate reaching MTL. However, at the higher pressures used in HESXRD, we either observe that the surface is poisoned by CO, with low reaction rate, or oxidized forming a surface oxide or bulk oxides, producing MTL reaction conditions. At the comparably higher pressures of the HESXRD measurements as compared to the NAPXPS pressures, the higher partial O_2 pressure has a more oxidizing effect on the surface after ignition, producing stable oxide structures and MTL reaction conditions. In between the CO poisoned surface and the oxygen-rich MTL reaction regions, we observe a rapid change in the activity, ignition or extinction. While the inactivity of the CO poisoned surface (see Figure 4a) is obvious, it is important to discuss the activity not only of the chemisorbed oxygen but also of the resulting oxides, since they appear more readily under more realistic conditions than at the relatively low pressures of NAPXPS. In addition, the PLIF measurements clearly show that the ignition produces a highly oxidizing environment close to the catalyst and therefore Pd oxides, accentuating the need to understand the activity of Pd oxides.

As soon as the CO desorbs from the surface, the O_2 may dissociate and oxidize CO into CO_2. Depending on the oxygen concentration, various oxygen induced structures form on the surface. The $(\sqrt{5} \times \sqrt{5})R27°$ and the related epitaxial PdO(101) shown in Figures 4b,c, respectively, have also been shown to be capable of oxidizing CO under UHV conditions. The reason for this capability can be found in the details of the surface structure. The $(\sqrt{5} \times \sqrt{5})R27°$ and PdO(101) surface contains Coordinatively Unsaturated Sites (CUS), at which CO may adsorb and O_2 dissociate.[52,58] The structure is similar to that of $RuO_2(110)$[59] and $IrO_2(110)$.[60] Hence, not only is the chemisorbed oxygen capable of producing CO oxidation rates resulting in a MTL reaction, but also the $(\sqrt{5} \times \sqrt{5})R27°$ and the epitaxial PdO(101) could have a similar capability, because of the unique surface structure. A similar behavior has recently been observed under UHV conditions.[61−63] In contrast, at even higher partial pressures the epitaxial PdO(101) breaks up and forms a bulk PdO powder, see Figure 4 d). The surface of the powder could transform into PdO(100) or PdO(001) since these are the most stable PdO surfaces.[64] These surfaces have no undercoordinated Pd atoms but are oxygen terminated, inhibiting both CO adsorption and O_2 dissociation, again poisoning the surface. However, the relative activities between the chemisorbed oxygen, the $(\sqrt{5} \times \sqrt{5})R27°$, and the epitaxial PdO(101) are close to impossible to disentangle due to the MTL issues related to CO oxidation.

6. CONCLUDING REMARKS

Using a powerful combination of novel spectroscopic and diffraction in situ techniques, we have demonstrated that we are able to shed new light on the seemingly simple catalytic CO oxidation reaction over a Pd(100) model catalyst under operating conditions. The studies demonstrate that the presence of a catalyst changes the gas phase composition significantly and thereby complicates the structure−function interpretation. Although the notion of this change is conceptually obvious, it is only by the direct visualization using PLIF that the significance of these changes are truly realized. We have shown that different oxygen induced structures may form on the surface of the model catalyst and have discussed the importance of CUS sites. It is clear that structures containing such sites, also under operating conditions, must be regarded as extremely promising structures for catalysis. It is not obvious which surface structures will form during a catalytic reaction. Therefore, controlled studies of metal surfaces exploring, for example, oxide formation are essential, since such surfaces may be difficult to identify under real operating conditions. We aim to step up the material and environmental complexity using our approach, addressing admittedly complex reactions and model catalysts. The processes that we seek to understand as they happen involve the important catalytic removal and transformation of greenhouse gases such as CO_2 and CH_4 into useful fuels, such as methanol. In such catalytic reactions, the activity is much lower than in CO oxidation, removing the MTL issues, which should facilitate the distinction between different surface structures in promoting catalytic reactions. Clearly the objectives are ambitious; however we believe that we have gathered enough information and experience to potentially create a new conceptual understanding of these exceptionally important chemical processes.

AUTHOR INFORMATION

Corresponding Author

*E-mail: edvin.lundgren@sljus.lu.se.

ORCID

Edvin Lundgren: 0000-0002-3692-6142
Sara Blomberg: 0000-0002-6475-013X
Jianfeng Zhou: 0000-0003-0862-7951
Johan Zetterberg: 0000-0002-0882-1482

Notes

The authors declare no competing financial interest.

Biographies

Edvin Lundgren received his Ph.D. in 1996 in Physics from Lund University with Prof. Ingolf Lindau and Jesper Andersen. His research interests focuses on the relation between the atomic scale surface structure and function in catalysis and electrochemistry.

Chu Zhang is a doctoral student with Dr. Johan Gustafson and Prof. Edvin Lundgren. Her research focus is on the chemical composition and atomic scale surface structure of model catalysts under operating conditions.

Lindsay R. Merte received his Ph.D. in 2011 in Nanoscience from Aarhus University with Prof. Flemming Besenbacher. His research interests focus on surface structure and operando surface studies of model catalysts.

Mikhail Shipilin received his Ph.D. in 2016 in Physics from Lund University with Prof. Edvin Lundgren and Dr. Johan Gustafson. His research interests focus on structural studies of model heterogeneous catalysts in situ under working conditions using synchrotron-based experimental techniques.

Sara Blomberg received her Ph.D. in 2017 in Physics from Lund University with Prof. Edvin Lundgren and Dr. Johan Gustafson. Her research interests focus on the correlation between surface structure and gas phase interaction in operando studies of CO oxidation.

Uta Hejral received her Ph.D. degree in 2015 in Physics from University of Hamburg with Prof. Andreas Stierle. Her research focus on operando surface characterization of model catalysts, using synchrotron radiation.

Jianfeng Zhou is a doctoral student with Dr. Johan Zetterberg and Prof. Edvin Lundgren. His research focus is on the application of laser-based techniques applied to catalysis.

Johan Zetterberg received his Ph.D. in 2008 in Physics from Lund University with Prof. Marcus Aldén and Dr. Z. S. Li. His research interests focus on laser based techniques applied to chemical reactions such as combustion and catalysis.

DOI: 10.1021/acs.accounts.7b00281
Acc. Chem. Res. 2017, 50, 2326−2333

Johan Gustafson received his Ph.D. in 2006 in Physics from Lund University with Prof. Jesper Andersen and Prof. Edvin Lundgren. His research focuses on in situ and operando studies of well-defined model catalysts under realistic conditions.

■ ACKNOWLEDGMENTS

This work was financially supported by the Swedish foundation for strategic research (SSF) ("Catalysts designed for demanding environments" (FUNCAT)" contract number RMA08-0085), the Swedish Research Council (VR) ("Catalysis on the atomic scale" contract number 349-2011-6491), and the Knut and Alice Wallenberg Foundation ("Atomistic design of catalysts" contract number KAW 2015.0058).

■ REFERENCES

(1) Ertl, G.; Knözinger, H.; Weitkamp, J. *Handbook of Heterogeneous Catalysis*; Wiley: New York, 1997.
(2) Heck, R. M.; Farrauto, R. J.; Gulati, S. T. *Catalytic air pollution control: commercial technology*; John Wiley & Sons, 2009.
(3) Bäumer, M.; Freund, H.-J. Metal deposits on well-ordered oxides. *Prog. Surf. Sci.* **1999**, *61*, 127−198.
(4) Duke, C. B., Plummer, E. W., Eds. Special Issue on Frontiers in surface and Interface Science, *Surf. Sci.* **2001**, *500*.
(5) Ertl, G. Reactions at surfaces: from atoms to complexity. *Angew. Chem., Int. Ed.* **2008**, *47*, 3524−3535.
(6) Over, H.; Kim, Y. D.; Seitsonen, A. P.; Wendt, S.; Lundgren, E.; Schmid, M.; Varga, P.; Morgante, A.; Ertl, G. Atomic-scale structure and catalytic reactivity of the RuO_2(110) surface. *Science* **2000**, *287*, 1474−1476.
(7) Stierle, A.; Molenbroek, A. M. Novel In Situ Probes for Nanocatalysis. *MRS Bull.* **2007**, *32*, 1001−1009.
(8) Lundgren, E.; Over, H. In gas-surface interactions: Approaching realistic conditions. *J. Phys.: Condens. Matter* **2008**, *20*, 180302−180305.
(9) Frenken, J.; Groot, I. *Operando Research in Heterogeneous Catalysis* Springer Series in Chemical Physics 114; Springer, 2017.
(10) Szanyi, J.; Goodman, D. W. Combined elevated pressure reactor and ultrahigh vacuum surface analysis system. *Rev. Sci. Instrum.* **1993**, *64*, 2350−2352.
(11) Ryczkowski, J. IR spectroscopy in catalysis. *Catal. Today* **2001**, *68*, 263−381.
(12) Hartfelder, U.; Singh, J.; Haase, J.; Nachtegaal, M.; Grolimund, D.; van Bokhoven, J. A. Detecting and utilizing minorityphases in heterogeneous catalysis. *Sci. Rep.* **2016**, *6*, 37597.
(13) Shen, Y. R. Surface properties probed by second-harmonic and sum-frequency generation. *Nature* **1989**, *337*, 519−525.
(14) Salmeron, M.; Schlögl, R. Ambient Pressure Photoelectron Spectroscopy: A new tool for surface science and nanotechnology. *Surf. Sci. Rep.* **2008**, *63*, 169−200.
(15) Trotochaud, L.; Head, A. R.; Karslioglu, O.; Kyhl, L.; Bluhm, H. Ambient pressure photoelectron spectroscopy: Practical considerations and experimental frontiers. *J. Phys.: Condens. Matter* **2017**, *29*, 053002.
(16) Toyoshima, R.; Kondoh, H. In-situ observations of catalytic surface reactions with soft x-rays under working conditions. *J. Phys.: Condens. Matter* **2015**, *27*, 083003.
(17) Frenken, J.; Groot, I. Live Observations of Catalysts Using High-Pressure Scanning Probe Microscopy. *Springer Ser. Chem. Phys.* **2017**, *114*, 1−30.
(18) Stierle, A.; Gustafson, J.; Lundgren, E. Surface-Sensitive X-ray Diffraction across the Pressure Gap. *Springer Ser. Chem. Phys.* **2017**, *114*, 59−87.
(19) Jinschek, J. R. Advances in the environmental transmission electron microscope (ETEM) for nanoscale in situ studies of gas-solid interactions. *Chem. Commun.* **2014**, *50*, 2696−2706.
(20) Gustafson, J.; Shipilin, M.; Zhang, C.; Stierle, A.; Hejral, U.; Ruett, U.; Gutowski, O.; Carlsson, P. A.; Skoglundh, M.; Lundgren, E. High-energy surface x-ray diffraction for fast surface structure determination. *Science* **2014**, *343*, 758−761.
(21) Shipilin, M.; Gustafson, J.; Zhang, C.; Merte, L. R.; Stierle, A.; Hejral, U.; Ruett, U.; Gutowski, O.; Skoglundh, M.; Carlsson, P.-A.; Lundgren, E. Quantitative surface structure determination using in situ high-energy SXRD:Surface oxide formation on Pd(100) during catalytic CO oxidation. *Surf. Sci.* **2014**, *630*, 229−235.
(22) Shipilin, M.; Gustafson, J.; Zhang, C.; Merte, L. R.; Stierle, A.; Hejral, U.; Ruett, U.; Gutowski, O.; Skoglundh, M.; Carlsson, P.-A.; Lundgren, E. Transient Structures of PdO during CO Oxidation over Pd(100). *J. Phys. Chem. C* **2015**, *119*, 15469−15476.
(23) Shipilin, M.; Gustafson, J.; Zhang, C.; Merte, L. R.; Lundgren, E. Step dynamics and oxide formation during COoxidation over a vicinal Pd surface. *Phys. Chem. Chem. Phys.* **2016**, *18*, 20312−20320.
(24) Shipilin, M.; Stierle, A.; Merte, R. M.; Gustafson, J.; Hejral, U.; Martin, N. M.; Zhang, C.; Franz, D.; Kilic, V.; Lundgren, E. The influence of incommensurability on the long-range periodicity of the Pd(100)-($\sqrt{5} \times \sqrt{5}$)$R27°$-PdO(101). *Surf. Sci.* **2017**, *660*, 1−8.
(25) Zetterberg, J.; Blomberg, S.; Gustafson, J.; Sun, Z. W.; Li, Z. S.; Lundgren, E.; Aldén, M. An in situ set up for the detection of CO_2 from catalytic CO oxidation by using planar laser induced fluorescence. *Rev. Sci. Instrum.* **2012**, *83*, 053104.
(26) Zetterberg, J.; Blomberg, S.; Gustafson, J.; Evertsson, J.; Zhou, J.; Adams, E. C.; Carlsson, P. A.; Aldén, M.; Lundgren, E. Spatially and temporally resolved gas distribution around heterogeneous catalysts using infrared planar laser-induced fluorescence. *Nat. Commun.* **2015**, *6*, 7076.
(27) Blomberg, S.; Brackmann, C.; Gustafson, J.; Aldén, M.; Lundgren, E.; Zetterberg, J. Real-Time gas phase Imaging over a Pd(110) Catalyst during CO Oxidation by Means of Planar Laser-Induced Fluorescence. *ACS Catal.* **2015**, *5*, 2028−2034.
(28) Blomberg, S.; Zetterberg, J.; Gustafson, J.; Zhou, J.; Brackmann, C.; Lundgren, E. Comparison of AP-XPS and PLIF measurements during CO oxidation over Pd single crystals. *Top. Catal.* **2016**, *59*, 478−486.
(29) Matera, S.; Blomberg, S.; Hoffmann, M. J.; Zetterberg, J.; Gustafson, J.; Lundgren, E.; Reuter, K. Evidence for the active phase of heterogeneous catalysts through in situ reaction product imaging and multiscale modeling. *ACS Catal.* **2015**, *5*, 4514−4518.
(30) Blomberg, S.; Zhou, J.; Gustafson, J.; Zetterberg, J.; Lundgren, E. 2D and 3D imaging of the gas phase close to an operating model catalyst by planar laser induced fluorescence. *J. Phys.: Condens. Matter* **2016**, *28*, 453002.
(31) Blomberg, S.; Zetterberg, J.; Zhou, J.; Merte, L. R.; Gustafson, J.; Shipilin, M.; Trinchero, A.; Miccio, L. A.; Magana, A.; Ilyn, M.; Schiller, F.; Ortega, J. E.; Bertram, F.; Grönbeck, H.; Lundgren, E. Strain dependent light-off temperature in catalysis revealed by planar laser-induced fluorescence. *ACS Catal.* **2017**, *7*, 110−114.
(32) Zhou, J.; Blomberg, S.; Gustafson, J.; Lundgren, E.; Zetterberg, J. Visualization of gas distribution in a model AP-XPS reactor by PLIF: CO oxidation over a Pd(100) catalyst. *Catalysts* **2017**, *7*, 29.
(33) Zhou, J.; Pfaff, S.; Lundgren, E.; Zetterberg, J. A convenient setup for laser-induced fluorescence imaging of both CO and CO_2 during catalytic CO oxidation. *Appl. Phys. B: Lasers Opt.* **2017**, *123*, 87.
(34) Lamy, C.; Leger, J. M. Electrocatalytic oxidation of small organic materials at platinum single crystal surfaces. *J. Chim. Phys. Phys.-Chim. Biol.* **1991**, *88*, 1649−1671.
(35) Gao, F.; Wang, Y.; Cai, Y.; Goodman, D. W. CO Oxidation on Pt-Group Metals from Ultrahigh Vacuum to Near Atmospheric Pressures.2. Palladium and Platinum. *J. Phys. Chem. C* **2009**, *113*, 174−181.
(36) van Rijn, R.; Balmes, O.; Resta, A.; Wermeille, D.; Westerström, R.; Gustafson, J.; Felici, R.; Lundgren, E.; Frenken, J. W. M. Surface structure and reactivity of Pd(100) during CO oxidation near ambient pressures. *Phys. Chem. Chem. Phys.* **2011**, *13*, 13167−13171.
(37) Freund, H. J.; Meijer, G.; Scheffler, M.; Schlögl, R.; Wolf, M. CO Oxidation as a Prototypical Reaction for Heterogeneous Processes. *Angew. Chem., Int. Ed.* **2011**, *50*, 10064−10094.
(38) Park, R. L.; Madden, H. H., Jr. Annealing changes on the (100) surface of palladium and their effect on CO adsorption. *Surf. Sci.* **1968**, *11*, 188−202.

DOI: 10.1021/acs.accounts.7b00281
Acc. Chem. Res. 2017, 50, 2326−2333

(39) Behm, R. J.; Christmann, K.; Ertl, G.; van Hove, M. A. Adsorption of CO on Pd(100). *J. Chem. Phys.* **1980**, *73*, 2984−2995.
(40) Uvdal, P.; Karlsson, P.-A.; Nyberg, C.; Andersson, S.; Richardson, N. V. On the structure of dense CO overlayers. *Surf. Sci.* **1988**, *202*, 167−182.
(41) Andersen, J. N.; Qvarford, M.; Nyholm, R.; Sorensen, S. L.; Wigren, C. Surface core-level shifts as a probe of the lLocal overlayer structure: CO on Pd(100). *Phys. Rev. Lett.* **1991**, *67*, 2822−2825.
(42) Berndt, W.; Bradshaw, A. M. Domain wall superlattices in high coverage CO adlayers on Pd(100). *Surf. Sci. Lett.* **1992**, *279*, L165−L169.
(43) Rogal, J.; Reuter, K.; Scheffler, M. CO oxidation at Pd(100): a first-principles constrained thermodynamics study. *Phys. Rev. B: Condens. Matter Mater. Phys.* **2007**, *75*, 205433.
(44) Orent, T. W.; Bader, S. D. LEED and ELS study of the initial oxidation of Pd(100). *Surf. Sci.* **1982**, *115*, 323−334.
(45) Todorova, M.; Lundgren, E.; Blum, V.; Mikkelsen, A.; Gray, S.; Gustafson, J.; Borg, M.; Rogal, J.; Reuter, K.; Andersen, J. N.; Scheffler, M. The Pd(100)-($\sqrt{5} \times \sqrt{5}$)*R*27°-O surface oxide revisited. *Surf. Sci.* **2003**, *541*, 101−112.
(46) Kostelnik, P.; Seriani, N.; Kresse, G.; Mikkelsen, A.; Lundgren, E.; Blum, V.; Sikola, T.; Varga, P.; Schmid, M. The Pd(100)-($\sqrt{5} \times \sqrt{5}$) *R*27°-O surface oxide: A LEED, DFT and STM study. *Surf. Sci.* **2007**, *601*, 1574−1581.
(47) Grass, M. E.; Karlsson, P. G.; Aksoy, F.; Lundqvist, M.; Wannberg, B.; Mun, B. S.; Hussain, Z.; Liu, Z. New ambient pressure photoemission endstation at Advanced Light Source beamline 9.3.2. *Rev. Sci. Instrum.* **2010**, *81*, 053106.
(48) Blomberg, S.; Hoffmann, M. J.; Gustafson, J.; Martin, N. M.; Fernandes, V. R.; Borg, A.; Liu, Z.; Chang, R.; Matera, S.; Reuter, K.; Lundgren, E. In situ X-Ray photoelectron spectroscopy of model catalysts: At the edge of the gap. *Phys. Rev. Lett.* **2013**, *110*, 117601.
(49) van Rijn, R.; Ackermann, M.; Balmes, O.; Dufrane, T.; Geluk, A.; Gonzalez, H.; Isern, H.; de Kuyper, E.; Petit, L.; Sole, V. A.; Wermeille, D.; Felici, R.; Frenken, J. W. M. Ultrahigh vacuum/high-pressure flow reactor for surface x-ray diffraction and grazing incidence small angle x-ray scattering studies close to conditions for industrial catalysis. *Rev. Sci. Instrum.* **2010**, *81*, 014101.
(50) Axnanda, S.; Scheele, M.; Crumlin, E.; Mao, B.; Chang, R.; Rani, S.; Faiz, M.; Wang, S.; Alivisatos, A. P.; Liu, Z. Direct work function measurement by gas phase photoelectron spectroscopy and its application on PbS nanoparticles. *Nano Lett.* **2013**, *13*, 6176−6182.
(51) Seriani, N.; Harl, J.; Mittendorfer, F.; Kresse, G. A first-principles study of bulk oxide formation on Pd(100). *J. Chem. Phys.* **2009**, *131*, 054701.
(52) Westerström, R.; Messing, M. E.; Blomberg, S.; Hellman, A.; Grönbeck, H.; Gustafson, J.; Martin, N. M.; Balmes, O.; van Rijn, R.; Andersen, J. N.; Deppert, K.; Bluhm, H.; Liu, Z.; Grass, M. E.; Hävecker, M.; Lundgren, E. The oxidation and reduction of Pd(100) and aerosol deposited Pd nanoparticles. *Phys. Rev. B: Condens. Matter Mater. Phys.* **2011**, *83*, 115440.
(53) Merte, L. R.; Gustafson, J.; Shipilin, M.; Zhang, C.; Lundgren, E. Redox behavior of iron at the surface of an O(100) single crystal studied by ambient-pressure photoelectron spectroscopy. *Catalysis Structure and Reactivity* **2017**, *3*, 95−103.
(54) Onderwaater, W. G.; Taranovskyy, A.; Bremmer, G. M.; van Baarle, G. C.; Frenken, J. W. M.; Groot, I. M. N. From dull to shiny: A novel setup for reflectance difference analysis under catalytic conditions. *Rev. Sci. Instrum.* **2017**, *88*, 023704.
(55) Lundgren, E.; Torrelles, X.; Alvarez, J.; Ferrer, S.; Over, H.; Beutler, A.; Andersen, J. N. A surface x-ray diffraction study of the Rh(111).(2 × 2)-3CO structure. *Phys. Rev. B: Condens. Matter Mater. Phys.* **1999**, *59*, 5876−5880.
(56) Matera, S.; Reuter, K. First-principles approach to heat and mass transfer effects in model catalyst studies. *Catal. Lett.* **2009**, *133*, 156−159.
(57) Matera, S.; Reuter, K. Transport limitations and bistability for in situ CO oxidation at RuO_2(110): First-principles based multiscale modeling. *Phys. Rev. B: Condens. Matter Mater. Phys.* **2010**, *82*, 085446.
(58) Weaver, J. F. Surface chemistry of late transition metal oxides. *Chem. Rev.* **2013**, *113*, 4164−4215.
(59) Over, H. Surface chemistry of ruthenium dioxide in heterogeneous catalysis and electrocatalysis: From fundamental to applied research. *Chem. Rev.* **2012**, *112*, 3356−3426.
(60) Liang, Z.; Li, T.; Kim, M.; Asthagiri, A.; Weaver, J. F. Low-temperature activation of methane on the IrO_2(110) surface. *Science* **2017**, *356*, 299−303.
(61) Zhang, F.; Li, T.; Pan, L.; Asthagiri, A.; Weaver, J. F. CO oxidation on single and multilayer Pd oxides on Pd(111): mechanistic insights from RAIRS. *Catal. Sci. Technol.* **2014**, *4*, 3826−3834.
(62) Zhang, F.; Pan, L.; Li, T.; Diulus, J. T.; Asthagiri, A.; Weaver, J. F. CO Oxidation on PdO(101) during Temperature-Programmed Reaction Spectroscopy: Role of Oxygen Vacancies. *J. Phys. Chem. C* **2014**, *118*, 28647−28661.
(63) Weaver, J. F.; Zhang, F.; Pan, L.; Li, T.; Asthagiri, A. Vacancy-Mediated Processes in the Oxidation of CO on PdO(101). *Acc. Chem. Res.* **2015**, *48*, 1515−1523.
(64) Rogal, J.; Reuter, K.; Scheffler, M. Thermodynamic stability of PdO surfaces. *Phys. Rev. B: Condens. Matter Mater. Phys.* **2004**, *69*, 075421.

DOI: 10.1021/acs.accounts.7b00281
Acc. Chem. Res. 2017, 50, 2326−2333

Paper VIII

nature COMMUNICATIONS

ARTICLE

Received 12 Feb 2015 | Accepted 31 Mar 2015 | Published 8 May 2015

DOI: 10.1038/ncomms8076 OPEN

Spatially and temporally resolved gas distributions around heterogeneous catalysts using infrared planar laser-induced fluorescence

Johan Zetterberg[1], Sara Blomberg[2], Johan Gustafson[2], Jonas Evertsson[2], Jianfeng Zhou[1], Emma C. Adams[3], Per-Anders Carlsson[3], Marcus Aldén[1] & Edvin Lundgren[2]

Visualizing and measuring the gas distribution in close proximity to a working catalyst is crucial for understanding how the catalytic activity depends on the structure of the catalyst. However, existing methods are not able to fully determine the gas distribution during a catalytic process. Here we report on how the distribution of a gas during a catalytic reaction can be imaged *in situ* with high spatial (400 μm) and temporal (15 μs) resolution using infrared planar laser-induced fluorescence. The technique is demonstrated by monitoring, in real-time, the distribution of carbon dioxide during catalytic oxidation of carbon monoxide above powder catalysts. Furthermore, we demonstrate the versatility and potential of the technique in catalysis research by providing a proof-of-principle demonstration of how the activity of several catalysts can be measured simultaneously, either in the same reactor chamber, or in parallel, in different reactor tubes.

[1] Division of Combustion Physics, Lund University, Lund 221 00, Sweden. [2] Division of Synchrotron Radiation Research, Lund University, Lund 221 00, Sweden. [3] Competence Centre for Catalysis, Chalmers University of Technology, 412 96 Göteborg, Sweden. Correspondence and requests for materials should be addressed to J.o.Z. (email: johan.zetterberg@forbrf.lth.se).

© 2015 Macmillan Publishers Limited. All rights reserved.

Catalysis research is highly relevant to society because industrial production of chemicals and environmental protection by pollution control rely heavily on (heterogeneous) catalyst technologies[1]. In this context the oxidation of carbon monoxide (CO) on Pt-group metals is one of the most-studied prototypical catalytic reactions because of its practical relevance and general applicability. Despite its apparent simplicity, the reaction is challenging to study and describe because of peculiar kinetics such as bistability and oscillations, and fascinating spatiotemporal behaviour[2].

In the case of industrial catalyst development, the efficiency of a material to catalyse a particular reaction is evaluated by analysing the end products, after the reactants have passed the catalyst containing the active material, using appropriate characterization techniques, such as mass spectrometry (MS), gas chromatography (GC), Fourier transform infrared spectrometry (FTIR) or specific analysers depending on the reaction. However, for model catalysts, such as single crystals, used to yield an understanding of the surface chemistry and structure, the evaluation is carried out by, for example, investigating catalytically active sites on the atomic scale, usually at ultrahigh vacuum. At more realistic and industrial-like operating conditions in the mbar pressure region and above, the gas-phase situation becomes more complicated. This is because in such investigations the reactants pass over the catalyst, causing gas-phase phenomena such as mass-transfer limitation and convection, which changes the conditions near the catalyst. In fact, this may induce the formation of surface structures not related to the catalytic processes in conjunction with a change in the catalytic activity, yielding an intense debate on the active sites or even the active phase[3,4].

Spatially resolved measurements with high quality using traditional analytics (MS, GC and FTIR) have been pursued in earlier studies. For instance, in the work described in refs 5,6,7 a scanning mass spectrometer with a capillary probe that can stepwise (2 s per step in ref. 5) be scanned over the sample was used. This approach allows for pointwise spatially resolved measurements but is unable to deliver two-dimensional (2D) measurements on a subsecond scale to catch dynamic changes in the gas phase. Furthermore, probing techniques are inherently intrusive and might affect the gas flow and temperature above the catalyst disturbing the dynamics. Another example of a technique that is traditionally used is FTIR[8–11], a nonintrusive method that has been extended to two dimensions for combinatorial screening of catalysts with a stated detection limit of 1,000 p.p.m. for propane[11] and 1% of CO_2 with a collection time of 17 s (ref. 12). However, FTIR is a so-called line-of-sight technique that relies on the absorption along a path, making it unable to resolve the gas phase in the third dimension and when temperatures are inhomogeneous in the integration path, the spectral signal is distorted. The integration time also limits the temporal resolution to $\sim$2 s per scan[13]. Nonintrusive laser-based techniques, such as Raman scattering, have also been successfully applied to catalysis studies[14–17]. The difficulty with Raman scattering is the low cross-section, limiting the measurements to one-dimension (1D) and most often with long collection times because of averaging, ranging from several minutes to an hour (although in other fields, and with a very sophisticated experimental set-up, single shot Raman has been achieved[18]). This makes it mostly suitable for stationary situations where changes in the gas-phase conditions are minimal or very slow. The mentioned techniques have the capability for multispecies detection, but are all limited either in the temporal or the spatial domain and are therefore less suitable for measurements of the 2D gas distributions above catalytically active surfaces in a changing environment.

Laser-induced fluorescence (LIF) has been used in numerous research fields, such as combustion and medical research[19,20], to measure temperature, velocity and the concentration of a probed gas. LIF has high spatial and temporal resolution, is nonintrusive and can be used to perform 2D measurements *in situ*, without disturbing the flow properties of the gas[21]. It is then often referred to as planar laser-induced fluorescence (PLIF).

Although recognized early as a potential method for catalysis research[22–25], its use has been very limited and restricted to the ulraviolet/visible spectral regime, meaning several gases important for catalysis, such as CO_2, CO and small hydrocarbons[26,27], have remained elusive because of excitation and detection limitations. However, the technical development during recent years in lasers and infrared detection capabilities[28] together with efficient detection and background suppression schemes developed in an earlier study[29] enables the use of PLIF for several of these previously undetectable gases. The first detection of CO_2 to study catalysis was made in a recent study by Zetterberg *et al.*[29]; however, it was limited to averaged data, lacking the capability of capturing single shot data with sufficient signal-to-noise to really make an impact. However, with further refinements of the experimental set-up and methodology we have been able to use infrared PLIF to capture instantaneous, 2D images of the probed CO_2 gas formed during oxidation of CO over porous supported noble metal catalysts. A schematic of the process is shown in Fig. 1. In this report we highlight the advantage of being able to perform spatially resolved, *in situ* measurements of the gas phase close to catalysts by means of infrared PLIF. First, we show how the catalytic ignition and extinction of the CO oxidation can be followed for a powder catalyst with a frame rate of 10 Hz, directly visualizing the change in the gas composition close to the catalyst surface. Second, the possibility to measure the CO_2 distribution above two catalysts that are simultaneously situated in the chamber is presented, and how the presence of the two samples affects each other is discussed. Finally, we show that by physically separating the catalytic samples, the differences in activation temperatures can be directly visualized, and activation energies extracted. The study sheds light on several aspects for catalysis research, especially the

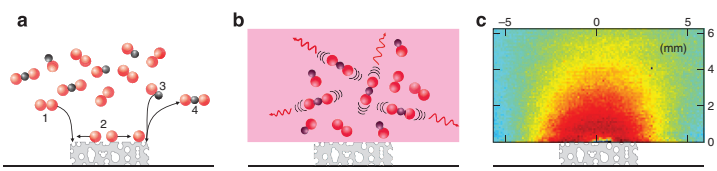

Figure 1 | Schematic of planar laser-induced fluorescence. Schematic of PLIF measurements of the activity of a model catalyst (**a**) shows the adsorption and dissociation of O_2 on the catalyst at points **1** and **2**, respectively, and the adsorption of CO and production of CO_2 at points **3** and **4**, respectively. (**b**) The laser sheet (pink) that excites the CO_2 molecules above the catalyst; the fluorescence from the excited molecules is detected. An example of the CO_2 distribution above an active catalyst at elevated temperature and realistic pressure is shown in **c**.

© 2015 Macmillan Publishers Limited. All rights reserved.

possibility to visualize an event, in this case the elusive CO_2 product, with high temporal and spatial resolution, at realistic industrial conditions.

Results

Experimental description. In our experiments we used infrared PLIF to image the temperature-dependent dynamics of CO_2 close to the surface of catalytic discs during ignition and extinction of catalytic CO oxidation. The samples studied were industrial-like pressed noble metal powder catalysts, and we specifically investigated how the gas distribution around the catalytic discs was changing with sample position, as well as in the presence of two samples in the chamber. In the end we give an example of how to perform combinatorial measurements on three samples simultaneously, without having the samples affecting each other, as a way of screening potential catalysts in the development phase both academically and industrially.

In all our measurements a mass spectrometer, connected to the outlet of the reactor via a leak valve, was used to monitor the global gas composition. The MS signals have a time lag of $\sim$5 s in the present set-up, compared with the LIF signal (which is almost instantaneous), and the increase in the CO_2 signal as the sample ignites is slower. The lag originates from the time it takes for the gas to reach the MS and is dependent on the flow speed, pressure and the volume of the gas has to pass to reach the leak valve.

Measuring CO_2 distributions over single-catalyst samples. We first investigated the CO_2 distribution over two samples, 2%Pd/CeO_2 (hereafter called the Pd-sample) and 2%Pt1%Pd/CeO_2 (hereafter called the Pt-Pd-sample). Worth noting is that the percentages given is by weight, meaning that the concentration of active atoms is the same in both samples. To that end we took infrared PLIF snapshots of the CO_2 distribution around each catalyst (Fig. 2a,b and Supplementary Movies 1 and 2). The gas flows were 18 $ml_n\,min^{-1}$ CO, 18 $ml_n\,min^{-1}$ O_2 and 36 $ml_n\,min^{-1}$ Ar at a total pressure of 105 mbar. The temperatures discussed in the text refer to the thermocouple temperatures.

Already at 137 °C (time I, Fig. 2a,d) the fluorescence signal close to the sample surface increased slightly, indicating the presence of CO_2, as both samples started to ignite. At 165 °C the Pd-sample ignited (time II, Fig. 2b), which was manifested as a circularly shaped CO_2 distribution above the sample that decreased away from the sample surface. This is expected because the CO_2 distribution around the sample is mainly determined by diffusion. In contrast, the fluorescence measured above the Pt-Pd-sample, while stronger than that measured at 137 °C, was still low at this temperature, thus providing evidence for a low catalytic activity (time II, Fig. 2e). Only when the temperature was ramped up to 220 °C the Pt-Pd-sample ignited, resulting in a circularly shaped CO_2 distribution similar to the one observed for the Pd-sample at 165 °C (time III, Fig. 2f).

Above these temperatures, both samples reached a steady-state CO_2 production, which resulted in only small changes in the distribution of the gas. A slight drag towards the right can be seen, which can be attributed to the gas flow passing from left to right in the image. At 250 °C, the samples reached equilibrium, the gas distribution was steady and the CO_2 concentration had stopped to increase.

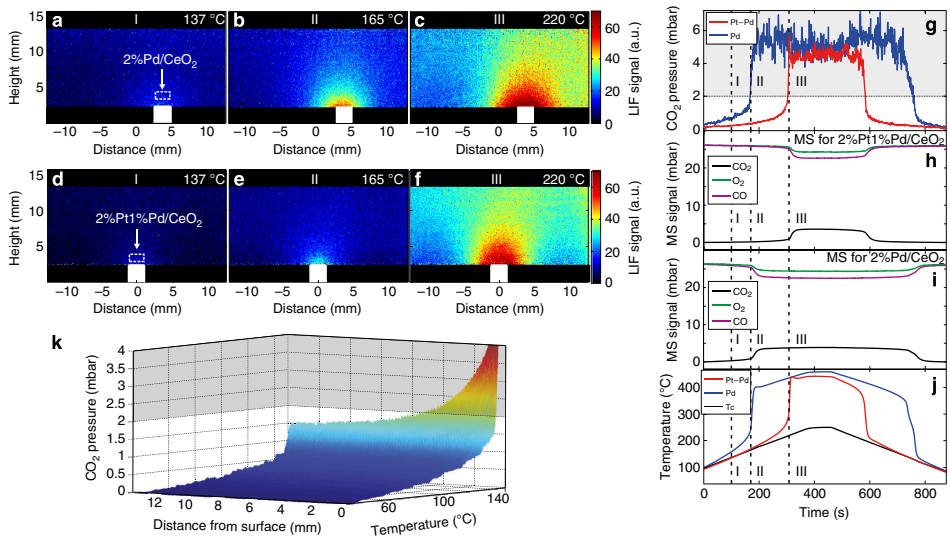

Figure 2 | CO_2 distribution over two single-catalyst samples. CO_2 distribution over two single-catalyst samples at different temperatures at a total pressure of 105 mbar, infrared PLIF single-shot images of the CO_2 distribution over (**a**–**c**) Pd sample and (**d**–**f**) Pt-Pd-sample surface at different temperatures (see also Supplementary Movies 1 and 2). For both samples, we also show (**g**) the fluorescence signals measured 1 mm over the surface of the samples, calibrated to CO_2 partial pressure below the shaded area, (**h**,**i**) the calibrated MS profile of CO, O_2 and CO_2 for the Pt–Pd and Pd samples, respectively, (**j**) the temperature of the samples' surface (red and blue) and sample holder (*Tc*) and (**k**) the CO_2 gradient (calibrated below the shaded area) from $\sim$0.2 mm above the sample as a function of temperature. The roman numerals indicate times during the experimental measurement that correspond to the time when the snapshots shown in Fig. 2a–f were recorded.

© 2015 Macmillan Publishers Limited. All rights reserved.

The fluorescence signal was extracted 1 mm above each sample's surface from each snapshot image (Fig. 2g). Furthermore, we measured the MS signal—normalized to the known initial partial pressure of CO and O_2; CO_2 was scaled to match the observed conversion of CO—to elucidate the signal's dependence on temperature (Fig. 2h,i), and the temperature of the samples' surface and sample holder (Fig. 2j).

One way to investigate the catalytic activity is to study the spatial gradient vertically away from the Pd-sample, something infrared PLIF gives the opportunity to do on a single-shot basis. The gradient was followed in time as a function of temperature (Fig. 2k). From the image it can then be seen that already in the kinetically controlled regime, at 100 °C, there is a significantly higher CO_2 concentration close to the surface than further away. Just before ignition the partial pressure of CO_2 ranges from ~1.5 mbar at 0.2 mm above the surface to 0.8 mbar at 2 mm from the surface (the latter being close to the pressure observed by the MS at the outlet of the reactor).

For both samples, the concentration plateaus both in the fluorescence and in the MS signal show that the reactions are limited by the CO diffusion to the catalyst, which occurs almost immediately after ignition, and that all the CO molecules that reach the surface are oxidized[30].

When the temperature was ramped down the signals concomitantly decreased as the catalytic activity of the samples decreased. The temperature at which the Pd-sample extinguishes is lower (133 °C) than the corresponding temperature at which the Pt–Pd extinguishes (199 °C), which mimics the corresponding trend in the ignition process where corresponding temperatures are 165 and 218 °C, respectively. The difference in temperatures for ignition and extinction is in agreement with previous studies of supported Pd and Pt catalysts[31].

In general, the averaged infrared PLIF signals (Fig. 2g) were in agreement with the ones obtained by MS (Fig. 2h,i), with only a slight delay of the latter relative to the former because of the time required for the gas distribution around the sample to reach the MS. The instant at which the samples became active also coincided with an increase in the surface temperature of the samples because of the exothermic nature of the reaction (Fig. 2j). Although the accuracy of the measured absolute temperatures was ~10–20 °C, these measurements provided an additional validation and understanding of the dynamics of the gas distribution during the experiment. The temperature measurements also did not suffer from the time-lag associated with the MS measurement, thus making a more accurate measurement of the activation temperatures possible. In the present case, the ignition can in principle be monitored by the thermocouple or better the infrared camera; however, for many other reactions (or for low concentrations of CO), the reaction is not as strongly exothermic as in the case of CO oxidation, disqualifying the thermocouple reading as a probe for the ignition.

Simultaneous measurements of CO_2 above two samples. To demonstrate the versatility and high-resolution measurement capabilities of infrared PLIF, we next measured the CO_2 distribution over the two samples discussed in the previous section, simultaneously and under the same conditions as above (18 $ml_n\,min^{-1}$ CO, 18 $ml_n\,min^{-1}$ O_2 and 36 $ml_n\,min^{-1}$ Ar at a total pressure of 105 mbar). To that end, we placed the two catalytic samples next to each other in the reactor (~8 mm apart) and measured and analysed the infrared PLIF signal, showing that it is possible to distinguish the CO_2 distribution around each sample.

The results of the temperature-dependent infrared PLIF measurements are shown in Fig. 3, alongside measurements of the MS signal, and the temperatures of the samples' surfaces and holder. We found minimal activity already at $T = 136$ °C (Fig. 3a) and the Pd-sample ignited at a temperature of 170 °C (Fig. 3b), resulting in the formation of a cloud-like CO_2 distribution similar to the one observed in the single-sample measurements. The

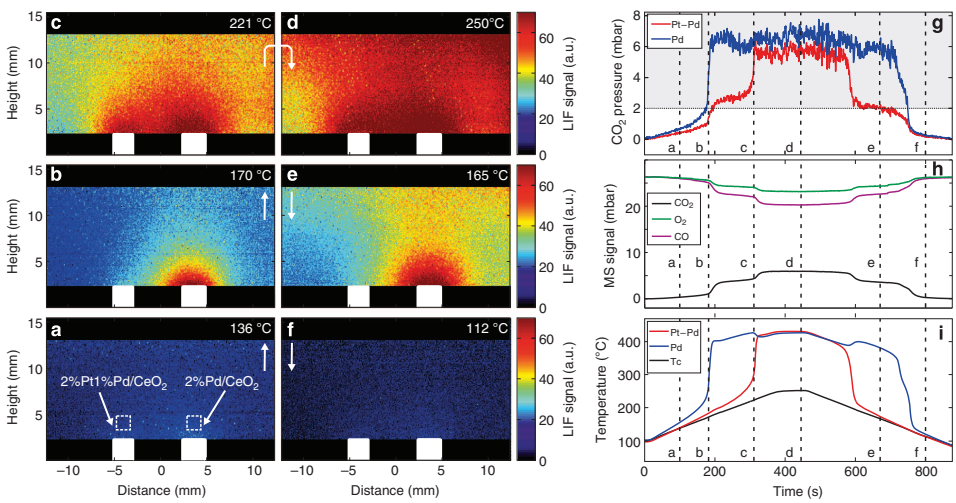

Figure 3 | The CO_2 distribution over two samples simultaneously positioned in the reactor. (**a**–**f**) Infrared PLIF single-shot images during the reaction showing the CO_2 distribution over a Pt–Pd sample and a Pd powder catalyst surfaces at different times and temperatures and at 105 mbar of total pressure (see Supplementary Movies 3). (**g**) The fluorescence signal 0.7 mm above each sample (red and blue). (**h**) The MS signal. (**i**) The temperature of the sample surfaces (red and blue) measured with the infrared camera together with the temperature of the sample holder, measured by a thermocouple (*Tc*).

© 2015 Macmillan Publishers Limited. All rights reserved.

spatial resolution of the experimental set-up is high enough to spatially distinguish which of the two samples that becomes active by probing the corresponding CO_2 distribution. As the temperature was further increased, the Pt–Pd sample also became active at ~221 °C (Fig. 3c), and a much larger cloud of CO_2 is now visible above the surface of the sample holder. However, the distributions are still highly localized and separable above each of the samples

At 250 °C (Fig. 3d), both samples reached equilibrium and the gas distribution around the samples was found to change very little with further increase in the temperature. The CO_2 concentration in the chamber was inhomogeneous, with a somewhat stronger fluorescence signal detectable on the right-hand side of the reactor, which can be attributed to the gas flowing through the reactor from left-to-right.

When the temperature was ramped down, the Pt–Pd sample was first to extinguish (Fig. 3e) soon thereafter followed by extinction of the Pd-sample (Fig. 3f). The ignition/extinction events for both samples give rise to corresponding signatures in the LIF trace, MS signal and temperature data (Fig. 3g–i). This experiment shows the potential of laser diagnostics and the advantage of having 2D, spatially resolved, nonintrusive measurements of the gas distribution, opening up for simultaneous characterization of more than one sample at a time and direct *in situ* comparisons, something very useful, for example, when studying systems where more than one active catalyst is needed to drive different reactions, and how the presence of one affects the other.

Probing the CO_2 production from three samples in parallel. Because of the possible interaction of the samples as demonstrated above, we also applied and demonstrated the versatility of the technique by probing the CO_2 production originating from three separate samples simultaneously and, in parallel, by placing these into three separated flow tubes. We pursued this solution for situations in which having more than one sample in the reactor changes the reaction of the adjacent samples and *vice versa*. To address this problem we developed our reactor to have the possibility to include three tubes (see Methods section). The experimental set-up used the same gas system as in the experiments on one and two samples, the only modification being that the gas was directed to flow through the three tubes. The tubes ended inside the middle of the vacuum chamber where the laser sheet was placed as close as possible (<1 mm) to the exits of the tubes. In this way the gas originating from each individual tube could be probed simultaneously by the laser. In each of the three tubes a monolith sample was placed, each containing Pd/CeO_2, Pt/CeO_2 and Pt/Al_2O_3, respectively.

We performed similar measurements, as with the one- and two-sample cases, of the infrared PLIF, MS and temperature of the samples, as a function of temperature (Fig. 4), but at higher pressure, 1 bar.

In contrast to our previous collection of snapshot images of the infrared PLIF, we here show averaged (over 10 laser pulses) infrared PLIF images that are measured at the exit of the three tubes (Fig. 4a–d). At 70 °C (Fig. 4a) none of the samples had ignited and no infrared PLIF signal was visible. As the temperature was increased, the Pd/CeO_2 sample ignited at 180 °C (Fig. 4b), followed by the Pt/CeO_2 at 278 °C (Fig. 4c) and Pt/ Al_2O_3 at 352 °C (Fig. 4d). The signals were not centred in the tubes because of the low flow out from the tubes and because the outlet was placed at the bottom of the reactor.

The onset of ignition for each of the samples yielded an abrupt increase in the averaged infrared PLIF signals at the exit of the tubes (Fig. 4e). This contrasts the MS results where it is not possible to extract the ignition times and temperatures for the different samples (Fig. 4f). While the MS signal changes with temperature, the changes are not as pronounced as in the infrared PLIF data, which makes it impossible to tell from which sample the signal originates. This also opens up for the possibility of extracting quantitative data for the individual catalysts. Activation energies are calculated from the three Arrhenius plots (Fig. 4h) that are extracted from the infrared PLIF signals (Fig. 4g). As expected, the activation energy of 0.25 and 0.53 eV found for the two CeO_2-supported samples are lower than for the Pt supported

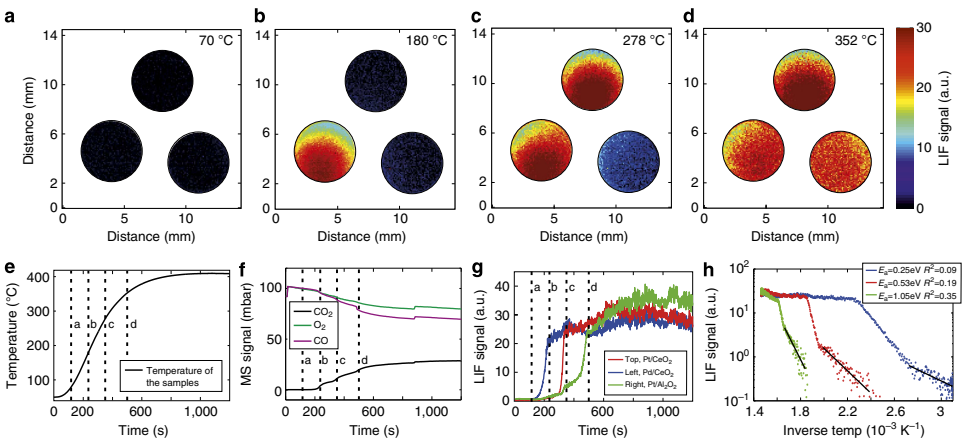

Figure 4 | The CO_2 signal from three different samples in three separate exhaust tubes. (**a**–**d**) The CO_2 signal from the gas exiting the three tube ends are shown in the top panel (see Supplementary Movie 4). (**e**) The temperature measured by the thermocouple located centred between the tubes at the same position as the samples, (**f**) the MS signal during the event and (**g**) the averaged infrared PLIF signal exiting each tube, which is also shown in three Arrhenius plots in **h**.

© 2015 Macmillan Publishers Limited. All rights reserved.

by Al_2O_3 (1.05 eV). This is also in good agreement with what is reported in literature[32,33]. In contrast, the overlapping CO_2 MS signals complicate the analysis of finding the individual reaction rates for each of the three catalysts and thus constrains the possibility to achieve the activation energy with the MS. The infrared PLIF method could therefore be used to study several catalysts in parallel in a way that has not been possible before.

Discussion

The present report shows that the technical development of lasers, detectors and data treatment during the last 15 years enables direct 2D detection of small molecules relevant for catalysis previously not attainable by LIF. To detect CO_2 at elevated temperatures and realistic gas conditions, it is necessary to excite the molecule with a wavelength of 2.7 μm, demanding a high-energy laser with a respectable power and narrow linewidth. Further, a fast gateable infrared camera with the ability to detect the fluorescence light at 4.3 μm is needed, since a fast subtraction scheme is required to remove the otherwise completely dominating thermal background, a short gate time (ns–μs regime) and a high enough frame rate makes this possible. Thus, both laser source and detector used in the present investigations are nonstandard making the combination truly unusual, and have not previously been used for catalysis-related studies.

With PLIF, whether in the infrared or ulraviolet/visible regime, the gas distribution around a catalyst can be visualized with high spatial and temporal resolution (below 500 μm and down to ~50 μm depending on excitation wavelength and from 10 μs down to below 10 ns for a single snapshot) with the only disturbance being the excitation of the interrogated species. For the direct product of CO oxidation, this has not been possible until now. The results presented here is an important step for a better understanding of gas phase-related phenomena in catalysis, where dynamics can be studied that are otherwise often hidden in averaged data.

The study implies several new aspects for catalysis research, for example, with PLIF it is possible to measure the gas surrounding the sample at realistic pressures, revealing the actual gas composition close to the surface previously not attainable, for a correct interpretation of the active site or phase. The study also shows with images that by following the gas distribution in time it is possible to distinguish whether the entire catalyst or only part of it is active, or by directly comparing two catalysts decide which has the lowest activation temperature.

By combining the present gas phase measurements with simultaneous X-ray diffraction measurements[34], the correct active site/phase should become available. In this way, it should be possible to determine the surface structure and the gas composition close to the surface of the catalyst, previously simultaneously unattainable properties. Furthermore, our study shows how PLIF applied to catalysis has a potential for simultaneous characterization or combinatorial studies of industrial catalysts in a straightforward way. While infrared PLIF applied to catalysis is just barely developed, a present drawback of optical and laser-based methods is the need for specialized reactors with optical access with at least one, but often as many as three transparent windows. Further, the present relatively complicated experimental set-up and data analysis limits the use to experienced and trained researchers.

To this end, we are in the process of developing more standardized reactors, lasers and software suitable for (infrared) PLIF, with the possibility of applying an additional experimental technique. An example of a step in this direction is the development of a reactor towards simultaneous synchrotron radiation and laser measurements, where surface and gas phase information can be extracted simultaneously under the same conditions and at the same sample.

Using modern laser and detection techniques (not limited to the infrared regime), the experiments presented here can be extended to a vast number of gas species, such as CO, CH_4, NH_3 and NO. Our present experiment highlights the principle of the experiment and the spatial resolution provided applying infrared PLIF to catalysis, where flows and gas distributions can be measured instantaneously in 2D, something conventional techniques such as MS, GC and FTIR lacks, and provides a tool that in principle can be used simultaneously with synchrotron-based measurements.

Methods

Infrared PLIF. The principles of infrared PLIF are (Fig. 1) as follows: (1) a laser beam excites a vibrational/rotational level in the molecule of interest; (2) the molecule fluoresces in response to the laser excitation by emitting light at a wavelength that is known *a priori*; (3) the emitted fluorescence is detected and analysed. In our study, the infrared laser beam was generated by difference-frequency mixing the output from a dye laser (Sirah PRSC-D-18) at 763 nm with the fundamental frequency from a Nd:YAG laser (Spectra Physics, PRO 290-10) at 1,064 nm in a $LiNbO_3$ crystal, yielding a 2.7-μm laser pulse (with a pulse energy of 4 mJ, 5 ns pulse duration and the linewidth estimated to 0.025 cm^{-1})[35]. The output from the laser was used to probe the P(12) line of the $(00^00) \rightarrow (10^001)$ combination band of the CO_2 molecules in the vicinity of the catalyst, and the fluorescence at 4.3 μm was detected by a 2D infrared camera (Santa Barbara Focal Plane, SBF LP134). The infrared PLIF images visualize the CO_2 distribution (Fig. 1c) in a 25 × 13-mm^2-sized rectangle above the catalyst. The images were collected every 0.1 s and with a temporal resolution for each frame, limited by the exposure time of the camera, of 15 μs, and the spatial resolution was ~400 μm and limited by the thickness of the lasersheet. The detection limit for CO_2 was estimated to 100 p.p.m. (or 0.1 mbar) in the present measurements. A schematic describing the laser set-up, optics and the collection of the images is shown in the Supplementary Fig. 1. The infrared background was subtracted with a scheme presented in ref. 29.

The CO_2 fluorescence intensity has been calibrated to mbar for concentrations lower than ~2 mbar. This is made possible by making calibration measurements at known CO_2 concentrations and temperatures, creating a calibration curve. As the temperature field in the reactor is inhomogeneous, it has to be corrected for in order to give a correct representation of the CO_2 concentration. Infrared PLIF images with a homogeneous CO_2 distribution is therefore collected at temperatures matching those of the experimental data. While the fluorescence signal is temperature-dependent, these images represent the temperature field and can be used to compensate the measurement data. In this way not only the density differences due to temperature is taken into account but also the difference in population. The dependence of fluorescence signal on temperature is covered more thoroughly in the Supplementary Methods section and is demonstrated in Supplementary Fig. 2.

Reaction chamber. The experiments were carried out in a cubical stainless steel reaction cell with a total volume of 240 ml. The samples were placed on a Mo sample holder in the middle of the reactor. The samples could be viewed in the reactor from four different directions through four CaF_2 windows. The Mo sample plate was heated by a boralectric heater (Métaux Céramiques Systèmes Engineering; BN) held by two Ta rods that were attached to current feed-throughs and connected to a 20-A power supply. The samples were thus indirectly heated via the Mo plate and the temperature of the sample holder was measured with type-C thermocouples attached to the Mo plate. The power supply was regulated via a LabView programme in order to increase and decrease the temperature in a controlled way. A schematic of the experimental set-up is shown in the Supplementary Fig 1.

The surface temperature of the samples was measured using an infrared camera (FLIRP620); however, as the emissivity changes with temperature, it is hard to get an absolute temperature from this measurement. It is, however, a very good indicator of when the sample ignites.

The gas flows were 18 $ml_n\,min^{-1}$ CO, 18 $ml_n\,min^{-1}$ O_2 and 36 $ml_n\,min^{-1}$ Ar at a pressure of 105 mbar for the first two experiments with one and two samples in the reactor.

A premixed 10% CO_2 in Ar was used for calibration purposes. The gases were introduced into the reactor cell via individual Bronkhorst mass-flow controllers (Bronkhorst EL-FLOW, 50 mln min^{-1}) that can vary the gas flow from 1 to 50 ml min^{-1}. To keep the pressure constant, a pressure controller (Bronkhorst EL-PRESS) was attached to the gas outlet. The gas composition was studied by a quadruple mass spectrometer (Pfeiffer PrismaPlus QMG220), connected to the reactor outlet via a leak valve.

© 2015 Macmillan Publishers Limited. All rights reserved.

The samples. The supported noble-metal catalysts were prepared by incipient wetness impregnation targeting the same molar amount of noble metal atoms. The alumina (Puralox SBa 200, Sasol) and ceria (99.5 H.S.A. 514, Rhône-Poulenc) support materials were first thermally stabilized by a treatment in air at 600 °C for 2 h. Each support was then dispersed in an aqueous solution consisting of distilled water and the relevant concentration of noble metal precursor, tetraammineplatinum(II)nitrate (4.0 wt.% $(NH_3)_4Pt(NO_3)_2$, Alfa Aesar GmbH & Co. KG) and/or tetraamminepalladium(II)nitrate (4.6 wt.% $(NH_3)_4Pd(NO_3)_2$, Alfa Aesar GmbH & Co. KG) to obtain the desired noble metal loading, that is, 4%Pt/alumina, 4%Pt/ceria, 2.2%Pd/ceria and 1.1 Pd%–2%Pt/ceria (% refers here weight percentage). For the co-impregnation of platinum and palladium, the noble metal precursors were completely mixed before impregnation. To increase the interaction between the noble metal complex and the support, the pH of the solution was adjusted by NH_4OH addition taking into account the isoelectric point of each oxide. The obtained slurry was then stirred for 20 min, frozen with liquid nitrogen and freeze-dried for 12 h to preserve high noble metal dispersion. The resulting powder was finally calcined in air at 550 °C for 1 h using a heating rate of 5 °C min^{-1} starting from room temperature. The total surface area of the powder samples was measured with N_2 physisorption at 77 K (Micromeritics Tristar). Using the BET method for $P/P_0 = 0.05–0.20$, the specific surface area was calculated to be 173, 156, 159 and 161 $m^2 g^{-1}$ for the 4%Pt/alumina, 4%Pt/ceria, 2.2%Pd/ceria and 1.1 Pd%–2%Pt/ceria, respectively.

The tube reactor set-up. A schematic of the experimental set-up is shown in Supplementary Fig. 3. The tube reactor consists of an outer fused silica (FS) tube with three smaller FS tubes inside. The larger tube has a diameter of 16 mm and is fitted with a CF16 end to connect to the cubical reaction cell described above, and the smaller tubes are 500 mm long and have an inner diameter of 5 mm. The smaller tubes are placed in such a way that they end in the middle of the cubical reaction cell. The reactor was heated by a resistance heating-wire coiled around the larger tube and the temperature measured with a type-K thermocouple placed in the centre of the larger tube between the smaller tubes. The CF16 end of the larger tube was used to connect to the CF40 cube and the smaller tubes were placed such that they ended in the middle of the cube.

The gas was supplied through the large tube, in which the gas was divided up into the smaller tubes where monolith samples (20 mm long and 3-mm thick 2 × 2 channels monolith impregnated with noble metal) were placed. The space between the large and the small tubes were sealed with quartz fibres, to prevent the gas from flowing outside the small tubes. The small tubes ended centred in the reaction cell and the laser sheet was placed as close as possible to the tube ends, in order to probe the exiting gas. The gases were regulated and pressure-controlled in the same way as in the measurements with one and two samples. The flow fed through the tubes consisted of 5 $ml_n\,min^{-1}$ CO, 5 $ml_n\,min^{-1}$ O_2 and 40 $ml_n\,min^{-1}$ Ar at a pressure of 1,000 mbar.

References

1. Heck, R. M., Farrauto, R. J. & Gulati, S. T. *Catalytic Air Pollution Control: Commercial Technology.* 3rd edn (John Wiley, 2009).
2. Ertl, G. *Handbook Of Heterogeneous Catalysis.* 2nd edn (Wiley-VCH, 2008).
3. van Rijn, R. *et al.* Comment on "CO oxidation on Pt-group metals from ultrahigh vacuum to near atmospheric pressures. 2. palladium and platinum". *J. Phys. Chem. C* **114,** 6875–6876 (2010).
4. Gao, F., Wang, Y. L. & Goodman, D. W. Reply to "Comment on 'CO Oxidation on Pt-Group Metals from Ultrahigh Vacuum to Near Atmospheric Pressures. 2. Palladium and Platinum''. *J. Phys. Chem. C* **114,** 6874–6874 (2010).
5. Roos, M. *et al.* Scanning mass spectrometer for quantitative reaction studies on catalytically active microstructures. *Rev. Sci. Instrum.* **78,** 084104 (2007).
6. Sidwell, R. W., Zhu, H. Y., Kee, R. J. & Wickham, D. T. Catalytic combustion of premixed methane-in-air on a high-temperature hexaaluminate stagnation surface. *Combust. Flame* **134,** 55–66 (2003).
7. Sidwell, R. W. *et al.* Catalytic combustion of premixed methane/air on a palladium-substituted hexaluminate stagnation surface. *Proc. Combust. Inst.* **29,** 1013–1020 (2002).
8. Snively, C. M., Katzenberger, S., Oskarsdottir, G. & Lauterbach, J. Fourier-transform infrared imaging using a rapid-scan spectrometer. *Opt. Lett.* **24,** 1841–1843 (1999).
9. Snively, C. M., Oskarsdottir, G. & Lauterbach, J. Chemically sensitive parallel analysis of combinatorial catalyst libraries. *Catal. Today* **67,** 357–368 (2001).
10. Tan, C. K. C., Delgass, W. N. & Baertsch, C. D. Spatially resolved in situ FTIR analysis of CO adsorption and reaction on Pt/SiO_2 in a silicon microreactor. *Appl. Catal. B Environ.* **93,** 66–74 (2009).
11. Snively, C. M., Oskarsdottir, G. & Lauterbach, J. Parallel analysis of the reaction products from combinatorial catalyst libraries. *Angew. Chem. Int. Ed.* **40,** 3028–3030 (2001).
12. Snively, C. M. & Lauterbach, J. Sampling accessories for the high-throughput analysis of combinatorial libraries using spectral imaging. *Spectroscopy* **17,** 26–33 (2002).
13. Hendershot, R. J., Fanson, P. T., Snively, C. M. & Lauterbach, J. A. High-throughput catalytic science: parallel analysis of transients in catalytic reactions. *Angew. Chem. Int. Ed.* **42,** 1152–1155 (2003).
14. Karagiannidis, S., Mantzaras, J., Bombach, R., Schenker, S. & Boulouchos, K. Experimental and numerical investigation of the hetero-/homogeneous combustion of lean propane/air mixtures over platinum. *Proc. Combust. Inst.* **32,** 1947–1955 (2009).
15. Reinke, M. *et al.* High-pressure catalytic combustion of methane over platinum: *in situ* experiments and detailed numerical predictions. *Combust. Flame* **136,** 217–240 (2004).
16. Schneider, A. *et al.* Laser induced fluorescence of formaldehyde and Raman measurements of major species during partial catalytic oxidation of methane with large H_2O and CO_2 dilution at pressures up to 10 bar. *Proc. Combust. Inst.* **31,** 1973–1981 (2007).
17. Zheng, X., Mantzaras, J. & Bombach, R. Kinetic interactions between hydrogen and carbon monoxide oxidation over platinum. *Combust. Flame* **161,** 332–346 (2014).
18. Karpetis, A. N., Settersten, T. B., Schefer, R. W. & Barlow, R. S. Laser imaging system for determination of three-dimensional scalar gradients in turbulent flames. *Opt. Lett.* **29,** 355–357 (2004).
19. Svanberg, S. Medical diagnostics using laser-induced fluorescence. *Phys. Script.* **T19b,** 469–475 (1987).
20. Aldén, M., Bood, J., Li, Z. & Richter, M. Visualization and understanding of combustion processes using spatially and temporally resolved laser diagnostic techniques. *Proc. Combust. Inst.* **33,** 69–97 (2011).
21. Kohse-Höinghaus, K. Laser techniques for the quantitative detection of reactive intermediates in combustion systems. *Prog. Energ. Combust.* **20,** 203–279 (1994).
22. Gudmundson, F., Fridell, E., Rosén, A. & Kasemo, B. Evaluation of OH desorption rates from Pt using spatially-resolved imaging of laser-induced fluorescence. *J. Phys. Chem-Us.* **97,** 12828–12834 (1993).
23. Gudmundson, F. *et al.* OH gas phase chemistry outside a Pt catalyst. *J. Catal.* **179,** 420–430 (1998).
24. Försth, M., Eisert, F., Gudmundson, F., Persson, J. & Rosén, A. Analysis of the kinetics for the $H_2 + 1/2O_2 <=> H_2O$ reaction on a hot Pt surface in the pressure range 0.10-10Torr. *Catal. Lett.* **66,** 63–69 (2000).
25. Su, H. & Yeung, E. S. High-throughput screening of heterogeneous catalysts by laser-induced fluorescence imaging. *J. Am. Chem. Soc.* **122,** 7422–7423 (2000).
26. Kirby, B. J. & Hanson, R. K. Imaging of CO and CO_2 using infrared planar laser-induced fluorescence. *Proc. Combust. Inst.* **28,** 253–259 (2000).
27. Li, Z. S., Rupinski, M., Zetterberg, J. & Aldén, M. Mid-infrared PS and LIF detection of CH_4 and C_2H_6 in cold flows and flames at atmospheric pressure. *Proc. Combust. Inst.* **30,** 1629–1636 (2005).
28. Kirby, B. J. & Hanson, R. K. Planar laser-induced fluorescence imaging of carbon monoxide using vibrational (infrared) transitions. *Appl. Phys. B Lasers O* **69,** 505–507 (1999).
29. Zetterberg, J. *et al.* An *in situ* set up for the detection of CO_2 from catalytic CO oxidation by using planar laser-induced fluorescence. *Rev. Sci. Instrum.* **83,** 053104 (2012).
30. Blomberg, S. *et al. In Situ* X-ray photoelectron spectroscopy of model catalysts: at the edge of the gap. *Phys. Rev. Lett.* **110,** 117601 (2013).
31. Skoglundh, M. & Fridell, E. Strategies for enhancing low-temperature activity. *Top. Catal.* **28,** 79–87 (2004).
32. Bourane, A. & Bianchi, D. Oxidation of CO on a Pt/Al_2O_3 catalyst: from the surface elementary steps to light-off tests I. Kinetic study of the oxidation of the linear CO species. *J. Catal.* **202,** 34–44 (2001).
33. Oran, U. & Uner, D. Mechanisms of CO oxidation reaction and effect of chlorine ions on the CO oxidation reaction over Pt/CeO_2 and Pt/CeO_2/gamma-Al_2O_3 catalysts. *Appl. Catal. B Environ.* **54,** 183–191 (2004).
34. Gustafson, J. *et al.* High-energy surface X-ray diffraction for fast surface structure determination. *Science* **343,** 758–761 (2014).
35. Li, Z. S., Rupinski, M., Zetterberg, J., Alwahabi, Z. T. & Aldén, M. Mid-infrared polarization spectroscopy of polyatomic molecules: detection of nascent CO_2 and H_2O in atmospheric pressure flames. *Chem. Phys. Lett.* **407,** 243–248 (2005).

Acknowledgements

This work was financially supported by the foundation for strategic research (SSF), the Swedish Research Council, the Crafoord Foundation, the Knut and Alice Wallenberg Foundation, the Anna and Edwin Berger Foundation, NordForsk and the Center of Combustion Science and Technology, CECOST. The Competence Centre for Catalysis (KCK) is hosted by the Chalmers University of Technology and financially supported by the Swedish Energy Agency and the member companies: AB Volvo, ECAPS AB, Haldor Topsøe A/S, Scania CV AB and Volvo Car Corporation AB.

© 2015 Macmillan Publishers Limited. All rights reserved.

Author contributions

J.Z.E. performed the measurements and did the data evaluation together with S.B. and had the major responsibility for preparing the paper (including SI), J.E. designed the reactor for combinatorial studies and took part in and evaluated those measurements. J.G. designed the reactor and took part in the development of the analysis methods, E.L. and P.A.C. wrote part of the paper. J.Z.H. made calibration measurements for quantitative CO_2 profiles. E.C.A. prepared the samples, and M.A. and E.L. supervised the project.

Additional Information

Supplementary Information accompanies this paper at http://www.nature.com/naturecommunications

Competing financial interests: The authors declare no competing financial interests.

Reprints and permission information is available online at http://npg.nature.com/reprintsandpermissions/

How to cite this article: Zetterberg, J. *et al.* Spatially and temporally resolved gas distributions around heterogeneous catalysts using infrared planar laser-induced fluorescence. *Nat. Commun.* 6:7076 doi: 10.1038/ncomms8076 (2015).

This work is licensed under a Creative Commons Attribution 4.0 International License. The images or other third party material in this article are included in the article's Creative Commons license, unless indicated otherwise in the credit line; if the material is not included under the Creative Commons license, users will need to obtain permission from the license holder to reproduce the material. To view a copy of this license, visit http://creativecommons.org/licenses/by/4.0/

© 2015 Macmillan Publishers Limited. All rights reserved.

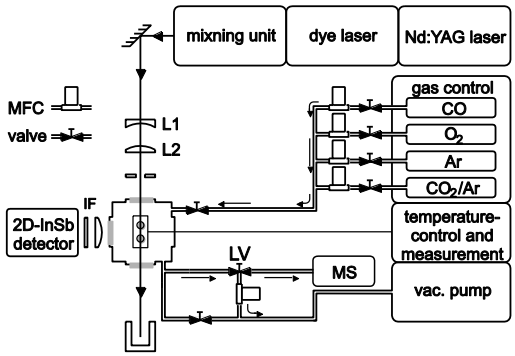

Supplementary Figure 1. Schematic of the experimental setup, the laser beam is formed into a laser sheet by two CaF_2 lenses (L1 is a negative cylindrical lens (f = -40 mm) and L2 a spherical lens (f = 250 mm)), the sheet is centered above the samples, the detector is placed at 90° with respect to the laser sheet to collect the LIF-signal which passes through an interference filter (IF). The gases are fed into the cell by mass flow controllers, and the pressure regulated by a pressure controller. All the gas that exits the reactor passes through the MS via a leak valve (LV).

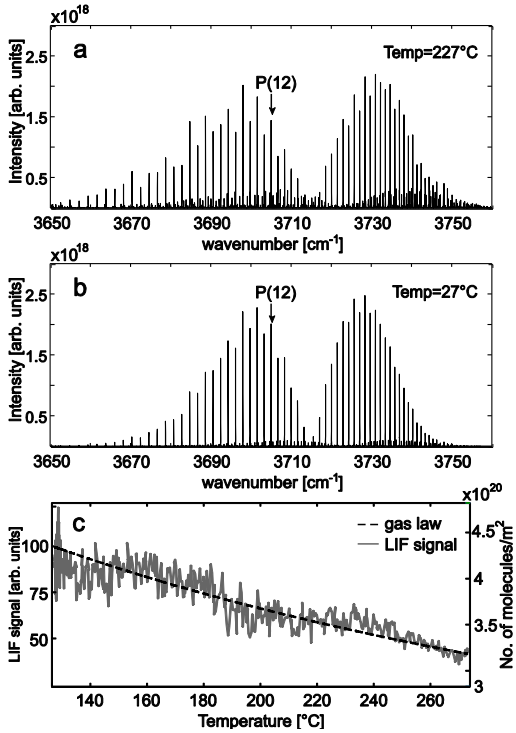

Supplementary Figure 2. Simulated absorption spectra and temperature dependence for CO_2, a) and b) show the simulated absorption-spectra of CO_2 at 227°C and 27°C respectively. c) shows the detected LIF signal at 1 mm above the sample, corrected for the change in population as a function of temperature. The dashed line shows the calculated density of molecules as a function of temperature, the P(12) line was used for laser excitation.

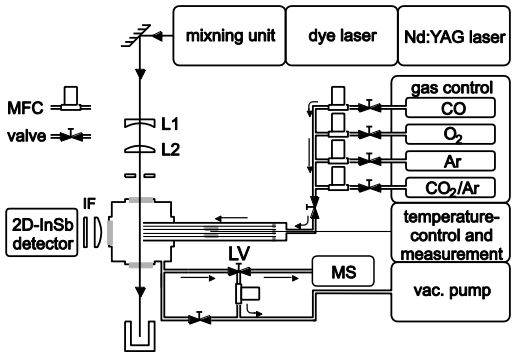

Supplementary Figure 3. A schematic of the experimental setup with the FS tubes, the laser beam is formed into a laser sheet by two CaF_2 lenses (L1 is a negative cylindrical lens (f = -40 mm) and L2 a spherical lens (f = 250 mm)), the sheet is placed as close as possible to the tube exits, the detector is placed at 90° with respect to the laser sheet to collect the LIF-signal. The gases are fed into the cell through the FS tubes and controlled by mass flow controllers, and the pressure regulated by a pressure controller. All the gas that exits the reactor passes through the MS via a leak valve (LV).

SUPPLEMENTARY METHODS

A more detailed description of laser-induced fluorescence

LIF is a common non-intrusive laser diagnostic technique for gas phase studies in many research fields[1,2], such as combustion and medical diagnostics, but is not as well-known to the catalytic community. LIF can be used to probe the temperature, velocity and concentration of a gas. The gas is probed with a laser tuned to a wavelength that perfectly matches an transition of the species of interest. If the wavelength is chosen wisely, the absorption cross section for the transition is high and no other interfering molecules will have an overlapping transition at the chosen energy. When the molecule relaxes, fluorescence light is emitted and the emitted light can then be detected. This results in an LIF signal originating from one specific species, making concentration measurements at sub-ppm levels possible.

To perform quantitative measurements with LIF is more difficult than qualitative measurements, mostly due to the collisional quenching[3]. There are several different approaches on how to quantify the LIF signal, the signal can e.g. be calibrated at known and similar conditions or the excitation can be performed in the saturated regime. It is also possible to use short-pulsed laser systems in order to quantify the collisional quenching and thereby correct for it[4].

Collisional quenching occurs when the molecules relax non-radiatively through collisions, resulting in signal loss. For the infrared (IR) spectral regime, however, where rotational (ro)-vibrational transitions are probed, the quantum yield can be described differently than for electronic transitions in the UV/visible spectral regime. This is because the vibrational-translational energy transfer, which serves to remove vibrational energy, often is slow (~1-100μs) compared to the camera integration time (~1-10μs)[5]. This is, of course, dependent on the interrogated species and its collisional partners and needs to be evaluated independently for each case and transition. In a previous study, using the same experimental set-up, the calibrated LIF signal of the CO_2 concentration over a Rh(553) single crystal was shown to be in good agreement with mass-spectrometry data[6]. In this report the aim is not to present quantitative data but to utilize the imaging capability of LIF to visualize the CO_2 distribution in the reactor with an emphasis on the extra information spatial resolution can give.

The detected signal is influenced by many physical parameters that have to be taken into account when analyzing the data. The expression for the LIF-signal S_{LIF} in the linear excitation regime is

$$S_{LIF} = \eta_c E g f(T) \sigma_0 \chi_{abs} \frac{P}{k_B T} \phi \qquad (1)$$

where η_c is the experimental collection efficiency, E is the laser energy, g is a function that describes the spectral overlap between the laser and the absorption spectral lineshape, $f(T)$ is the Boltzmann fraction, σ_0 is the absorption cross section of the interrogated species, χ_{abs} is the mole fraction of the interrogated species that, together with P/k_BT, gives the number density of the same and ϕ is the fluorescence quantum yield. The fluorescence quantum yield, which is the fraction of excited molecules that emits fluorescence, embodies the excited-state emission rates, the collisional interaction and energy transfer between the interrogated species and the bath gas. A more detailed description of the quantum yield related to LIF in the IR spectral regime is given by Kirby et al.[5]. The expression shows that the detected LIF signal is linearly dependent on the gas density and the fraction of molecules in the state from which the laser excites the molecule, $f(T)$. The population of the energy levels in a molecule follows the Boltzmann dispersion and the signal is therefore indirect dependent on the gas temperature. Hence, determining the gas temperature requires performing and analyzing an excitation scan over the energy levels of the probed gas. Because of this temperature dependence it is desirable to choose an absorption line that is relatively insensitive (within the investigated temperature interval) when concentrations or distributions are investigated and the change should be accounted for. The present measurements were performed exciting the P12 line in the $(00^00) \rightarrow (10^001)$ transition of CO_2. In these experiments the change in the population

of the probed transition was simulated using input parameters from the HITRAN database[7], an example of a simulated ro-vibrational absorption spectra at 227°C and at 27°C of CO_2 gas is shown in Supplementary Figure 2a and b, respectively, for comparison. The signal, however, is also proportional to the number density of the probed gas. The number density, *N,* can be described by the mole fraction and the ideal gas law according to,

$$N = \chi_{abs} \frac{P}{k_B T} \tag{2}$$

where P is the total pressure, k_B the Boltzmann coefficient and T the temperature of the gas. From the expression above it can be seen that the signal will decrease as a function of temperature. In order to analyze the influence of temperature in the present measurements an experiment was carried out, where the LIF signal was collected during an increase of the temperature of the sample holder, at a constant pressure and with a known concentration of CO_2. The total pressure was regulated and kept constant by a pressure controller (Bronkhorst EL-PRESS) at 136 mbar with a continuous flow of CO_2 and Ar through the reactor. The LIF signal was recorded at 10 Hz while the temperature of the sample was increased from 120°C to 280°C. Supplementary Figure 2c shows the theoretically calculated density of molecules/m^3 (dashed line) from the ideal gas law where the gas is assumed to have the same temperature as the sample, together with the measured LIF signal (gray solid line) 1 mm above the sample surface. The LIF signal is corrected for the change in population due to the increase in temperature using data from the HITRAN database[7]. It can be seen that when both the dependence on population (for the LIF signal) and density as a function of temperature is taken into account the signal behavior can be well reproduced.

SUPPLEMENTARY REFERENCES

1 Svanberg, S. Medical Diagnostics Using Laser-Induced Fluorescence. *Phys Scripta* **T19b**, 469-475, (1987).

2 Aldén, M., Bood, J., Li, Z. & Richter, M. Visualization and understanding of combustion processes using spatially and temporally resolved laser diagnostic techniques. *Proceedings of the Combustion Institute* **33**, 69-97, (2011).

3 Kohse-Höinghaus, K. Laser Techniques for the Quantitative Detection of Reactive Intermediates in Combustion Systems. *Prog Energ Combust* **20**, 203-279, (1994).

4 Ehn, A., Johansson, O., Arvidsson, A., Aldén, M. & Bood, J. Single-laser shot fluorescence lifetime imaging on the nanosecond timescale using a Dual Image and Modeling Evaluation algorithm. *Opt Express* **20**, 3043-3056, (2012).

5 Kirby, B. J. & Hanson, R. K. Imaging of CO and CO_2 using infrared planar laser-induced fluorescence. *Proceedings of the Combustion Institute* **28**, 253-259, (2000).

6 Zetterberg, J. *et al.* An in situ set up for the detection of CO_2 from catalytic CO oxidation by using planar laser-induced fluorescence. *Rev Sci Instrum* **83**, 053104, (2012).

7 Rothman, L. S. *et al.* The HITRAN 2008 molecular spectroscopic database. *J Quant Spectrosc Ra* **110**, 533-572, (2009).

Paper IX

JOURNAL OF SYNCHROTRON RADIATION
ISSN 1600-5775

Combining synchrotron light with laser technology in catalysis research

Sara Blomberg,[a]* Johan Zetterberg,[b] Johan Gustafson,[a] Jianfeng Zhou,[b] Mikhail Shipilin,[a] Sebastian Pfaff,[b] Uta Hejral,[a] Per-Anders Carlsson,[c] Olof Gutowski,[d] Florian Bertram[d] and Edvin Lundgren[a]

[a]Synchrotron Radiation Research, Lund University, Box 118, Lund 22100, Sweden, [b]Combustion Physics, Lund University, Box 118, Lund 22100, Sweden, [c]Competence Centre for Catalysis, Chalmers University of Technology, Gothenburg 41296, Sweden, and [d]Photon Science, DESY, Notkestrasse 85, Hamburg 22607, Germany. *Correspondence e-mail: sara.blomberg@chemeng.lth.se

Received 1 March 2018
Accepted 23 July 2018

Edited by Y. Amemiya, University of Tokyo, Japan

Keywords: high-energy surface X-ray diffraction (HESXRD); planar laser-induced fluorescence (PLIF); CO oxidation; Pd(100).

High-energy surface X-ray diffraction (HESXRD) provides surface structural information with high temporal resolution, facilitating the understanding of the surface dynamics and structure of the active phase of catalytic surfaces. The surface structure detected during the reaction is sensitive to the composition of the gas phase close to the catalyst surface, and the catalytic activity of the sample itself may affect the surface structure, which in turn may complicate the assignment of the active phase. For this reason, planar laser-induced fluorescence (PLIF) and HESXRD have been combined during the oxidation of CO over a Pd(100) crystal. PLIF complements the structural studies with an instantaneous two-dimensional image of the CO_2 gas phase in the vicinity of the active model catalyst. Here the combined HESXRD and PLIF *operando* measurements of CO oxidation over Pd(100) are presented, allowing for an improved assignment of the correlation between sample structure and the CO_2 distribution above the sample surface with sub-second time resolution.

1. Introduction

Catalysis is widely used in the industrial production of, for instance, base and speciality chemicals and fuels but is also used in the reduction of toxic emissions from stationary and mobile sources.

The catalyst accelerates a chemical reaction by providing an alternative pathway with a lower-energy barrier for the reaction, without being consumed. The heterogeneously catalyzed pathway often proceeds *via* adsorption of the reactants from a fluid phase onto the surface of a solid catalyst, which mediates the catalytic reaction. A common type of catalyst is the so-called supported catalyst, which often consists of catalytically active nanoparticles embedded in a porous high-surface-area oxide. The complex composition of industrial catalysts and the harsh environmental conditions in the reactor make the feasibility for fundamental surface studies of the catalyst under operating conditions challenging. The details of a catalytic reaction are therefore, in most cases, not fully understood under realistic reaction conditions.

Simplified model systems with, for example, single crystals are therefore used to gain fundamental knowledge about the catalytically active surface (Ertl *et al.*, 1997). The well defined surface of a single crystal enables the study of specific properties of surface sites or surface structures that are present on the industrial catalytic nanoparticle, and how they contribute to the catalytic activity (Westerström *et al.*, 2007; Todorova *et*

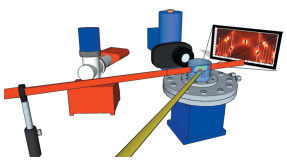

OPEN ACCESS

al., 2003; Mavrikakis *et al.*, 1998; Hammer, 2006; Gustafson *et al.*, 2005; Gao *et al.*, 2009; Somorjai & Li, 2010).

CO oxidation is considered one of the simplest reactions and is therefore traditionally chosen as a model reaction when surface-science studies are performed (Freund *et al.*, 2011). The experiments are often performed *ex situ* or during exposures at low pressures, typically ranging from 10^{-10} mbar to 10^{-6} mbar. In this manner, the well defined model of the industrial catalyst can be investigated under well controlled conditions and reliable data can be obtained. Despite these previously well controlled *ex situ* studies, the active phase of CO oxidation on a Pd-based catalyst is still under debate (Gao *et al.*, 2009, 2010; Rijn, Balmes *et al.*, 2010). In *operando* studies, the catalyst is studied under working conditions such that the surface structure interacting with gas-phase molecules can be correlated to the function of the catalyst (Blomberg *et al.*, 2013; Hendriksen *et al.*, 2010; Ackermann *et al.*, 2005; Gustafson *et al.*, 2008; Gao *et al.*, 2009; Toyoshima & Kondoh, 2015; Lundgren *et al.*, 2017; Chen *et al.*, 2007; Rupprechter & Weilach, 2007). To achieve a better understanding of the gas–surface interaction, the advantage of having experimental setups which allow the combination of several techniques have been highlighted in the last decade (Head *et al.*, 2017; Tinnemans *et al.*, 2006). Some of the advantages of collecting data with several techniques in the same setup are that the results can be achieved under the same conditions. In the ideal case, the techniques can operate simultaneously under operating conditions, giving the opportunity to reach a more detailed understanding of the processes under study.

The activity of the catalyst is often measured by studying the gas composition detected by a mass spectrometer (MS). When the MS is positioned at the outlet of the reactor, as in the present study, the result is a poor spatially resolved measurement and delayed detection of the gas-phase molecules, determined by the path length that the gas molecules travel before reaching the MS detector. For this purpose, we have used planar laser-induced fluorescence (PLIF) to probe the gas phase instantaneously and visualize it close to the catalyst surface (Blomberg *et al.*, 2016). In the present study, PLIF has been used in combination with high-energy surface X-ray diffraction (HESXRD) for surface structure determination (Gustafson *et al.*, 2014). By combining these techniques, we can link the surface structure to the CO_2 production (detected 0.3 mm above the surface non-intrusively) on a sub-second scale. Our observations show that the position of the MS is crucial in determining a correct correlation between catalytic activity and the surface structure of the catalyst.

2. Methods

The experiments were performed at beamline P07 at PETRA III positioned at Deutsches Elektronen-Synchrotron (DESY). This beamline is designed for material studies with hard X-ray radiation (King *et al.*, 2014). The high-energy X-rays enable full surface-structure determination, where each detector image contains the projection of a large area of the reciprocal space, on a time scale suitable for *operando* studies (Gustafson *et al.*, 2014; Shipilin *et al.*, 2014, 2016; Hejral *et al.*, 2016, 2017). The incident angle of the X-rays was set to 0.04°, close to the critical angle of Pd(100) at the photon energy used (85 keV). The diffraction pattern was detected with a temporal resolution of 2 Hz by a two-dimensional Perkin–Elmer detector positioned 1.75 m from the sample. The detector was protected from high-intensity X-rays at the positions of the Pd(100) and the sapphire reactor walls' Bragg reflections by W pieces. These blocks are seen as dark rectangles in the diffraction images (Fig. 2).

In addition, a laser in the infrared spectral region (2.7 µm) was used to probe CO_2 in the gas phase in the vicinity (0.3 mm) of the Pd(100) surface at a repetition rate of 10 Hz. PLIF is a species-specific technique, in which the molecule of interest is excited by a laser sheet and then relaxes by emission of a photon (*i.e.* fluorescence), and the fluorescence is detected using a camera. Our target molecule (CO_2) can be probed *via* ro-vibrational transitions in the mid-infrared. There are several detection schemes that can be employed for probing CO_2, *e.g.* the overtone and combination band at around 2.0 µm (12^01) → (00^00) (Alwahabi *et al.*, 2007), the combination band at 2.7 µm (00^00) → (10^01) (Zetterberg *et al.*, 2012; Kirby & Hanson, 2002) and the fundamental band at around 4.3 µm (Goldenstein *et al.*, 2015). In this study, the combination band was probed in the CO_2 molecule using a pulsed laser at ∼2.7 µm with a pulse duration of ∼5 ns and a power of ∼7 mJ pulse^{-1}. The laser beam formed a thin laser sheet of ∼6 mm height by sheet-shaping optics and then sent through the sapphire reactor dome ∼0.3 mm above the sample surface. The CO_2 fluorescence was then imaged onto a two-dimensional focal plane array (FPA) (SBF LP134, Santa Barbara Focal Plane) perpendicular to the laser sheet. The camera exposure time was set to 30 µs and chosen for efficient collection of the CO_2 fluorescence signal while avoiding detector saturation by the thermal background. To address the varying thermal background, the FPA was triggered at 20 Hz, thus taking an extra image between every laser shot, making subtraction of the thermal background possible on a single-shot basis. A more detailed description of the experimental setup and detection scheme can be found in previous work (Zhou *et al.*, 2017). Images of the CO_2 distribution were acquired every 0.1 s, but, for better statistics (signal to noise ratio) in the images and to match the HESXRD repetition rate, the PLIF data were averaged with the result of an image every 0.5 s. Calibration measurements with known CO_2 partial pressures were performed in order to correlate the detected PLIF signal to partial pressures. A schematic of the setup is shown in in Fig. 1.

2.1. Reactor and sample preparation

The reactor used for the experiment is based on the same design as the reactor described by Rijn, Ackermann *et al.*, (2010). For the present experiment, a reactor dome, with a volume of 25 ml, made of sapphire for the transmission of both X-ray and IR wavelengths, was used. Individual gas mass flow controllers (Bronkhorst EL-FLOW) were used for each gas

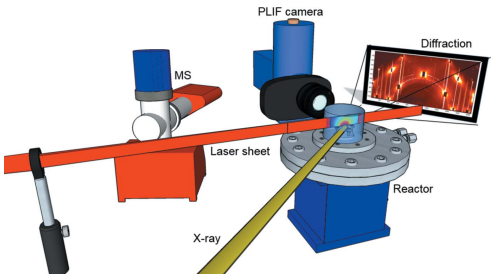

Figure 1
Schematic view of the experimental setup. The diffraction pattern from the (100) surface was detected in the forward direction with respect to the incoming X-rays. The laser sheet, with a wavelength of 2.7 μm, used to probe the CO_2 gas phase, was sent through the reactor at an angle of approximately 45° relative to the X-rays. The camera for CO_2 detection was positioned perpendicular to the laser sheet. In addition, an MS was connected to the outlet of the reactor to measure the global gas concentration.

with a capacity to individually flow up to 200 $ml_n\ min^{-1}$. A pressure controller (Bronkhorst EL-PRESS) was attached to the outlet to keep the pressure constant throughout the experiments. The gas composition in the reactor was measured with a quadrupole MS (Pfeiffer PrismaPlus QMG220). The MS was connected to the outlet of the reactor *via* a 4 m-long tube (diameter 6 mm), and a specially made automatic leak valve (LPM Leiden Probe Microscopy BV) was used to regulate the pressure in the MS. An implemented feedback system in the leak valve made it possible to control and keep the pressure constant in the MS, even though drastic changes in the gas flows were applied. The MS data were synchronized with the PLIF images using *LabView* while the HESXRD data and PLIF/MS were synchronized *via* timestamps in their individual data files.

The experimental setup is equipped with an ultra-high vacuum part where cleaning of the sample was carried out. The single crystal was cleaned by Ar^+ sputtering using an ion energy of 1.5 keV in an Ar pressure of 1×10^{-5} Torr. Oxygen treatments removed carbon contaminations by exposing the surface to 1×10^{-6} Torr of O_2 and heating the sample to 900 K.

3. Results

To establish a better picture of the CO oxidation over Pd(100), we performed an *operando* surface-structure determination in combination with CO_2 gas-phase visualization experiments. HESXRD data images acquired with a photon energy of 85 keV cover a large part of the reciprocal space and reveal the Pd(100) surface structure. Simultaneously recorded PLIF images gained with a laser wavelength of 2.7 μm show the CO_2 gas-phase distribution above the Pd(100) surface. The surface-structure and gas-phase images were matched, and the CO oxidation could be followed with an updating frequency of 0.5 s. In addition, an MS was positioned at the outlet of the reactor, sampling the global gas concentrations in the reactor.

To demonstrate the possibility of correlating the surface structure with a change in the gas-phase composition using PLIF and HESXRD, the catalytic activity was modulated by varying the gas ratios of CO and O_2 at a constant temperature of 200 °C of the sample. The advantage of performing spatially resolved *operando* measurements with high temporal resolution is emphasized in Fig. 2, where the ignition of the catalyst can be followed in detail over time. At the start of the experiment, we exposed the Pd(100) to 6 mbar of CO and 144 mbar of Ar but no O_2, which generated an inactive and CO poisoned sample. The diffraction data recorded under this condition (Fig. 2*a*) shows Bragg reflections from the bulk and crystal truncation rods from the surface of the Pd(100), demonstrating that a well ordered metallic surface is present when no CO_2 signal is detected in the gas phase over the surface (Fig. 2*b*). To activate the Pd(100) catalyst, the gas composition was changed to reaction conditions by adding 24 mbar of O_2 simultaneously as the Ar pressure was decreased to 120 mbar in order to maintain a total pressure of 150 mbar constant. Using these reaction conditions, we found that a sample temperature of 200 °C was sufficient to bring the reaction into the mass-transfer limited (MTL) regime where a characteristic boundary layer of CO_2 was observed (Figs. 2*d* and 2*f*), consistent with previous PLIF studies of the gas phase in the MTL regime (Zetterberg *et al.*, 2015). The boundary layer of the CO_2 product species accumulated around the surface inhibits the CO molecules reaching the surface and the reaction becomes CO-diffusion limited (Matera & Reuter, 2012). As a consequence of the boundary layer formation , the gas composition within the boundary layer is significantly different compared with the rest of the reactor, resulting in a more oxidizing environment above the surface in this regime (Blomberg *et al.*, 2016). At this early stage in the MTL regime, a well ordered oxidized surface is not yet formed and the metallic phase of the surface is still detected in the HESXRD image (Fig. 2*c*). We conclude that, approximately 2 s after ignition of the catalyst (Fig. 2*e*), a diffraction pattern with surface truncation rods corresponding to the $(\sqrt{5} \times \sqrt{5})$-R27° surface oxide (Todorova *et al.*, 2003; Gustafson *et al.*, 2014; Shipilin *et al.*, 2014) could be observed. After that, the surface oxide rods become more intense and the CO_2 boundary layer is continuously observed for the remaining time of the experiment.

For the purpose of deactivating the catalyst, the flow of oxygen was turned off, and the same initial conditions of the experiment were present in the reactor. As the CO_2 PLIF signal dropped, the surface oxide was reduced and could not be observed in the diffraction data when the CO_2 signal close to the sample was approximately zero.

To correlate the presence of a surface oxide with the CO_2 concentration above the catalyst surface, the intensity variation of the truncation rods originating from the $(\sqrt{5} \times \sqrt{5})$-R27° surface oxide during the CO oxidation experiment, is studied more in detail and compared with the CO_2 PLIF signal extracted from an area of 1.65 mm^2, 0.3 mm above the surface

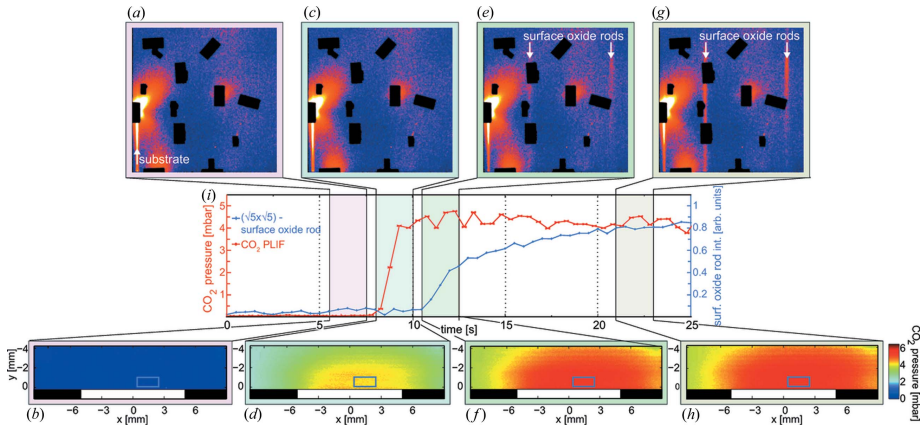

Figure 2
CO oxidation over Pd(100). Each image (HESXRD and PLIF) is averaged over 2.5 s (shown as a colored area in the graph) for better statistics. The graph in (*i*) shows how the CO_2 PLIF signal, extracted from the area marked with a blue rectangle in (*b*), (*d*), (*f*) and (*h*), together with the intensity of the surface-oxide rod, changes over time. A linear background is subtracted from the plotted HESXRD surface-oxide rod intensity. The data are plotted with an updating frequency of 0.5 s. (*a*) HESXRD image of an inactive sample. A surface truncation rod from the (100) substrate is detected (lower left corner), indicating that a metallic surface is present. (*b*) No CO_2 is detected in the gas phase above the sample surface. (*c*) A metallic surface is detected in the HESXRD data. (*d*) PLIF image showing the ignition of the reaction as the sample becomes active. (*e*) After the sample has been active for about 2.5 s, superstructure rods from the diffraction of the $(\sqrt{5} \times \sqrt{5})$-R27° surface oxide (white arrows) appear in the diffraction pattern. (*f*) As the sample becomes active, a prominent boundary layer of CO_2 is detected using PLIF. (*g*) After additional reaction time, the $(\sqrt{5} \times \sqrt{5})$-R27° surface-oxide diffraction pattern intensifies. (*h*) PLIF images showing that the CO_2 boundary layer is still present over the surface.

(Fig. 3*a*). The graph illustrates that the temporal resolution with which we can follow the reaction (HESXRD 2 Hz, PLIF 10 Hz) is sufficient to monitor the ignition of the reaction both in the gas phase and through the surface reconstruction. The sudden increase in CO_2 production upon sample ignition is easily captured by PLIF though it is clear that the dynamics on the surface forming a well ordered surface oxide is slower. The growth can be followed by studying the intensity of the diffraction rod from the surface oxide, which shows that it takes 2.5 s before any sign of the oxide can be detected. Our results indicate that a metallic surface is present at the ignition of the reaction, but we cannot exclude small domains that are not visible in the diffraction pattern of the $(\sqrt{5} \times \sqrt{5})$-R27° structure present at the surface. The intensity of the surface-oxide rods increases slowly for around 10 s during the experiment, consistent with a growth of the $(\sqrt{5} \times \sqrt{5})$-R27° islands and is interpreted as the surface being, to a large extent, covered with the $(\sqrt{5} \times \sqrt{5})$-R27° surface oxide 10 s after ignition.

An MS attached *via* a 4 m-long (diameter 6 mm) gas line at the outlet of the reactor enabled us to achieve information on the global gas concentrations in the reactor. For the purpose of evaluating the gas detecting techniques used in our setup, we compared the MS signal with the PLIF signal (Fig. 3*b*). The PLIF signal originates from the CO_2 gas molecules that are

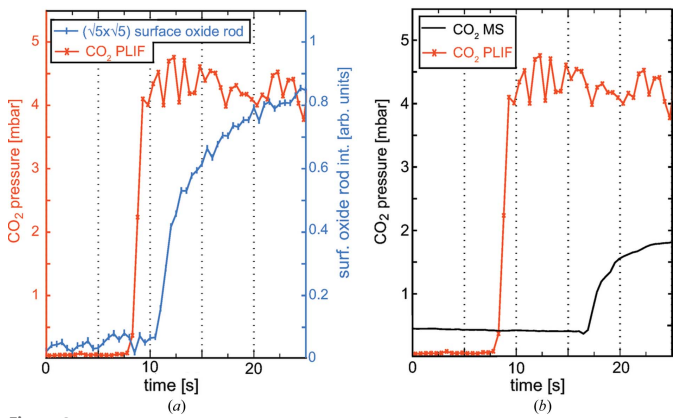

Figure 3
Data extracted from a series of images recorded during the experiment shown in Fig. 2. (*a*) The total intensity of the superstructure rod from the $(\sqrt{5} \times \sqrt{5})$-R27° surface oxide plotted together with the CO_2 PLIF signal extracted from the blue rectangle indicated in the PLIF images in Fig. 2, allowing for a better correlation between the surface structure and CO_2 production. (*b*) The same PLIF CO_2 signal as in (*a*) plotted together with the CO_2 MS signal.

detected almost instantaneously after they desorb from the active surface. Using the PLIF signal as a reference, we determined the response time of the MS to be 9 s. By comparing the PLIF and MS signals, we could also conclude that a CO_2 partial pressure of around 4–4.5 mbar was measured just above the surface in the MTL regime, while surprisingly, only 2 mbar was detected by the MS during the same period. Neither of the detected CO_2 concentrations indicate a 100% conversion of CO, but the MS shows a significantly lower concentration than that detected close to the surface using PLIF. The large discrepancy between the measured CO_2 partial pressures can be explained by the global detection of the gas by MS that suffers from the complex gas-flow configuration in the reactor (Matera *et al.*, 2014), which smears out the signal as compared with the CO_2 signal detected just above the surface by PLIF.

4. Conclusions and discussion

The CO oxidation over Pd(100) has previously been studied in great detail, but the question remains whether it is the metallic or oxidized surface that is the most active phase. Herein, we report on the first *operando* measurement where HESXRD, used for surface-structure determination, is combined with PLIF to detect the CO_2 gas in the vicinity of a catalyst surface. PLIF provides an image of the CO_2 almost instantaneously as the CO_2 desorbs from the surface, which enables a correlation to be made between the active surface structure and the gas-phase environment.

PLIF images reveal a boundary layer of CO_2 close to the surface when the Pd(100) model catalyst is in the MTL regime, resulting in a gas composition in the vicinity of the surface that is significantly different to the concentration detected by the MS at the outlet of the reactor. We conclude that the oxidizing environment, caused by the boundary layer, oxidizes the surface to a large extent, which implies that the catalytic activity of the sample itself affects the surface structure. Our findings show that the surface is not fully oxidized when the ignition of the catalyst occurs, but we cannot exclude that oxidized islands, not detectable with the diffraction, are present on the surface. After several seconds in the highly active regime, however, a strong signal from the surface oxide is detected in the diffraction pattern. Moreover, our data confirm that the response time of the MS is critical when establishing a correlation between surface structure and activity. The delay time of the MS, which is dependent on both the experimental setup and conditions applied, may introduce an uncertainty when measuring and comparing the catalytic activity of a catalyst at different setups, even though identical conditions have been applied. Fortunately, in the present setup, it is possible to measure the response time for the MS by comparing the signals from the MS and PLIF, but to estimate the time delay for the gas detection by MS is generally not trivial. The advantage of using PLIF to complement MS is also demonstrated by extracting the partial pressure of CO_2, located above the sample surface, which differs significantly from the pressure detected by the MS at the reactor outlet.

In the present study, our measurements were limited by a constant temperature as a result of the critical alignment of the X-rays that should have an incident angle of 0.04° on the sample surface and temperature variation may misalign the sample. It would therefore be interesting to combine PLIF with transmission X-ray diffraction (Reikowski *et al.*, 2017; Acciarri *et al.*, 1996), where X-rays penetrate the sample and as a result are less sensitive to temperature variations. The transmission mode of the X-rays would also generate a smaller footprint of the X-ray on the sample surface, which opens up for better spatially resolved surface structure measurements. In the meantime, our results show a unique possibility to relate the activity of the catalyst to the surface structure by combining PLIF and HESXRD. These observations were possible because of the high temporal and spatial resolution in conjunction with immediate detection of desorbed CO_2 molecules from the active surface.

References

Acciarri, M. *et al.* (1996). *Phys. Lett. B*, **371**, 137–148.
Ackermann, M. D., Pedersen, T. M., Hendriksen, B. L. M., Robach, O., Bobaru, S. C., Popa, I., Quiros, C., Kim, H., Hammer, B., Ferrer, S. & Frenken, J. W. M. (2005). *Phys. Rev. Lett.* **95**, 255505.
Alwahabi, Z. T., Zetterberg, J., Li, Z. S. & Aldén, M. (2007). *Eur. Phys. J. D*, **42**, 41–47.
Blomberg, S., Hoffmann, M. J., Gustafson, J., Martin, N. M., Fernandes, V. R., Borg, A., Liu, Z., Chang, R., Matera, S., Reuter, K. & Lundgren, E. (2013). *Phys. Rev. Lett.* **110**, 117601.
Blomberg, S., Zhou, J. F., Gustafson, J., Zetterberg, J. & Lundgren, E. (2016). *J. Phys. Condens. Matter*, **28**, 453002.
Chen, M. S., Cai, Y., Yan, Z., Gath, K. K., Axnanda, S. & Goodman, D. W. (2007). *Surf. Sci.* **601**, 5326–5331.
Ertl, G., Knozinger, H. & Weitkamp, J. (1997). *Handbook of Heterogeneous Catalysis.* Weinheim: Wiley-VCH.
Freund, H. J., Meijer, G., Scheffler, M., Schlögl, R. & Wolf, M. (2011). *Angew. Chem. Int. Ed.* **50**, 10064–10094.
Gao, F., Wang, Y., Cai, Y. & Goodman, D. W. (2009). *J. Phys. Chem. C*, **113**, 174–181.
Gao, F., Wang, Y. L. & Goodman, D. W. (2010). *J. Phys. Chem. C*, **114**, 6874.
Goldenstein, C. S., Miller, V. A. & Hanson, R. K. (2015). *Appl. Phys. B*, **120**, 185–199.
Gustafson, J., Mikkelsen, A., Borg, M., Andersen, J. N., Lundgren, E., Klein, C., Hofer, W., Schmid, M., Varga, P., Köhler, L., Kresse, G., Kasper, N., Stierle, A. & Dosch, H. (2005). *Phys. Rev. B*, **71**, 115442.
Gustafson, J., Shipilin, M., Zhang, C., Stierle, A., Hejral, U., Ruett, U., Gutowski, O., Carlsson, P. A., Skoglundh, M. & Lundgren, E. (2014). *Science*, **343**, 758–761.
Gustafson, J., Westerström, R., Mikkelsen, A., Torrelles, X., Balmes, O., Bovet, N., Andersen, J. N., Baddeley, C. J. & Lundgren, E. (2008). *Phys. Rev. B*, **78**, 045423.
Hammer, B. (2006). *Top. Catal.* **37**, 3–16.
Head, A. R., Karslıoğlu, O., Gerber, T., Yu, Y., Trotochaud, L., Raso, J., Kerger, P. & Bluhm, H. (2017). *Surf. Sci.* **665**, 51–55.
Hejral, U., Muller, P., Balmes, O., Pontoni, D. & Stierle, A. (2016). *Nat. Commun.* **7**, 10964.
Hejral, U., Muller, P., Shipilin, M., Gustafson, J., Franz, D., Shayduk, R., Rutt, U., Zhang, C., Merte, L. R., Lundgren, E., Vonk, V. & Stierle, A. (2017). *Phys. Rev. B*, **96,** 195433.

Hendriksen, B. L. M., Ackermann, M. D., van Rijn, R., Stoltz, D., Popa, I., Balmes, O., Resta, A., Wermeille, D., Felici, R., Ferrer, S. & Frenken, J. W. M. (2010). *Nat. Chem.* **2**, 730–734.
King, A., Beckmann, F., Muller, M., Schreyer, A., Schell, N. & Fischer, T. (2014). *Mechanical Stress Evaluation by Neutrons and Synchrotron Radiation VI*, Vol. 772, pp. 57–61. Trans Tech Publications.
Kirby, B. J. & Hanson, R. K. (2002). *Appl. Opt.* **41**, 1190–1201.
Lundgren, E., Zhang, C., Merte, L. R., Shipilin, M., Blomberg, S., Hejral, U., Zhou, J. F., Zetterberg, J. & Gustafson, J. (2017). *Acc. Chem. Res.* **50**, 2326–2333.
Matera, S., Maestri, M., Cuoci, A. & Reuter, K. (2014). *ACS Catal.* **4**, 4081–4092.
Matera, S. & Reuter, K. (2012). *J. Catal.* **295**, 261–268.
Mavrikakis, M., Hammer, B. & Nørskov, J. K. (1998). *Phys. Rev. Lett.* **81**, 2819–2822.
Reikowski, F., Wiegmann, T., Stettner, J., Drnec, J., Honkimäki, V., Maroun, F., Allongue, P. & Magnussen, O. M. (2017). *J. Phys. Chem. Lett.* **8**, 1067–1071.
Rijn, R. van, Ackermann, M. D., Balmes, O., Dufrane, T., Geluk, A., Gonzalez, H., Isern, H., de Kuyper, E., Petit, L., Sole, V. A., Wermeille, D., Felici, R. & Frenken, J. W. M. (2010). *Rev. Sci. Instrum.* **81**, 014101.
Rijn, R. van, Balmes, O., Felici, R., Gustafson, J., Wermeille, D., Westerström, R., Lundgren, E. & Frenken, J. W. M. (2010). *J. Phys. Chem. C*, **114**, 6875–6876.
Rupprechter, G. & Weilach, C. (2007). *Nano Today* **2**, 20–29.
Shipilin, M., Gustafson, J., Zhang, C., Merte, L. R. & Lundgren, E. (2016). *Phys. Chem. Chem. Phys.* **18**, 20312–20320.
Shipilin, M., Hejral, U., Lundgren, E., Merte, L. R., Zhang, C., Stierle, A., Ruett, U., Gutowski, O., Skoglundh, M., Carlsson, P. A. & Gustafson, J. (2014). *Surf. Sci.* **630**, 229–235.
Somorjai, G. A. & Li, Y. (2010). *Introduction to Surface Chemistry and Catalysis*, 2nd ed. Hoboken: Wiley–Blackwell.
Tinnemans, S. J., Mesu, J. G., Kervinen, K., Visser, T., Nijhuis, T. A., Beale, A. M., Keller, D. E., van der Eerden, A. M. J. & Weckhuysen, B. M. (2006). *Catal. Today*, **113**, 3–15.
Todorova, M., Lundgren, E., Blum, V., Mikkelsen, A., Gray, S., Gustafson, J., Borg, M., Rogal, J., Reuter, K., Andersen, J. N. & Scheffler, M. (2003). *Surf. Sci.* **541**, 101–112.
Toyoshima, R. & Kondoh, H. (2015). *J. Phys. Condens. Matter*, **27**, 083003.
Westerström, R., Gustafson, J., Resta, A., Mikkelsen, A., Andersen, J. N., Lundgren, E., Seriani, N., Mittendorfer, F., Schmid, M., Klikovits, J., Varga, P., Ackermann, M. D., Frenken, J. W. M., Kasper, N. & Stierle, A. (2007). *Phys. Rev. B*, **76**, 155410.
Zetterberg, J., Blomberg, S., Gustafson, J., Evertsson, J., Zhou, J., Adams, C. E., Carlsson, P. A., Aldén, M. & Lundgren, E. (2015). *Nat. Commun.* **6**, 7076.
Zetterberg, J., Blomberg, S., Gustafson, J., Sun, Z. W., Li, Z. S., Lundgren, E. & Alden, M. (2012). *Rev. Sci. Instrum.* **83**, 053104.
Zhou, J. F., Pfaff, S., Lundgren, E. & Zetterberg, J. (2017). *Appl. Phys. B*, **123**, 3.

Paper X

Experimental and modeling studies of the gas phase of model catalysts in a stagnation flow

Jianfeng Zhou [1], Sebastian Matera [2], Sebastian Pfaff [1], Sara Blomberg [3], Edvin Lundgren [4] and Johan Zetterberg [1]*

AUTHOR ADDRESS

[1] Division of Combustion Physics, Lund University, SE-22100 Lund, Sweden

[2] Institute for Mathematics, Freie Universität Berlin, D-14195 Berlin, Germany

[3] Department of Chemical Engineering, Lund University, SE-22100 Lund, Sweden

[4] Division of Synchrotron Radiation Research, Lund University, SE-22100 Lund, Sweden

ABSTRACT

A stagnation flow reactor has been designed and characterized for both experimental and modeling studies of single crystal model catalysts in heterogeneous catalysis. Using CO oxidation over a Pd(100) single crystal as a showcase, we have employed planar laser-induced fluorescence (PLIF) to visualize the CO_2 distribution over the catalyst under reaction conditions and subsequently used the 2D spatially resolved gas phase data to characterize the stagnation flow reactor. With a comparison of the experimental data and the stagnation flow model, it was found that a good stagnation flow can be achieved with the reactor. Furthermore, the combined stagnation flow/PLIF/modeling approach makes it possible to estimate the turn over frequency (TOF) of the catalytic surface from the measured CO_2 concentration profiles above the surface and to predict the CO_2, CO and O_2 concentrations at the surface under reaction conditions.

INTRODUCTION

Most of our atomic scale understanding of heterogeneous catalysis stems from surface science experiments performed under well controlled conditions, i.e. at low temperatures and ultra-high vacuum (UHV). These conditions differ largely from those in industrial catalysis. The awareness of the so-called "pressure gap" has in recent years resulted in an increasing number of *in-situ* surface sensitive techniques targeting at more realistic gas conditions.[1-2] Prominent examples are near ambient-pressure X-ray photoelectron spectroscopy (AP-XPS),[3-5] high-pressure scanning tunneling microscopy/atomic force microscopy (HPSTM/AFM),[6-7] polarization-modulated infrared absorption spectroscopy (PM-IRAS),[8-9] and surface X-ray diffraction (SXRD).[10-11]

As the pressure increases, the gas phase above a catalyst surface starts to play a complex role.[12] At semi-realistic conditions, the gas phase transport is not ballistic anymore and a product boundary layer (BL) might form above the catalyst hindering the reactants to efficiently reach the catalytic surface. As a consequence, the gas concentrations at the catalyst surface might differ significantly from the applied ones at the inlet, depending on the activity of the catalyst.[13-15] This coupling of surface chemistry and gas transport has not only a quantitative effect, but qualitatively new features might arise, such as hysteresis or strong lateral variation of the reaction conditions and concomitant reactivity and surface atomic structure.[15-16] Experimentally, the latter has been observed for the CO oxidation on a Pd(100) surface, where it has been shown that a gradient of the gas concentrations across the surface can lead to a gradient of the surface optical reflectivity, a strong indication of a spatial inhomogeneity of oxide thickness or roughness on the surface.[17-18] For a better understanding of the surface chemistry or the catalytic processes

at realistic gas conditions, knowledge of the effect of flow and reactor geometries on model catalysts becomes important.[16, 19]

Conventional methods to acquire gas phase data are e.g. mass spectrometry (MS) and Fourier transform infrared spectrometry (FTIR). However, neither can spatially probe the gas phase close to the sample in an easy manner. With a scanning mass spectrometer, one can spatially sample the gas phase above the sample with a capillary.[20] This would, however, inherently affect the gas flow and temperature above the sample. Conventional FTIR can be modified to spatially measure the gas phase above a catalyst.[21] It is, however, a line-of-sight technique, thus not being able to resolve the gas phase in all dimensions. In this context, planar laser-induced fluorescence (PLIF) is a valuable technique that can provide 2D spatially resolved gas phase information, non-intrusively and with a spatial resolution down to 70 μm.[22-23]

Ideally, gas phase measurements are complemented with a theoretical/computational analysis of the coupling of gas flow and catalytic activity, e.g. by the recently developed combined first-principles kinetic Monte Carlo (1p-kmc) and computational fluid dynamics (CFD) approach.[24] With the combination, a maximum of insight into the surface chemistry can be gained.[25]

In general geometries, CFD might become prohibitively expensive, especially when targeting for the elucidation of the pressure/reactivity correlation, which would require to solve the inverse problem. For the use of single crystal model catalysts, stagnation flow reactors are especially appealing, as they ensure a highly homogeneous gas phase distribution across the catalyst. If properly designed, the transport can be modeled by a simple one-dimensional boundary value problem, allowing for an efficient numerical treatment.[26-27]

In this work, we present our attempts to realize combined PLIF/stagnation flow experiments for gas phase studies of single crystal model catalysts and demonstrate their capabilities on the prototypical CO oxidation over a Pd(100) surface. We have used PLIF to spatially resolve the CO_2 concentration distribution above the catalyst under reaction conditions. With a stagnation flow model, we extract the turnover of frequency (TOF) of the catalyst surface from the measured concentration of CO_2 above the surface and use the TOF to predict the concentrations of CO_2, CO and O_2 at the catalyst surface.

EXPERIMENTAL STUDY

Reactor chamber

A schematic picture of our setup is shown in Figure 1. A cubical chamber of volume 23 ml with three windows for optical access was used for the PLIF measurements. The sample used for this study is a hat-shaped Pd single crystal with a diameter of 6 mm, a height of 2 mm and with the (100) structure. A pipe is positioned above the sample from the top of the chamber and used as the gas inlet, which allows for a gas stream towards the sample surface, as shown in Figure 1b. The distance between the pipe and the sample surface is ~5.5 mm. The sample was supported and heated by a boralectric heater and, the temperature was measured by a type-D thermocouple.

The inlet gas flow of each species was set by individual mass flow controllers (Bronkhorst EL-FLOW), and the gas pressure in the reactor was controlled by a digital pressure controller (Bronkhorst EL-PRESS) at the gas outlet. In addition to PLIF, the gas composition in the reactor was measured by a quadruple mass spectrometer (MS, Pfeiffer, QME 220) connected to the

outlet of the reactor by a gas tube (length = 80 cm and diameter = 1/16 in.). An automatic leak valve was used to regulate the amount of gas from the outlet leaking into the MS for analysis, and to stabilize the pressure in the MS at 5×10^{-6} mbar. A more complete description of the gas system can be found in ref 28. The MS signal is converted into mbar by normalizing the MS CO signal to the known initial partial pressure, and the MS CO_2 signal was scaled to match the measured conversion of CO.

In a stagnation flow, the gas transport in the central region above the catalyst can be modeled using the stagnation flow equations, when the diameters of the catalyst surface and the inlet are large compared to the distance between the inlet and the catalyst.[26] In this work, the diameters of the single crystal sample and the inlet are 6 mm and 7 mm, respectively, which are similar to the distance between the inlet and catalyst. The deviation from the ideal case has been considered in our modeling, and we found that the necessary modifications to the model for the ideal case are rather small, such that the computational efficiency is not affected and, especially, that the parameters, needed for the modified model, can efficiently be determined from the measured PLIF signal.

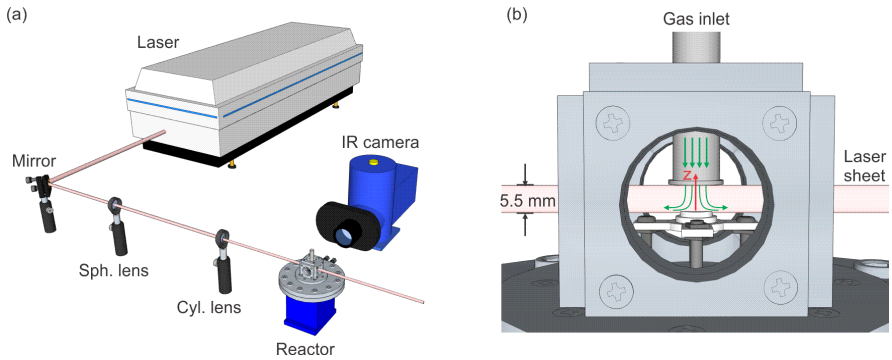

Figure 1 Schematic of the experimental set-up (a) overview and (b) a close-up of the reactor chamber with the laser sheet. The green arrows show the flow schematically, and the red arrow indicates the z-axis in the modeling.

PLIF

Laser-induced fluorescence (LIF) is a highly sensitive, species specific technique that can be used for gas detection with high spatial resolution.[29-30] As illustrated in Figure 1, when a laser beam is formed into a laser sheet using a pair of lenses, the gas molecules in a 2D region can be excited by the laser light tuned to a specific wavelength. Upon relaxation, these gas molecules fluoresce, and a camera positioned perpendicular to the laser sheet can be used to record or image the fluorescence signal (usually) at another wavelength. In this way, 2D information (e.g. concentrations and temperature) of the gas of interest can be obtained. This 2D spatially resolved technique is called planar Laser-induced fluorescence (PLIF).

The experimental setup and detection scheme for the CO_2 PLIF have been described in detail previously,[31] and only a brief description will be given here. The CO_2 was excited through the $(00^00) \rightarrow (10^01)$ combination band at ~2.7 µm and the following fluorescence from the fundamental band was detected at ~4.3 µm. The fundamental 1064 nm laser beam from a single-mode Nd:YAG laser, was used to pump a broadband infrared optical parametric oscillator (IR-

OPO, GWU, versaScan-L 1064), generating a signal beam at ~1.7 μm and an idler beam at ~2.7 μm, with ~8 mJ/pulse and ~7 mJ/pulse, respectively, both operating at 10 Hz. As shown in Figure 1, the idler beam was formed into a thin laser sheet of ~6 mm height by a spherical (f = +500 mm) and a cylindrical lens (f = +100 mm), and then sent through the reactor between the gas inlet and the catalyst. The CO_2 fluorescence was imaged by a liquid-nitrogen-cooled IR camera (Santa Barbara Focal Plane, SBF LP134). An interference filter inside the camera was used to suppress the strong thermal background. The PLIF signal can be reliably estimated from ~300 μm above the sample surface, limited by the alignment of the sample with respect to the camera and the imaging system of the current setup, which gives a ~70 μm/pixel resolution. Quantification of the detected PLIF signal was achieved by calibration measurements with known CO_2 partial pressures at similar conditions (temperatures and pressures) to real measurements. Due to the lack of a reference cell in the current set-up, which can be used to compensate for wavelength drifting and energy fluctuation of the laser,[23] the calibration of the CO_2 signal has an estimated uncertainty of ~20%.

CO_2 visualization

For the measurements, the Pd(100) sample was first cleaned in a UHV chamber with several sputtering and annealing cycles, and then transferred, through open air, to the stagnation flow reactor for measurements. To reduce surface contamination from transferring the sample, the temperature of the sample was ramped up and down under CO oxidation reaction conditions with an excess of O_2, prior to the start of the measurements.

As an example, we considered an inlet gas mixture with 92% Ar, 4% CO and 4% O_2 at a total pressure of 300 mbar and a total flow of 200 ml_n/min. We ramped the temperature up and down

between room temperature and 360 °C at a rate of 10.5 °C/min, which ensured quasi-stationary flows. These measurements also revealed that we achieved a highly uniform gas phase composition across the surface, as shown in Examples for the recorded CO_2 PLIF images are shown in Figure 2a-f, taken at successive times t_1 - t_6.

The PLIF images in Figure 2a-c have been taken during increasing the temperature and reveal that the sample activity has gone through three phases: i) the whole sample is in the low activity regime; ii) the sides (here referred to the rest of the sample) of the sample are highly active (indicated by the red arrow in Figure 2b); while the (100) surface is still in the low activity regime; iii) the whole sample is highly active. During the temperature ramp-down, the sample has gone through the three phases in the opposite direction, as shown by the PLIF images in Figure 2d-f. See also Movies M1 and M2 showing the CO_2 PLIF measurements during the up and down temperature ramps in the SI, respectively. By integrating the region ~0.3 mm above the catalyst surface (the dashed line in Figure 2a), we obtain the CO_2 LIF signal trends for both the up and down branch, as shown in Figure 2g. It is worth noting that the CO_2 intensity reaches a plateau at phase iii and does not increase further with increasing temperature, indicating a mass transfer limited (MTL) reaction at the surface. By comparing the LIF signal in Figure 2g with the MS signal in Figure 2h, the CO_2 pressure close to the catalyst surface measured by PLIF is significantly higher than that measured by the MS, with a factor of 2. In addition, there are no obvious steps in the LIF trends while there are distinct steps in the MS trends, arising from the ignition of the sides of the sample. This demonstrates that PLIF can measure a well-defined CO_2 signal generated from the (100) surface, which is not or very little affected by the signal generated from the sides of the sample. This is due to the feature of the stagnation flow where the gas is pushed away from the

central region above the catalyst, such that activity originating from downstream part of the sample does not influence the gas composition over the center of the investigated catalyst surface. It is also interesting to see that the first step in the MS trend, corresponding to the activity of the sides, is much larger than the second step originating from the (100) surface. This could be due to the flow geometry. However, the strong signal generated from the sides has very little impact on the PLIF signal from the center of the sample. Thanks to this characteristic, the PLIF signal is well suited to characterize the reactor for a comparison with the stagnation flow model, as will be presented below.

The case with a non-stagnation flow geometry can be found in the S1, which shows that the active sides of a Pd(111) sample can contribute significantly to the CO_2 signal in the vicinity of the (111) surface. This has practical implications as single crystals are being widely used in *in-situ* or *operando* catalysis studies, and they are in practice manufactured to have grooves or to be hat-shaped for easy-to-hold purposes. This could introduce undefined catalytic surfaces, which are often exposed to the same gas environment as the well-defined catalytic surface that is under investigation. If both are equally active, as in the cases shown above, it would be difficult to avoid the resulting interference using prototypical flow reactor geometries, leading to not well-defined correlation in structure-function analysis. To overcome this problem, the presented combined stagnation flow with PLIF approach could serve as a useful alternative.

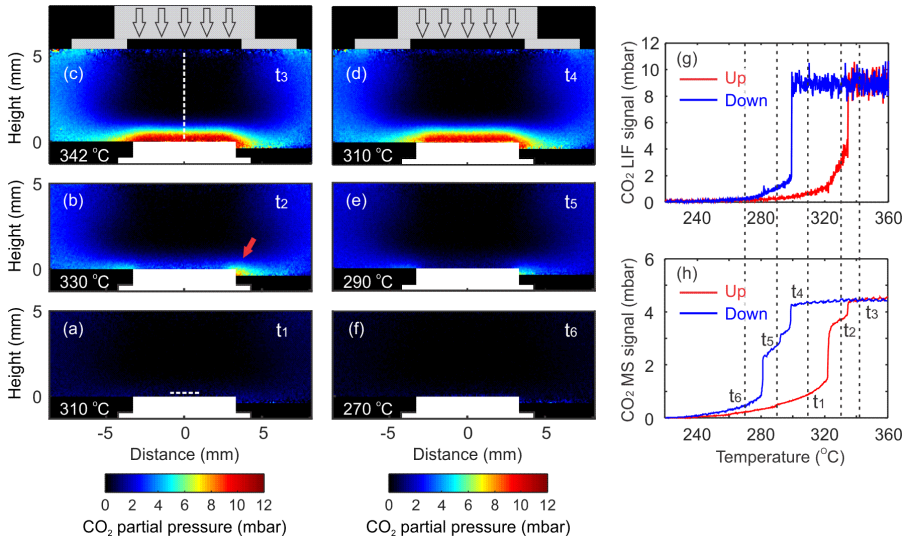

Figure 2 The CO_2 distribution over a Pd(100) single crystal during CO oxidation at 200 ml_n/min total flow and 300 mbar total pressure, and with 4:4:92 O_2:CO:Ar ratio. (a)-(c), 10-shot average PLIF images recorded at different times and temperatures during the temperature ramp up. (d)-(f), 10-shot average PLIF images recorded at different times and temperatures during the temperature ramp down. (g) The integrated PLIF signal 0.3 mm above the sample, as indicated by the dashed line in (a). (h) The corresponding MS signal. The dashed line in (c) indicates the central region between the inlet and the surface. The red arrow in (b) indicates the active side of the sample.

MODELING

As indicated by the white dashed line in Figure 2c, gas concentration in the central region between catalyst and inlet varies only normal to the catalyst surface, i.e. the concentration depends only on the distance z from the catalyst, as indicated by the red arrow in Figure 1b. Then the mass fractions Y^{β} of the different gaseous species between the center of the catalyst (z = 0) and the inlet ($z = L$ = 5.5 mm) can be modeled with the one-dimensional boundary value problem

$$\rho v_z \frac{d}{dz} Y^{\alpha} - \frac{d}{dz} \sum_{\beta} D^{\alpha\beta} \frac{d}{dz} Y^{\beta} = 0 \qquad (1)$$

with (boundary conditions at inlet)

$$Y^{\alpha}(z = L) = Y^{\alpha}_{inl.} \qquad (2)$$

and (boundary conditions at catalyst)

$$D^{\alpha\beta}\frac{d}{dz}Y^{\beta}(z = L) = -\nu^{\alpha}M^{\alpha}TOF\left(Y^{\beta}(z = L)\right) \qquad (3)$$

where ρ is the mass density and υ_z is the axial velocity, both depending on the normal distance *z* to the catalyst, ν^{α} is the stoichiometric coefficient, M^{α} is the molecular mass, and *TOF* is the turn over frequency in units of reactions per unit time and unit area. For eq. 1, we assume stationary operation and negligible gas phase chemical reactions. The inlet mass fractions $Y^{\alpha}_{inl.}$ are given from the applied gas phase composition. The second boundary condition at *z* = 0 (the position of the catalyst) accounts for the chemical conversion due to the catalyst. The diffusion coefficients $D^{\alpha\beta}$ and other transports as well as thermochemical properties of the gas phase are taken to obey the commonly employed semi-empirical correlations.[26] As we are operating at a large excess of Ar and rather low velocities, the density ρ, the temperature *T*, the axial velocity υ_z and the diffusivities $D^{\alpha\beta}$ can be assumed to be independent of the actual reactivity. Equation 1 is then linear in the mass fractions and the normalized partial pressures (NPP)

$$p^{\alpha}_{n}(z) \coloneqq \frac{p^{\alpha}(z) - p^{\alpha}_{inl.}}{\int_{z_0}^{z_e} p^{\alpha}(z') - p^{\alpha}_{inl.}dz'} \qquad (4)$$

are independent of the employed catalyst and depend only on the characteristics of the reaction chamber and the flow conditions. Because of this property, these quantities are especially suited to test our model for the mass transport. The integration can be done between any two points along the z-axis for which the integral does not equal zero.

The solution of eq. 1-3 requires the velocity and temperature fields as an input. In principle these could be obtained from a non-reactive CFD for the whole chamber.[32] However, besides of being computationally demanding, this would require boundary conditions for the temperature at the reactor walls, to which we have no access. Instead, we will infer the relevant information from the measured NPP of CO_2. We constrain $v_z(z)$ and $T(z)$ to obey the ideal stagnation flow equations, but with the boundary conditions at the inlet for these fields as adjustable parameter. The reason for this choice is as follows: Only within a rather thin BL above the catalyst, we have a deviation from the applied concentrations. As the BL is small compared to the catalyst diameter, the ideal stagnation flow equations will be a good approximation there. By adjusting the boundary conditions for the velocity and temperature field, we can now realize any solution to the stagnation flow equation within the BL. Outside the BL, the stagnation flow equations are not valid and therefore the velocity and temperature fields might be wrong. However, as the concentration gradients vanish there, this does not matter as eq. 1 is automatically fulfilled. In practice, we observed that variation of the inlet temperature has only a minor effect on the shape of the NPP and that we can reproduce the experimental signal sufficiently accurate by leaving the inlet radial velocity at its nominal value of zero and only increasing the axial velocity by a factor of 2 from its nominal value defined by the applied flow rate of 200 ml_n/min.

The axial inlet velocity, as an input for the modelling, is determined by solving the reactive stagnation flow equations, i.e. eq. 1-3 together with corresponding equations for the velocity and the temperature, at a constant low *TOF* and adjusting its value to reproduce the experimental NPP. Our approach to solve the stagnation flow equations and the employed thermochemical and transport models can be found in ref 19. Due to the linearity of eq. 1, the actual *TOF*

responsible for the experimental signal can conveniently be determined from the *TOF* used for the simulation and the ratio of the denominators in the experimental and simulated NPPs.

RESULTS AND DISCUSSION

Figure 3 compares the experimental CO_2 NPPs (crosses) and the simulated CO_2 NPPs (solid lines) in the central region along the z-axis between the inlet and the sample surface, for a range of catalyst temperatures from the up and down branches, shown in Figure 2g. The nominal inlet velocity has been increased by a factor of 1.9 and 1.8 for the up and down branch, respectively. Although the stagnation flow equation is expected to be valid in the BL, the inlet velocity parameters in principle need to be adjusted for every single case, as the flow field above the BL might depend on uncontrolled aspects of the experiment such as the temperature distribution of the reactor walls. For simplicity, we have used only the two different values for the inlet velocity for up and down branch and their values have been chosen to give the best visual agreement between simulated and experimental NPPs.

Our theoretical model matches the experimental findings very well, indicating that we can achieve a good stagnation flow in the reactor. As can be seen in Figure 3, the curves in both branches show a small systematic disagreement at lower temperatures. This is because the sample is not highly active at lower temperatures, thus producing only a small amount of CO_2 (less than 0.5 mbar, compared to ~9 mbar when the sample is highly active), which results in nosier PLIF signal.

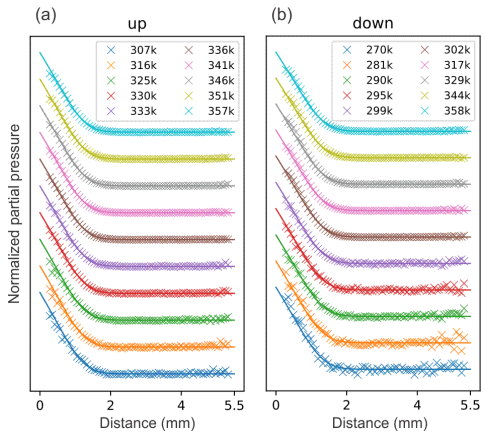

Figure 3 Comparison between the experimental CO_2 NPPs (crosses) and the simulated CO_2 NPPs (solid lines) for a range of catalyst temperatures from the temperature ramp up (a) and down branch (b) in Figure 2. Note that the first data point (cross) corresponds to a measured signal at 0.3 mm above the surface.

Our model can now be used to extract the TOF from the experimental PLIF data from the ratio of the denominators in the experimental and simulated NPPs. This TOF estimation can then be used to predict the gas concentrations at the surface. Figure 4 shows the partial pressures of CO_2, CO and O_2 at the surface as a function of temperature for the up and the down branch. As can be seen, the CO and O_2 partial pressures decrease as the CO_2 pressure increases. As one might expect, the relative drop in the O_2 pressure is roughly half of that of CO, as we have an over-stoichiometric mixture with twice as much oxygen as needed. Notably, the CO partial pressure drops to a value of ~3 mbar (25% of its nominal value). Once this value is reached, a further increase of the temperature does not lead to lower values, indicating an MTL reaction at the surface. In the MTL regime, the CO_2 pressure is modeled to be ~10.5 mbar at the surface, as shown in Figure 4a, compared to 9 mbar as measured by PLIF at 0.3 mm above the surface, as shown in Figure 2g.

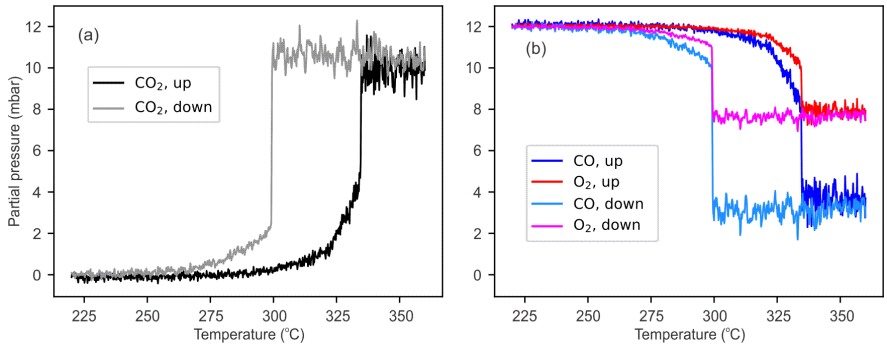

Figure 4 Simulated partial pressures at the sample surface as a function of temperature in the up and down branch. (a) CO_2 profile and (b) corresponding CO and O_2 profiles, simulated from the measured CO_2 pressure profiles above the surface.

The results in this and the previous sections demonstrate the benefits of the employed stagnation flow reactor geometry combined with PLIF measurements. The flow geometry ensures a highly uniform gas phase across the catalyst surface and the PLIF allows to spatially probe the gas phase close to the surface. The combined features of stagnation flow and PLIF make it possible to measure the signal which is only from the activity of the surface under study and does not contain any contaminations from the activity of other parts of catalyst as it is, for instance, the case for a MS signal measured at the outlet of the reactor. Moreover, these features allow to use a simple one-dimensional model and the spatial resolution of the PLIF measurements allows to adjust the flow parameters of the model. With this model, we can extract the TOF and thereby partial pressures at the surface without the need for a kinetic model of the catalyst. It should be mentioned that this kinetic model-free analysis has some limitations. First, gas phase reactions need to be negligible, which, however, is the case for many reactions studied in surface science catalysis. Second, if there is more than one TOF, e.g. in competitive oxidation, one can only extract either only one, or a superposition of the TOFs from the PLIF signal of a single species. In these cases, one could repeat the experiment with PLIF probing another molecule, or ideally,

modify the PLIF experiment such that multiple species can be detected simultaneously.[33] Using a model for the surface kinetics could solve this problem because this will likely introduce a correlation between the different TOFs.

SUMMARY and OUTLOOK

We have presented the gas phase study of a Pd(100) single crystal during CO oxidation to demonstrate the advantages of the combined approach of stagnation flow and PLIF, such as a highly uniform gas phase composition across the sample and measurements which are not affected by the interference from the sides of the catalyst. Albeit not an ideal stagnation flow, the reactor can be analyzed using a similar simple model. With the model, we can estimate the TOF of the catalyst surface and simulate gas concentration profiles at the surface, even without a kinetic model for the catalyst. This could only be achieved due to the combination of a dedicated reactor geometry, PLIF and modeling which can exploit the spatially resolved gas phase information provided by PLIF.

For future work, it would be of great interest to analyze the plateau (MTL or kinetic feature of the Pd(100) surface) and the present hysteresis in Figures 4 using our recently developed 1p-kMC+CFD approach,[24-25] as the combined stagnation flow and PLIF approach presented here shows great advantages in obtaining the gas phase information right at catalyst surfaces.

ASSOCIATED CONTENT

Supporting Information

CO_2 distribution over a Pd(111) single crystal in a non-stagnation flow (PDF)

Movie M1 showing the CO_2 PLIF signal in a stagnation flow during temperature ramp-up (AVI)

Movie M2 showing the CO_2 PLIF signal in a stagnation flow during temperature ramp-down (AVI)

AUTHOR INFORMATION

Corresponding Author

* E-mail: johan.zetterberg@forbrf.lth.se. Phone: +46 (0) 46 222 7728.

Notes

The authors declare no competing financial interest.

ACKNOWLEDGMENTS

The authors thank the Knut & Alice Wallenberg Foundation and the Swedish Research Council for financially supporting this work. S. Matera's research is carried out in the framework of MATHEON supported by the Einstein Foundation Berlin.

REFERENCES

1. Rupprechter, G.; Weilach, C., Mind the Gap! Spectroscopy of Catalytically Active Phases. *Nano Today* **2007**, *2*, 20-29.
2. Frenken, J., Groot, Irene, Operando Research in Heterogeneous Catalysis. Frenken, J., Groot, Irene, Ed. Springer: 2017.
3. Blomberg, S., et al., In-Situ X-Ray Photoelectron Spectroscopy of Model Catalysts: At the Edge of the Gap. *Phys. Rev. Lett.* **2013**, *110*, 117601.
4. Karslıoğlu, O.; Bluhm, H., Ambient-Pressure X-ray Photoelectron Spectroscopy (APXPS). In *Operando Research in Heterogeneous Catalysis*, Frenken, J.; Groot, I., Eds. Springer International Publishing: Cham, 2017; pp 31-57.

5. Toyoshima, R.; Yoshida, M.; Monya, Y.; Suzuki, K.; Mun, B. S.; Amemiya, K.; Mase, K.; Kondoh, H., Active Surface Oxygen for Catalytic CO Oxidation on Pd(100) Proceeding under Near Ambient Pressure Conditions. *J. Phys. Chem. Lett.* **2012**, *3*, 3182-3187.

6. Frenken, J.; Groot, I., Live Observations of Catalysts Using High-Pressure Scanning Probe Microscopy. In *Operando Research in Heterogeneous Catalysis*, Frenken, J.; Groot, I., Eds. Springer International Publishing: Cham, 2017; pp 1-30.

7. Hendriksen, B. L. M.; Bobaru, S. C.; Frenken, J. W. M., Looking at Heterogeneous Catalysis at Atmospheric Pressure Using Tunnel Vision. *Top. Catal.* **2005**, *36*, 43-54.

8. Gao, F.; McClure, S. M.; Cai, Y.; Gath, K. K.; Wang, Y.; Chen, M. S.; Guo, Q. L.; Goodman, D. W., CO oxidation Trends on Pt-Group Metals from Ultrahigh Vacuum to Near Atmospheric Pressures: A Combined In Situ PM-IRAS and Reaction Kinetics Study. *Surf. Sci.* **2009**, *603*, 65-70.

9. Ryczkowski, J., IR Spectroscopy in Catalysis. *Catalysis Today* **2001**, *68*, 263-381.

10. Gustafson, J.; Shipilin, M.; Zhang, C.; Stierle, A.; Hejral, U.; Ruett, U.; Gutowski, O.; Carlsson, P.-A.; Skoglundh, M.; Lundgren, E., High-Energy Surface X-ray Diffraction for Fast Surface Structure Determination. *Science* **2014**, *343*, 758-761.

11. Stierle, A.; Gustafson, J.; Lundgren, E., Surface-Sensitive X-ray Diffraction Across the Pressure Gap. In *Operando Research in Heterogeneous Catalysis*, Frenken, J.; Groot, I., Eds. Springer International Publishing: Cham, 2017; pp 59-87.

12. Lundgren, E.; Zhang, C.; Merte, L. R.; Shipilin, M.; Blomberg, S.; Hejral, U.; Zhou, J.; Zetterberg, J.; Gustafson, J., Novel in Situ Techniques for Studies of Model Catalysts. *Acc. Chem. Res.* **2017**, *50*, 2326-2333.

13. Zhou, J.; Blomberg, S.; Gustafson, J.; Lundgren, E.; Zetterberg, J., Visualization of Gas Distribution in a Model AP-XPS Reactor by PLIF: CO Oxidation over a Pd(100) Catalyst. *Catalysts* **2017**, *7*, 29.

14. Zellner, A.; Suntz, R.; Deutschmann, O., Two-Dimensional Spatial Resolution of Concentration Profiles in Catalytic Reactors by Planar Laser-Induced Fluorescence: NO Reduction over Diesel Oxidation Catalysts. *Angew. Chem. Int. Ed.* **2015**, *54*, 2653-2655.

15. Matera, S.; Reuter, K., First-Principles Approach to Heat and Mass Transfer Effects in Model Catalyst Studies. *Catal. Lett.* **2009**, *133*, 156-159.

16. Matera, S.; Reuter, K., When Atomic-Scale Resolution Is Not Enough: Spatial Effects on In Situ Model Catalyst Studies. *J. Catal.* **2012**, *295*, 261-268.

17. Zhou, J.; Blomberg, S.; Gustafson, J.; Lundgren, E.; Zetterberg, J., Simultaneous Imaging of Gas Phase over and Surface Reflectance of a Pd(100) Single Crystal during CO Oxidation. *J. Phys. Chem. C* **2017**, *121*, 23511-23519.

18. Onderwaater, W. G.; Taranovskyy, A.; van Baarle, G. C.; Frenken, J. W. M.; Groot, I. M. N., In Situ Optical Reflectance Difference Observations of CO Oxidation over Pd(100). *J. Phys. Chem. C* **2017**, *121*, 11407-11415.

19. Matera, S.; Reuter, K., Transport Limitations and Bistability for *In Situ* CO Oxidation at RuO_2(110): First-Principles Based Multiscale Modeling. *Phys. Rev. B* **2010**, *82*, 085446.

20. Roos, M.; Kielbassa, S.; Schirling, C.; Häring, T.; Bansmann, J.; Behm, R. J., Scanning Mass Spectrometer for Quantitative Reaction Studies on Catalytically Active Microstructures. *Rev. Sci. Instrum.* **2007**, *78*, 084104.

21. Tan, C. K. C.; Delgass, W. N.; Baertsch, C. D., Spatially Resolved In Situ FTIR Analysis of CO Adsorption and Reaction on Pt/SiO_2 in a Silicon Microreactor. *Appl. Catal. B Environ.* **2009**, *93*, 66-74.

22. Zetterberg, J.; Blomberg, S.; Gustafson, J.; Evertsson, J.; Zhou, J.; Adams, E. C.; Carlsson, P.-A.; Aldén, M.; Lundgren, E., Spatially and Temporally Resolved Gas Distributions around Heterogeneous Catalysts using Infrared Planar Laser-Induced Fluorescence. *Nat. Commun.* **2015**, *6*, 7076.

23. Blomberg, S.; Zhou, J.; Gustafson, J.; Zetterberg, J.; Lundgren, E., 2D and 3D Imaging of the Gas Phase Close to an Operating Model Catalyst by Planar Laser Induced Fluorescence. *J. Phys. Condens. Matter* **2016**, *28*, 453002.

24. Matera, S.; Maestri, M.; Cuoci, A.; Reuter, K., Predictive-Quality Surface Reaction Chemistry in Real Reactor Models: Integrating First-Principles Kinetic Monte Carlo Simulations into Computational Fluid Dynamics. *ACS Catal.* **2014**, *4*, 4081-4092.

25. Matera, S.; Blomberg, S.; Hoffmann, M. J.; Zetterberg, J.; Gustafson, J.; Lundgren, E.; Reuter, K., Evidence for the Active Phase of Heterogeneous Catalysts through In Situ Reaction Product Imaging and Multiscale Modeling. *ACS Catal.* **2015**, *5*, 4514-4518.

26. Kee, R. J.; Coltrin, M. E.; Glarborg, P.; Zhu, H., *Chemically Reacting Flow: Theory, Modeling, and Simulation*; John Wiley & Sons, 2017.

27. Zanier, F.; Michelon, N.; Canu, P., Design and Characterization of a Stagnation Flow Reactor for Heterogeneous Microkinetic Studies. *Chem. Eng. J.* **2017**, *315*, 67-82.

28. Zetterberg, J.; Blomberg, S.; Zhou, J.; Gustafson, J.; Lundgren, E., Planar Laser Induced Fluorescence Applied to Catalysis. In *Operando Research in Heterogeneous Catalysis*, Springer International Publishing: 2017; pp 131-149.

29. Kohsehoinghaus, K., Laser Techniques for the Quantitative Detection of Reactive Intermediates in Combustion Systems. *Prog. Energy Combust. Sci.* **1994**, *20*, 203-279.

30. Alden, M.; Bood, J.; Li, Z.; Richter, M., Visualization and understanding of combustion processes using spatially and temporally resolved laser diagnostic techniques. *Proc. Combust. Inst.* **2011**, *33*, 69-97.

31. Zhou, J.; Pfaff, S.; Lundgren, E.; Zetterberg, J., A Convenient Setup for Laser-Induced Fluorescence Imaging of both CO and CO_2 during Catalytic CO Oxidation. *Appl. Phys. B* **2017**, *123*, 87.

32. Gudmundson, F.; Persson, J. L.; Försth, M.; Behrendt, F.; Kasemo, B.; Rosén, A., OH Gas Phase Chemistry outside a Pt Catalyst. *J. Catal.* **1998**, *179*, 420-430.

33. Rosell, J.; Bai, X.-S.; Sjoholm, J.; Zhou, B.; Li, Z.; Wang, Z.; Pettersson, P.; Li, Z.; Richter, M.; Aldén, M., Multi-Species PLIF Study of the Structures of Turbulent Premixed Methane/Air Jet Flames in the Flamelet and Thin-Reaction Zones Regimes. *Combust. Flame* **2017**, *182*, 324-338.

Table of Contents Image

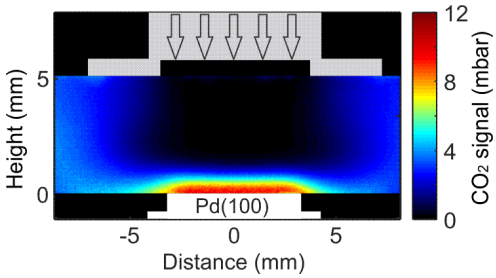

Experimental and modeling studies of the gas phase of model catalysts in a stagnation flow

Jianfeng Zhou [1], Sebastian Matera [2], Sebastian Pfaff [1], Sara Blomberg [3], Edvin Lundgren [4] and Johan Zetterberg [1]*

AUTHOR ADDRESS

[1] Division of Combustion Physics, Lund University, SE-22100 Lund, Sweden

[2] Institute for Mathematics, Freie Universität Berlin, D-14195 Berlin, Germany

[3] Department of Chemical Engineering, Lund University, SE-22100 Lund, Sweden

[4] Division of Synchrotron Radiation Research, Lund University, SE-22100 Lund, Sweden

The CO_2 distribution over a Pd(111) single crystal (2 mm thick) has been studied with PLIF to demonstrate the effect of active edges of the sample in a non-stagnation flow geometry (as shown in S1). The measurement was performed with 4:4:92 ratio of CO, O2 and Ar at 150 mbar total pressure and 100 ml_n/min total flow. The results are summarized in S2. The PLIF images recorded at different temperatures during the ramp up, as shown in S1 (a-c), reveal that the sides of the sample become active before the (111) surface. Compared to the stagnation flow case in Figure 2, there are two distinct steps in both the PLIF and MS trends of the CO_2 signal, as shown in S2 (d) and (e) respectively. The PLIF image in S2 (b) and the PLIF trends in S2 (d) clearly demonstrate that there is a significant amount of CO_2 signal that spills over from the sides to the (111) surface. This spill-over signal could be a potential problem when one tries to correlate the activity (indicated by the production of CO_2 in the gas phase) with the surface change of a catalyst sample in *operando* studies, if 2D spatially resolve information is lacking.

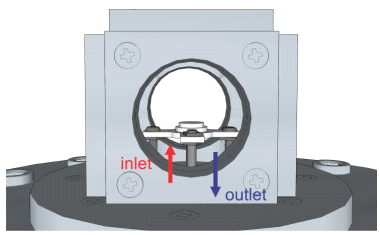

S1 A reactor with a non-stagnation flow geometry. The gas inlet and outlet are indicated by the red and blue arrow, respectively.

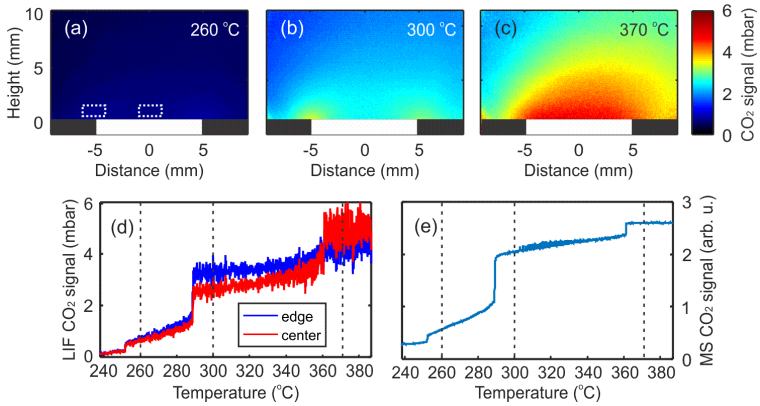

S2 CO_2 distribution over a Pd(111) single crystal during CO oxidation. (a-c) PLIF 10-shot average images recorded at different temperatures during the ramp up. (d) The integrated PLIF trends 0.5 mm above the sample at the edge (blue), at the center (red). (e) The MS signal measured at the gas outlet. The white rectangular indicates the sample.

Paper XI

Combining HESXRD with LED reflectance and PLIF for *operando* catalyst surface characterization

S. Pfaff, J. Zhou, U. Hejral, J. Gustafsson, M. Shipilin, S. Albertin, S. Blomberg, O Gutowski, A. C. Dippel, E. Lundgren and J. Zetterberg

Correspondence email: sebastian.pfaff@forbrf.lth.se

Abstract

We report simultaneous high energy surface X-ray diffraction (HESXRD), planer laser-induced fluorescence (PLIF), and surface optical reflectance (SOR) measurements of CO oxidation over a Pd(100) single crystal under *operando* conditions. HESXRD is a technique well suited to gain knowledge about the microscopic surface structure of the sample. PLIF enables spatially resolve measurements of the gas phase composition above the sample surface. SOR provides a macroscopic map of the entire single crystal surface. Combining the three techniques, we have shown a clear spatial correlation between a reduced surface reflectance and an increased CO_2 concentration in the gas phase. Additionally, through the sub-second temporal resolution of PLIF, we have determined the delay between a measurable change of the surface structure using HESXRD and a change in gas composition as the catalyst switches between high and low activity.

Keywords: High energy surface X-ray diffraction HESXRD; surface optical reflectance SOR; planer laser-induced fluorescence PLIF; CO oxidation; Pd(100)

Introduction

In order to improve our understanding of the underlying mechanisms involved in a heterogeneous catalyst reaction, correlations between the produced products and the catalyst surface structure are of great importance [1]. Thus, in recent years, there has been an increasing interest in so-called *operando* studies where not only the exhaust gas is probed while the catalyst is exposed to varying temperature or gas conditions, but an attempt is also made to probe the intermediate reaction stages, both spatially and temporally [1].

Since industrial catalysts involving metal nanoparticles or zeolites often have very complicated surface structures which can be challenging to quantify, studies where the aim is to further gain knowledge about specific reaction mechanisms are commonly conducted on single crystal model catalysts with well-defined metal surfaces [2, 3].

Further, it has been shown that the surface structure and as such the reaction characteristics of catalysts can change depending on the surrounding gas total pressure [4]. Thus, it is important to perform any *operando* experiments in as realistic gas and temperature conditions (>1 bar, 300-1000 °C) as possible, even if this adds experimental challenges. Otherwise it could be problematic to relate any findings to actual industrial processes.

Specifically, an *operando* experiment often involves probing the surface structure or composition with techniques such as Surface X-Ray Diffraction (SXRD) [5], Ambient Pressure X-Ray Photoelectron Spectroscopy (AP-XPS) [6] or High-Pressure Surface Tunnelling Microscopy (HP-STM) [7] while changing a reaction variable such as gas composition or sample temperature. Other techniques for surface structure determination do exist but they often require the sample to be in a much lower pressure environment which makes them impractical for *operando* studies where catalyst is used at more realistic operating conditions.

A caveat of these techniques is that while they provide detailed information about the surface, they only probe a very small area (tens of μm^2 on a catalyst with a surface area of 0.5 cm^2). The structural

or chemical changes in this limited area are then often correlated with changes in the global gas composition as measured by a mass spectrometer (MS) at the reactor outlet. Recent studies, however, have found that the catalyst surface does not always behave homogenously [8]. This is attributed to variables such as reactor geometry or an inhomogeneous gas distribution around the catalyst effectively exposing distinct parts of the surface to different gas conditions. Further, at ambient pressure conditions, the product gas forms in a cloud around the sample. This means that the global average gas composition probed by the MS is often not representative of the gas conditions experienced by the catalyst surface. As such it is of importance to monitor the gas distribution over the catalyst as well as the surface as a whole to ensure the surface data collected is representative of the surface.

Planar Laser Induced Fluorescence (PLIF) is a laser-based species sensitive technique which provides a spatial image of a gas distribution with high spatial and temporal resolution. The technique has been widely employed in combustion diagnosis in the past [9]. More recently, it has also been used for catalysis research [10-13]. In this study, we have used PLIF to detect CO_2 through fluorescence in the mid-IR regime. Apart from CO_2, PLIF can also be used to detect other gases of relevance to catalysis such as CO [14], NO [15] or OH [16].

High Energy X-Ray Diffraction (HESXRD) is a technique shown to be excellent for the characterization of surface structures on the atomic level. Due to its photon-in-photon-out nature, HESXRD is not limited by the mean-free-path of electrons in the gas surrounding the surface. As such it also works well at ambient pressures. By using high energy X-Rays in combination with a 2D detector it is possible to create a comprehensive image of the diffraction signal with high (0.5 s) temporal resolution. This is especially important in catalysis research to catch the rapid surface changes exhibited as the catalyst moves into the active state. The technique is described in more detail in [5].

Further, it has recently been shown that the reflectance of LED light by an active catalyst will change depending on the surface roughness, catalyst activity and oxidation state [8, 17-19]. We will

henceforth refer to this technique as Surface Optical Reflectance (SOR). Since this technique can probe the entire sample surface simultaneously, it provides a useful overview of the reaction from a macroscopic point of view.

In this work, we have simultaneously combined SOR with HESXRD and PLIF for detailed surface characterization and instant 2D gas phase characterisation during CO oxidation on a Pd(100) single crystal catalyst. To be able to perform the combined measurements, the entire reactor, laser, and SOR setups were transported to the high energy X-Ray beamline P07 at Petra III. Through the obtained data, we have further correlated changes of the microscopic surface structure as seen in the HESXRD signal with changes in the macroscopic surface structure visualised by SOR. Since SOR gives an overview of the entire sample, it is easy to see where the sample surface structure changes and if the change occurs in a location probed by HESXRD.

While SOR alone does not give any detailed information about the surface composition or atomic structure, it may be possible to correlate the SOR signal with HESXRD data to obtain a form of "calibration", which can later be used to gain a rudimentary understanding of structural surface changes without the need of a synchrotron.

Experiment

The experimental setup used at the P07 beamline at PETRA III consists of four parts**;** the reactor together with its gas system and heater, the optical setup for the PLIF measurement, a separate optical setup used to create and image the LED reflection as well as the beamline equipment used for the HESXRD measurement as shown in Figure 1.

The reactor consists of a boralectric heating cross through which a heating current is supplied. The heating cross temperature was monitored using a Type D thermocouple connected to the heating cross. The reactor is covered by a sapphire dome to gain optical access to the sample from all angles. Further details on the heating system and reactor geometry are available in [20].

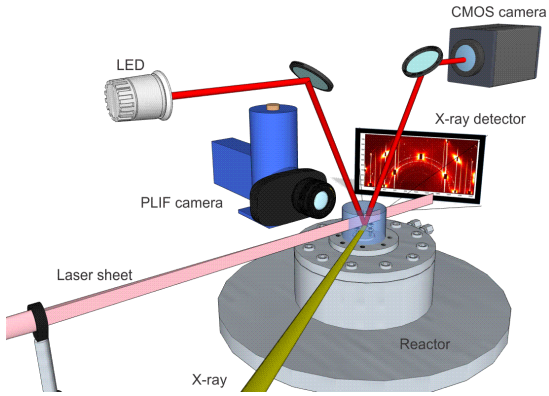

Figure 1: Schematic setup for simultaneous measurements of PLIF, HESXRD and SOR

The gas supply of the reactor was regulated through a set of mass flow controllers (Bronkhorst EL-FLOW) and a pressure regulator (Bronkhorst EL-PRESS) which allowed for fine adjustments of the gas flow. This supports flows through the reactor ranging from a few ml/min to around 500 ml/min at pressures between a few mbar and 1 bar. The reactor gas outlet was connected to a quadruple mass spectrometer (Pfeiffer QMP 220) via an automated leak valve (LPM) to determine the global gas composition in the reactor. The reactor pressure is calibrated by connecting a pressure gauge directly to the cell post-measurement. More details regarding the reactor and gas system are presented in ref [21].

The sample was a hat shaped Pd(100) single crystal with a diameter of 6 mm at the top and 8 mm at the base and a thickness of 2 mm. The sample was placed into an SXRD flow reactor (LPM) with a cylindrical sapphire top. Sapphire was chosen as it is transmissive for all involved wavelengths of light.

For the PLIF measurement, a pulsed Nd:Yag laser was used to pump an Optical Parametric Oscillator (OPO) which produced the IR beam used for CO_2 detection. The IR beam was tuned to around 2.7 µm to target the $(00^00) \rightarrow (10^01)$ transition, with energy of around 8 mJ/pulse. Subsequently, the beam was directed into the reaction cell using mirrors. Prior to the cell, the beam was shaped into a laser sheet using a convex cylindrical lens (f = 100 mm). The resulting fluorescence at 4.3 µm [22] was

imaged using a 256×256 px LN_2-cooled InSb camera (Santa Barbara Focalplane SBF-134). Since there is a large, varying thermal background, the camera was set up to also trigger between laser pulses to record the current background. This yields a special resolution of 80 µm in the image plane and a resolution of around 0.1 mm in the normal plane which is limited by the thickness of the laser sheet. Since the laser has a 10 Hz repetition rate, one instant snapshot image is recorded every 100 ms. For more in depth information about the PLIF setup, refer to [21].

For the HESXRD measurements, the X-ray energy was set to 85 keV. Since the setup was mounted on a diffractometer, it was possible to align the surface to the beam at a grazing angle of 0.04° which ensures high surface sensitivity. A square 2D detector with an area of ~0.17 m^2 placed 1.75 m away detected the diffraction signal.

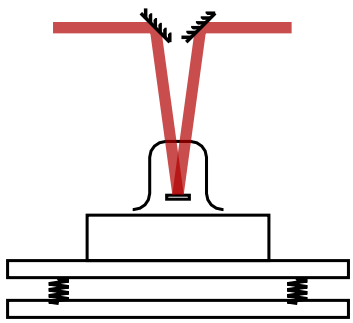

Figure 2: Schematic side view of the reactor and the LED beam.

For the SOR measurement, an LED light (at 625 nm) was first diffused using a spatial filter to suppress intensity irregularities caused by the internal LED pattern. Next, the light was collimated into a beam before it was directed towards the cell from above. Two mirrors, each placed at a 10° angle from the cell, were used to reflect the beam down onto the sample and to catch the reflection as shown in Figure 2. The reflection was then imaged using a 4*f*-setup onto the chip of an sCMOS camera (Andor Zyla). To this end, an LED and optics were mounted onto the diffractometer. This was done to avoid misalignment as the diffractometer was tilted or rotated, which is necessary for the HESXRD measurements. Furthermore, the setup was mounted around 10 cm above the reactor to be

able to image the sample from the top. During most measurements, this camera was triggered at 10 Hz (same repetition rate as the laser).

In post processing, all resulting images are divided on a per-pixel basis by an average of a series of images acquired when the surface is reduced to obtain the reflectance difference in per cent. This makes it possible to visualise even small reflectivity changes in the spatially resolved image. Since the three techniques all rely on different detectors and detection apparatus, synchronization between them is key for a simultaneous measurement. A measurement run was initiated by the SPEC software controlling the synchrotron detector and motors. When the detector began to acquire for the first time during a measurement run, a trigger signal is sent to a separate computer controlling the flow controllers and reading the reactor parameters such as pressure and temperature. The computer polls for a trigger signal every 50 ms. As a signal is detected acquisition of the reactor parameters begins. The same computer also sends signals to the sCMOS camera capturing the LED images and to the InSb camera capturing the PLIF fluorescence. The sCMOS camera will begin acquiring immediately while the InSb camera will begin acquiring on the following laser shot, which might be up to 100 ms later. This results in a maximum PLIF delay of 200 ms. As the HESXRD detector has an exposure time of 500 ms, this is deemed acceptable.

Results and Discussion

We performed several combined measurements where the PLIF, HESXRD and SOR were used simultaneously in combination with traditional catalysis diagnosis methods such as a thermocouple and a mass spectrometer.

One experiment was carried out at constant sample temperature of 230 °C, where, during 10 minutes, the flow ratio between CO (we use 10% CO in Ar) and O_2 was varied. Initially, the sample was subjected to reducing conditions with only CO and Ar, but no O_2 being flown. After 50 s, a small amount of O_2 was introduced. The ratio initially altered by decreasing the CO flow for three minutes. Subsequently, the CO flow was fixed and the O_2 flow incrementally increased to alter the O_2/CO

ratio. The ratio was first slowly raised to 1:2 after which it was raised more rapidly until it reached 10:1 as show in in Figure 3a. Ar was used as buffer gas during the entire measurement to keep a constant total flow of 164 ml/min which resulted in a pressure at the sample of around 181 mbar.

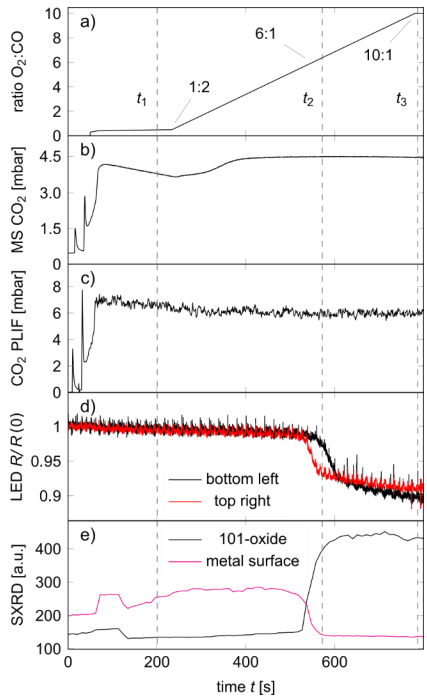

Figure 3: Measurement where the sample is exposed to an incrementally increasing O_2:CO ratio. Panel a) shows the O_2:CO ratio flow by the mass flow controllers. Panel b) shows The MS signal of CO_2. Panel c) shows the concentration close to the sample surface (black box in Figure 4c) as measured by PLIF. Panel d) shows the difference in reflectivity from a fully reduced surface in the indicated regions in Figure 4a. Panel e) shows the intensity of the metallic surface and oxide refraction spots from the HESXRD signal.

To fully probe the reciprocal space, the sample was rotated back and forth 15° with each rotation taking 10.3 s. During the rotation, images were acquired at 2 Hz. In post-processing, the maximum of each pixel value during one rotation was then used to construct one final image per rotation. This results in a time resolution of 10.3 s. Subsequently, two regions representing a (101) surface oxide peak and a crystal truncation rod (CTR) originating from the metal surface were isolated and trended over time.

Figure 3d-e show the parameters collected during the measurement while Figure 4 shows SOR (a), HESXRD (b) and PLIF (c) images recorded at three points during the measurement (1-3). The rectangles in the SOR, HESXRD and PLIF images correspond to the regions of interest trended in Figure 3d, e and c, respectively. The prevalent circular patterns in the reflectivity image are due to an imperfection in the sapphire dome. We also attribute the wavy patterns to dome imperfections.

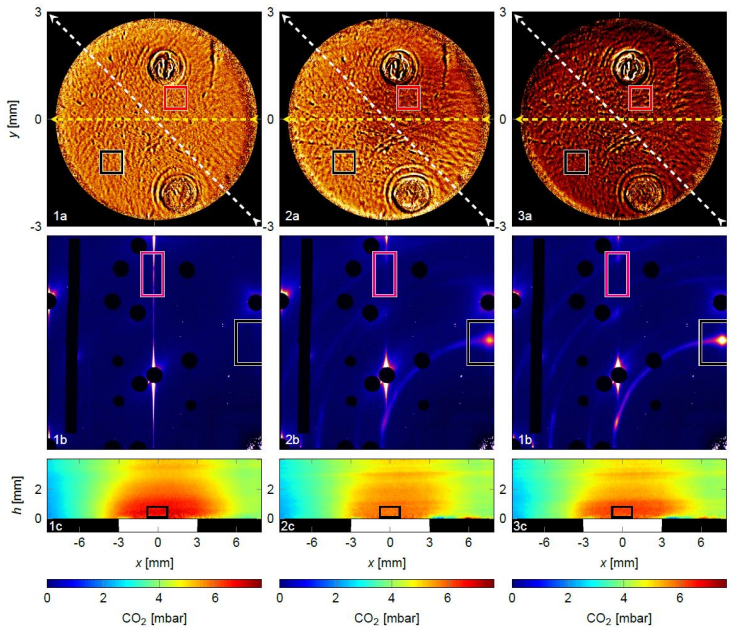

Figure 4: Simultaneous SOR (a), HESXRD (b) and PLIF (c) data at three O_2:CO ratios corresponding to t_1 (1), t_2 (2), and t_3 (3) in Figure 3. Note how the oxidization begins to form in the upper-right area to then spread over the entire sample area during the following minute. Also note the simultaneous weakening of the rod corresponding to the metal surface (purple box) and the simultaneous increase of the oxide peak (black box). The PLIF signal remains stable since the reaction is mass transfer limited.

It is noteworthy that as the O_2/CO ratio approached 6:1 at t_2, the surface began to oxidize, which is represented by an increase in the oxide peak with a concurrent decrease in the metal peak in the HESXRD data shown in Figure 3e. Simultaneously, the reflectivity of the sample begins to decrease as shown in Figure 3d. Note that the reflectivity of the different sides of the sample decreases at different times; the oxidation spot begins to grow in the top right after which it spreads to cover the

full sample surface. However, the HESXRD signal change due to the oxidation correlates only with a reflectivity decrease in the top right area of the sample indicating that the X-Ray beam is probing that region. This means that care must be taken when correlating point measurement data with global condition changes as the probed surface does not always change homogeneously and emphasises the importance of monitoring the whole surface area. Since the amount of CO_2 produced does not increase during the surface changes, as shown in Figure 3c, the reaction is concluded to be mass transfer limited.

Another benefit of the setup is the possibility to accurately determine the time delays involved in the experiment. Since the PLIF signal is instantaneous, it allows for a precise determination of the time it takes for the gas to reach the cell after a change in flow is set at the flow controller. The instantaneous nature of the PLIF and SOR signals also means the combination of techniques is useful for determining if any oxide formation precedes or succeeds the advent of catalytic activity after a change in gas conditions. Figure 5 shows a different measurement to further illustrate the responses of the various techniques to a change in gas conditions. In this short measurement, the sample is first exposed to only CO after which the oxygen flow is suddenly turned after 61.4 s. Around one second later, an increase can be seen in the CO_2 PLIF signal as the gas reaches the reactor and the catalytic reaction begins. Once the PLIF signal shows the reaction is in MTL, it takes another second for the surface reflectance to begin decreasing suggesting roughening or oxide formation is taking place. Simultaneously to this decrease, the HESXRD peak corresponding to the metal surface also loses intensity which confirms the results of a previous study where PLIF and HESXRD were combined [23]. Finally, after an additional 2 s the change of gas composition induced by the catalytic reaction becomes visible in the MS signal.

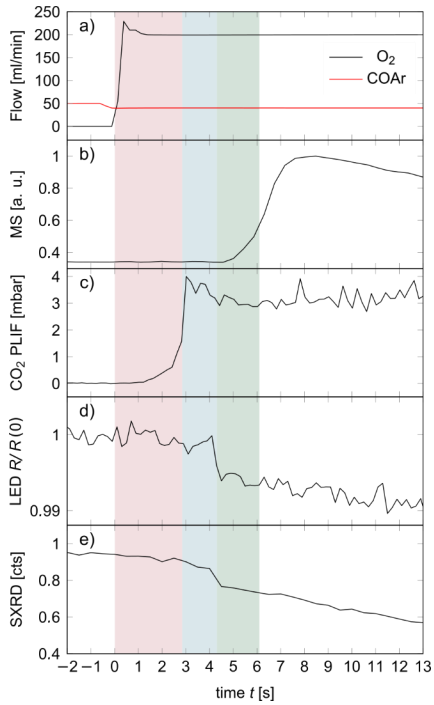

Figure 5: Simultaneously acquired data showing a clear difference in timing of the signals. In this measurement the O_2 flow is suddenly turned on to initiate the catalytic reaction. Due to the instantaneous nature of the PLIF, SOR (and HESXRD) techniques, it is possible to determine the order and timing of the oxide appearance and the rise in activity. A few seconds after the gas change, the gas has reached the reactor and the PLIF signal increases as CO_2 production is initiated. Catalyst ignition into MTL is then reached after ~3 s (pink). 1.4 s later (blue) both SOR and HESXRD signals indicate oxide formation. After an additional 1.5 s (green), the MS finally picks up the change in gas constituents.

Conclusion

We have successfully built and used a setup combining PLIF and SOR with HESXRD. The availability of a compact technique like SOR probing the global sample surface is highly useful for determining if the behaviour of the region probed by a technique such as HESXRD is representative of the sample surface. In combination with PLIF, the two techniques provide a complete picture of the macroscopic reaction conditions. This is essential to ensure that any conclusions drawn from correlations between data of macroscopic and microscopic origin are sound. In particular in *operando* experiments, the gas is normally exchanged fast enough to not diffuse which creates gas gradients

and surface structure gradients which have to be accounted for. In short, the combination gives a clear overview of the reaction from a macroscopic point of view.

Moreover, as SOR is a technique which similarly to PLIF provides delay free probing of the sample. We have shown that this can be useful to resolve the sub-second delay between the catalyst ignition and the appearance of a surface oxide. Also, it is often useful to be able to determine the response time of the MS which is easily done if PLIF data is available.

Altogether, we have developed and implemented a combination of SOR and PLIF with HESXRD which provides detailed macroscopic information on both the sample surface and the surrounding gas in addition to the atomic surface data provided by HESXRD. This gives a clearer overview of the reaction on a larger scale which is important to draw sound conclusions in *operando* studies.

References

1. Morgan, K., et al., *Evolution and Enabling Capabilities of Spatially Resolved Techniques for the Characterization of Heterogeneously Catalyzed Reactions.* ACS Catalysis, 2016. **6**(2): p. 1356-1381.
2. Toyoshima, R., et al., *In Situ Ambient Pressure XPS Study of CO Oxidation Reaction on Pd(111) Surfaces.* The Journal of Physical Chemistry C, 2012. **116**(35): p. 18691-18697.
3. Goodman, D.W., *Model Studies in Catalysis Using Surface Science Probes.* Chemical Reviews, 1995. **95**(3): p. 523-536.
4. Gao, F., et al., *CO Oxidation on Pt-Group Metals from Ultrahigh Vacuum to Near Atmospheric Pressures. 2. Palladium and Platinum.* The Journal of Physical Chemistry C, 2009. **113**(1): p. 174-181.
5. Gustafson, J., et al., *High-Energy Surface X-ray Diffraction for Fast Surface Structure Determination.* Science, 2014. **343**(6172): p. 758-761.

6. Kanak, R., A. Luca, and v.B.J. A., *Ambient Pressure Photoelectron Spectroscopy: Opportunities in Catalysis from Solids to Liquids and Introducing Time Resolution.* ChemCatChem, 2018. **10**(4): p. 666-682.

7. Herbschleb, C.T., et al., *The ReactorSTM: Atomically resolved scanning tunneling microscopy under high-pressure, high-temperature catalytic reaction conditions.* Review of Scientific Instruments, 2014. **85**(8): p. 083703.

8. Zhou, J., et al., *Simultaneous Imaging of Gas Phase over and Surface Reflectance of a Pd(100) Single Crystal during CO Oxidation.* The Journal of Physical Chemistry C, 2017. **121**(42): p. 23511-23519.

9. Kohse Höinghaus, K., *Laser Techniques for the Quantitative Detection of Reactive Intermediates in Combustion Systems.* Progress in Energy and Combustion Science, 1994. **20**(3): p. 203-279.

10. Blomberg, S., et al., *2D and 3D Imaging of the Gas Phase Close to an Operating Model Catalyst by Planar Laser Induced Fluorescence.* Journal of Physics: Condensed Matter, 2016. **28**(45): p. 453002.

11. Zetterberg, J., et al., *Spatially and temporally resolved gas distributions around heterogeneous catalysts using infrared planar laser-induced fluorescence.* Nat Commun, 2015. **6**.

12. Zetterberg, J., et al., *An in situ set up for the detection of CO2 from catalytic CO oxidation by using planar laser-induced fluorescence.* Review of Scientific Instruments, 2012. **83**(5).

13. Gudmundson, F., et al., *Evaluation of hydroxyl desorption rates from platinum using spatially resolved imaging of laser-induced fluorescence.* The Journal of Physical Chemistry, 1993. **97**(49): p. 12828-12834.

14. Aldén, M., S. Wallin, and W. Wendt, *Applications of two-photon absorption for detection of CO in combustion gases.* Applied Physics B, 1984. **33**(4): p. 205-208.

15. Lee, M.P., B.K. McMillin, and R.K. Hanson, - *Temperature measurements in gases by use of planar laser-inducedfluorescence imaging of NO.* 1993. **- 32**(- 27): p. - 5396.

16. Petersson, P., et al., - *Simultaneous PIV/OH-PLIF, Rayleigh thermometry/OH-PLIF and stereo PIV measurements in a low-swirl flame.* 2007. **- 46**(- 19): p. - 3936.

17. Eriksson, S., et al., *Experimental and numerical investigation of supported rhodium catalysts for partial oxidation of methane in exhaust gas diluted reaction mixtures.* Chemical Engineering Science, 2007. **62**(15): p. 3991-4011.

18. Onderwaater, W.G., et al., *In Situ Optical Reflectance Difference Observations of CO Oxidation over Pd(100).* The Journal of Physical Chemistry C, 2017. **121**(21): p. 11407-11415.

19. Onderwaater, W.G., et al., *From dull to shiny: A novel setup for reflectance difference analysis under catalytic conditions.* Review of Scientific Instruments, 2017. **88**(2): p. 023704.

20. Rijn, R.v., et al., *Ultrahigh vacuum/high-pressure flow reactor for surface x-ray diffraction and grazing incidence small angle x-ray scattering studies close to conditions for industrial catalysis.* Review of Scientific Instruments, 2010. **81**(1): p. 014101.

21. Zhou, J., et al., *A Convenient Setup for Laser-Induced Fluorescence Imaging of both CO and CO_2 during Catalytic CO Oxidation.* Applied Physics B, 2017. **123**(3): p. 87.

22. James, T.C., and J. B. Kumer, *Fluorescence of CO2 near 4.3 microns: Application to daytime limb radiance calculations.* Journal of Geophysical Research, 1973. **78**(34): p. 8320-8329.

23. Blomberg, S., et al., *Combining synchrotron light with laser technology in catalysis research.* Journal of Synchrotron Radiation, 2018. **25**(5): p. 1389-1394.

Paper XII

Appl. Phys. B (2015) 121:123–130
DOI 10.1007/s00340-015-6208-8

Applied Physics B
Lasers and Optics

Non-intrusive detection of methanol in gas phase using infrared degenerate four-wave mixing

J. Zhou[1] · A. L. Sahlberg[1] · H. Nilsson[2] · E. Lundgren[3] · J. Zetterberg[1]

Received: 25 June 2015 / Accepted: 20 August 2015 / Published online: 29 August 2015
© Springer-Verlag Berlin Heidelberg 2015

Abstract Sensitive and non-intrusive detection of gas-phase methanol with high spatial and temporal resolution has for the first time been reported using mid-infrared degenerate four-wave mixing (IR-DFWM). IR-DFWM spectra of methanol have been successfully recorded in nitrogen-diluted gas flows at room temperature and at 300 °C, by probing ro-vibrational transitions belonging to the fundamental C–H stretching modes, ν_2 and ν_9, and the O–H stretching mode, ν_1. The detection limit of methanol vapor at room temperature and atmospheric pressure is estimated to be 250 ppm with the present setup. Potential interference from CH_4 and CO_2 is discussed from recorded IR-DFWM spectra of CH_4 and CO_2, and it was found that detection of methanol free from CH_4 and CO_2 interference is possible. These results show the potential of the detection of methanol with IR-DFWM for applications in both combustion and catalytic environments, such as CO_2 hydrogenation and CH_4 oxidation.

1 Introduction

Methanol is one of the most important chemicals with industrial applications in a vast variety of areas. It is mainly used as a feedstock in the manufacturing of other chemicals, including formaldehyde, acetic acid, and olefins, all of which are basic building blocks for a number of common products of modern life. But its use is also increasingly important as a transportation fuel, a fuel cell hydrogen carrier, a source for electricity generation as well as a key component in biodiesel transesterification and wastewater denitrification [1].

The most common method for the production of methanol is to convert feedstock (e.g., natural gas) into syngas (a mixture of carbon monoxide and hydrogen) through gasification process. Syngas can then be converted into methanol through catalytic processes. Direct conversion of CO_2 and CH_4 into methanol through catalytic processes has been a hot topic in both academia and industry over the past decades [2–4]. In such situations, monitoring gas concentrations is necessary to give quantitative information from the processes.

In the operation of direct methanol fuel cells (DMFCs), loss of methanol through gas bubbles at the anode will occur. In this situation, monitoring the concentration of the gas-phase methanol in the exhaust gases will potentially give more valuable quantitative information of the performance of a fuel cell together with the detection of the concentration of the aqueous methanol fed into the fuel cells [5].

Traditionally, Fourier transform infrared spectrometry (FTIR) has been used to detect methanol in the gas phase. Recent work includes measurements of the infrared absorption cross section of methanol at low temperature and pressure (204.5 K and 50.92 Torr) with high resolution [6], and at atmospheric pressure and elevated temperatures (up to 778 K) [7], but with lower resolution. However, FTIR is a line-of-sight technique, which cannot provide spatial resolution along the light-propagating axis, introducing distortions in the spectral features due to species and temperature

✉ J. Zhou
Jianfeng.zhou@forbrf.lth.se

[1] Division of Combustion Physics, Lund University, 221 00 Lund, Sweden

[2] Department of Astronomy and Theoretical Physics, Lund University, 221 00 Lund, Sweden

[3] Division of Synchrotron Radiation Research, Lund University, 221 00 Lund, Sweden

variations along the propagating path, and its temporal resolution is limited by the integration time (typically on the order of seconds or more). Recent developments of cavity-enhanced absorption spectroscopy with quantum cascade lasers can provide detection of infrared active species with millisecond resolution [8]. However, it is a technique based on multi-path absorption and cannot provide high spatial resolution. In several applications, such as catalysis, monitoring methanol non-intrusively is very attractive and would contribute to better understanding when characterizing catalysts in the catalytic processes. This calls for a method to provide in situ detection of methanol with both high temporal and spatial resolution.

Degenerate four-wave mixing (DFWM) is a nonlinear optical technique that can provide high temporal and spatial resolution. The theory of DFWM was first presented by Abrams and Lind in 1978 [9, 10]. This study assumed the phase-conjugate geometry and a weak probe beam compared to the pump beams. The theory of DFWM has been extensively treated afterward, both numerically and analytically [11, 12]. The first application for the detection of flame species was performed by Ewart et al. [13] for the detection of the OH radical. Since then, DFWM with UV–Visible lasers has been widely applied in combustion diagnostics for the detection of molecules and radicals [14–17]. The theory and applications of DFWM were recently reviewed by Kiefer and Ewart [18].

Compared to UV–Visible DFWM, mid-infrared DFWM (IR-DFWM) has been less widely applied, in part due to the lack of suitable lasers and detectors in this spectral region. Advances in the field of lasers and infrared detectors have made IR-DFWM an attractive laser technique for the detection of molecules that lack accessible transitions in the UV–Visible range, such as HF [19], HCl [20], CH_4 [21, 22], and C_2H_2 [21, 23]. Sun et al. recently reported the design of infrared BOXCAR plates for stable alignment of IR-DFWM in the forward phase-matching geometry for the detection of C_2H_2 and HCl [24]. A similar setup was used by Sahlberg et al. [25] for the detection of CH_3Cl in hot gas flows. These studies prove the potential of IR-DFWM as a powerful spectroscopic tool for sensitive in situ spectroscopic measurements of infrared active species with high spatial and temporal resolution.

Methanol has four fundamental vibrational modes in the mid-infrared spectral region that can be probed using IR-DFWM: the ν_1 O–H stretching near 3681 cm^{-1}, the ν_2 C–H asymmetric stretching (A′) near 3000 cm^{-1}, the ν_9 C–H asymmetric stretching (A″) near 2970 cm^{-1}, and the ν_3 C–H parallel symmetric stretch (A′) near 2844 cm^{-1}. Studies and modeling of the C–H stretching region of methanol can be found in a number of works [26–29].

In this study, the ν_2 and ν_9 C–H stretching in the frequency range from 2960 to 3030 cm^{-1} and the ν_1 O–H stretching in the frequency range from 3650 to 3700 cm^{-1} were probed using IR-DFWM, and measurements were taken both at room temperature and at 300 °C and compared to simulated absorption spectra. Trace concentrations of CH_4 and CO_2 were separately seeded into the methanol gas flow, and the position of the CH_4 and CO_2 spectral lines was used for wavelength calibration, as well as for demonstrating that methanol detection with IR-DFWM can be made free from interference of CH_4 and CO_2.

2 Experiment

A schematic of the IR-DFWM setup is shown in Fig. 1. The laser system for the generation of mid-infrared light has been described previously [30], and only a brief account will be given here. The second harmonic of an injection seeded Nd:YAG laser (Spectra Physics, PRO 290-10) at 532 nm was used to pump a dye laser system (Sirah, PRSC-D-18) running on LDS 798 and LDS 765 dye (Exiton), with ethanol as solvent, which gives tunable pulsed laser radiation over a broad wavelength range 758–826 and 738–800 nm, respectively. The dye laser light was then difference frequency mixed in a $LiNbO_3$ crystal together with the residual fundamental 1064-nm laser light from the Nd:YAG laser, generating mid-infrared laser pulses. The mid-infrared laser light was further amplified in another

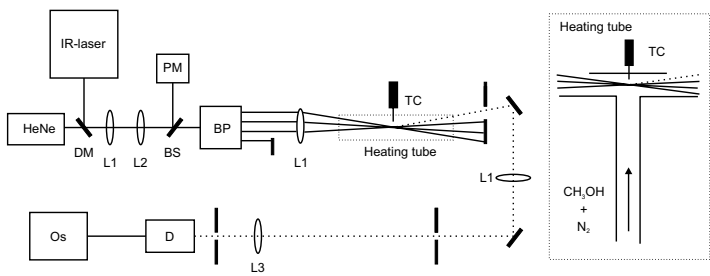

Fig. 1 Schematic of the experimental setup. *BP* BOXCAR plates, *TC* thermocouple, *DM* dichroic mirror, *BS* beam splitter (CaF_2 window) *L1* CaF_2 lens, $f = 300$ mm, *L2* CaF_2 lens, $f = -200$ mm, *L3* CaF_2 lens, $f = 100$ mm, *D* InSb detector, *Os* oscilloscope, *PM* power meter

$LiNbO_3$ crystal pumped by 1064-nm light. This process generates tunable mid-infrared laser light with 10-Hz repetition rate, ~4-ns pulse length with a pulse energy of ~3 mJ and a linewidth of 0.025 cm^{-1} [31]. A telescope was used to shrink the beam size down to approximately 3 mm. The reflection from a CaF_2 window was sent to a power meter to monitor the laser energy during the scan. The mid-IR beam was overlapped with a He–Ne laser beam to facilitate the alignment. The laser wavelength was scanned over the wavelength of the absorption peaks by tuning the dye laser wavelength.

The laser beam was split into four parallel beams using a set of IR-BOXCAR plates, which have been described elsewhere [24]. Three of the parallel laser beams were crossed using an $f = 300$ mm CaF_2 focusing lens, and the IR-DFWM signal is generated in the crossing point of the three beams. The probe volume in this setup was estimated to be $0.4 \times 0.4 \times 6$ mm^3. The signal will follow the path of the fourth laser beam; thus, this beam was used to trace the signal to the detector. The signal beam was collimated using another $f = 300$ mm CaF_2 lens and focused onto an InSb liquid-nitrogen-cooled photodetector (Judson technologies, J10D-M204-R04 M-60). A number of apertures were used to block background scattering, and the signal from the detector was logged by a digital oscilloscope (LeCroy Waverunner 6K).

Methanol vapor was prepared using a bubbler, which was bathed in ice water to keep the temperature of the bubbler at 0 ˚C, ensuring no condensation will occur along the way to the measurement region. Carrier flow (N_2) entering into bubbler was kept below 2 l/min to make sure that the mole fraction of methanol vapor is stabilized. The gas flows were controlled by Bronkhorst mass flow controllers, and the concentration of methanol was adjusted by diluting the flow from the bubbler with a second N_2 flow. When used, CH_4 or CO_2 was also mixed into the flow after the bubbler. The gas flows were directed to an open T-shaped gas tube as illustrated in Fig. 1. The total flow of the gases through the tube was kept around 4.5 l/min, giving a flow speed at room temperature of about 25 cm/s at the measurement point.

The heating gas tube is made of fused silica glass and surrounded by an electric heating wire and insulation. A thermocouple was inserted through the top of the gas tube, to monitor the gas temperature. The temperature in the crossing point of the laser beams was assumed to be uniform and to be the same as that which the thermocouple measured.

To measure the concentrations of methanol vapor prepared by the method described above, an absorption spectrum of methanol was recorded with the Lund Observatory Bruker IFS 125 HR Fourier transform spectrometer. The maximum resolution of the instrument is 0.0021 cm^{-1}, which is achieved by using the full optical path difference of 4.3 m. However, the resolution used to resolve the methanol spectrum was 0.1 cm^{-1}. A total of 200 scans were co-added in order to achieve a high signal-to-noise ratio. The spectrum was recorded from a 10-cm-long gas cell illuminated by a continuous tungsten ribbon lamp with known relative intensity distribution.

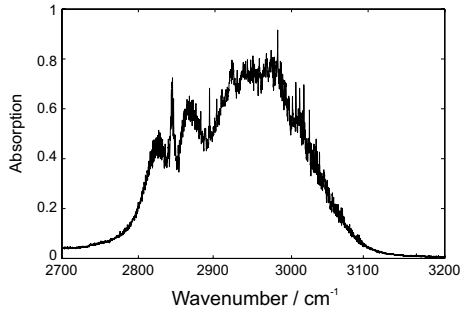

Fig. 2 An FTIR absorption measurement of methanol vapor in a 10-cm-long gas cell at room temperature and atmospheric pressure

3 Measurements and results

An FTIR absorption spectrum of methanol vapor at room temperature and atmospheric pressure in a 10-cm gas cell is shown in Fig. 2. By using the Beer–Lambert law in Eq. (1),

$$1 - \alpha_v = \exp\left(-\frac{qPx}{kT}\sigma_v\right) \tag{1}$$

where α_v is the absorptivity, σ_v is the IR cross section, q is concentration, P is the pressure, T is the temperature, k is Boltzmann's constant, and x is the path length; the concentration of methanol at a vapor pressure of 0 °C is calculated to be 4 %. With this known concentration, the methanol vapor was further diluted with N_2 for quantitative studies in the following.

To investigate the ν_2 and ν_9 modes of methanol, IR-DFWM spectra were recorded and compared to simulated absorption spectrum, based on the IR cross section of methanol from the NIST IR database [32]. Figure 3a shows a simulated absorption spectrum of 3200 ppm methanol at room temperature and atmospheric pressure, for a path length of 10 cm. Two IR-DFWM scans were recorded, one in a gas flow of 3200 ppm methanol in nitrogen at room temperature and one in a gas flow of 8300 ppm methanol in nitrogen at 300 °C, shown in Fig. 3b, c respectively.

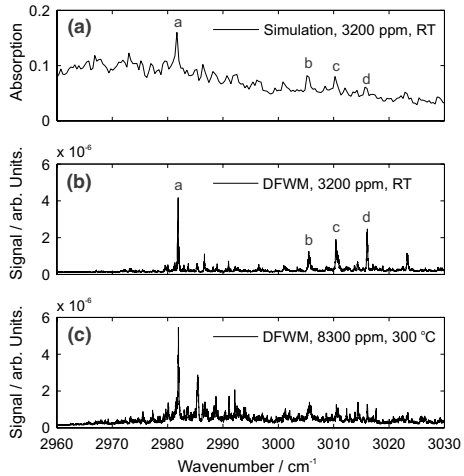

Fig. 3 A comparison between a simulated absorption spectrum and the measured IR-DFWM spectrum for the ν_2 and ν_9 modes of methanol. **a** A simulated absorption spectrum of 3200 ppm methanol at room temperature, atmospheric pressure, and for a path length of 10 cm. **b** A measured IR-DFWM spectrum of 3200 ppm methanol at room temperature. **c** A measured IR-DFWM spectrum of 8300 ppm methanol at 300 °C. Transitions for Q-branches in features *a*–*d* are shown in Table 1

Due to the large amplitude of the internal rotation and the small amplitude vibrations, the vibrational spectra in the infrared are highly congested at room temperature [28]. Therefore, the simulated absorption spectrum exhibits a very broad feature. Interestingly, compared to the absorption spectrum, the IR-DFWM spectrum in panel (b) shows a highly enhanced signal for the features labeled *a*–*d*. These features cannot be resolved in the IR-DFWM spectra, but can be identified as Q-branches following the work of Xu et al. [28]. As listed in Table 1, feature *a* consists of two *A* symmetry Q-branches: $K = 2 \leftarrow 3$ and $K = 1 \leftarrow 2$; feature *b* consists of one *E* symmetry Q-branch $K = 2 \leftarrow 1$ and one *A* symmetry Q-branch $K = 2 \leftarrow 1$; feature *c* consists of one *A* symmetry Q-branch $K = 3 \leftarrow 2$; and feature *d* consists of one *E* symmetry Q-branch $K = -3 \leftarrow -2$. Each of these Q-branches contains a number of closely spaced transitions, resulting in a coherent enhancement of the IR-DFWM signal, making the spectral feature more distinct. A similar phenomenon has been observed in the IR-DFWM spectra of CH_3Cl [25]. There have been studies of the interaction of closely spaced spectral lines in DFWM [33–35], showing that closely spaced lines can constructively interfere to produce a stronger signal. Those studies also suggest that destructive interference might also occur depending on the absolute line positions and laser power and detuning. This, however, was not observed in this study, which might be also due to the fact that the phase-conjugate geometry is

Table 1 *A* and *E* symmetry transitions (in cm^{-1}) for the selected methanol features in Fig. 3

Feature	a		b		c	d
Symmetry type	*A*	*A*	*E*	*A*	*A*	*E*
Q-branch	$K = 2 \leftarrow 3$	$K = 1 \leftarrow 2$	$K = 2 \leftarrow 1$	$K = 2 \leftarrow 1$	$K = 3 \leftarrow 2$	$K = -3 \leftarrow -2$
Transitions wave number (cm^{-1})	2981.8084	2982.4590	3005.4221	3006.2705	3010.3242	3016.0252
	2981.8146	2982.5005	3005.4312	3006.2334	3010.3384	3016.0356
	2981.8147	2982.5554	3005.4426	3006.1848	3010.3574	3016.0483
		2982.6235	3005.4575	3006.1257	3010.3838	3016.0630
		2982.7046	3005.4751	3006.0576	3010.4126	3016.0784
		2982.7966	3005.4945	3006.9783	3010.3782	
		2982.3909	3005.5134	3006.8933	3010.4053	
		2982.3648		3006.8010		
		2982.3298		3006.3538		
		2982.2864		3006.3992		
		2982.2351		3006.4602		
		2982.1751		3006.5359		
				3006.6277		
				3006.7324		
				3006.8543		

Data extracted from Ref. [28]

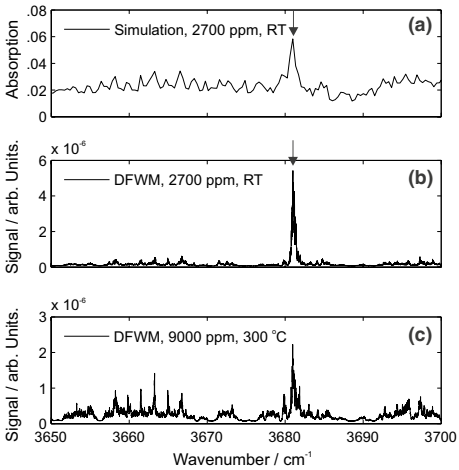

Fig. 4 A comparison between the simulated absorption spectrum and the measured IR-DFWM spectra in the ν_1 band of methanol. The *arrow* indicates the Q-branch feature near 3681 cm^{-1}. **a** A simulated absorption spectrum of 2700 ppm methanol at room temperature and atmospheric pressure with a path length of 10 cm. **b** A measured IR-DFWM spectrum of 2700 ppm methanol at room temperature. **c** A measured IR-DFWM spectrum of 9000 ppm methanol at 300 °C

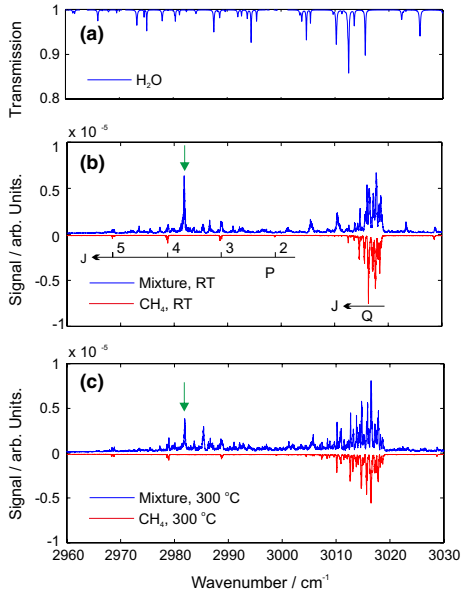

Fig. 5 Illustration of the CH_4 interference around 3000 cm^{-1}. **a** A simulated transmission spectrum of 0.5 % H_2O vapor in the ambient air and a path length of 3 m. **b** A measured IR-DFWM spectrum (*in blue*) in a mixture of 3200 ppm methanol and 250 ppm CH_4 gas flow, and a measured IR-DFWM spectrum (*in red*) in 270 ppm CH_4 gas flow at room temperature. Partial assignments for CH_4 lines have been made. **c** A measured IR-DFWM spectrum (*in blue*) in a mixture of 8300 ppm methanol and 850 ppm CH_4 gas flow, and a measured IR-DFWM spectrum (*in red*) in 800 ppm CH_4 gas flow at 300 °C. The *green arrow* indicates the Q-branch feature of methanol near 2982 cm^{-1}

assumed in those studies, as opposed to the forward phase-matching geometry investigated in this work. In panel (c), a continuous background-like signal arises at higher temperature, which is due to many upper vibrational levels of methanol molecules are further populated. The Q-branch feature near 2982 cm^{-1} is, however, very easy to identify. Therefore, this feature will be focused on in the discussion later.

A similar investigation was performed for the ν_1 mode of methanol. A simulated absorption spectrum of 2700 ppm methanol at room temperature and atmospheric pressure with a path length of 10 cm is shown in Fig. 4a. Two IR-DFWM scans were recorded, one in a gas flow of 2700 ppm of methanol in nitrogen at room temperature and one in a gas flow of 9000 ppm of methanol in nitrogen at 300 °C, respectively, shown in Fig. 4b, c. According to the work of Kleiner et al. [36], the unresolved feature marked with an arrow near 3681 cm^{-1} consists of two Q-branches: E: $J_{-1} \leftarrow J_0$ and E: $J_{+1} \leftarrow J_{+2}$. Each of these Q-branches contains many closely spaced transitions. Therefore, following the same argument, enhancement of the signal for this feature in the IR-DFWM spectra can also be seen.

As water vapor in the ambient air is a strong absorber in the mid-infrared spectral region, spectral lines that are not overlapping with strong water absorption lines need to be chosen when detecting methanol. A simulated transmission spectrum, based on molecular parameters extracted from the HITRAN database [37], with 0.5 % H_2O vapor in the ambient air and with a path length of 3 m (simulating the present setup), is shown in Fig. 5a. It can be seen that laser attenuation by H_2O absorption is negligible in the selected frequency range. Another species that could potentially interfere with methanol in several applications is CH_4. To illustrate that potential interference around 3000 cm^{-1}, a trace concentration of CH_4 was seeded into the methanol–nitrogen flow, preparing a mixture of methanol and CH_4, which were then further diluted in a nitrogen flow. Figure 5b shows an IR-DFWM spectrum (in blue) from a mixture of 3200 ppm methanol and 250 ppm CH_4 in nitrogen, and an IR-DFWM spectrum (in red) of 270 ppm CH_4 in nitrogen at room temperature. Figure 5c shows an IR-DFWM spectrum (in blue) in a mixture of 8300 ppm

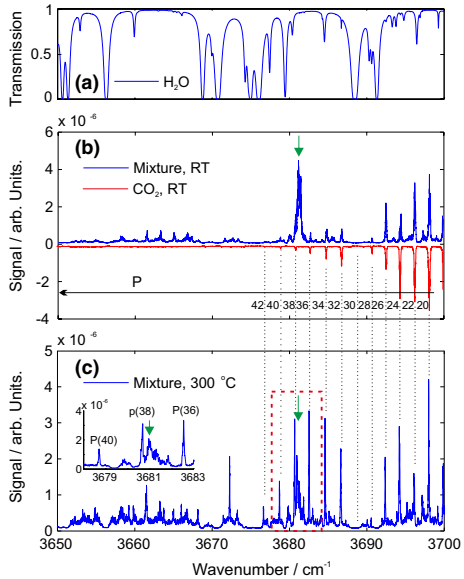

Fig. 6 Illustration of the CO_2 interference around 3680 cm^{-1}. **a** A simulated transmission spectrum of 0.5 % H_2O vapor in the ambient air and a path length of 3 m. **b** A measured IR-DFWM spectrum (*in blue*) in a mixture of 2700 ppm methanol and 1300 ppm CO_2 gas flow, and a measured IR-DFWM spectrum (*in red*) in 1300 ppm CO_2 gas flow at room temperature. Partial assignments for CO_2 lines have been made. **c** A measured IR-DFWM spectrum in a mixture of 8800 ppm methanol and 2100 ppm CO_2 gas flow at 300 °C. A zoom of part of the spectrum (marked by the *red dashed box*) is shown in the *inset*. The *green arrow* indicates the Q-branch feature of methanol near 3681 cm^{-1}

methanol and 850 ppm CH_4 in nitrogen, and an IR-DFWM spectrum (in red) of 800 ppm CH_4 in nitrogen at 300 °C. Hot CH_4 lines in the Q-branch can be identified by comparing the CH_4 spectra in Fig. 5b, c. It can be clearly seen that both at room temperature and at 300 °C, the methanol feature near 2982 cm^{-1} (marked by the green arrow) is free from CH_4 interference.

In the same manner as the previous section, water vapor absorption in the ambient air was studied to investigate the suitability of detecting methanol by its ν_1 band. Figure 6a shows a simulated transmission spectrum of 0.5 % H_2O vapor in the ambient air with a path length of 3 m. As can be seen, absorption due to water vapor is much more pronounced in this frequency range. Interference from CO_2 should also be considered when detecting methanol in combustion environments, since CO_2 is one of the most common product gases in combustion. To demonstrate the interference from CO_2 around 3680 cm^{-1}, a trace concentration of CO_2 was seeded into the methanol flow, preparing a mixture of methanol and CO_2 at trace concentration in the nitrogen flow. Figure 6b shows an IR-DFWM spectrum (in blue) acquired in a mixture of 2700 ppm methanol and 1300 ppm CO_2 gas flow, and an IR-DFWM spectrum (in red) in 1300 ppm CO_2 gas flow, both diluted in nitrogen and at room temperature. Figure 6c shows an IR-DFWM spectrum in a mixture of 8800 ppm methanol and 2100 ppm CO_2 diluted in nitrogen at 300 °C. An inset in Fig. 6c zooms in on the region where the methanol feature near 3681 cm^{-1}, marked by a green arrow, is close to the P(38) line of CO_2. Even though these two lines are partly overlapped in the wings, detection of methanol is free from CO_2 interference. It can be seen that the missing of P(30) line of CO_2 is due to strong laser attenuation by absorption from water vapor in the ambient air. However, detection of the methanol line near 3681 cm^{-1} is still feasible due to significantly lower H_2O absorption in the range from 3680 to 3682 cm^{-1}.

The dependency of the IR-DFWM signal on methanol number densities was investigated to demonstrate the quantitative ability of IR-DFWM. Figure 7 shows the line-integrated IR-DFWM signal intensities collected at different methanol concentrations at room temperature, by scanning over the Q-branch features near 2982 and 3681 cm^{-1}, respectively. The line-integrated IR-DFWM signals of three repeated scans were averaged for each concentration, and the error bars show the standard deviation. The line-integrated DFWM signal is expected to have a quadratic dependence on the concentration of the absorbed species under optically thin conditions [18]. Therefore, a quadratic function $S = a \cdot X^2$ was adopted to fit the signal–concentration curve, with which a satisfactory fitting was obtained. The small deviation from the quadratic fitting can be attributed to the self-absorption of the signal inside the tube, and the fact that the scanned methanol features contain many closely spaced transitions instead of only one transition which is assumed in the model. Based on the signal-to-noise ratio, detection limits were estimated to be approximately 350 and 250 ppm by detecting the Q-branch features near 2982 and 3681 cm^{-1}, respectively. The insets in Fig. 7 show the raw signals at 500 and 690 ppm methanol concentrations accordingly and illustrate the high signal levels obtained at these relatively low concentrations. The underlying regular pattern of fringes in the raw IR-DFWM signal is from periodic variations in the laser energy due to etalon effect in the dye laser during scanning.

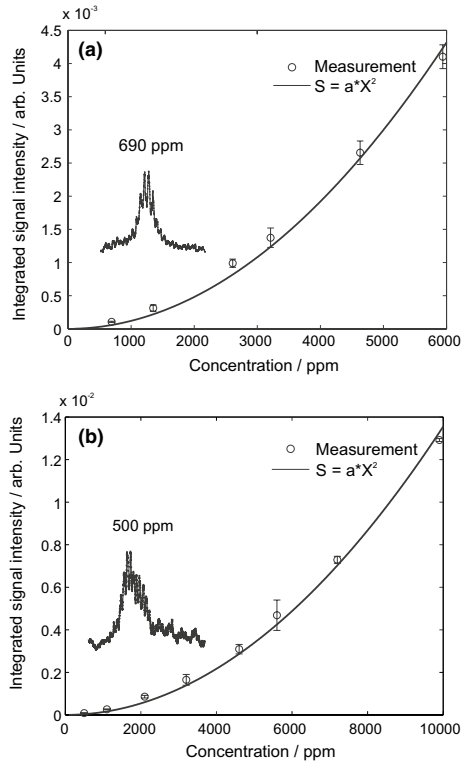

Fig. 7 Dependency of the IR-DFWM signal on methanol concentration by scanning over the Q-branch features near 2982 cm^{-1} (**a**) and 3681 cm^{-1} (**b**). The *insets* of **a**, **b** show the IR-DFWM signal at 690 ppm and 500 ppm, respectively. A quadratic function is used to fit the signal–concentration curve

4 Conclusions

In this work, we have demonstrated the potential of IR-DFWM as an in situ tool for sensitive and non-intrusive detection of gas-phase methanol with a spatial resolution of about 0.4 × 0.4 × 6 mm^3 and a temporal resolution of about 4 ns. This makes IR-DFWM an attractive candidate for the detection of gas-phase methanol. Traditional FTIR methods, often used for methanol detection, have limited spatial and temporal resolution, something the presented IR-DFWM technique can deliver and makes it a good complement for the detection of gas-phase methanol.

Owing to the coherent enhancement of the IR-DFWM signal from many closely spaced transitions in the Q-branches of methanol, the IR-DFWM spectra show much enhanced signal for the Q-branch features, making the spectra much more distinct than the absorption spectra. At the same time, the line-integrated IR-DFWM signal still shows a simple quadratic dependence on the methanol number density to a satisfactory degree, simplifying the quantitative analysis significantly.

Two interference-free detection schemes (by detecting Q-branch features near 2982 and 3681 cm^{-1}) have been proposed. Laser attenuation by water vapor absorption in the ambient air has been shown theoretically to be insignificant. Both detection schemes can achieve detection limits down to hundreds of ppm at room temperature and atmospheric pressure. When the Q-branch feature near 2982 cm^{-1} is used, its close proximity to the P(4) line of CH_4 provides the possibility of combined detection of methanol and CH_4. Similarly, when the Q-branch feature near 3681 cm^{-1} is used, its close proximity to P(38) line of CO_2 gives the possibility of combined detection of methanol and CO_2. This can be very useful when detecting methanol in catalytic reactions, e.g., CO_2 hydrogenation and CH_4 oxidation.

Acknowledgments This work was financially supported by the Knut and Alice Wallenberg Foundation and the Carl Trygger Foundation for Scientific Research.

References

1. http://www.methanol.org/. Accessed May 2015
2. I. Ganesh, Renew. Sustain. Energy Rev. **31**, 221 (2014)
3. W. Wang, S.P. Wang, X.B. Ma, J.L. Gong, Chem. Soc. Rev. **40**, 3703 (2011)
4. Y.M. Chen, D.E. Clemmer, P.B. Armentrout, J. Am. Chem. Soc. **116**, 7815 (1994)
5. M.Z. Florian, J.B. Euan, K. Johannes, Meas. Sci. Technol. **23**, 045602 (2012)
6. J.J. Harrison, N.D.C. Allen, P.F. Bernath, J. Quant. Spectrosc. Radiat. Transfer **113**, 2189 (2012)
7. M. Alrefae, E.T. Es-sebbar, A. Farooq, J. Mol. Spectrosc. **303**, 8 (2014)
8. G. Maisons, P.G. Carbajo, M. Carras, D. Romanini, Opt. Lett. **35**, 3607 (2010)
9. R.L. Abrams, R.C. Lind, Opt. Lett. **2**, 94 (1978)
10. R.L. Abrams, R.C. Lind, Opt. Lett. **3**, 205 (1978)
11. T.A. Reichardt, R.P. Lucht, P.M. Danehy, R.L. Farrow, J. Opt. Soc. Am. B Opt. Phys. **15**, 2566 (1998)
12. R.T. Bratfalean, G.M. Lloyd, P. Ewart, J. Opt. Soc. Am. B Opt. Phys. **16**, 952 (1999)
13. P. Ewart, S.V. Oleary, Opt. Lett. **11**, 279 (1986)
14. P. Ewart, P. Snowdon, Opt. Lett. **15**, 1403 (1990)
15. R.L. Farrow, D.J. Rakestraw, Science **257**, 1894 (1992)
16. K. Kohsehoinghaus, Prog. Energy Combust. Sci. **20**, 203 (1994)
17. A.C. Eckbreth, *Laser Diagnostics for Combustion Temperature and Species* (Gordon and Breach, Amsterdam, 1996)
18. J. Kiefer, P. Ewart, Prog. Energy Combust. Sci. **37**, 525 (2011)
19. R.L. Vanderwal, B.E. Holmes, J.B. Jeffries, P.M. Danehy, R.L. Farrow, D.J. Rakestraw, Chem. Phys. Lett. **191**, 251 (1992)

20. G.J. Germann, D.J. Rakestraw, Science **264**, 1750 (1994)
21. G.J. Germann, R.L. Farrow, D.J. Rakestraw, J. Opt. Soc. Am. B Opt. Phys. **12**, 25 (1995)
22. K. Richard, P. Ewart, Appl. Phys. B Lasers Opt. **94**, 715 (2009)
23. Y. Tang, S.A. Reid, Chem. Phys. Lett. **248**, 476 (1996)
24. Z.W. Sun, Z.S. Li, B. Li, M. Alden, P. Ewart, Appl. Phys. B Lasers Opt. **98**, 593 (2010)
25. A.L. Sahlberg, J. Zhou, M. Aldén, Z.S. Li, J. Raman. Spectrosc. **46**, 695 (2015)
26. R.H. Hunt, W.N. Shelton, W.B. Cook, O.N. Bignall, J.W. Mirick, F.A. Flaherty, J. Mol. Spectrosc. **149**, 252 (1991)
27. O.N. Bignall, R.H. Hunt, W.N. Shelton, J. Mol. Spectrosc. **166**, 137 (1994)
28. L.H. Xu, X. Wang, T.J. Cronin, D.S. Perry, G.T. Fraser, A.S. Pine, J. Mol. Spectrosc. **185**, 158 (1997)
29. G.L. Villanueva, M.A. DiSanti, M.J. Mumma, L.H. Xu, Astrophys. J. **747**, 37 (2012)
30. Z.T. Alwahabi, J. Zetterberg, Z.S. Li, M. Alden, Eur. Phys. J. D **42**, 41 (2007)
31. Z.S. Li, M. Rupinski, J. Zetterberg, Z.T. Alwahabi, M. Alden, Chem. Phys. Lett. **407**, 243 (2005)
32. P.M. Chu, F.R. Guenther, G.C. Rhoderick, W.J. Lafferty, *Quantitative Infrared Database* (National Institute of Standards and Technology, Gaithersburg, 1999), p. 20899
33. T.A. Reichardt, R.P. Lucht, J. Opt. Soc. Am. B Opt. Phys. **14**, 2449 (1997)
34. C.F. Kaminski, I.G. Hughes, P. Ewart, J. Chem. Phys. **106**, 5324 (1997)
35. G.M. Lloyd, P. Ewart, J. Chem. Phys. **110**, 385 (1999)
36. I. Kleiner, G.T. Fraser, J.T. Hougen, A.S. Pine, J. Mol. Spectrosc. **147**, 155 (1991)
37. L.S. Rothman, I.E. Gordon, A. Barbe, D.C. Benner, P.E. Bernath, M. Birk, V. Boudon, L.R. Brown, A. Campargue, J.P. Champion, K. Chance, L.H. Coudert, V. Dana, V.M. Devi, S. Fally, J.M. Flaud, R.R. Gamache, A. Goldman, D. Jacquemart, I. Kleiner, N. Lacome, W.J. Lafferty, J.Y. Mandin, S.T. Massie, S.N. Mikhailenko, C.E. Miller, N. Moazzen-Ahmadi, O.V. Naumenko, A.V. Nikitin, J. Orphal, V.I. Perevalov, A. Perrin, A. Predoi-Cross, C.P. Rinsland, M. Rotger, M. Simeckova, M.A.H. Smith, K. Sung, S.A. Tashkun, J. Tennyson, R.A. Toth, A.C. Vandaele, J. Vander Auwera, J. Quant. Spectrosc. Radiat. Transfer **110**, 533 (2009)

Printed by Media-Tryck, Lund 2018 NORDIC SWAN ECOLABEL 3041 0903

Faculty of Engineering
Department of Physics

Lund Reports on Combustion Physics, LRCP-216
ISBN 978-91-7753-864-6
ISSN 1102-8718